To the Graduate Council:

I am submitting herewith a dissertation written by Ismail entitled "The Structure and Dynamics of Magnesium Surfaces." I have examined the final copy of this dissertation for form and content and recommend that it be accepted in partial fulfillment of the requirements for the degree of Doctor of Philosophy, with a major in Physics.

E. Ward Plummer, Major Professor

We have read this dissertation
and recommend its acceptance:

Accepted for the Council:

Associate Vice Chancellor and
Dean of The Graduate School

THE STRUCTURE AND DYNAMICS OF MAGNESIUM SURFACES

A Dissertation

Presented for the

Doctor of Philosophy

Degree

The University of Tennessee, Knoxville

ISMAIL

August 1999

DEDICATION

This thesis is dedicated to:

my parents, brothers, and sisters;

my sons Haris and Pendry;

my wife, Tri Hartini, for supporting and loving.

ACKNOWLEDGMENTS

I have been truly blessed by God (Allah s.w.t.) to be surrounded by a wonderful family, special friends, and outstanding people.

There are many people to whom I should be thankful for making my time during my graduate school life at the University of Tennessee so meaningful. First and foremost, I would like to thank my advisor Dr. E. Ward Plummer, for his support, guidance, and encouragement during my entire doctoral program. I would also like to thank Dr. D. M. Zehner who has supplied guidance and support. I am indebted to Prof. P. J. Rous for teaching me how to determine the surface determination by LEED *I-V* analysis. I am also indebted to Philip Hofmann and Jim Hannon for teaching how to do EELS experiment.

I am grateful for the time and expertise of my graduate committee members Dr. T. A. Callcott, Dr. H. H. Weitering, Dr. C. S. Feigerle, and Dr. Z. Y. Zhang. I would like to thank all of you for suggestions and contributions to this thesis project. I would also like to thank Kirsten Benson and Timothy O. Edwards for a great source of help and advise about my English.

The students in the group, including Curt, Karsten, Aubrey, Joe, Bong-Ok, Girish, Tolik, John, and Dane have provided me a great source of help over the years. The new student in the group, including Jian, Alex, and Haihang have also been great to have around. I would like to thank the postdocs in the group, including Jiandi, Larry, Rene, and Jens for a great source of advise about physics. I would also like to thank Nikki and Mary Jo, the secretaries in the group.

The staff at ORNL has been very nice. I am particularly grateful to Art Baddorf, Gary Ownby, and John Wandelken for a great source of advice and help. I would like to thank David Zehner again for letting me joint the surface physics group at ORNL. I would also like to thank Vicki Barn, the secretary in the surface physics group at ORNL. I am

indebted to Sharron King for a great source of advise and help when it came to computer problems with Solid and The Flange.

Lastly, I would like to thank my incredible wife, Tri Hartini. Without her help, encouragement, and support I would never have reached for this moment.

ABSTRACT

THE STRUCTURE AND DYNAMICS OF MAGNESIUM SURFACES

ISMAIL

E. WARD PLUMMER

Low-energy electron diffraction (LEED) *I-V* and momentum resolved inelastic electron scattering have been utilized to study the structure and dynamics of the Mg(0001) and Mg(10$\bar{1}$0) surfaces. Magnesium was chosen since it is a free-electron-like metal, which is an ideal test for first principles calculations.

No reconstruction was found on the Mg(0001) and Mg(10$\bar{1}$0) surfaces from temperatures 120 K to 400 K. For the Mg(0001) surface, the first interlayer spacing is expanded by +1.96 % at T=130 K, +2.34 % at T=300 K, and +2.48 % at T=400 K. The thermal expansion of this surface is almost the same as in the bulk Mg. The temperature dependent measurements of the atomic structure of the Mg(10$\bar{1}$0) surface revealed that the interlayer spacings, $d_{i,i+1}$, exhibited *a remarkable oscillatory thermal expansion.* As the temperature increases, the short interplanar spacings $d_{1,2}$, $d_{3,4}$, and $d_{5,6}$ contract, while the long interplanar spacings $d_{2,3}$, $d_{4,5}$, and $d_{6,7}$ expand. The surface thermal expansion for the first short interlayer spacing is -7 x α_B, where $\alpha_B \approx 25\text{x}10^{-6}$ K^{-1} (bulk thermal expansion); while the first long interlayer spacing d_{23} exhibits a large thermal expansion +5 x α_B. The second short interlayer spacing displays a negative thermal expansion of -10 x α_B, the second long interlayer d_{45} shows a positive thermal expansion of 2 x α_B, the third short interlayer d_{56} shows a negative thermal expansion (-1 x α_B), and the third long interlayer

spacing d_{67} displays a positive thermal expansion (+3 x α_B). The net thermal expansion of the whole surface region, defined as the spacing between plane 1 and 7 is about the same as for the bulk. This is *the first time* such deep oscillatory interplanar thermal expansion has been observed at a surface. First-principles density-functional calculations indicate that the unusual oscillatory thermal relaxation is driven by the tendency of the short interlayer or bilayer to collapse into a single layer. For both surfaces, when the temperature dependent measurements are extrapolated to T=0 K, they are in excellent agreement with the T=0 K calculations.

For Mg(0001), there are three layers involved in the surface dynamics; while for Mg(10$\bar{1}$0), the surface dynamics involve up to six layers (deep layers). The number of layers involved in the surface dynamics is strongly related to the interlayer spacing. Qualitatively, the bulk force constant model is able to reproduce the measured Rayleigh wave dispersion along the zone boundary $\bar{K}$-$\bar{M}$ for the Mg(0001) surface, which is similar to the case of the Al(111) surface, but contradicted to the case of the Be(0001) surface. In general, the surface lattice dynamics of Mg(0001) are similar to those of Be(0001) and Al(111), which are consistent with their electronic properties. Nonetheless, the nature of the surface force constants for an *open* surface metal, i.e., the Mg(10$\bar{1}$0) surface, is *significantly* different than in the bulk.

No enhanced surface anharmonicity at the Mg(0001) and Mg(10$\bar{1}$0) surfaces was observed. For the Mg(10$\bar{1}$0) surface, the enhanced surface anharmonicity could be in the sublayers, which is difficult to be detected experimentally. The vibrational modes localized in the sublayers could be important to explain the oscillatory thermal expansion at the Mg(10$\bar{1}$0) surface.

TABLE OF CONTENTS

	PAGE
Chapter 1: Structure and Dynamics of Surfaces	1
1.1 Friedel Oscillations	2
1.2 Charge Smoothing	5
1.3 Electronic Surface States	7
1.4 Surface Structure	11
1.4.1 First Interlayer Relaxation	11
1.4.2 Stress and Reconstruction	14
1.4.3 Deep Interlayer Relaxation	16
1.4.4 The Contribution of Surface States to Surface Structure	20
1.5 Surface Phonons	21
1.6 Temperature Effects at Surfaces	36
1.7 Magnesium Surfaces	44
1.8 Thesis Syllabus	51
1.9 References	52
Chapter 2: Experimental Techniques and Analytical Procedures	58
2.1 Ultra High Vacuum System	58
2.2 Sample Preparation	58
2.3 Low Energy Electron Scattering from Surfaces	62
2.3.1 Theory	62
2.3.1.1 Atomic Phase Shifts	84

2.3.1.2 Multiple Scattering 90

2.3.1.3 Structural and Non-structural parameters 94

2.3.1.4 Tensor LEED Approximation 96

2.3.1.5 Reliability Factor and Error-bar in the LEED *I-V* Calculations 98

2.3.2 Computer Codes 102

2.3.3 LEED Experiment 102

2.4 Electron Energy Loss Spectroscopy (EELS) 112

2.5 References 119

Chapter 3: Thermal Effects on the Surface Structure of Mg(0001) and Mg(10$\bar{1}$0) 121

3.1 The Mg(0001) Surface 123

3.1.1 Introduction 123

3.1.2 Experiment and Analysis 126

3.1.3 Results and Discussion 137

3.1.4 Conclusions 147

3.2 The Mg(10$\bar{1}$0) Surface 147

3.2.1 Introduction 147

3.2.2 Experiment and Analysis 149

3.2.3 Results and Discussion 154

3.2.4 Conclusions 183

3.3 References 185

Chapter 4: Surface Lattice Dynamics of Mg(0001) and Mg(10$\bar{1}$0) 188

4.1 Introduction 188

4.2 Surface Phonons of Mg(0001) 193

4.2.1 Experimental data 193

4.2.2 A Comparison of Mg(0001) with Be(0001) and Al(111) 202

4.2.3 Ab Initio Calculations at T=0 K 212

4.2.4 Surface Anharmonicity of Mg(0001) 220

4.3 Surface Phonons of Mg(10$\bar{1}$0) 223

4.3.1 Experimental data 223

4.3.2 A Comparison of Mg(10$\bar{1}$0) with Be(10$\bar{1}$0) and Al(110) 235

4.3.3 Ab Initio Calculations at T=0 K 244

4.3.4 Surface Anharmonicity of Mg(10$\bar{1}$0) 249

4.4 Conclusions 253

4.5 References 255

Chapter 5: Overview: The Interplay between the Structure and Dynamics of Simple Metal Surfaces 257

5.1 Geometric Structure of Surfaces 257

5.2 Surface Dynamics 263

5.3 Thermal Effects at Metal Surfaces 264

5.4 Conclusions 270

5.5 References 272

Bibliography 274

Appendices 284

Appendix A: Atomic Phase Shifts 285

Appendix B: Conversions 294

Appendix C: Formulae for the Free Electron Gas 295

Vita 296

LIST OF TABLES

TABLE		PAGE
1.1.	Some examples of multilayer relaxations for close metal surfaces	17
1.2.	Some examples of multilayer relaxations for open metal surfaces	17
1.3.	Some examples of multilayer relaxations for open metal surfaces for high Miller indices	18
1.4.	Simulated vibrational occupancy probabilities for a Morse potential with $\hbar\omega$=14.75 meV and X_a=0.035	33
1.5.	Simulated vibrational occupancy probabilities for a Morse potential with $\hbar\omega$=43.0 meV and X_a=0.035	33
1.6.	List of the first interlayer relaxation from calculations and experiments at finite temperatures	38
1.7.	Comparison of bulk properties of magnesium (Mg) and aluminum (Al)	47
3.1.	Lattice constants of bulk magnesium and the interlayer distance of the Mg(0001) surface for three temperatures studied	137
3.2.	Geometric parameters extracted from the best-fit spectra to the LEED *I-V* data of Mg(0001) as a function of temperature	138
3.3.	Comparison of the first interlayer relaxation for the Mg(0001) surface between calculations and our experimental results (extrapolated to T=0 K)	144
3.4.	Comparison between the structure of Mg($10\bar{1}0$) at T=120 K and the previous structural studies of hcp($10\bar{1}0$)	155
3.5.	Geometric parameters extracted from the best-fit spectra to the LEED *I-V* data of model I (only one layer was varied in the calculations) for Mg($10\bar{1}0$) as a function of temperature	161

TABLE PAGE

3.6. Geometric parameters extracted from the best-fit spectra to the LEED *I-V* data of model II (only two layers were varied in the calculations) for $Mg(10\bar{1}0)$ as a function of temperature 162

3.7. Geometric parameters extracted from the best-fit spectra to the LEED *I-V* data of model III (only three layers were varied in the calculations) for $Mg(10\bar{1}0)$ as a function of temperature 164

3.8. Geometric parameters extracted from the best-fit spectra to the LEED *I-V* data of model IV (four layers were varied in the calculations) for $Mg(10\bar{1}0)$ as a function of temperature 165

3.9. Geometric parameters extracted from the best-fit spectra to the LEED *I-V* data of model V (five layers were varied in the calculations) for $Mg(10\bar{1}0)$ as a function of temperature 167

3.10. Geometric parameters extracted from the best-fit spectra to the LEED *I-V* data of model VI (six layers were varied in the calculations) for $Mg(10\bar{1}0)$ as a function of temperature 168

3.11. *Rp* factors for models I - VI for all three temperatures studied 177

3.12. Surface thermal expansion of $Mg(10\bar{1}0)$ with respect to the bulk for models I - VI 177

3.13. Comparison of the experimental data extrapolated to T=0 K for the $Mg(10\bar{1}0)$ surface with the T=0 K calculations 179

TABLE		PAGE
4.1.	Force constants (FC's) for bulk magnesium determined from Neutron scattering data	200
4.2.	Measured Rayleigh wave (*RW*) with respect to the *RW* from BT calculations (using bulk force constants) at the zone boundaries for close packed simple metal surfaces	205
4.3.	Rayleigh wave (*RW*) at the zone boundaries from experiment and bulk truncated calculations for close packed metal surfaces	208
4.4.	Calculated and measured surface phonon frequencies of Mg(0001) at the two high symmetry points of SBZ, $\overline{K}$ and $\overline{M}$	215
4.5.	Displacement amplitudes (normalized to unity) and the phase (in degree) for surface modes at the zone boundary $\overline{M}$ of the Mg($10\bar{1}0$) surface	231
4.6.	Displacement amplitudes and the phase for surface modes at the zone boundary $\overline{A}$ of the Mg($10\bar{1}0$) surface	234
4.7.	Rayleigh wave (*RW*) at the zone boundaries from experiment and BT calculations for open simple metal surfaces	237
4.8.	Measured Rayleigh wave (*RW*) with respect to the *RW* from BT calculations (using bulk force constants) at the zone boundaries for open simple metal surfaces	241
A.1.	Phase shifts for magnesium (Mg)	285
A.2.	Phase shifts for Sn (tin)	288
A.3.	Phase shifts for Ge (germanium)	291

LIST OF FIGURES

FIGURE		PAGE
1.1.	Charge density profile near the metal surface in the jellium model (Lang-Kohn charge density profile) for r_s=2 a.u. and r_s=5 a.u.	4
1.2.	Illustration of the Smoluchoski effect	6
1.3.	Layer-resolved local density of states for a surface	8
1.4.	Measured surface states for the Al(110) surface	9
1.5.	Calculated and measured dispersion of surface states of Be(0001)	10
1.6.	Relaxation in the first interlayer for simple metal surfaces	13
1.7.	Vibrational modes of an infinite diatomic chain	23
1.8.	Calculated surface phonon dispersion for a hcp$(10\bar{1}0)$ surface by using the Born-von Kármán scheme	26
1.9.	Harmonic and anharmonic interatomic potentials	31
1.10.	Simulated vibrational spectra at temperatures T=10 K, 120 K, and 300 K for a Morse potential with $\hbar\omega$=14.75 meV and X_a=0.035	35
1.11.	First-principles calculations at T=0 K and our experimental data of the temperature-dependent relaxations at the Mg$(10\bar{1}0)$ surface	43
1.12.	Bulk hexagonal close-packed structure	45
1.13.	Geometry of the Mg(0001) surface	47
1.14.	Measured surface states at the Mg(0001) surface	49
1.15.	Calculated surface electronic structure at the Mg(0001) surface	49
1.16.	The geometry of bulk truncated models (*short termination* and *long termination*) of the Mg$(10\bar{1}0)$ surface	50

FIGURE PAGE

2.1. Laue pattern from the magnesium crystal used for the experiment in this thesis 59

2.2. LEED photo from the Mg(0001) surface at the kinetic energy of electron E=50 eV at room-temperature 61

2.3. Auger spectrum for the clean Mg(10$\bar{1}$0) surface 63

2.4. EELS spectrum for the clean Mg(10$\bar{1}$0) surface 63

2.5. Universal Curve of electron mean-free paths in various materials 64

2.6. Electron scattering process in LEED 65

2.7. Calculated intensity as a function of the energy in the kinematic approximation by ignoring lifetime of the electron for the model described in the text 69

2.8. "Universal Curve" of electron mean-free path in various metals together with the electron mean-free path from a simple calculation 71

2.9. Reflected intensities for various imaginary parts of the optical potential and an infinite electron mean-free-path 72

2.10. Reflected intensities for various real parts of the optical potential 74

2.11. Schematic multiple scattering process for a simple 75

2.12. Reflected intensities for a simple model in the kinematic approximation and multiple scattering 77

2.13. Reflected intensities from multiple scattering calculations 78

2.14. Reflected intensities from the (00) beam 79

2.15. Surface structure determination by techniques until the end of 1997 81

FIGURE PAGE

2.16. Number of surface structure determinations vs year: by LEED and LEED plus other thechniques 82

2.17. Muffin-tin potential: plan view and sectional view 83

2.18. Muffin-tin potential for magnesium 87

2.19. Atomic phase shifts (δ_l) as a function of energy for magnesium 88

2.20. The scattering amplitude squared for l_{max}=9, 12, 13, and 14 as a function of the energy for magnesium 89

2.21. The scattering amplitude squared as a function of polar angle for magnesium 91

2.22. Mechanism of the renormalized forward scattering (RFS) perturbation method used in the LEED *I-V* calculations 93

2.23. Typical LEED *I-V* spectra as a function of temperature 95

2.24. The *Rp*-factor versus the displacement of the first interlayer spacing from the optimized position 101

2.25. Flowchart for structural determination by LEED 103

2.26. Schematic of a four grids LEED display system 105

2.27. Schematic set up of LEED *I-V* experiment 106

2.28. Measured LEED *I-V* spectra of the Mg(0001) surface 108

2.29. Scattering geometry in electron energy loss spectroscopy 113

2.30. Layout of EELS spectrometer - HIB 1000 (VSW) 117

2.31. EELS spectrum at the Mg(0001) surface 118

FIGURE		PAGE
3.1.	LEED photo from the Mg(0001) surface at energy E=50 eV at room-temperature	127
3.2.	Bulk truncated model of the Mg(0001) surface	128
3.3.	Beam assignments for LEED pattern of the Mg(0001) surface	129
3.4.	Measured and calculated LEED I-V spectra for the optimized structures of Mg(0001) at the temperatures$T$=130 K, 300 K, and 400 K	131
3.5.	The intensities of the (01) beam at energy E=111 eV as a function of temperature at the Mg(0001) surface	135
3.6.	Displacement of the first interlayer spacing from the optimized value, while the other parameters are fixed at the optimized values given in Table 3.2	140
3.7.	Measured interplanar relaxations as a function of temperature for Mg(0001) together with the previous the previous studies	143
3.8.	The first and second interlayer relaxations with respect to the bulk as a function of temperatures for the Be(0001) and Mg(0001) surfaces	146
3.9.	Structural model for the $Mg(10\bar{1}0)$ surface	148
3.10.	LEED pattern of $Mg(10\bar{1}0)$ at E=50 eV at room-temperature	150
3.11.	Reciprocal vectors and beams assignment for the $Mg(10\bar{1}0)$ surface	149
3.12.	The intensities of the (01) beams at E=111 eV for the Mg(0001) surface and at E=116.5 eV for the $Mg(10\bar{1}0)$ surface as a function of temperature together with the fit by exponential functions	153
3.13.	Measured and calculated relaxations of simple metal surfaces	157

FIGURE PAGE

3.14. Measured and calculated LEED *I-V* spectra for the optimized structures of Mg(10$\bar{1}$0) at temperatures *T*=120 K, 300 K, and 400 K 169

3.15. Surface relaxations for the Mg(10$\bar{1}$0) surface versus the normal distance from the surface toward the bulk for models I-VI at temperature *T*=120 K 176

3.16. Relaxations of the Mg(10$\bar{1}$0) surface as a function of temperatures 180

3.17. Calculated dependency of d_{12} with varying d_{23} by keeping all other layers fixed at the relaxed values for *T*=0 K 182

4.1. Dispersion of vibrational modes at the Be(0001) surface 190

4.2. The geometry of bulk truncated model of the hcp(0001) surface and its surface Brillouin zone 194

4.3. EELS spectrum from the Mg(0001) surface at $\overline{\mathrm{K}}$(q=1.304 Å^{-1}) along the $\overline{\Gamma}$-$\overline{\mathrm{K}}$-$\overline{\mathrm{M}}$ direction with the energy resolution FWHM of 4.2 meV 195

4.4. A series of EELS spectra from the Mg(0001) surface along the $\overline{\Gamma}$-$\overline{\mathrm{K}}$-$\overline{\mathrm{M}}$ and $\overline{\Gamma}$-$\overline{\mathrm{M}}$ directions 197

4.5. EELS spectra at $\overline{\mathrm{K}}$ at three different geometries 198

4.6. EELS spectra at $\overline{\mathrm{M}}$ from two different directions, along the $\overline{\Gamma}$-$\overline{\mathrm{K}}$-$\overline{\mathrm{M}}$ direction and along the $\overline{\Gamma}$-$\overline{\mathrm{M}}$ direction 199

4.7. Measured surface phonon dispersion for Mg(0001) together with a calculation for a bulk-terminated 150 layer slab 201

4.8. Surface phonons for the Al(111) surface 204

FIGURE PAGE

4.9. Measured bulk phonon dispersion along the Γ-K direction for magnesium and beryllium 209

4.10. Measured bulk phonons for Al together with the calculations by using central forces (axially symmetric forces) 211

4.11. Surface phonon dispersion at the Mg(0001) surface 213

4.12. Square of the amplitude of the atomic displacements for the surface vibration at $\overline{K}$ point at the Mg(0001) surface 216

4.13. Square of the amplitude of the atomic displacements for the surface vibrations at the $\overline{M}$ points at the Mg(0001) surface 218

4.14. Temperature dependent phonons at the Mg(0001) surface along the $\overline{\Gamma}$-$\overline{K}$ direction at q=1.304 $\AA^{-1}$ (at $\overline{K}$ point) 221

4.15. Energy and intrinsic width of surface phonons for the Mg(0001) surface as a function of temperatures at the zone boundary $\overline{K}$ along the $\overline{\Gamma}$-$\overline{K}$ direction 222

4.16. Top view of the bulk truncated geometric of the hcp(10$\bar{1}$0) surface and its surface Brillouin zone 224

4.17. EELS spectrum from the Mg(10$\bar{1}$0) surface at $\overline{M}$ along the $\overline{\Gamma}$-$\overline{M}$ direction 225

4.18. EELS spectrum from the Mg(10$\bar{1}$0) surface at $\overline{A}$ along the $\overline{\Gamma}$-$\overline{A}$ direction 227

4.19. A series of EELS spectra at the Mg(10$\bar{1}$0) surface along the $\overline{\Gamma}$-$\overline{M}$ direction 228

FIGURE PAGE

4.20. A series of EELS spectra at the Mg(10$\bar{1}$0) surface along the $\bar{\Gamma}$-$\bar{A}$ direction 229

4.21. Measured surface phonon dispersion for Mg(10$\bar{1}$0) together with a calculation for a bulk-terminated 254 layer slab 230

4.22. Measured surface phonon dispersion for the Be(10$\bar{1}$0) surface together with a bulk-truncated calculations by using the bulk force constants 239

4.23. Surface phonon dispersion for the Al(110) surface 240

4.24. Vertical atomic displacements at $\bar{M}$ for the Mg(10$\bar{1}$0) surface 243

4.25. Vertical atomic displacements at $\bar{A}$ for the Mg(10$\bar{1}$0) surface 245

4.26. Surface phonon dispersion at the Mg(10$\bar{1}$0) surface from *ab initio* calculations together with our experimental data 247

4.27. Square of the amplitude of the atomic displacements for the Rayleigh waves in the surface layer and second layer at $\bar{M}$ points for the Mg(10$\bar{1}$0) surface from *ab initio* calculations 248

4.28. Temperature dependent phonons for the Mg(10$\bar{1}$0) surface at $\bar{A}$ along the $\bar{\Gamma}$-$\bar{A}$ direction 250

4.29. Temperature dependent phonons for the Mg(10$\bar{1}$0) surface at $\bar{M}$ along the $\bar{\Gamma}$-$\bar{M}$ direction 251

4.30. Temperature dependent energy and intrinsic width of the surface phonons for the Mg(10$\bar{1}$0) surface at $\bar{A}$ along the $\bar{\Gamma}$-$\bar{A}$ direction and at $\bar{M}$ along the $\bar{\Gamma}$-$\bar{M}$ direction 252

FIGURE PAGE

5.1. Measured and calculated relaxations of simple metal surfaces 260

5.2. Vertical atomic displacements at $\overline{M}$ of the Mg(10$\bar{1}$0) surface 265

5.3. Vertical atomic displacements at $\overline{A}$ of the Mg(10$\bar{1}$0) surface 266

5.4. Measured interplanar relaxations as a function of temperature for Mg(0001) together with the previous experimental study and theoretical studies 267

5.5. Relaxations of the Mg(10$\bar{1}$0) surface as a function of temperature 269

Chapter 1

Structure and Dynamics of Surfaces

When a bulk material is separated into two halves exposing two pristine surfaces, the atoms at the surface lose some of their coordinations, the translation symmetry perpendicular to the surface is broken, i.e., the translation vectors from three dimensions (bulk) become two dimensions (parallel to surface), and the surface then becomes a *new body* that has a new symmetry. The electrons near the surface will respond to this new environment, readjusting themselves rapidly due to the presence of a local charge imbalance or the presence of the surface in order to lower their kinetic energy, which is known as the phenomenon of screening. This phenomenon is very important because many physical properties of a material are governed by the screening-electrons. These charge rearrangements in the vicinity of surface lead the properties of the surface to be different than the bulk. For example, the creation of the surface leads to inherently *anisotropic screening and enhanced noncentral force constants at the surface* [1] and *thermal contraction at metal surfaces* [2-4]. The most commonly observed phenomena as the consequences of broken symmetry are surface states, narrow bandwidths, reconstruction, relaxations, surface vibrational modes, and surface magnetism.

Even though theoretical calculations of surface properties are relatively more difficult compared to bulk properties because of the loss of transitional symmetry of lattice perpendicular to surface, state-of-the-art calculations with help from fast computer processors have elucidated many fundamental concepts of the properties of surfaces. In the next sections I will discuss how electrons readjust themselves and what electrons do in the vicinity of surface as the consequences of broken symmetry, a creation of the surface.

1.1 Friedel Oscillations

As mentioned above, one of the most important concepts in solid state physics is screening: the rearrangement of the electrons in order to minimize their kinetic energy due to the disturbance of an impurity or defect. Friedel showed that the screening of a point-charged impurity in the bulk metal results in long-range damped oscillatory behavior of the electron density [5]. The wave-vector of these oscillations is $2k_F$, where k_F is the Fermi wave-vector. At a metal surface, the screening of a defect due to the presence of a surface results in an oscillation of the charge density perpendicular to the surface [6], while the screening of a point-charged impurity or defect on the surface results in charge density oscillations parallel to the surface [7,8].

An early work of an approximately self-consistent calculation in electronic structure was performed by Bardeen [9]. Subsequently, Kohn and Sham [10,11] introduced a formulation of theory for inhomogeneous electron density systems that can be applied for electronic structure calculations of metal surfaces. Bennet and Duke [12] used the Hohenberg-Kohn-Sham's theory to perform an approximately self-consistent calculation in electronic structure for a metal surface in which the ion cores are replaced by a uniform semi-infinite positive charge density. Then in 1970, Lang and Kohn [6] performed a *fully self-consistent* calculation for the jellium model (the discrete ion cores are replaced by a uniform background semi-infinite positive charge with density equal to a density of homogeneous electron gas) of a metal surface. The density of homogeneous electron gas n_o is given by:

$$\frac{1}{n_0 a_0^3} = \frac{4\pi}{3} r_s^3 \qquad (1.1)$$

where a_0 is the Bohr radius and r_s is the radius of the sphere containing one electron. A high density metal has small r_s, while a low density metal has large r_s.

Their results revealed two very important features of a metal surface, as shown in Figure 1.1, which has had a significant impact on surface physics. First, due to the creation of the surface, the charge densities of electrons at the surface "spill out" into the vacuum region, creating an electrostatic dipole layer at the surface. There is no sharp edge to the electron charge density distribution between vacuum and metal regions. Second, the long-range charge density oscillations (Friedel oscillations) arise perpendicular to the normal surface as the electrons screen out the presence of the surface. This oscillation is a damped oscillatory, which is perpendicular into the bulk with a periodicity equal to one-half of the Fermi wave length, i.e., $\lambda = \pi/k_F$. These charge densities have long-range interaction in metals. For a metal having small r_s, such as aluminum (i.e., r_s=2.07), the amplitude of the Friedel oscillations is less pronounced and less charge "spills out" into the vacuum in comparison to a metal having large r_s. Beyond the jellium model, in the real lattice when the ionic potentials are considered explicitly, this Friedel oscillation exists, as shown in the case of magnesium [13,14]. The period of the oscillations is very close to the value within the jellium model of an electron gas, while the amplitudes of the oscillations in the presence of the lattice are attenuated by about a factor of two if compared with that of the Lang-Kohn charge density profile [6,13]. This Friedel oscillation perpendicular to the surface contributes to the oscillatory relaxations of metal surfaces [13,14].

The Friedel oscillations parallel to the surface have been observed recently by using low temperature Scanning Tunneling Microscopy (STM) [7,8]. Sprunger *et al.* observed the surface Friedel oscillations on the Be(0001) surface [7]. The two dimensional Fourier transforms of their STM images can be directly related to the two-dimensional electronic band structure at the surface (the surface Brillouin zone), leading to a direct measurement of the surface Fermi wavevector. Similarly, this kind of Friedel oscillation was also observed in the case of the $Be(10\bar{1}0)$ surface [8].

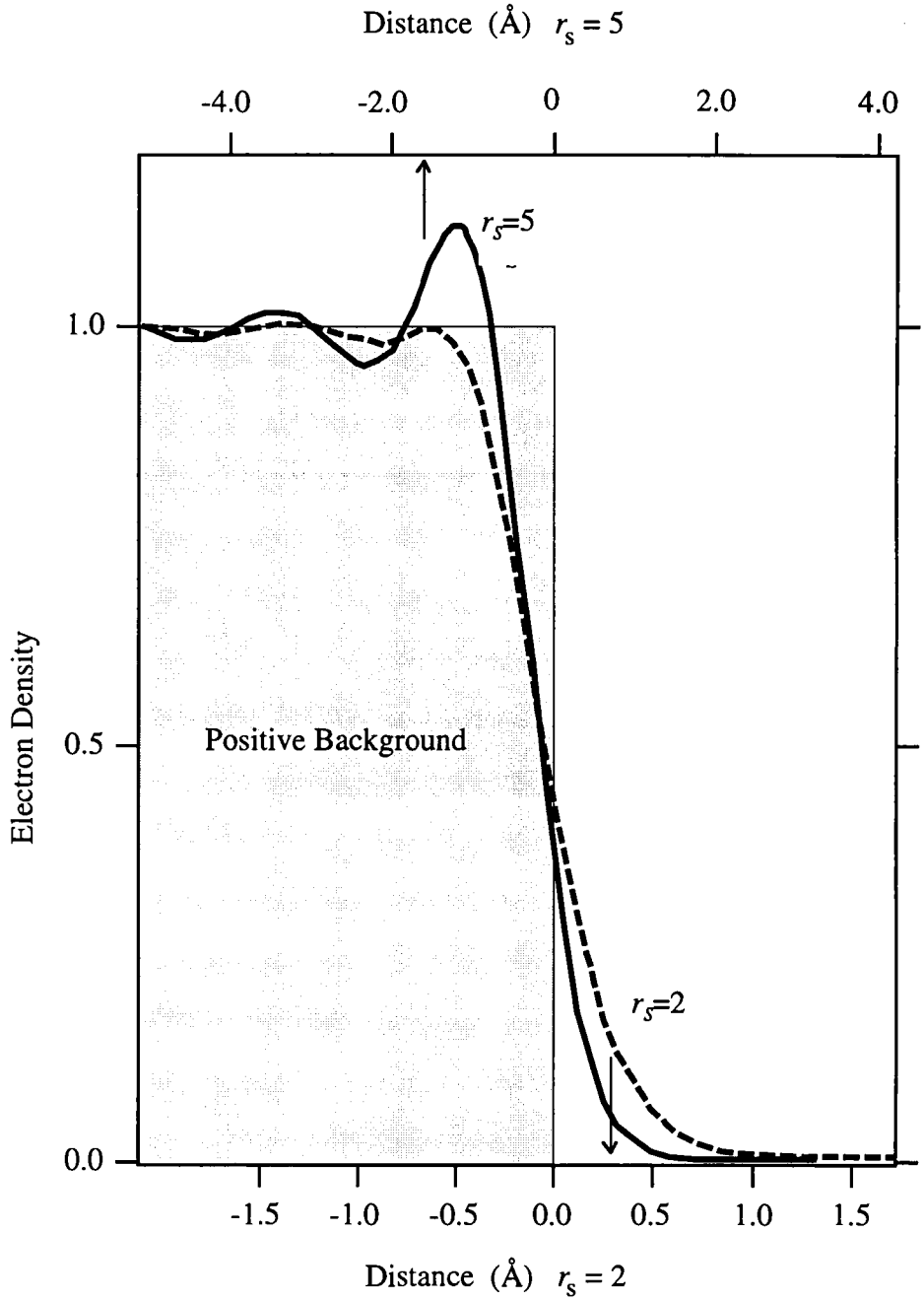


Figure 1.1: Charge density profile near the metal surface in the jellium model (Lang-Kohn charge density profile) for r_s=2 a.u. (dashed line) and r_s=5 a.u. (solid line) [6].

1.2 Charge Smoothing

In 1941, Smoluchowski introduced the concept of charge spreading and smoothing at a metal surface in an attempt to understand the electronic work function at metal surfaces [15], (work function is the energy required to remove an electron from a solid to the vacuum level). The idea of his concept is actually rather trivial. Assume we have a surface metal that was cut along the (110) direction of the bulk Wigner-Seitz unit cells, as shown in Figure 1.2. A creation of the surface will cause the electrons to rearrange themselves in order to lower their kinetic energy; the charge above the ion (the "hills") flows into the "valleys" and smoothes the surface, as shown in Figure 1.2 (b). These processes will produce a net positive charge on the "hills" and a negative charge in the "valleys." For a close surface, there are few electrons that flow from the "hills" to the "valleys." Therefore, the surface is less corrugated, making it more difficult for electrons to escape from the surface (the work function is large). However, for an open surface, the surface is highly corrugated, where there are more electrons that flow from the "hills" to the "valleys." Therefore the work function of the open surface is smaller.

This argument suggests that the work function at a metal surface is different for different faces of a crystal. A (111) face is a close surface, while a (110) face is an open surface. Then, the trend of the work function would be: $\Phi_{(111)} > \Phi_{(100)} > \Phi_{(110)}$. In general this trend is true for fcc metal surfaces such as Cu, Ni, and Ag [19]. Nonetheless, this trend is violated in the case of aluminum. The work function for aluminum is [20]: $\Phi_{(111)}$=4.24 eV, $\Phi_{(100)}$=4.40 eV, and $\Phi_{(110)}$=4.28 eV, (i.e., $\Phi_{(100)} > \Phi_{(110)} \approx \Phi_{(111)}$). This shows that the charge smoothing effect (Smoluchowski's effect) is *not* dominant at high density free-electron-like metal surfaces.

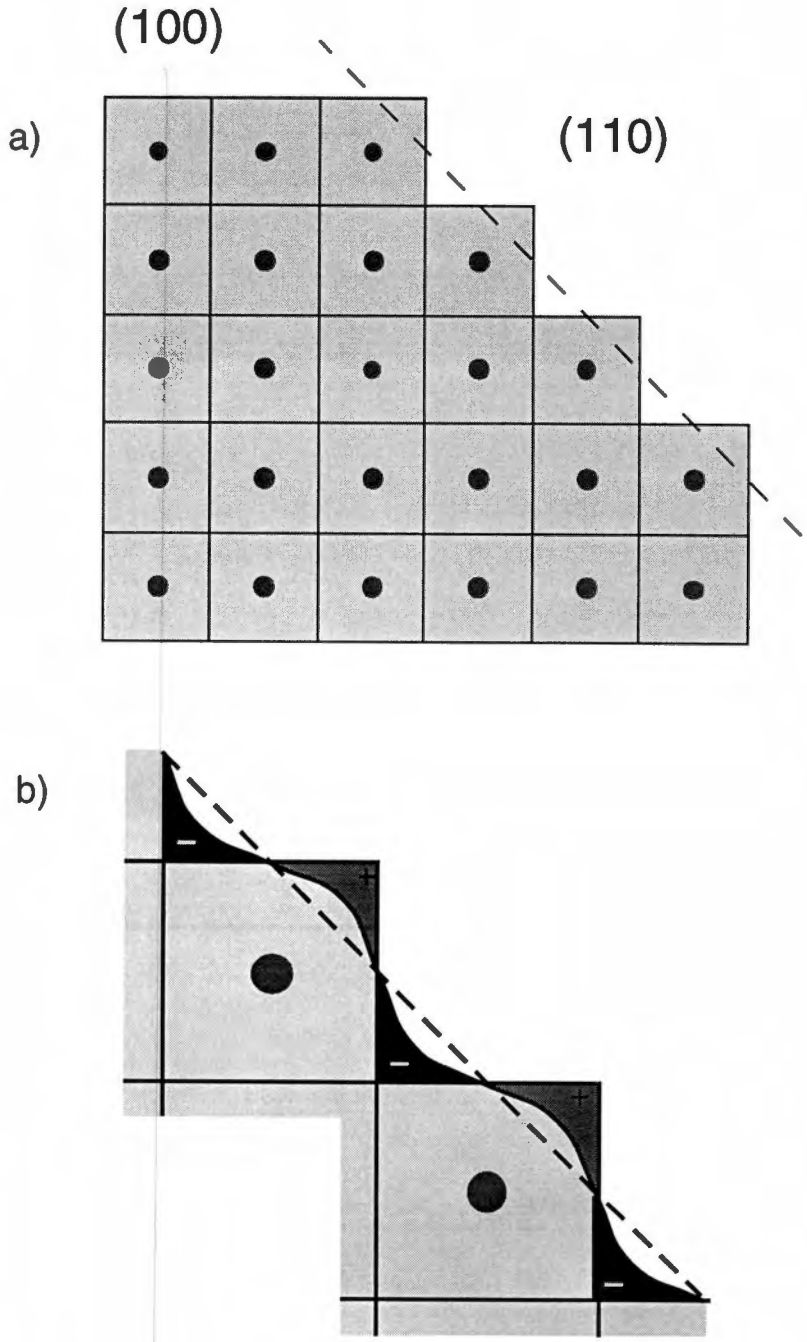


Figure 1.2: Illustration of the Smoluchoski effect [15]: a) Wigner-Seitz cells of a simple cubic crystal is cut to form a surface (dashed line) in the (110) direction and b) the process of redistribution of the charge density at the surface. Solid line is the surface after charge spreading and smoothing.

1.3 Electronic Surface States

As a consequence of broken symmetry, the atoms at the surface lose some of their coordinations (the number of their nearest neighbors is reduced) and the electrons near the surface readjust themselves rapidly in order to lower their kinetic energy, and thus there exist several common features of electronic properties at the surface.

First, the bandwidth at the surface layer is narrower than in the bulk, which has been demonstrated by Kalkstein and Soven in their investigation of the local density of states (LDOS) at a surface by using a Green's function formalism [16]. Figure 1.3 illustrates the narrowing bandwidth feature; layer-resolved local density of states for the surface, where the surface layer is denoted by S, the second layer is denoted by S-1, etc., the solid lines indicate the band, and the dashed lines indicate the surface states. As shown in Figure 1.3, the bandwidth at the surface layer is significantly narrower than in the bulk. This narrowing of the surface bandwidth is a real effect of the reduced number of the nearest neighbor atoms at the surface, due to the creation of the surface.

Second, the core level binding energies of the atoms at a surface differ from those in the bulk. This phenomenon is known as the surface core level shift (SCLS). The measured quantity is the difference between the energy required to remove one electron from a certain core state of a surface atom and that of a bulk atom. Egelhoff measured the SCLS for the Ni(100) surface by using x-ray photoelectron spectroscopy (XPS), and he found that the SCLS for the Ni(100) surface is -0.46 eV [17]. In general, the largest SCLS is for the surface layer (top layer). The second largest is for the second layer, etc. However, recent first-principles calculations and experimental data revealed that the largest shift of SCLS for the Be($10\bar{1}0$) surface is not from the first top layer but rather from the second layer [18].

Third, there are electronic surface states, also known as Tamm states or Shockley states. Early work by Bardeen showed that the surface states exist at the surface of a

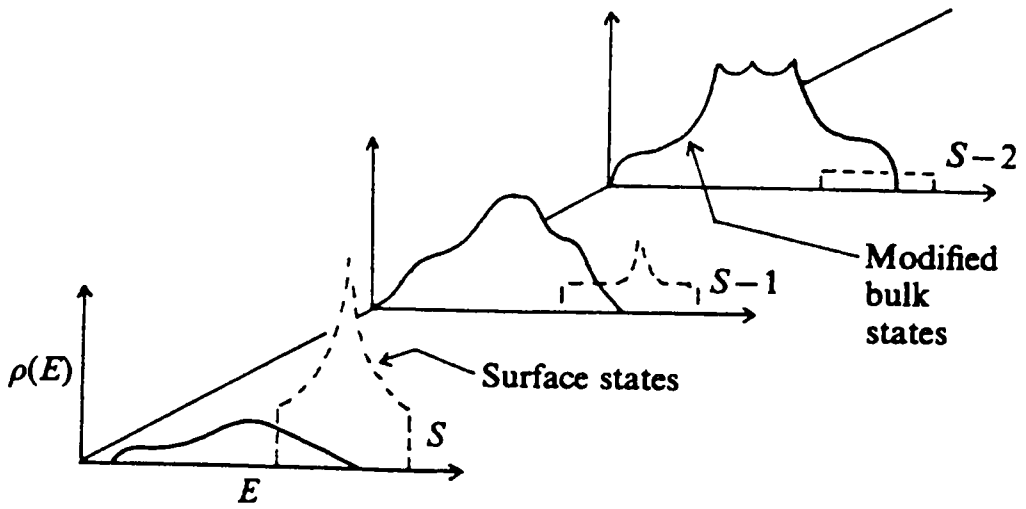


Figure 1.3: Layer-resolved local density of states for a surface [16]. **S** denotes the surface layer (first layer), **S-1** denotes the second layer, etc.

semiconductor [9]. The surface states of metal surfaces have been measured by using the angle-resolved photoemission technique and confirmed by first-principles calculations for many cases. These surface states are localized near the surface region and their energies are distributed in the gaps of the projection of bulk band structures onto the surface. The size of the gap is determined by the strength of the potential in the solid; i.e., a weak potential results in a small gap. The number of surface localized electronic states is governed by the size of the gap, i.e., a large gap will cause the surface states to have a large contribution to the density of states.

Figure 1.4 shows the dispersion of the surface states along the $\overline{\Gamma}$-$\overline{X}$ and $\overline{\Gamma}$-$\overline{M}$ directions for the Al(100) surface measured by angular resolved photoemission [21]. Unfilled circles indicate the experimental data (surface states) and the shaded region is the projected bulk band gap onto the (100) face. The dispersion of the surface states for the Al(100) surface follows the projected bulk band edge that is fitted by a free-electron-like parabola with an effective mass $m^*=1.02 \times m_e$, where m_e is the free electron mass.

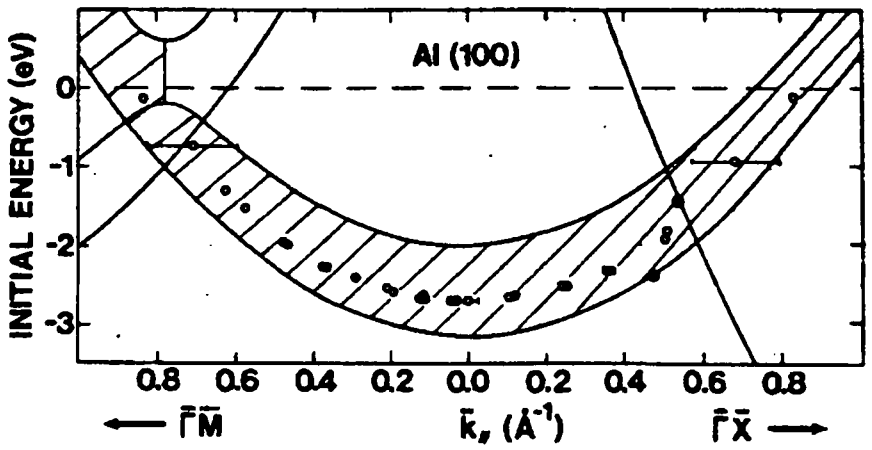


Figure 1.4: Measured surface states for the Al(100) surface [21]. Unfilled circles are experimental data and shaded region is the projected bulk band gap onto the (100) face.

The experimental data are in good agreement with the local density functional calculations [22]. The electronic properties of the Al(100) surface is free-electron-like, which is similar to the bulk. More interestingly, the electronic properties of bulk Be is nearly semiconducting where the density of states of the bulk Be is minimum near the Fermi level; however, the electronic properties of the Be(0001) surface is nearly free-electron-like and dominated by surface states [77]. Figure 1.5 shows the measured surface states for the Be(0001) surface by using the photoemission technique (filled circles) together with the calculations (solid lines) [77,78]. Clearly, the dispersion of the surface states for the Be(0001) surface is a nearly free-electron-like parabola.

Very recently, Sprunger *et al.* [7] and Hofmann *et al.* [8] showed that the two dimensional Fourier transforms of the STM images (the Friedel oscillations parallel to the surface) were related directly to the two-dimensional electronic band structure (surface states) at a metal surface. In other words, by using STM, one can measure the surface electronic structure where the data are in good agreement with the data from the photoemission experiment. The presence of electronic surface states at a surface must be important, leading the properties of the surface to be different than in the bulk [23].

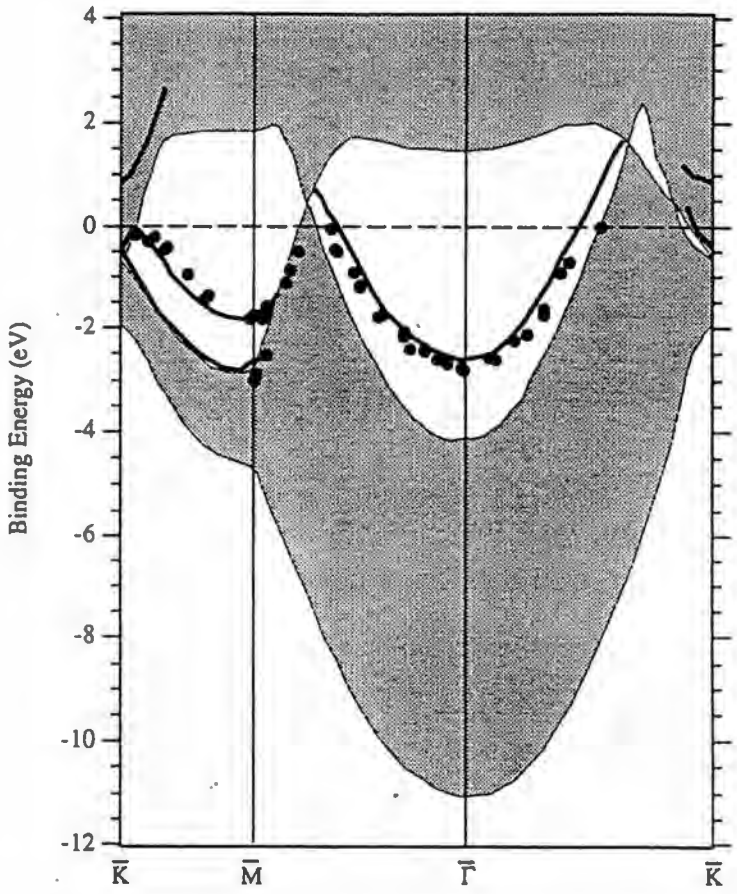


Figure 1.5: Calculated (solid lines) [77] and measured (filled circles) [78] dispersion of surface states of Be(0001). The shaded region is the projected bulk bands onto the (0001) face.

1.4 Surface Structure

So far, we have seen that some features (Friedel oscillations, charge smoothing, narrow bandwidth, SCLS, and surface states) exist at the surface of a material due to the charge rearrangement or electron-screening and reduced coordinations (the atoms at the surface lose some of their coordinations) as a consequence of the creation of a surface. In this section, I will show that the charge rearrangement at a surface plays an important role in the surface structure.

As has been discussed, when a bulk material is separated into two halves exposing two pristine surfaces, the electrons near the surface will respond to the new environment, readjusting to lower their kinetic energy and to screen out the presence of the surface. The atoms near a surface will move to a new equilibrium position due to the forces created by the redistributed electrons at the surface. In the most severe case, the surface equilibrium structure has a different symmetry compared to that of the underlying bulk known as a surface reconstruction. However in the most common cases, especially for metal, the surface equilibrium structure has the same symmetry parallel to the surface as in the bulk but the interlayer spacing in the vicinity of surface tends to relax.

1.4.1 First Interlayer Relaxation

The study of surface relaxations has fascinated scientists for decades. An important key in understanding the atomic arrangement in a solid was proposed by Feynman [24]. He pointed out that the force on a nucleus (an ion core) in a solid is just the classical electrostatic force that would be exerted on this nucleus by other nuclei and by the charge distribution of the electrons in solid, known as the Hellmann-Feynman theorem. Subsequently, Finnis and Heine used the Smoluchowski's concept of charge spreading and smoothing at a metal surface to explain the atomic arrangement at a surface [25]. As shown in Figure 1.2, the redistributed charge density produces an electrostatic force on the ion

core in the top layer that causes the first interlayer to move toward the bulk, i.e., contraction of the first interlayer spacing. The position of the ion core is then determined by the electrostatic force inside its own Wigner-Seitz unit cell. Finnis and Heine applied this theory to predict the first interlayer spacing of the (111), (100), and (110) surfaces of aluminum [25]. They reported that the first interlayer spacing of the Al(111) and Al(100) surfaces are contracted by 1.6% and 4.6% respectively. On the other hand, they found the first interlayer spacing of the Al(100) surface is contracted by 16%, and it can be understood that the Smoluchowski effect is more pronounced on a corrugated surface (an open surface). So the more open surface, the more contraction of the first interlayer spacing there will be.

However for a close-packed surface the charge smoothing effect is small. In fact experimental observations showed that the first interlayer spacing of close-packed surfaces is expanded with respect to the bulk, such as: Al(111) [37], Mg(0001) [this work], and Be(0001) [36]. Lang and Kohn have shown that there is a charge "spill out" into the vacuum (see Figure 1.1), due to the presence of the surface [6] which would drive a small expansion of the first interlayer spacing due to the outward pressure of the conduction electrons for a high electron density metal.

The development of sophisticated calculational methods with help from fast computer processors has made it possible to carry out *ab initio* calculations of atomic structure at surfaces. The results are quite encouraging, especially for simple metal surfaces. Figure 1.6 shows the plot of the change in the first interlayer spacing from the bulk value normalized to the volume per bulk atom ($\Delta d_{12}/V_0^{1/3}$) as a function of the inverse area per unit cell normalized to the volume per bulk atom ($V_0^{2/3}/A$) for simple metal surfaces from calculations and experimental data; where V_0 is the volume per bulk atom, i.e., the volume of bulk unit cell is divided by the number of atoms in the bulk unit cell, and A is the area of the surface unit cell. Figure 1.6 shows that the change of the first interlayer spacing

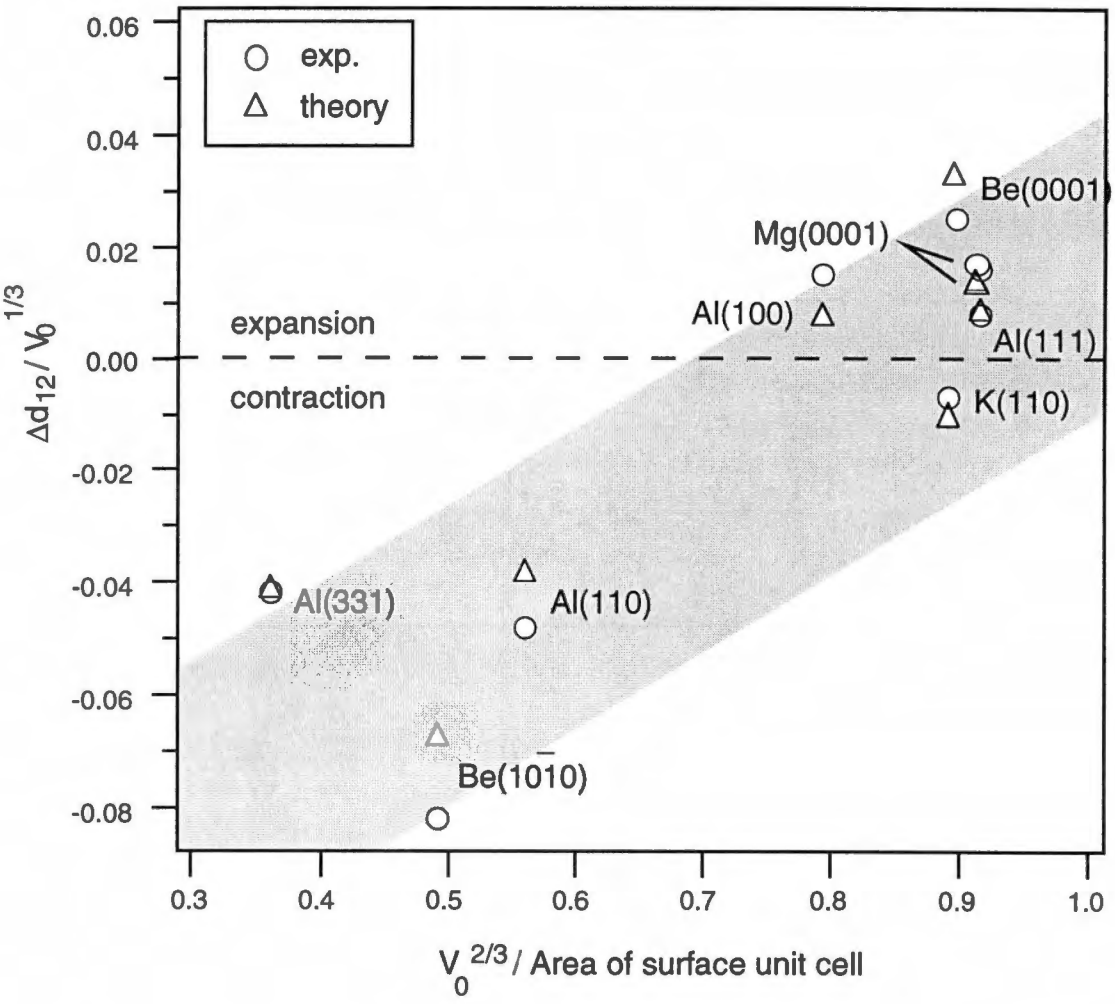


Figure 1.6: Relaxation in the first interlayer spacing for simple metal surfaces: the change in d_{12} as a function of the inverse area per surface unit cell, both normalized by the volume per bulk atom V_0. The references for the points are: Be(0001) [ref. 36], Mg(0001) th. [ref. 101], exp. [ref. 55], Al(111) th. [ref. 102], exp. [103], K(110) th. [ref. 104], exp. [105], Al(100) th. [ref. 102], exp. [ref. 106], Al(110) th. [ref. 102], exp. [ref. 106], Be(10$\bar{1}$0) [ref. 40], and Al(331) th. [ref. 107], exp. [ref. 108].

is linear to the inverse area of the surface unit cell. The first interlayer spacing is expanded for a close metal surface but contracted for an open metal surface. In general, the theory for such a *s-p* bonded metal is remarkably accurate see the calculations are in good agreement with the experimental data.

1.4.2 Stress and Reconstruction

The electrons near the surface will readjust themselves rapidly and smooth the surface in order to lower their kinetic energy. At a metal surface, this charge rearrangement can easily lead to a surface stress due to the force within the surface plane exerted by the redistributed electrons at the surface, as has been shown by Needs [26] in the case of the aluminum (111) and (110) surfaces.

The surface stress tensor is given by [26]:

$$g_{\alpha\beta} = \gamma\delta_{\alpha\beta} + \frac{\partial\gamma}{\partial\varepsilon_{\alpha\beta}} \qquad (1.2)$$

where γ is the surface energy per unit area, $\delta_{\alpha\beta}$ is the Kronecker delta function, and $\varepsilon_{\alpha\beta}$ is the strain tensor. $\partial\gamma / \partial\varepsilon_{\alpha\beta}$ is known as the strain derivative. In general, the stress at a metal surface is tensile stress ($g > 0$) where the lattice constant at the surface wants to be smaller than the bulk value in the directions parallel to the surface, or compressive stress ($g < 0$) where the lattice constant at the surface wants to be larger than in the bulk [26,27]. A tensile stress surface favors contraction in the first interlayer spacing while compressive stress surface favors expansion. Besides favoring the lattice constant at the surface layer that is larger or smaller than in the bulk, the surface stress could also cause the stacking sequence of atoms at the surface layer to be different than in the bulk.

Surface stress will affect the dynamics of surface. Lehwald *et al.* have shown that, in the case of phonon dispersion at the Ni(110) surface, the substantial disagreement

between experimental data and lattice dynamical calculations could be attributed to the presence of surface stress [28]. The experimental data are in good agreement with calculations when the surface stress is taken into account in the calculations [28]. A similar study of the surface phonon dispersion for an iron film on a Cu(001) substrate showed that a significant softening for the surface modes at the zone boundary is attributable to the presence of surface stress [29].

The presence of a large surface stress can lead to surface instabilities producing a new symmetry parallel to the surface known as surface reconstruction [30], which has been observed in many cases. A plausible criterion for a reconstruction surface was developed by Payne *et al.* [31] by defining a parameter $\alpha = g \cdot A/E_{coh}$, where g is the surface stress, A is the surface area per atom, and E_{coh} is the cohesive energy per atom in the bulk. If α is greater than one, this implies that the surface has a tendency to reconstruct. Besides semiconductors, there are many clean metal surfaces exhibiting reconstruction which involve breaking the symmetry parallel to the surface; for example, a missing row reconstruction. Reconstruction at metal surfaces usually occurs for open surfaces. A surface reconstruction was observed at the Pt(100) surface [32]. This surface is reconstructed to (1x2) periodicity as observed by LEED based on a missing row atom model. This kind of reconstruction also has been observed for surfaces of Au(110) [33] and Ir(100) [34]. The surface reconstruction also has been observed at a simple metal surface [35]. By using LEED *I-V* analysis, Hannon *et al.* found that the surface of Be($11\bar{2}0$) exhibits (1x3) reconstruction with a missing row atom model [35]. Very recent theoretical calculations at T=0 K predicted reconstruction at the Mg($10\bar{1}0$) and Mg($11\bar{2}0$) surfaces [14]. However, my experimental data showed no reconstruction at the Mg($10\bar{1}0$) surface at temperatures from 120 K to 400 K.

1.4.3 Deep Interlayer Relaxation

A consequence of the creation of a surface (broken symmetry) causes not only the first interlayer but also the deep layers to relax, which is known as multilayer relaxation. This means the atomic planes in the surface region shift inward and/or outward, perpendicular to the surface normal (interlayer relaxation) and in-plane relaxation, with or without preserving the symmetry parallel to the surface. Multilayer relaxations have been observed for many cases [35-49]. Table 1.1 lists some examples of multilayer relaxations for close metal surfaces. For close surfaces, where in general the bulk interlayer spacing is rather long about 2.0 - 2.5 Å, the first and second interlayer spacings are usually expanded and there is no in-plane relaxation, preserving the symmetry parallel to the surface. The interlayer relaxations occur up to the third atomic plane. Table 1.2 lists some examples of multilayer relaxations for open metal surfaces for *low* Miller indices. For open metal surfaces, where the bulk interlayer spacing is short, about 1.0 - 1.5 Å in contrast to the case of a close surface, the first interlayer spacings are contracted, the second interlayer spacing is expanded, the third interlayer spacings are contracted, etc. The relaxation pattern is of an oscillatory character with the alternating contraction and expansion following the trend - + - + - +. The interlayer relaxations usually occur up to the fourth or fifth atomic planes and there is no in-plane relaxation or the symmetry parallel to the surface is preserved. Table 1.3 lists some examples of multilayer relaxations for open metal surfaces for *high* Miller indices. For this case, the bulk interlayer spacing is very short, usually less than 1.0 Å. There are in-plane relaxations, i.e., registry shifts. However, it still preserves a (1x1) LEED pattern. The first interlayer spacing is contracted, the second interlayer spacing is contracted, the third interlayer spacings are expanded etc. The relaxation pattern is of an oscillatory character with the alternating contraction , contraction, and expansion following the trend - - + - - + - - +. The interlayer relaxations occur up to the fourth or fifth atomic planes.

Table 1.1: Some examples of multilayer relaxations for close metal surfaces.

	$\Delta d_{12}/d_o(\%)$	$\Delta d_{23}/d_o(\%)$	$\Delta d_{34}/d_o(\%)$
Mg(0001) [this work]	+1.96	+0.19	+0.04
Be(0001) [36]	+3.1	+1.4	+0.9
Al(111) [37]	+1.7	+0.5	---
Cu(100) [38]	-1.1	+1.7	---
Pd(100) [39]	+3.0	-1.0	---

Table 1.2: Some examples of multilayer relaxations for open metal surfaces.

	$\Delta d_{12}/d_o(\%)$	$\Delta d_{23}/d_o(\%)$	$\Delta d_{34}/d_o(\%)$	$\Delta d_{45}/d_o(\%)$
Mg$(10\bar{1}0)$ [this work]	-16.4	+7.8	-10.5	+3.8
Be$(10\bar{1}0)$ [40]	-25.0	+5.0	-11.0	+2.0
Co$(10\bar{1}0)$ [41]	-12.8	+0.8	---	---
Al(110) [42]	-8.6	+5.0	-1.6	+1.0
Cu(110) [38]	-7.9	+2.4	---	---
Ni(110) [43]	-8.7	+3.0	-0.5	---
Ag(110) [44]	-7.8	+4.3	---	---
Pd(110) [45]	-6.0	+1.0	---	---

Table 1.3: Some examples of multilayer relaxations for open metal surfaces for high Miller indices.

	Al(210) [46]	Pt(210) [47]	Cu(210) [48]	Al(331) [49]
Interlayer relaxations				
$\Delta d_{12}/d_o$ (%)	-16.0	-23.0	-11.12	-11.7
$\Delta d_{23}/d_o$ (%)	-1.0	-12.0	-5.68	-4.1
$\Delta d_{34}/d_o$ (%)	+9.0	+4.0	+3.83	+10.3
$\Delta d_{45}/d_o$ (%)	-4.0	-3.0	+0.06	-4.8
$\Delta d_{56}/d_o$ (%)	-1.0	----	-0.66	---
Registry relaxations				
$\Delta r_{12}/r_o$ (%)	-0.00	+1.14	-1.83	-2.8
$\Delta r_{23}/r_o$ (%)	-3.00	-1.71	-2.51	---
$\Delta r_{34}/r_o$ (%)	+2.00	-4.56	+1.68	---
$\Delta r_{45}/r_o$ (%)	-2.00	-0.57	-0.48	---
$\Delta r_{56}/r_o$ (%)	-1.00	----	+0.06	---

The origin of multilayer relaxations has attracted a considerable attention from scientists for decades. Landman, Hill, and Mostoller [50] used a simple electrostatic model to explore the influence of different trial electronic densities (an abrupt terminated step density profile, an exponential variation form, and a self-consistent distribution derived from the jellium model or the Lang Kohn profile) on the multilayer relaxations of several model systems, and found that there is in general a simple correlation between the stacking sequence of the crystal. The effect of allowing more than one or two layers to relax is significant. Subsequently, Jiang *et al.* [51] and Adams *et al.* [46] used even simpler versions of the electrostatic model to calculate the electrostatic forces on the point ions in a uniform (truncated) electronic background density, reaching the same qualitative conclusion. All of these electrostatic models actually ignored the essential role of electrons in screening out the ions as well as the presence of the surface.

Barnett, Landman, and Cleveland studied relaxation at simple metal surfaces via minimization of the total energy of a semi-infinite crystal where the expression for the total energy depends explicitly on the ionic positions, with the use of a pseudopotential theory and linear response [52]. Their results exhibit damped oscillatory multilayer relaxations with a period of oscillations equal to the period of the layer stacking sequence. For the model system of Al(110), a similar conclusion was reached by Ho and Bohnen [53] using first-principles calculations, where the response of the electrons to the ionic positions was included self-consistently. Eguiluz [54] performed the calculation of multilayer relaxation at the Al(110) surface based on the numerical minimization of the total energy of a metal slab with the use of pseudopotential and self consistent linear electronic response. He found that the electronic screening of the ions plays an important role in the process of multilayer relaxations and consequently the oscillatory relaxation pattern does not necessarily correlate with the stacking sequence of the bulk layers.

Cho *et al.* performed a first-principles total energy calculation using density-functional theory within the local density approximation for the Mg($10\bar{1}0$) surface, where the electronic screening was considered in the calculations. They found that the pronounced charge density oscillations (Friedel oscillations) still exist at this metal surface even when the effects of the ionic cores are considered [13]. These Friedel oscillations contributes to drive the ions to relax in an oscillatory fashion at metal surfaces. The same conclusion was reached by Staikov and Rahman [14] by using the electrostatic calculations.

All of the theoretical works at T=0 K mentioned above have demonstrated the existence of the oscillatory multilayer relaxations at metal surfaces and are in qualitative agreement with the experimental observations. Nevertheless, the physics is still not quite clear yet, i.e., all models discussed above (Friedel oscillations and electrostatic sums or even simple electrostatic calculations) produce the oscillatory multilayer relaxation at a metal surface.

1.4.4 The Contribution of Surface States to Surface Structure

As was discussed before, the existence of localized electronic states (surface states) at a surface is due to the creation of a surface. The presence of surface states at a surface will lead the properties of surface to be different than in the bulk. However, so far there is no any study that shows the surface states determine the surface structure explicitly.

Nonetheless, let's see the case of beryllium in comparison with magnesium. The bulk of the band gap of beryllium is larger than that of magnesium. The bulk beryllium is semiconductor-like, while the bulk magnesium is free-electron-like. The Be(0001) surface is dominated by surface states in contrast to the Mg(0001) surface. The electronic structure of the Be(0001) surface is nearly free-electron-like, which is very different than its bulk electronic structure properties, leading to the nature of bonding in bulk beryllium is so different than at the Be(0001) surface. The consequence is that the first interlayer spacing

of Be(0001) is large ($\Delta d_{12}/d_0 = +3.1$ %) [36], in comparison to that of Mg(0001) ($\Delta d_{12}/d_0$ = + 1.96 % [this work] and +1.90 % [55]. This behavior is also true for the surface thermal expansion of Be(0001) and Mg(0001): the surface thermal expansion of Be(0001) is about six times larger than in bulk [36], while our temperature dependent structure measurement of the Mg(0001) surface showed that the surface thermal expansion of this surface is almost the same as in the bulk. Qualitative argument suggests that the large expansion and thermal expansion at the Be(0001) surface is governed by surface states. Another example is that the surface state is a driving mechanism for the surface reconstruction of the Mo(001) surface [56].

1.5 Surface Phonons

There are a lot of phenomena in solid that can be understood via the static lattice model, such as electronic structure, electrical properties, etc. In this approximation, the atoms in the solid are assumed fix or rigid. By using this model, one would be able to understand the properties of metals where those properties are dominated by the behavior of valence electrons (conduction electrons) in solid. However, there are many phenomena which can not be explained within the static situation such as the phenomenon of thermal expansion, heat capacity, transport properties, the existence of phase transitions, dielectrics, etc. In this case the dynamic model needs to be taken account in order to explain such phenomena.

The study of the vibrational properties of atoms in solid has fascinated scientists for decades [57-70]. Einstein proposed a very simple model where the atoms in solid are assumed to be independent oscillators; each atom has the same frequency and vibrates isotropically [61]. Debye introduced a simple model where the frequency of atomic vibrations in a solid is proportional to the momentum wavevector [61]. Both Einstein and Debye models have explained the influence of the vibrational modes on many physical

properties of solids. Subsequent studies proposed a more realistic model where the vibrational atoms in solid are collective motions in the form of traveling waves called lattice vibrations [57,58]. A quantized lattice vibrational or normal mode is called a phonon, which has "particle like" properties. The energy of a phonon mode is determined by the restoring force on the atoms as they are displaced from equilibrium. The total interatomic force constants are given by the direct force constant for ions (bare Coulomb interaction) and the force constants from electronic contributions. Nowadays, total interatomic force constants in a solid can be obtained from the *ab initio* calculations, providing an accurate result [62-66]. The knowledge of the vibrational energies and the displacement patterns of atoms in a solid will provide us the understanding of phase transformation, crystal stability, thermal expansion, heat capacity, and other thermodynamic properties.

The harmonic approximation is perhaps the starting point for the theory of lattice dynamics. In this approximation, the force on an atom is proportional to its displacement that is relative to its neighbors. This is the same as Hook's law. Besides harmonic approximation, the adiabatic approximation is also applied to the theory of lattice dynamics. The idea is that the ions are about $2x10^3$ - $2x10^5$ times heavier that the electrons. The ions move much more slowly than the electrons. Therefore, when the ions move the electrons also move as though the ions were fixed in their instantaneous positions or the electrons "see" the ions fixed at all times. The detailed theory of lattice dynamics is explained in many text books, such as: *"Dynamical Theory of Crystal Lattice"* by M. Born and K. Huang [57] and *"The Dynamical Properties of Solid"* by A. A. Maradudin [58].

A very simple model of the lattice dynamics is a classical mechanics of the infinite linear diatomic chain with nearest-neighbor interactions. Consider a diatomic chain crystal structure with equal masses M connected by springs with force constants K_1 and K_2. Let a be the lattice constant of the crystal or the repeat distance of the chain. The dynamical solution can be determined analytically [61], as shown in Figure 1.7.

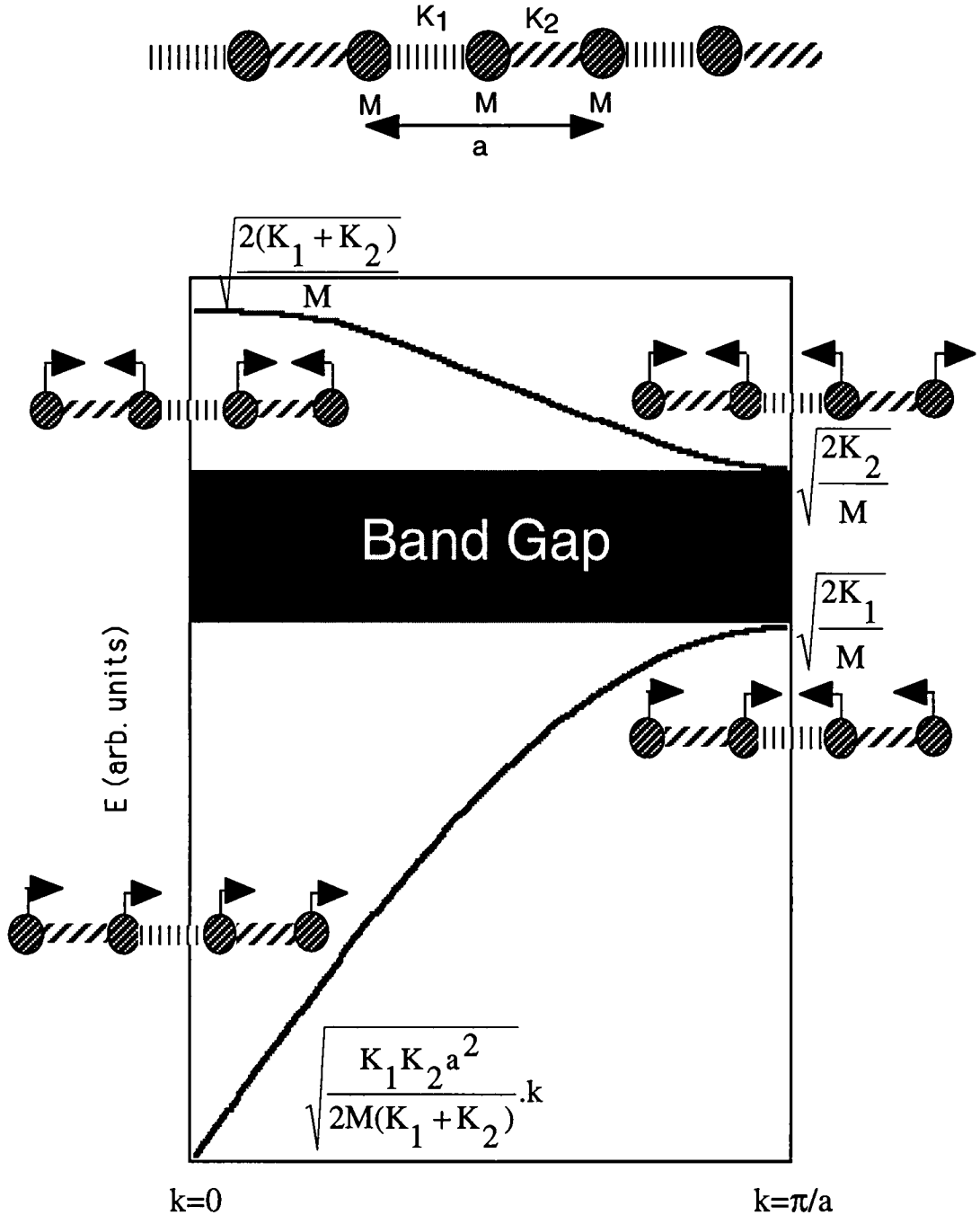


Figure 1.7: Vibrational modes of an infinite diatomic chain.

The solutions in the long wavelength limit (small wavevector) are: $\omega_1 = \sqrt{K_1 K_2 a^2/(2M(K_1 + K_2)}\cdot k$ and $\omega_2 = \sqrt{2(K_1 + K_2)/M}$. The frequency of the lower mode (ω_1) is proportional to the wavevector k and can be written as $\omega_1 = v_g \cdot k$, where v_g is known as a group velocity that is the velocity of energy propagation in the medium. This velocity is equivalent to the velocity of sound in a crystal. Because of the relationship to sound waves, this vibrational mode (ω_1) is called an acoustic mode. In the long wavelength limit, the atoms move in the same direction for this mode (see Figure 1.7). The mode ω_2, having the displacements of atoms in the opposite direction, is called an optical mode because if these two atoms carry opposite charges then we may have a light due to the motions of atoms. At the zone boundary (k=π/a): the frequency of acoustic mode $\omega_1 = \sqrt{2K_1/M}$ has the displacement of atoms in the same direction, while the frequency of optical mode $\omega_2 = \sqrt{2K_2/M}$ has the displacement of atoms in the opposite direction in the unit cell. Since k=π/a is at the zone boundary, the displacement of atoms in neighboring cells are out of phase by 180°. There is an energy gap at the zone boundary between the energies $\sqrt{2K_1/M}$ and $\sqrt{2K_2/M}$, where the size of the gap depends on the value of the force constants of springs K_1 and K_2. The strength of the dispersion of acoustic branch depends highly on the strength of the coupling between the atoms or the interatomic forces in a solid.

As a consequence of the creation of a surface, the translation symmetry is lost in one direction normal to the surface, the atoms near the surface region lose some of their coordinations, and thus there exist surface phonons or vibrational surface states localized near the surface region that decay into the bulk perpendicular to the surface. The surface phonon dispersion curves can be obtained by solving for the vibrational modes of a slab or semi-infinite solid by using the Born-von Kármán (BVK) scheme, where the potential energy **U** of the lattice is expanded to the second order of the ion displacements.

$$\mathbf{U} = \frac{1}{2}\sum_{\substack{i,j \\ \alpha,\beta}} \phi_{\alpha\beta}(i,j) u_i^{\alpha} u_j^{\beta} \qquad (1.3)$$

where α and β label the Cartesian coordinates, and i and j specify the ions. The interaction between atom i and j is described by $\phi_{\alpha\beta}(i,j)$. The dynamical matrix $D_{\alpha\beta}(\bar{q})$ for a momentum transfer $\bar{q}$ (a wavevector in the Brillouin zone) can be written as [58]:

$$D_{\alpha\beta}(\bar{q}) = \frac{1}{M}\sum_{j} e^{-i\,\bar{q}\cdot(\bar{x}(i)-\bar{x}(j))}\,\phi_{\alpha\beta}(i,j) \qquad (1.4)$$

where M is the mass of ions. The eigenvalues of this dynamical matrix as a function of wavevector ($\bar{q}$) in the Brillouin zone define the phonon dispersion relations, and the eigenvectors of the dynamical matrix specify the pattern of the displacement of atoms related to the vibrational modes (phonons). Figure 1.8 shows the calculated surface phonon dispersion for an hcp($10\bar{1}0$) surface along the $\bar{\Gamma}$-$\bar{\mathrm{M}}$ direction by using the BVK scheme, where the filled circles are the surface modes (as the consequence of a creation of the surface) and the shaded area is the projected bulk band onto the surface. There are seven modes predicted at $\bar{\mathrm{M}}$, starting with the lowest to highest energy: M_1, M_2, M_3, etc. The two lowest modes below the projected bulk band edge are the Rayleigh modes or Rayleigh waves (RW). These modes are the surface acoustical phonons localized near the surface region and decay exponentially into the bulk. The decay length is proportional to the wavelength parallel to the surface. In the long wavelength limit (small momentum wave-vector) where the wavelength is much larger than the interatomic distance, the periodicity of the lattice can be neglected; therefore the dispersion of the RW can be expressed in terms of the macroscopic elastic properties of the medium. The displacement pattern of this mode extends father into the bulk and its energy is a linear function of the momentum wavevector k: $\omega(\mathrm{k}) = \xi \cdot \mathrm{c_t} \cdot \mathrm{k}$, where ξ is a parameter (its value is in the range of 0.87 - 0.96) [71] and $\mathrm{c_t}$ is the transverse velocity of sound. Since the parameter ξ is less than one, the

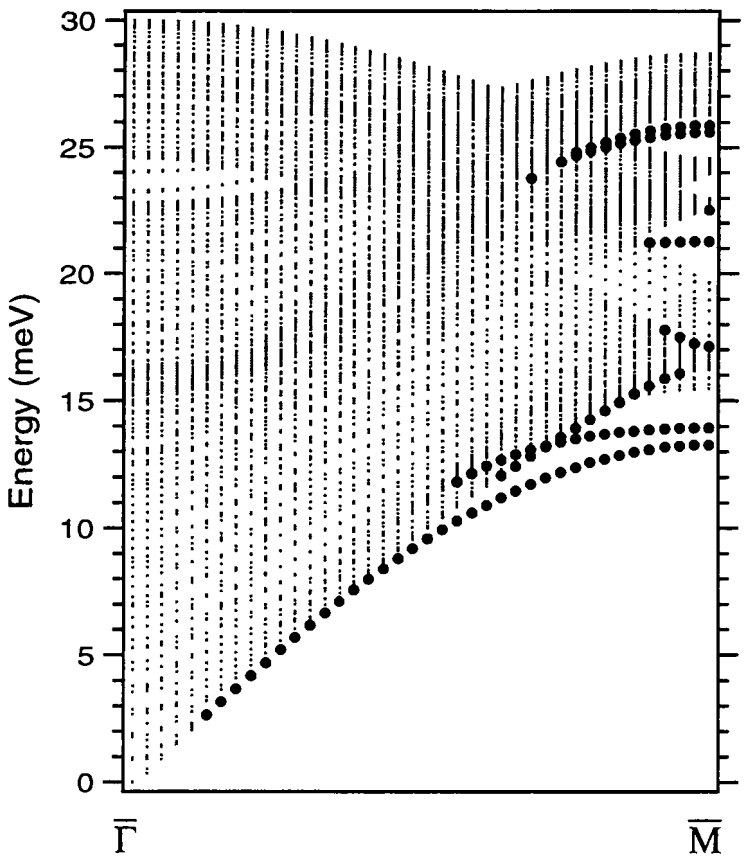


Figure 1.8: Calculated surface phonon dispersion for a hcp($10\bar{1}0$) surface by using the Born-von Kármán scheme. The filled circles are the surface modes. The shaded area is the projected bulk band onto the surface.

energy of the Rayleigh modes should be below the projected bulk band at the zone boundary. In the long wavelength, however, the Rayleigh modes penetrate into the bulk bands for some metals. At a large wavevector or the zone boundary, the atomic displacement of this mode (RW) is localized in the surface layer; therefore the energy of this mode is highly determined by the shape of the interatomic potential near the surface region. Above the RW modes is a Shear horizontal mode where the atomic displacements are parallel to the surface. The surface mode M_4 is a surface mode where the atomic displacements are mainly vertical but localized in the third layer, while the mode M_5 is a surface mode where the atomic displacements are mainly vertical localized in the fourth layer. The surface modes M_6 and M_7 have the atomic displacements parallel to the surface. All of these surface modes are related to the atomic bonding in the surface region.

In the phonon calculations, the value of force constants between the ions inside the crystal can be deduced from the measured phonon dispersion curves in the bulk. In order to reproduce the experimental data of the surface phonon dispersion, the force constants coupling atoms near the surface usually need to be modified. This method may give an ambiguity in a force constant model, i.e., one may have more than one model that can explain the same experimental data. Nowadays, the force constants in a solid can be obtained from first-principles calculations by taking into account the screening.

The screening effect can be described in term of a response function or correlation function. The induced electron charge density $\delta n_{ind}(\bar{x},t)$ is given by [72]:

$$\delta n_{ind}(\bar{x},t) = \int_{-\infty}^{+\infty} dt' \int d\bar{x}' \ \chi(\bar{x},\bar{x}' \mid t-t') \ \delta U_{ext}(\bar{x}',t') \qquad (1.5)$$

where δU_{ext} is the external energy potential. $\chi(\bar{x},\bar{x}' \mid t-t')$ is known as a density response function for the interacting electron, containing the essential physics of the screening in a solid. This density response function $\chi(\bar{x},\bar{x}' \mid t-t')$ can be written as [63]:

$$\chi(\bar{x},\bar{x}') = \chi^{(0)}(\bar{x},\bar{x}') + \chi^{(0)}(\bar{x},\bar{x}')\, V(\bar{x},\bar{x}')\, \chi(\bar{x},\bar{x}') \qquad (1.6)$$

where $\chi^{(0)}(\bar{x},\bar{x}')$ is the density response function for the non-interacting electrons [73] and $V(\bar{x},\bar{x}')$ is the potential of full electron-electron interactions. In the local density approximation (LDA), $V(\bar{x},\bar{x}')$ is given by:

$$V(\bar{x},\bar{x}') = v(\bar{x}-\bar{x}') + \frac{dV_{xc}(\bar{x})}{dn(\bar{x})}\delta(\bar{x}-\bar{x}') \qquad (1.7)$$

where $v(\bar{x}-\bar{x}')$ is the electron-ion interaction and $V_{XC}(\bar{x})$ is the self-consistent exchange-correlation potential for the electron number density $n(\bar{x})$ [37]. The electronic contribution to the force constant in a solid can be written as [64]:

$$\phi^{(el)}_{\alpha\beta}(i,j) = \int d\bar{x} \int d\bar{x}' \frac{\partial v(\bar{x}-\bar{x}(i))}{\partial x(i)_\alpha} \chi(\bar{x},\bar{x}' \mid \omega = 0^+) \frac{\partial v(\bar{x}-\bar{x}(j))}{\partial x(j)_\beta} \qquad (1.8)$$

The total interatomic force constants are given by the equation:

$$\phi_{\alpha\beta}(i,j) = \phi^{(d)}_{\alpha\beta}(i,j) + \phi^{(el)}_{\alpha\beta}(i,j) \qquad (1.9)$$

where $\phi^{(d)}_{\alpha\beta}(i,j)$ is the direct force constant for ions (bare Coulomb interaction). By using the total force constants given in the equation (1.9), one can obtain the phonon dispersion relations and the pattern of the displacement of atoms related to the phonon by solving the dynamical matrix equation (1.4).

The force constants near the surface region, which are usually different than in the bulk as the consequence of a creation of the surface, lead to a surface phonon anomaly; the measured energies of the RW for large wavevectors are appreciably higher than the values obtained from the calculations using bulk interatomic force constants. This kind of anomaly has been found for several cases, such as: Cu(100) [74], Ni(100) [75], and Al(100) [1,76]. In the case of Cu and Ni, the mechanism of the anomaly is suggested by a stiffening of the interplanar radial force constant at the surface and the presence of the surface stress [74-76]. However, in the case of the Al(100) surface, Gaspar and Eguiluz

found that the tangential force constant coupling nearest neighbors at the surface layer plays an important role for the anomaly [1]. The value of the tangential force constant coupling first nearest neighbors at the surface layer along the surface normal is appreciably different than the value in the bulk. The cause of the discrepancy comes from the electronic contribution (as a consequence of charge rearrangement at the surface) [1]. Be(0001) is another interesting example; Hannon *et al.* reported that the measured surface phonon dispersion at the Be(0001) surface was significantly different than expected by a bulk-truncated model [68,70]. Most significantly, the agreement between the measured and calculated Rayleigh mode dispersion of Be(0001) along the zone boundary can only be obtained when non-central forces are substantially reduced in magnitude at the surface. They interpreted this feature as being caused by the unique electronic properties of the Be(0001) surface; where the bulk of Be is a nearly-semiconductor-like, however, the surface is a high-density free-electron-like metal [77,78]. The calculations and experimental data for the surface states of the Be(0001) surface are in good agreement, as shown in Figure 1.5. Hannon's speculation, by using the results from BVK calculations, was that the more free-electron behavior at the surface would lead to central forces in contrast to the bulk [68,70]. Lazzeri and Gironcoli performed *ab-initio* first-principles calculations of the dynamical properties of the Be(0001) surface by using a pseudopotential where a non-linear core correction was included [66]. Their results are in excellent agreement with experimental data [68], showing that there are only three layers involved in the surface dynamics [66], but they indicated that the situation was more complicated than the simple central-force model of Hannon [68]. *The surface force constants continue to have a strong non-central component.* In addition, they predicted two additional modes below the bulk band edge, which have never been observed experimentally. They suggested that these additional modes are peaked in subsurface layers and have both in-plane and out-of-plane components. Based on the unique electronic properties of the Be(0001) surface, non-

central forces should be substantially reduced at the surface. However, *ab-initio* first-principles calculation encounter this argument, showing that the surface force constants continue to have a strong non-central component. The surface phonon anomaly was also found in the case of the Mg(0001) surface [this study]. The Rayleigh mode of the ideally bulk truncated surface is softer and has a different curvature. The measured (bulk-truncated calculations) Rayleigh mode at the Mg(0001) surface is 14.50 (13.00) meV at $\overline{K}$ and 13.50 (12.90) meV at $\overline{M}$, respectively. The calculated Rayleigh mode at the Mg(0001) surface is almost dispersionless along the $\overline{K}$-$\overline{M}$ direction; ($\omega(\overline{M})$-$\omega(\overline{K})$=+0.1 meV), while the measured Rayleigh mode dispersion has a higher frequency at $\overline{K}$ than at $\overline{M}$; ($\omega(\overline{M})$-$\omega(\overline{K})$=+1.0 meV). The sign of the Rayleigh mode at the Mg(0001) surface along the zone boundary $\overline{K}$-$\overline{M}$ is correct in experiment and theoretical prediction of ideally bulk truncated model. Similar to the case of the Al(100) surface [1], the value of the tangential force constants coupling second nearest neighbors (in-plane) at surface layer along the surface normal for Mg(0001) is appreciably different than the value in the bulk that plays an important role for the anomaly.

The mean separation of the atoms in a solid is governed by the interatomic potential. As the temperature of a solid is increased, the occupancy of the vibrational level is changed; the higher level will be occupied. However, if the potential in solid were purely harmonic, as shown in Figure 1.9(a), the energy separation of adjacent levels or the vibrational excitation energies and the mean positions of the atoms (marked by vertical lines) would not change as the temperature of solid is increased, even though the amplitude of atomic vibration is large. Because the interatomic potential in a solid is anharmonic, as shown in Figure 1.9(b), as the temperature of solid is increased, then the vibrational excitation energies are decreased. Consequently, the mean separation of the ionic positions in solid is increased or expanded (the average location of atoms in a given vibrational energy level is

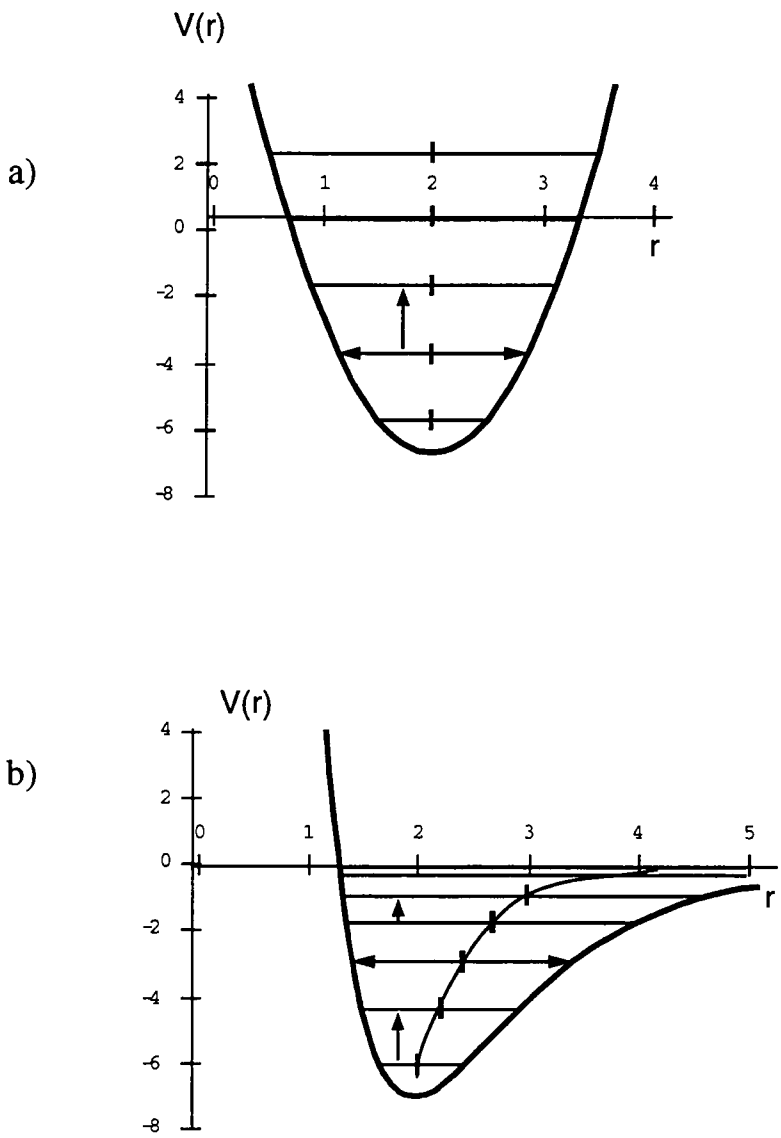


Figure 1.9: (a) Harmonic and (b) anharmonic interatomic potentials. Horizontal lines indicate the vibrational energy levels and the mean-distance of an atom in a given vibrational level marked by vertical lines.

marked by vertical lines). Therefore, it is well known that the thermal expansion is directed by the nature of anharmonicity of the interatomic force in a solid.

To illustrate the anharmonic interactions in a solid, a Morse potential can be used, since it has been successful in reproducing the experimental data [109,110], and the solution of the vibrational energy levels can be evaluated analytically [111,112]. A Morse potential is given as the following:

$$V(r) = A \cdot \left(e^{-2\alpha \cdot r} - 2 \cdot e^{-\alpha \cdot r}\right) \tag{1.10}$$

and the vibrational energy levels:

$$E_n = \left(n + \frac{1}{2}\right)\hbar\omega - X_a\left(n + \frac{1}{2}\right)^2 \hbar\omega \tag{1.11}$$

where n=0,1,2,... (levels), and $X_a = \frac{\hbar\omega}{4A}$ which is a dimensionless constant, representing the anharmonicity, and $\hbar\omega = \hbar\alpha\left(\frac{2A}{m}\right)^{1/2}$, which represents the excitation energy in the absence of the anharmonicity. If X_a is zero, the vibrational energy levels are equal to the pure harmonic solution. The vibrational excitation energies are given by:

$$\Delta E_n = E_n - E_{n-1} = (1 - 2 \cdot X_a \cdot n)\hbar\omega \tag{1.12}$$

The negative sign in this equation will lead the excitation energies to decrease as the occupancy level increases. The occupancy of the vibrational level depends on the temperature with the probability of occupancy of a energy level E_n is given by:

$$P(E_n) = \frac{e^{-E_n / k_B T}}{\sum_n e^{-E_n / k_B T}} \tag{1.13}$$

where T is the temperature, and k_B is the Boltzmann's constant (k_B=8.617x10^{-5} eV/K).

Tables 1.4 and 1.5 list the excitation energies and probabilities at T=10 K, T=120 K, and T=300 K with X_a=0.035 for a Morse potential with $\hbar\omega$=14.75 meV and $\hbar\omega$=43.0 meV, respectively. The excitation energies decrease at the higher levels. At T=10 K, the

Table 1.4: Simulated vibrational occupancy probabilities for a Morse potential with $\hbar\omega$=14.75 meV and X_a=0.035.

Level (n)	Excitation Energy (meV)	Probability T=10 K	Probability T=120 K	Probability T=300 K
0		1.000	0.729	0.367
1	13.950	0.000	0.189	0.214
2	12.900	0.000	0.054	0.130
3	11.850	0.000	0.017	0.082
4	10.800	0.000	0.006	0.054
5	9.750	0.000	0.002	0.037
6	8.700	0.000	0.001	0.026
7	7.650	0.000	0.000	0.020
8	6.600	0.000	0.000	0.015
9	5.550	0.000	0.000	0.012
10	4.500	0.000	0.000	0.010
11	3.450	0.000	0.000	0.009
12	2.400	0.000	0.000	0.008
13	1.350	0.000	0.000	0.008
14	0.300	0.000	0.000	0.008

Table 1.5: Simulated vibrational occupancy probabilities for a Morse potential with $\hbar\omega$=43.0 meV and X_a=0.035.

Level (n)	Excitation Energy (meV)	Probability T=10 K	Probability T=120 K	Probability T=300 K
0		1.000	0.979	0.779
1	39.990	0.000	0.020	0.166
2	36.980	0.000	0.001	0.040
3	33.970	0.000	0.000	0.011
4	30.960	0.000	0.000	0.003
5	27.950	0.000	0.000	0.001
6	24.940	0.000	0.000	0.000
7	21.930	0.000	0.000	0.000
8	18.920	0.000	0.000	0.000
9	15.910	0.000	0.000	0.000
10	12.900	0.000	0.000	0.000

probabilities of occupancies is 100% in the zero level (n=0) for both cases. As the temperature increases, the probabilities of occupancies are changed. In the case of $\hbar\omega$=14.75 meV: at T=120 K, the probability of occupancy at zero level decreases to 72.9% and the other levels are occupied (the n=0 $\Rightarrow$ n=4 excitation has strength), and at T=300 K, the probability of occupancy at zero level becomes 36.7% and the levels 0 to 10 are occupied with the probabilities of occupancies more than 1%; while in the case of $\hbar\omega$=43.0 meV: at T=120 K, the probability of occupancy at zero and first levels are 97.9% and 2.0% (the only n=0 $\Rightarrow$ n=1 excitation has any strength), and at T=300 K, the probability of occupancy at zero level is 77.9% and the levels 0 to 3 are occupied with the probabilities of occupancies more than 1%. For a given of excitation energies and occupancy probabilities, one can simulate the vibrational spectra by using the Gaussian function:

$$I(E) \propto \sum_n P(E_n) \cdot e^{-\left(\frac{E-\Delta E_n}{W}\right)^2} \qquad (1.14)$$

where w is the width of Gaussian. Figure 1.10 shows the simulated vibrational spectra at temperatures T=10 K, 120 K, and 300 K for a Morse potential with $\hbar\omega$=14.75 meV and X_a=0.035. The widths of Gaussian for T=10 K, 120 K, and 300 K are 3.0 meV, 4.0 meV, and 6.0 meV, respectively. The widths of Gaussian are added to imitate the EELS (electron energy loss spectroscopy) spectra. As the temperature is increased, the spectral peaks (vertical lines) shift toward lower energies referred to as phonon energy shifts, leading the mean separation of atoms in a solid to increase. In other words, the thermal expansion is governed by the nature of anharmonicity of the interatomic force in a solid. Tables 1.4 and 1.5 show clearly that besides the temperature, the probabilities of occupancies of the energy level depend on the magnitude of $\hbar\omega$, which is the excitation energy in the absence of the anharmonicity that depends on a certain material.

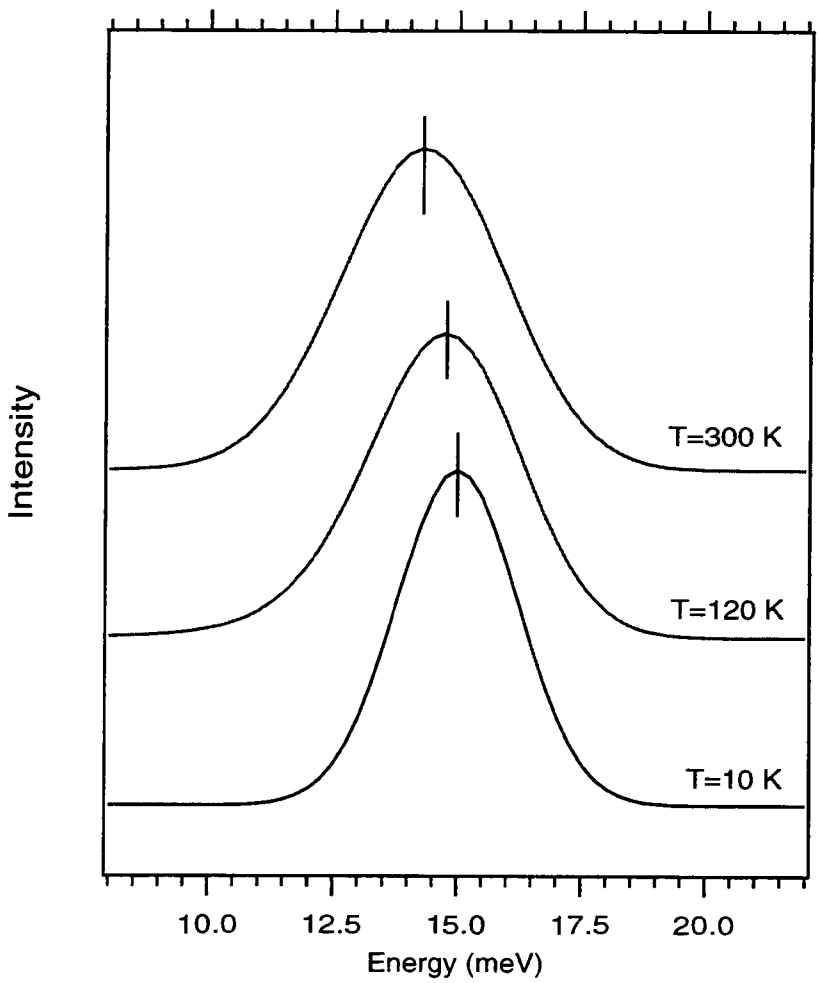


Figure 1.10: Simulated vibrational spectra at temperatures T=10 K, 120 K, and 300 K for a Morse potential with $\hbar\omega$=14.75 meV and X_a=0.035. The widths of the Gaussian function at temperatures T=10 K, 120 K, and 300 K are 3.0 meV, 4.0 meV, and 6.0 meV, respectively. The shifts of the spectral peaks (vertical lines) toward lower energies are referred to as phonon energy shifts.

1.6 Temperature Effects at Surfaces

Studying thermal effects on a surface is one of the most important subjects in Solid State Physics because experiments are performed at a finite temperature. Understanding the thermal effects on the surface structure is inherently more complex than determining the ground state structure (T=0 K). The first theoretical work in understanding the thermal expansion at the surface was done by Allen *et al.* by minimizing the Helmholtz free energy [80,81]. The main finding from their studies was that the thermal expansion at the surface is considerably larger than in the bulk. Theoretical investigation via free energy calculations with pairpotentials suggested that the anharmonicity for the (100), (110), and the (111) surfaces of Cu is expected to be 2 - 3 times greater than in the bulk [80-83]. This enhanced anharmonicity at the surface is the consequence of the creation of the surface: the number of the nearest neighbors of atoms near the surface region is reduced and the translation symmetry perpendicular to the surface is lost. Consequently, the interlayer potential near the surface region becomes more asymmetric than in the bulk. The first enhanced surface anharmonicity was observed by Baddorf and Plummer by using high resolution electron energy loss spectroscopy [74]. They measured the surface anharmonicity on Cu(110) by examining the temperature dependence of the surface phonon energies and lifetimes, which revealed the vibrational anharmonicity for normal to the Cu(110) surface is 4 - 5 times greater than in the bulk [79]. Therefore, the thermal expansion at this surface should be larger than in the bulk. Indeed, X-ray reflectivity measurements on Cu(110) in the temperature range of 300 K to 900 K showed an enhanced surface thermal expansion (2-3 times the bulk value) [84].

The observation of thermal expansion for Pb(110), using double alignment ion scattering, showed that a gradual increase in the surface thermal expansion coefficient relative to the bulk was observed in the temperature range of 29 K to ~460 K, but a precipitous increase occurred at 485 K in the premelting regime [85]. A kinematic analysis

of electron diffraction data from Ni(100) in 1990 showed a rapid increase in the surface thermal expansion compared to the bulk above 900 K, reaching a value ~20 times larger than the bulk expansion [86]. Another kinematic analysis of electron diffraction in 1993, from the Al(110) surface indicated a negative thermal expansion of the surface interplanar spacing in the temperature range of 40 K to 450 K, with the surface thermal expansion coefficient equal to -1 times the bulk thermal expansion coefficient [87]. A double alignment ion scattering study of Ag(111) in 1994 revealed an anamolously large surface thermal expansion for temperatures above ~600 K [88]. In this case, there was a sign reversal in the surface relaxation, from contraction at low temperature to expansion at high temperature. By using electron energy loss spectroscopy, Hannon measured the temperature dependence of the surface Rayleigh wave on Be(0001) [70]. He found that there is very little anharmonicity behavior at the Be(0001) surface (measured at the zone boundary $\overline{K}$ and $\overline{M}$ points, suggesting that (according to common belief) the surface thermal expansion on Be(0001) is similar to the bulk thermal expansion or no enhanced thermal expansion at this surface. Nonetheless, recent measurements of thermal surface expansion of Be(0001) by using low-energy electron diffraction (LEED) with multiple scattering analysis at temperatures 110 K to 700 K show that there is a large thermal surface expansion of Be(0001), a 6 enhancement with respect to the bulk [36]. Table 1.6 lists the temperature dependent of the change in the first interlayer spacing with respect to the bulk from calculations and experimental data. Most of these measurements are at a high-temperature or close to a melting regime, which are not quite sufficient to explain the behavior of the surface thermal expansion at a low temperature.

Narasimham and Scheffler [89] proposed a theoretical calculation model to study the thermal expansion of surfaces, wherein the phonon frequencies are obtained from *ab initio* total energy calculations. Anharmonic effects are treated exactly in the direction normal to the surface, and within the quasiharmonic approximation in the plane of the

Table 1.6: List of the first interlayer relaxation from calculations and experiments at finite temperatures.

Pb(110)	T=0K	T=100K	T=300K	T=450 K	T=485 K
Experiment [ref. 85]:					
$\Delta d_{12}/d_0$(%)	---	-15.2	-13.75	-12.2	-3.0
Theory [ref. 113]:					
$\Delta d_{12}/d_0$(%)	-15.9	---	---	---	---

Cu(110)	T=0K	T=300K	T=500K	T=700 K	T=925 K
Experiment [ref. 84]:					
$\Delta d_{12}/d_0$(%)	---	-6.0	-5.3	-5.4	-2.8
Theory [ref. 114]:					
$\Delta d_{12}/d_0$(%)	-8.73	---	---	---	---

Ag(111)	T=0K	T=300K	T=500K	T=750 K	T=1150 K
Experiment [ref. 88]:					
$\Delta d_{12}/d_0$(%)	---	-2.5	-2.4	-0.0	+10.0
Theory:					
$\Delta d_{12}/d_0$(%)[89]	-2.2	-1.0	-0.3	+1.7	> +20
$\Delta d_{12}/d_0$(%)[91]	-1.4	-1.2	-1.05	-0.9	+0.00

Table 1.6: (continued)
List of the first interlayer relaxation from calculations and experiments at a finite temperature.

Be(0001)	T=0K	T=110K	T=300K	T=700 K
Experiment [ref. 36]:				
$\Delta d_{12}/d_0$(%)	---	+3.1	+4.3	+6.7
Theory:				
$\Delta d_{12}/d_0$(%)[36]	+3.7	+3.9	+4.6	+7.0
$\Delta d_{12}/d_0$(%)[93]	+3.3	+3.35	+3.45	+4.1

Rh(001)	T=50K	T=100K	T=300K	T=400 K	T=500 K
Experiment [ref. 115]:					
$\Delta d_{12}/d_0$(%)	---	---	-1.16	---	---
Theory [ref. 90]:					
$\Delta d_{12}/d_0$(%)	-2.4	-2.2	-1.4	-1.0	-0.5

surfaces. At a finite temperature, the equilibrium structure is determined by the minimum of the free energy with respect to the structural parameters, where both the electrons and phonons are important in determining the structure. They suggested that the large thermal expansion for Ag(111) can be attributed to a rapid softening of the *in-plane* phonon frequencies with increasing temperature rather than anharmonicity in the out-of-plane modes [89]. This behavior is similar to the case of Rh(001) [90]. Therefore, the reduction in symmetry at the surface would allow for coupling between the atomic motion parallel to the surface (phonons) and the perpendicular (interplanar) relaxation. Kara *et al.* also studied the thermal expansion of the Ag(111) surface with several approximations [91]. By using molecular dynamic simulations, they found that there is no sign reversal in the relaxation of the first interlayer spacing of the Ag(111) surface up to 1100 K, contradictory to the experimental observation [88] and Narasimham's model [89]. They also performed the thermal expansion calculations within the quasiharmonic approximation with embedded atom method potentials by examining the contributions of the different phonon modes to the vibrational free energy of the Ag(111) surface. They reported that different sampling modes could lead to a different result in the surface thermal expansion [91]. Very recently, Xie and Scheffler studied the temperature dependent structure of the Rh(100) and Rh(110) surfaces by using the density functional theory and the full-potential linearized augmented plane wave (LAPW) method [92]. They obtained the force constants directly from calculated atomic forces by using a slab model. The free energy was obtained by including the contribution of phonons in the quasiharmonic approximation. The temperature dependence of the first interlayer spacing was obtained by minimizing the free energy with respect to the first interlayer spacing by considering several different phonon modes. The main finding from their study is that the *in-plane* vibrations contribute significantly to the surface thermal expansion, which is the same conclusion as for the Ag(111) surface proposed by Narasimham [89]. The observation of thermal expansion of the Be(0001)

surface [36] was supported by the density-functional calculations within the quasiharmonic approximation [36]. They suggested that the enhanced thermal expansion at the Be(0001) surface is caused primarily by a softening of the in-plane vibrations [36]. But this conclusion has been dramatically challenged by an *ab initio* study of the surface thermal expansion within the quasiharmonic approximation where the free energy is obtained from *full* vibrational dispersions computed via the density-functional perturbation theory by Lazzeri and de Gironcoli [93]. They claimed that there is no an anomalously large thermal expansion at the Be(0001) surface and the experiments must be a consequence of the surface morphology [93]. Clearly, there is an anomaly in the theoretical calculations of the surface thermal expansion at a metal surface.

In the quasiharmonic approximation, the first interlayer distance d_{12} at a finite temperature is obtained by minimizing the free energy for the surface with d_{12}. The free energy for the surface is given by [89]:

$$F(d_{12},T) = V(d_{12}) + k_B T \sum_i \ln\left\{2\sinh\left(\frac{\hbar\omega_i(d_{12})}{2k_B T}\right)\right\} \qquad (1.10)$$

where k_B and $\hbar$ are the Boltzmann's and Planck's constants, respectively. T is the temperature. The first term in the equation (1.10) is the static interlayer potential of d_{12} and the second term is the vibrational free energy corresponding to the vibrations in the *i*-th direction. The sum in the equation (1.10) runs over all phonon bands in the entire surface Brillouin zone. $\omega_i(d_{12})$ is the frequency of the phonon mode polarized along the i-th direction when the first interlayer spacing is fixed at d_{12}. The in-plane parameters and *all other interlayer distances are assumed to be the same as in the bulk.* This assumption might be true only at low-temperature (below Debye-temperature) or in the system where the interlayer spacing between the second and the third layers (d_{23}) is almost the same as in the bulk; while for the system where the interlayer spacing between the second and the third

layer (d_{23}) is significantly larger than in the bulk, the quasiharmonic approximation may fail at high-temperature.

There is another mechanism in understanding the thermal expansion at a metal surface; a very recent theoretical investigation of the Al(110) surface, by using finite temperature density functional molecular dynamic simulations, revealed that a *thermal contraction* in the first interlayer (the first interlayer spacing becomes shorter as the temperature increases) as a consequence of a strongly anharmonic mean-square displacement of atoms in the *second layer* (not in the surface layer) perpendicular to the surface [94].

My temperature-dependent low-energy electron diffraction (LEED) *I-V* measurements at the Mg($10\bar{1}0$) surface revealed *a remarkable oscillatory thermal relaxation.* As the temperature increases, the short interplanar spacings $d_{1,2}$, $d_{3,4}$, and $d_{5,6}$ contract, while the long interplanar spacings $d_{2,3}$, $d_{4,5}$, and $d_{6,7}$ expand, as shown in Figure 1.11. The experimental data extrapolated to T=0 K are in excellent agreement with the self-consistent density-functional theory calculations (by taking into account the effect of the screening) [13] and electrostatic calculations [51]. It is rather surprising that both calculations produce the same result, an oscillatory multilayer relaxation at the metal surface, even though the physics of both models is quite different.

It is clear that understanding the temperature dependence of the surface properties is a very interesting subject. Surfaces offer a unique environment for the observation of new physical phenomena associated with the coupling of lattice structure, lattice dynamics and electronic structure. The goal of the research presented in this thesis is to attempt to understand the interplay between the temperature-dependent geometric structure and dynamical properties of the metal surfaces that relates to the surface electronic structure as the consequence of the broken symmetry and reduced dimensionality due to the creation of the surface from a bulk material.

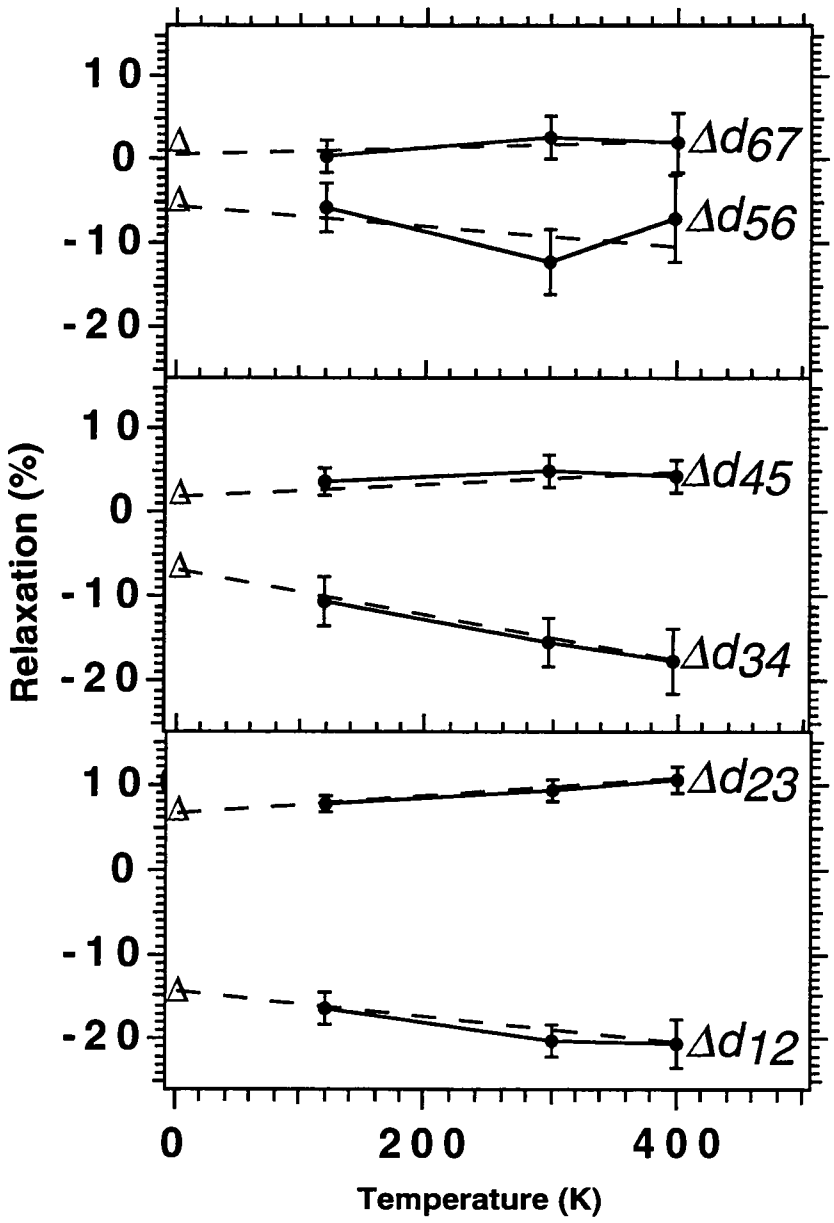


Figure 1.11: First-principles calculations at T=0 K (unfilled triangles) [13] and our experimental data of the temperature-dependent relaxations at the Mg(10$\bar{1}$0) surface. Dashed lines are the extrapolation lines to T=0 K.

1.7 Magnesium Surfaces

Magnesium (Mg) is a hexagonal closed-packed (hcp) crystal structure, which can be viewed as a two simple hexagonal displaced from one another vertically along the common axis-c by a distance c/2 and shifted horizontally as shown in Figure 1.12. The *c/a* ratio of this element is 1.62 [61], which is almost equal to the ideal value (*c/a*=1.63) calculated from the packing of hard spheres. The atomic number of Mg is 12 a.u. with the atomic configuration is $1s^2 2s^2 2p^6 3s^2$. Magnesium has two valence electrons and its electronic spectrum is defined by s-p states. Its bulk density of state is nearly free-electron-like [95]; therefore magnesium is considered to be one of the most free-electron-like metals, besides aluminum. The cohesive energy of magnesium is 1.51 eV/atom [96], indicating a weak binding crystal and the bulk thermal expansion $\alpha_B \approx 25 \times 10^{-6}$ K^{-1}, which is almost the same as the bulk thermal expansion of aluminum [97]. The Mg_2 dimer bond length is 3.89 Å [97], which is 22% longer than the nearest neighbor distance in bulk Mg, suggesting that the Mg_2 is weakly bound. However the dimer bond length of aluminum is 2.70 Å [97], which is 6% shorter than the nearest neighbor distance in bulk Al. This shows that magnesium does not obey the usual bond order bond length correlation, suggesting a weak van der Waals interaction. The bulk properties of magnesium are tabulated in Table 1.7, in comparison with the bulk properties of aluminum.

The (0001) face is a basal plane of a hexagonal close-packed crystal. The surface normal is parallel to the *c* axis (common axis). This surface is stacked by A-B-A-B plane sequences with the interlayer spacing of *c*/2, as shown in Figure 1.13. The electronic structure of the Mg(0001) surface had been measured by Karlsson *et al.* [98] and Bartynski *et al.* [99] by using photoemission. They found the surface states at $\overline{\Gamma}$ and $\overline{M}$ with a binding energy 1.6 eV and 1.1 eV, respectively [99]. The main finding from their study is that the dispersion of the surface states of Mg(0001) surface follows the projected bulk band edge, which is fitted by a free-electron-like parabola with an effective mass m^*=1.31

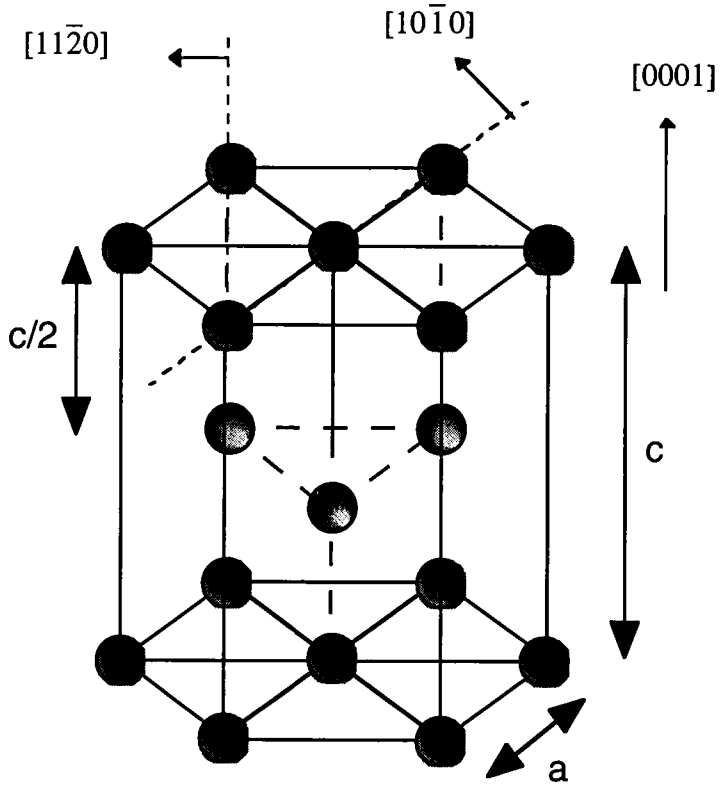


Figure 1.12: Bulk hexagonal close-packed structure. *a* and *c* are lattice constants.

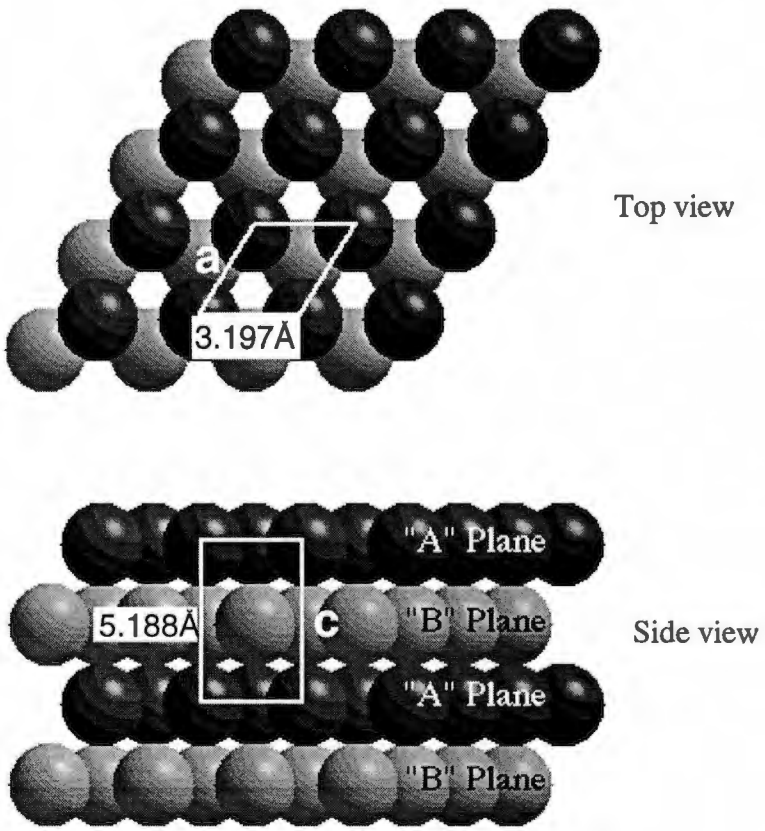


Figure 1.13: Geometry of the Mg(0001) surface with the stacking sequence of A-B-A-B. The lattice constants a=3.197 Å and c=5.188 Å.

Table 1.7: Comparison of bulk properties of magnesium (Mg) and aluminum (Al).

Property	Mg	Al
Dimer bond length (Å)	3.89 [Ref.97]	2.70 [Ref.97]
NN bond length (Å)	3.20 [Ref.19]	2.86 [Ref.19]
c/a ratio	1.62 [Ref.19]	1.63 [Ref.19]
Cohesive energy per bond (eV)	0.25 [Ref.19]	0.56 [Ref.19]
Electron density radius r_s (bohr)	2.65 [Ref.96]	2.07 [Ref.96]
$N(E_F)$ (states/eV-atom)	0.45 [Ref. 95]	0.41 [Ref.95]
Thermal expansion (10^{-6} K^{-1})	24.3 ($\perp$) [Ref.96]	23.6 [Ref.96]
	25.7 (II)	
Debye temperature (K)	400 [Ref.19]	428 [Ref.19]

x m_e, as shown in Figure 1.14. Chulkov *et al.* performed the calculation of the electronic structure of the Mg(0001) surface [100]. Their results are (as shown in Figure 1.15) in good agreement with the experimental data [99]. From the experimental data and calculations, it is clear that the electronic properties of the Mg(0001) surface are free-electron-like.

The $Mg(10\bar{1}0)$ surface has a higher corrugation than the Mg(0001) surface. This $Mg(10\bar{1}0)$ surface has two possible surface terminations: *short termination* and *long termination*, as illustrated in Figure 1.16. The *short termination* has the interlayer spacing of d_{12} shorter than that of d_{23} (d_{12} = 0.923 Å and d_{23} = 1.846 Å) and each atom of the top surface layer is surrounded by six nearest neighbors (four atoms in the second layer and two atoms in the third layer). However, for *long termination*, the interlayer spacing of d_{12} is longer than that of d_{23} and each atom of the top surface layer is surrounded by only four nearest neighbors (two atoms in the second layer and two atoms in the third layer). For *short termination*, the first interlayer may be thought of as a bi-layer and the crystal may be thought of as a stack of such bi-layers. Unfortunately, the electronic properties of the $Mg(10\bar{1}0)$ surface is still unknown.

Magnesium was chosen as a prototypical system in this study because it is a free-electron-like metal and an ideal test for first-principles calculations. The presented research will focus on two low Miller index surfaces of magnesium, which are a closed-surface and an open surface: the Mg(0001) and $Mg(10\bar{1}0)$ surfaces. The open surface or the $Mg(10\bar{1}0)$ surface has a short interlayer spacing, where d_{12} is 0.923 Å and d_{23} is 1.846 Å, allowing one to observe the effects of the broken symmetry in deep layers. The information collected from this research will have a significant impact on the other metal surfaces, especially for simple metal.

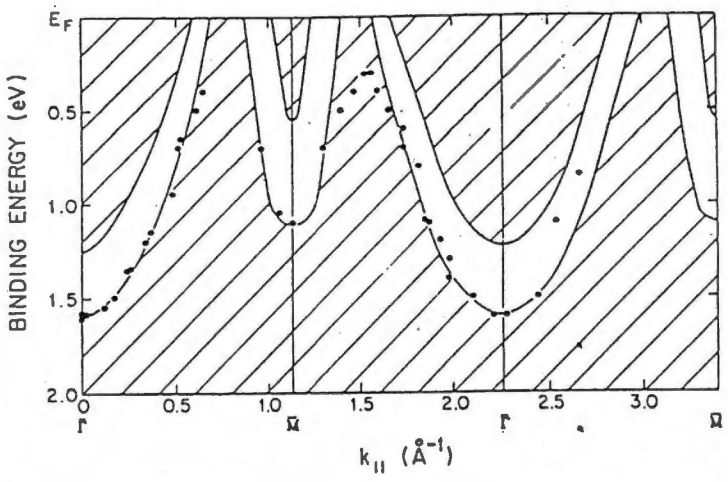


Figure 1.14: Measured surface states at the Mg(0001) surface by Bartynski [99]. The dots are experimental data and the shaded region is the projected bulk bands onto the (0001) face.

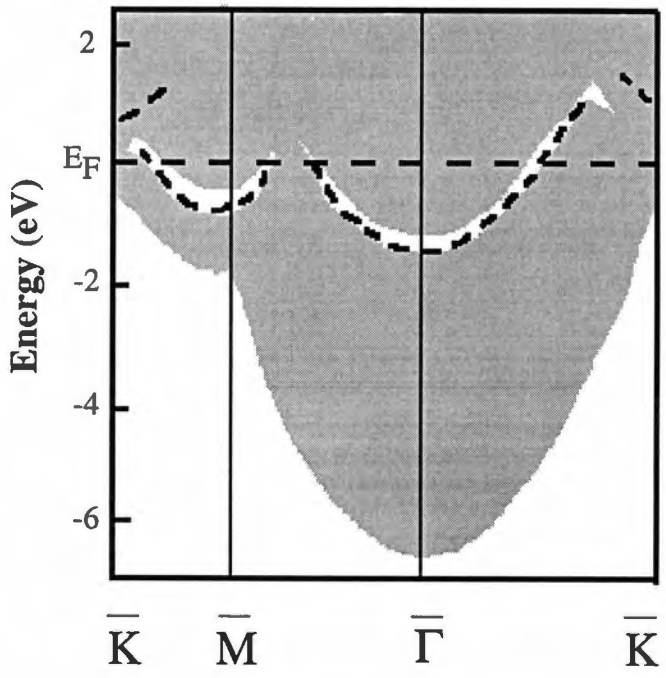


Figure 1.15: Calculated surface electronic structure at the Mg(0001) surface by Chulkov [77]. The surface modes are denoted by the dashed lines. The shaded region is the projected bulk bands onto the (0001) face.

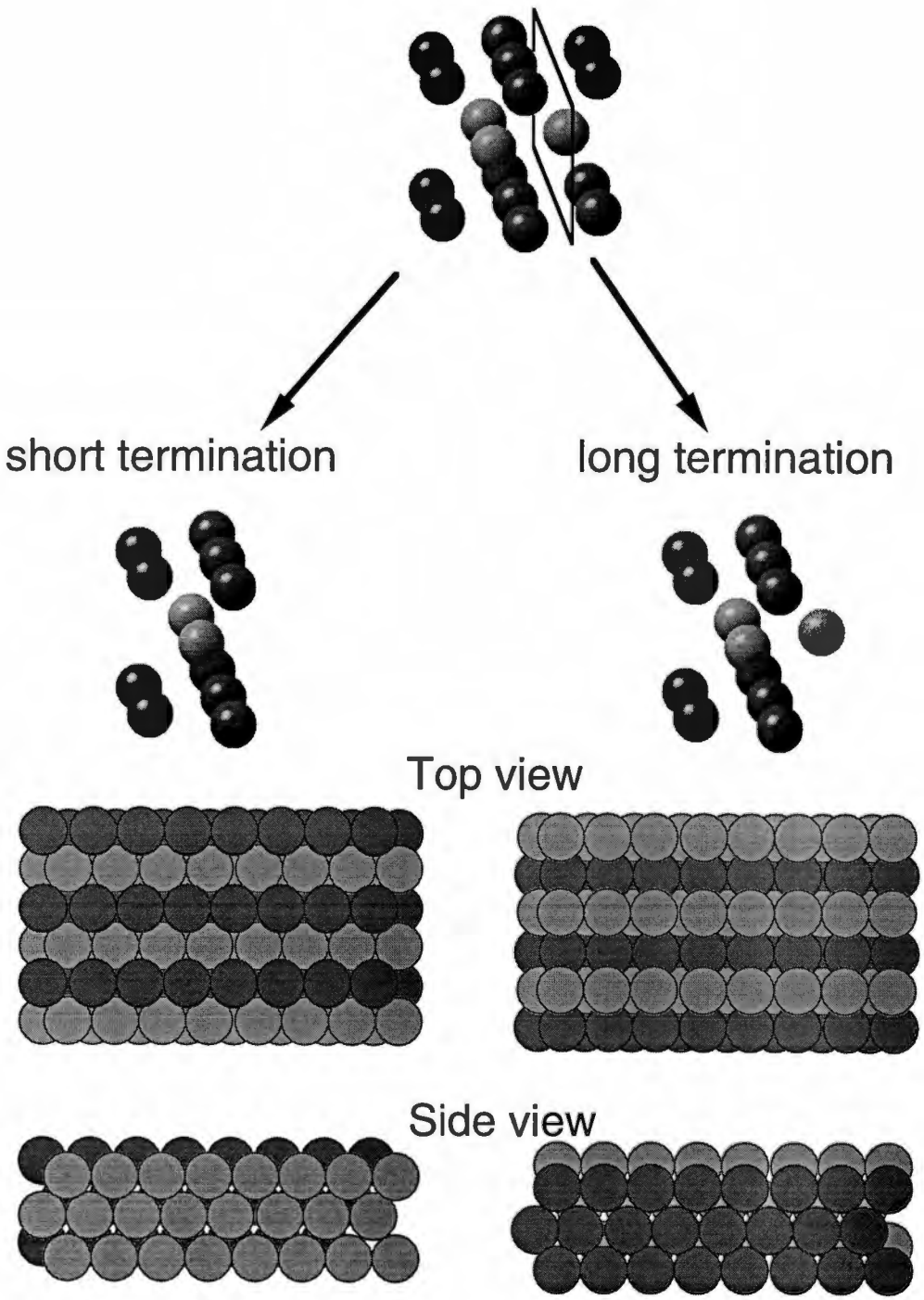


Figure 1.16: The geometry of bulk truncated models (*short termination* and *long termination*) of the Mg$(10\bar{1}0)$ surface.

1.8 Thesis Syllabus

This thesis is organized in the following way: detailed information about the experimental techniques and analytical procedures are discussed in Chapter 2. The geometric structure of the Mg(0001) and Mg$(10\bar{1}0)$ surfaces and their thermal effects are discussed in Chapter 3. In Chapter 4, the surface dynamics of the Mg(0001) and Mg$(10\bar{1}0)$ surfaces are discussed, and the overview of the interplay between the structure and dynamics at the metal surfaces is discussed in Chapter 5.

1.9 References

1. J. A. Gaspar and A. G. Eguiluz, Phys. Rev. B **40**, 11976 (1989).
2. Ismail, J.-H. Cho, Zhenyu Zhang, and E. W. Plummer, To be published.
3. H. Göbel and P. von Blanckenhagen, Phys. Rev. B **47**, 2378 (1993).
4. N. Marzari, D. Vanderbilt, A. De Vita, and M. C. Payne, Phys. Rev. Lett. **82**, 3296 (1999).
5. J. Friedel, Nuovo Cimento Suppl. **7**, 287 (1958).
6. N. D. Lang and W. Kohn, Phys. Rev. B **1**, 4555 (1970).
7. P.T. Sprunger, L. Petersen, E.W. Plummer, E. Laegsgaard, and F. Besenbacher, Science **275**, 1764 (1997).
8. Ph. Hofmann, B.G. Briner, M. Doering, H.-P. Rust, E.W. Plummer, and A.M. Bradshaw, Phys. Rev. Lett. **79**, 265 (1997).
9. J. Bardeen, Phys. Rev. **49**, 653 (1936).
10. P. Hohenberg and W. Kohn, Phys. Rev. **136**, B864 (1964).
11. W. Kohn and L. J. Sham, Phys. Rev. **140**, A1133 (1965).
12. A.J. Bennett and C.B. Duke, in *Structure and Chemistry of Solid Surfaces*, edited by G. A. Somorjai (Wiley, New York, 1969).
13. J.-H. Cho, Ismail, Zhenyu Zhang, and E. Ward Plummer, Phys. Rev. B **59**, 1677 (1999).
14. Pavlin Staikov and Talat S. Rahman, To be published.
15. R. Smoluchowski, Phys. Rev. **60**, 661 (1941).
16. D. Kalkstein and P. Soven, Surf. Sci. **26**, 85 (1971).
17. W. F. Egelhoff, Phys. Rev. Lett. **50**, 587 (1983).
18. S. Lizzit, K. Pohl, A. Baraldi, G. Comeli, V. Fritzsche, E.W. Plummer, R. Stumpf, and Ph. Hofmann, Phy. Rev. Lett. **81**, 3271 (1998).
19. C. Kittel: *Introduction to Solid State Physics* – 7th ed. Wiley, New York, 1996.
20. J.K. Grepstad, P.O. Gartland, and B.J. Slagvold, Surf. Sci. **57**, 348 (1976).
21. G.V. Hansson and S.A. Flodström, Phys. Rev. B **18**, 1562 (1978).
22. M. Heinrichsmeier, A. Fleszar, and A. G. Eguiluz, Surf. Sci. **285**, 129 (1993).

23. *Electronic Surface and Interface States on Metallic Systems*, Proceeding of the 134th We-Heraeus Seminar, ed. E. Bertel and M. Donath, World Sci., Singapore, 1995.

24. R. P. Feynman, Phys. Rev. **56**, 340 (1939).

25. M. W. Finnis and V. Heine, J. Phys. F **4**, L37 (1974).

26. R. J. Needs, Phys. Rev. Lett. **58**, 53 (1987).

27. R. J. Needs, M. J. Godfrey, and M. Mansfield, Surf. Sci. **242**, 215 (1991).

28. S. Lehwald, F. Wolf, H. Ibach, B. M. Hall, and D. L. Mills, Surf. Sci. **192**, 131 (1987).

29. W. Daum, C. Stuhlmann, and H. Ibach, Phys. Rev. Lett **60**, 2741 (1988).

30. C. Herring, *The Physics of Powder Metallurgy,* Ed. W. E. Kingston (McGraw Hill, New York, 1951).

31. M.C. Payne, N. Roberts, R. J. Needs, M. Needels, and J.D. Joannopoulos, Surf. Sci. **211/212,** 1 (1989).

32. D. L. Adams, H. B. Nielsen, M. A. Van Hove, and A. Ignatiev, Surf. Sci. **104**, 47 (1981).

33. W. Moritz and D. Wolf, Surf. Sci. **163**, L655 (1985).

34. C.-M. Chan and M. A. Van Hove, Surf. Sci. **171**, 226 (1986).

35. J. B. Hannon, K. Pohl, P. J. Rous, and E. W. Plummer, Surf. Sci. **364**, L617 (1996).

36. K. Pohl, J. -H. Cho, K. Terakura, M. Scheffler, and E. W. Plummer, Phys. Rev. Letter. **80**, 2853 (1998).

37. J.R. Noonan and H. L. Davis, J. Vac. Sci. Tech. A **8**, 2671 (1990).

38. H. L. Davis and J.R. Noonan, Surf. Sci. **126**, 245 (1983).

39. J. Quinn, Y.S. Li, D. Tian, H. Li, F. Jona, and P.M. Marcus, Phys. Rev. B **42**, 11348 (1990).

40. Ph. Hofmann, K. Pohl, R. Stumpf, and E.W. Plummer, Phys. Rev. B **53**, 13715 (1996).

41. H. Over, G. Kleinle, G. Ertl, W. Moritz, K. -H. Ernst, H. Wohlgemuth, K. Christmann, and E. Schwarz, Surf. Sci. **254**, L469 (1991).

42. J.N. Andersen, H.B. Nielsen, L. Petersen, and D.L. Adams, J. Phys. C **17**, 173 (1984).

43. D.L. Adams, L. Petersen, C.S. SØrensen, J. Phys. C **18**, 1753 (1985).

44. Y. Kuk and L.C. Feldman, Phys. Rev. B **30**, 5811 (1984).

45. C.J. Barnes, M.Q. Ding, M. Lindroos, R.D. Diehl, and D.A. King, Surf. Sci. **162**, 59 (1985).

46. D. L. Adams, V. Jensen, X. F. Sun, and J. H. Vollesen, Phys. Rev. B **38**, 7913 (1988).

47. X. -G. Zhang *et al.*, Phys. Rev. Lett. **67**, 1298 (1991).

48. Ismail, A. T. Hanbicki , S. Chandravakar, D. M. Zehner, and E. Ward Plummer, To be published.

49. D.L. Adams and C.S. SØrensen, Surf. Sci. **166**, 495 (1986).

50. U. Landman, R. N. Hill, and M. Mostoller, Phys. Rev. B **21**, 448 (1980).

51. P. Jiang, P. M. Marcus, and F. Jona, Solid State Comm. **59**, 275 (1986).

52. R. N. Barnett, U. Landman, and C. L. Cleveland, Phys. Rev. B **28**, 1685 (1983).

53. K. M. Ho and K. P. Bohnen, Phys. Rev. B **32**, 3446 (1985).

54. A. G. Eguiluz, Phys. Rev. B **35**, 5473 (1987).

55. P. T. Sprunger, K. Pohl, H. L. Davis, and E. W. Plummer, Surf. Sci. **297**, L48 (1993).

56. J.W. Chung, in *Electronic Surface and Interface States on Metallic Systems*, Proceeding of the 134th We-Heraeus Seminar, ed. E. Bertel and M. Donath, pg. 127, World Sci., Singapore, 1995.

57. M. Born and K. Huang: *Dynamical Theory of Crystal Lattice* (Oxford Univ. Press, London, 1954).

58. A. A. Maradudin: *The Dynamical Properties of Solids,* Vol. 1 edited by G.K. Horton, A.A. Maradudin (Nort-Holland, Amsterdam, American Elsevier, New York 1974).

59. R. Pynn and G. L. Squires, Proc. Roy. Soc. (London) A **326**, 347 (1972).

60. R. Stedman and G. Nilsson, Phys. Rev. **145**, 492 (1966).

61. N. W. Ashcroft and N. D. Mermin, *Solid State Physics*, Holt, Rinehart, and Winston, 1976.

62. K. M. Ho and K. P. Bohnen, Phys. Rev. Lett. **56**, 934 (1986).

63. A. G. Eguiluz, A. A. Maradudin, and R. F. Wallis, Phys. Rev. Lett. **60**, 309 (1988).

64. A. G. Eguiluz and A. A. Quong, *Dynamical Properties of Solids*, Ed. G. K. Horton and A. A. Maradudin, Vol. 7 (North-Holland, Amsterdam, 1995).

65. C. Bungaro, S. de Gironcoli, and S. Baroni Phys. Rev. Lett. **77**, 2491 (1996).

66. M. Lazzeri and S. de Gironcoli, Surf. Sci. **402**, 715 (1998).

67. J.P. Toennies and Ch. Wöll, Phys. Rev. B **36**, 4475 (1987).

68. J. B. Hannon, E. J. Mele, and E. W. Plummer, Phys. Rev. B **53**, 2090 (1996).

69. H. Ibach and D.L. Mills: *Electron Energy Loss Spectroscopy* (Academic Press, New York, 1982).

70. J. B. Hannon, Ph.D. Thesis, University of Pennsylvania, USA, 1994.

71. L.D. Landau and E.M. Lifshitz, *Theory of Elasticity*, Course of Theoretical Physics, vol. 7, Permagnon Press, Oxford, 1986.

72. D. Pines and P. Nozières, *The Theory of Quantum Liquids*, Vol. 1 (Benjamin, New York, 1966).

73. A. G. Eguiluz, Phys. Rev. B **31**, 3303 (1985).

74. M. Wuttig, R. Franchy, and H. Ibach, Solid State Comm. **57**, 455 (1986).

75. S. Lehwald, F. Wolf, H. Ibach, B. M. Hall, and D. L. Mills, Surf. Sci. **192**, 131 (1987).

76. M. H. Mohamed and L. L. Kesmodel, Phys. Rev. B **37**, 6519 (1988).

77. E. V. Chulkov, V. M. Silkin, and E. N. Shirykalov, Surf. Sci. **188**, 287 (1987).

78. R.A. Bartynski, E. Jepsen, T. Gustafsson, and E. W. Plummer, Phys. Rev. B **32**, 1921 (1985).

79. A. P. Baddorf and E. W. Plummer, Phys. Rev. Lett. **66**, 2770 (1991).

80. R. E. Allen and F. W. deWette, Phys. Rev. **179**, 873 (1969).

81. R. E. Allen, F. W. deWette, and A. Rahman, Phys. Rev. **179**, 887 (1969).

82. S. K. S. Ma, F. W. de Wette, and G. P. Alldredge, Surf. Sci. **78**, 598 (1978).

83. C. S. Jayanthi, E. Tosatti, and L. Pietronero, Phys. Rev. B **31**, 3456 (1985).

84. G. Helgesen, D. Gibbs, A.P. Baddorf, D.M. Zehner, and S.G.J. Mochrie, Phys. Rev. **48**, 15320 (1993).

85. J.W.M. Frenken, F. Huussen, and J.F. van der Veen, Phys. Rev. Lett. **58**, 401 (1987).

86. Y. Cao and E. Conrad, Phys. Rev. Lett. **65**, 2808 (1990).

87. H. Göbel and P. von Blanckenhagen, Phys. Rev. B **47**, 2378 (1993).

88. P. Statiris, H.C. Lu, and T. Gustafsson, Phys. Rev. Lett. **72**, 3574 (1994).

89. S. Narasimhan and M. Scheffler, Z. Phys. Chem. **202**, 253 (1997).

90. Jun-Hyung Cho and M. Scheffler, Phys. Rev. Lett. **78**, 1299 (1997).

91. A. Kara, P. Staikov, A. N. Al-Rawi, and T. S. Rahman, Phys. Rev. B **55**, R13440 (1997).

92. J. Xie and M. Scheffler, Phys. Rev. B **78**, 4768 (1998).

93. M. Lazzeri and S. de Gironcoli, Phys. Rev. Letter. **81**, 2096 (1998).

94. N. Marzari, D. Vanderbilt, A. De Vita, and M. C. Payne, Phys. Rev. Lett. **82**, 3296 (1999).

95. V. L. Moruzzi, J. F. Janak, and A. R. Williams, *Calculated Electronic Properties of Metal,* Plenum, New York, 1978.

96. N. W. Ashcroft and N. D. Mermin, *Solid State Physics*, Holt, Rinehart, and Winston, 1976.

97. *American Institute of Physics Handbook* – 3 ed. McGraw-Hill, New York, 1972.

98. U. O. Karlsson, G. Hansson, P. Persson, and S. A. Flodström, Phys. Rev. B **26**, 1852 (1982).

99. R.A. Bartynski, R.H. Gaylord, T. Gustafsson, and E. W. Plummer, Phys. Rev. B **33**, 3644 (1986).

100. E.V. Chulkov and V.M. Silkin, Solid State Comm. **58**, 273 (1986).

101. Alan F. Wright, P. J. Feibelman, Susan R. Atlas, Surf. Sci. **302**, 215 (1994).

102. A. P. Seitsonen, B. Hammer, and M. Scheffler (unpublished).

103. H. B. Nielsen and D. L. Adams, J. Phys. C **15**, 615 (1982).

104. Alan F. Wright and D. C. Chrzan, Phys. Rev. Lett. **70**, 1964 (1993).

105. B. S. Itchkawitz, A. P. Baddorf, H. L. Davis, and E. W. Plummer, Phys. Rev. Lett. **68**, 2488 (1992).

106. J. R. Noonan and H. L. Davis, Phys. Rev. B **29**, 4349 (1984).

107. J. S. Nelson and P. J. Feibelman, Phys. Rev. Lett. **68**, 2188 (1992).

108. D. L. Adams and C. S. SØrensen, Surf. Sci. **166**, 495 (1986).

109. F.W. DeWette, R.M.J. Cotterill, and M.Doyama, Phys. Lett. **23**, 309 (1966).

110. A.P. Baddorf and E.W. Plummer, J. Electron Spec. And Related Phenomena, **54/55**, 541 (1990).

111. H.B. Rosenstock, Phys. Rev. B **9**, 1963 (1974).

112. A.P. Baddorf, Ph.D. Thesis, University of Pennsylvania, USA, (1987).

113. J.W. frenken, J.F. van er Veen, R.N. Barnett, U. Landman, and C.L. Cleveland, Surf. Sci. **172**, 319 (1986).

114. T.Ning, Q. Yu, and Y.Ye, Surf. Sci. Lett. **206**, L857 (1988).

115. A.M. Begley, S.K. Kim, F. Jona, and P.M. Marcus, Phys. Rev. B **48**, 12326 (1993).

Chapter 2

Experimental Techniques and Analytical Procedures

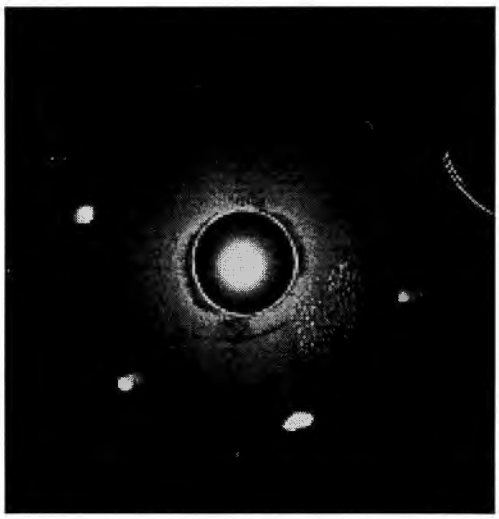
2.1 Ultra High Vacuum System

To conduct controlled experiments on clean and characterized surfaces of a material, it is necessary to have the pressure inside the chamber as low as possible or an ultra high vacuum in order to maintain the surface (sample) free from contamination for the duration of the experiment performed. For example, if we could prepare the sample in the air it would contaminate within a few nanoseconds. At a pressure of about $1x10^{-6}$ Torr, the gas will form a monolayer on the surface of a reactive material in approximately one second after exposure [1,2]. Nowadays, modern commercial equipment is available that can maintain the pressure inside the chamber below 10^{-10} Torr or ultra high vacuum (UHV). The UHV chamber system is made from a stainless steel vessel pumped by a turbo pump, an ion pump, and a titanium sublimation pump. All experimental apparatus and pumps mounted onto stainless steel flanges are sealed by standard commercial copper gaskets from UHV companies.

2.2 Sample Preparation

There were two samples of magnesium single crystal (the Mg(0001) and Mg$(10\bar{1}0)$ surfaces) used in the research presented in this thesis. The quality of the samples is quite good where the purity is 5N (99.99999 %) [3]. The orientation of the crystal was accomplished by using Laue X-ray diffraction with an orientation accuracy better than 0.1°. The crystals were mechanically polished with 1μm alumina beads in order to have a flat surface. Figure 2.1 shows the Laue pattern from the crystal of the Mg(0001) and

(a)



(b)

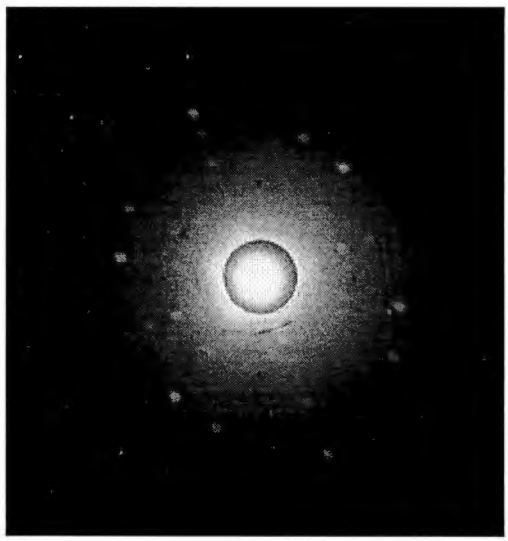


Figure 2.1: Laue pattern from the magnesium crystal used for the experiment in this thesis: (a) the Mg(0001) surface and (b) the Mg($10\bar{1}0$) surface.

Mg$(10\bar{1}0)$ surfaces after polishing in order to verify the crystallinity and the surface bulk truncation of the samples.

The crystal was mounted with highly thermal contact on the sample holder that is connected to cold fingers. The sample can be heated resistively and cooled to about 100 K by filling a dewar with liquid nitrogen. The temperature of the sample was measured by using thermocouple wires connected directly to the sample. After baking the UHV chamber, a series of sputtering and annealing cycles was done in order to remove the contaminants and the oxide layer on the surface of the sample. Magnesium is very reactive with oxygen and it is difficult to have a clean surface. At first (after baking the UHV chamber), the magnesium sample was sputtered by using Ne^+ ion bombardment with kinetic energy 1 keV at high-sputtering current 15 μA at the temperature of the sample 400 K for 1.0 hour (each cycle) to remove the thick MgO layers. The collision between the Ne^+ ions and the surface results in removal of several top layers including contaminants. The sputtering was done at +15° off normal incident for 0.5 hours and -15° off normal incident for 0.5 hours. The off-normal incident sputtering helps to remove the oxide layers quickly and reduces the damage at the surface. After sputtering, the sample was annealed at a temperature of 425 - 450 K for 10 minutes (each cycle) to restore the surface composition and "heal" the damage at the surface due to the sputtering. Extreme care was taken not to allow the temperature of the sample rise above 450 K, in order to prevent sublimation. After repeating this cleaning process for about 15 cycles, the LEED pattern can be observed. The next cleaning procedure was done by sputtering the sample with the Ne^+ ion bombardment at the kinetic energy 1 keV and the sputtering current 10 μA at room-temperature for 0.5 - 1.0 hour (each cycle). Subsequently, the sample was annealed at the temperature 425 - 450 K for 10 minutes (each cycle). This procedure was repeated until it produced a sharp LEED pattern, as shown in Figure 2.2. The cleanliness of the sample was monitored by Auger electron spectroscopy (AES), where the contamination of oxygen is at

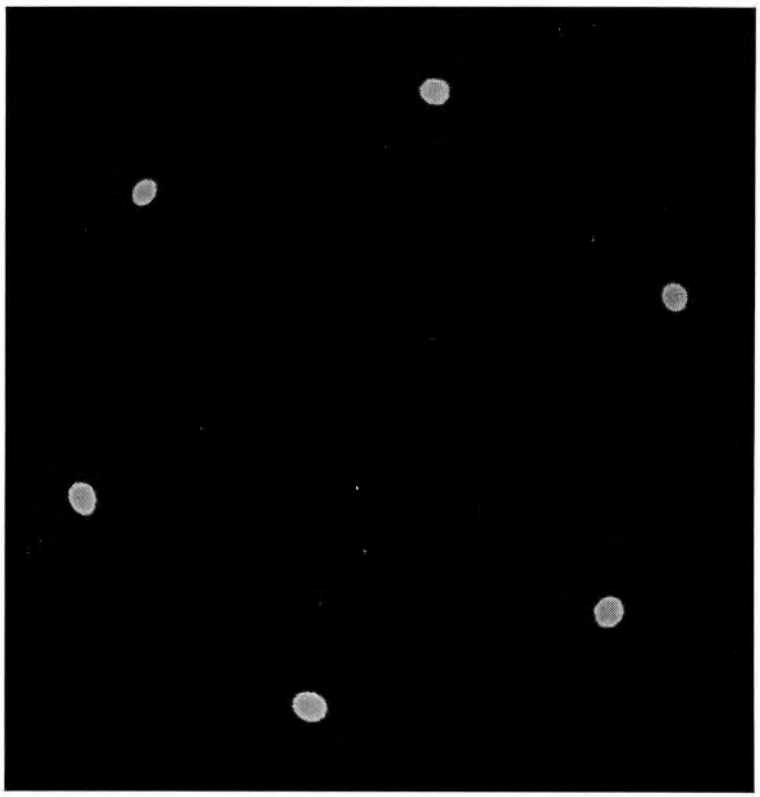


Figure 2.2: LEED photo from the Mg(0001) surface at the kinetic energy of electron E=50 eV at room-temperature.

energy 510 eV and of carbon is at energy 275 eV. Figure 2.3 shows the Auger spectra for a clean surface of magnesium. Besides AES, we also used electron energy loss spectroscopy (EELS) to check the cleanliness of the sample, especially from oxygen contamination since magnesium is very reactive with oxygen. The vibrational energy of the Mg-O stretching is at 60-80 meV. Figure 2.4 shows the EELS spectra at the specular direction for a clean surface of magnesium. The preparation of magnesium sample was also explained elsewhere [3].

2.3 Low Energy Electron Scattering from Surfaces

2.3.1 Theory

The main reason why electron probes are used in most experimental techniques is that the mean free path of electrons in a solid with the kinetic energy 10 - 1000 eV is about 10 Å, as shown in Figure 2.5 (the universal curves of the electron mean free-path in solids) [4]. When an electron hits the surface of a solid, in general it will penetrate only about 5 atomic layers from the surface, i.e., in general the atomic interlayer distance in solid is about 2 Å. Therefore, the experiment by using an electron probe will provide the information in the vicinity of the surface.

Low energy electron diffraction (LEED) was discovered in 1927 by Davisson and Germer [7]. Subsequently, Park and Farnsworth [8] found that the modulation of the diffraction intensity from the surface of a material as a function of energy (known as *I-V* spectra) is related to the information of the geometric structure near the surface region. The basic idea of LEED is rather simple [9,11]. Assume that a mono-energetic electron beam with the momentum wave vector $\bar{k}_i$ is directed toward a layer of a two-dimensional array of atoms, as shown in Figure 2.6 (a). This electron can be represented by a plane wave that is described by:

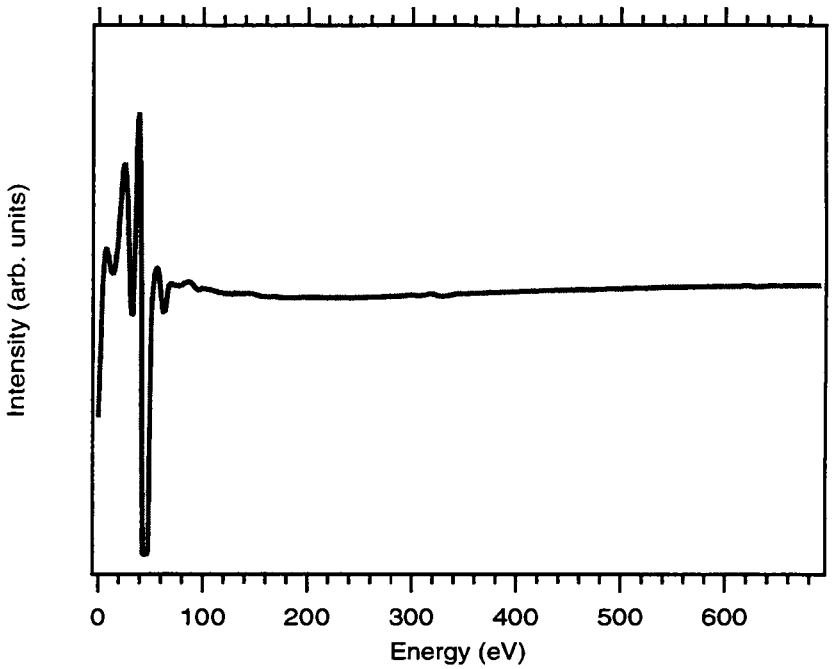


Figure 2.3: Auger spectrum for the clean Mg(10$\bar{1}$0) surface.

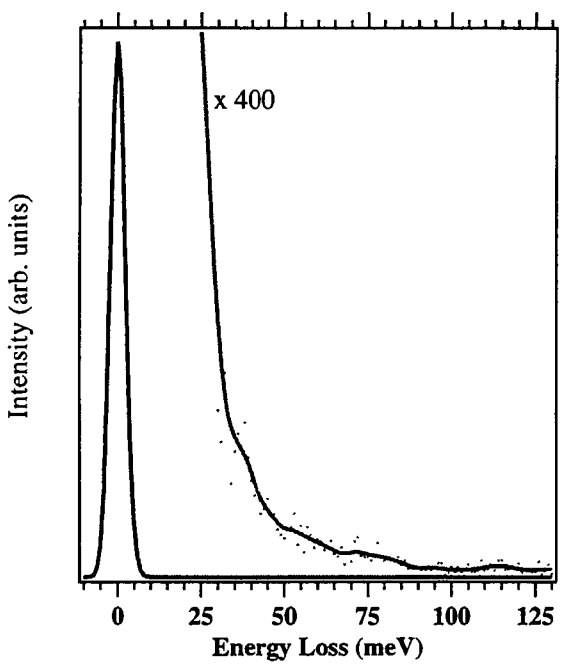


Figure 2.4: EELS spectrum for the clean Mg(10$\bar{1}$0) surface.

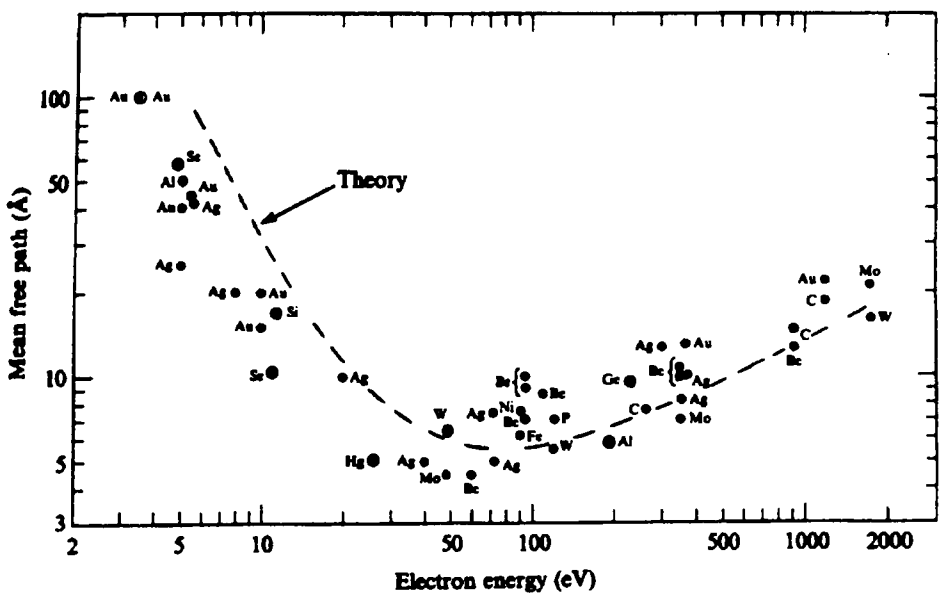


Figure 2.5: "Universal Curve" of electron mean-free paths in various materials [4].

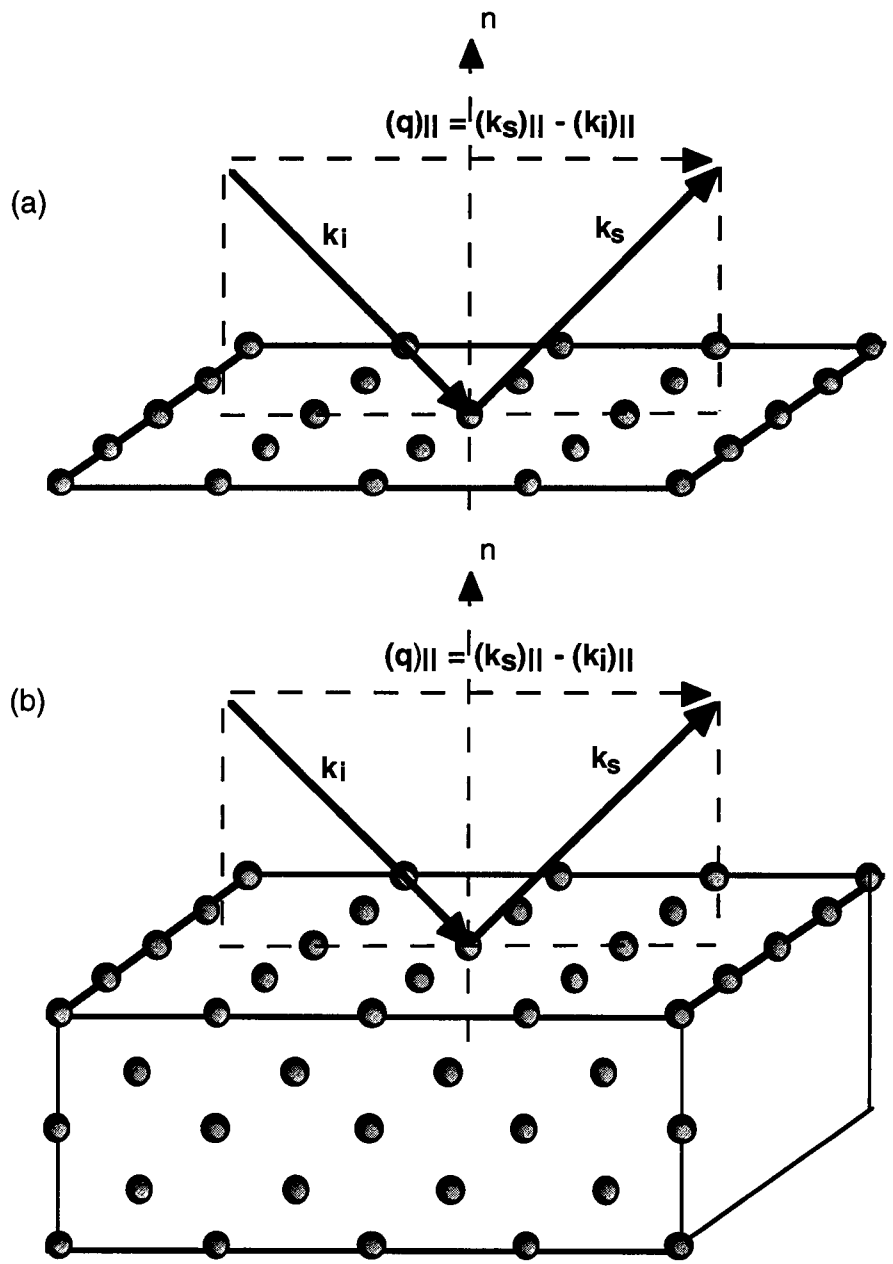


Figure 2.6: Electron scattering process in LEED.

$$A_i = A_o \cdot e^{-i\bar{k}_i \cdot \bar{r}} \tag{2.1}$$

where A_o is a constant and $\bar{r}$ is a space vector. Because the wavelength of an electron (for energy E=10 - 1000 eV) is comparable to the interatomic distance in a solid, then this electron can diffract from this ordered array of atoms.

In the kinematic approximation (where multiple scattering is neglected), the amplitude of this diffracted electron with the momentum wave vector $\bar{k}_{sc}$ can be represented by the following equation:

$$A_s = A_o \cdot \{\sum_n f_n \cdot e^{i\bar{q}_{\|} \cdot \bar{r}_n}\} \cdot e^{i\bar{k}_{sc} \cdot \bar{r}} \tag{2.2}$$

where f_n is known as a scattering-factor for the nth atom located at $\bar{r}_n$ and $\bar{q}_{\|}$ is a momentum transfer parallel to the surface, $\bar{q}_{\|} = (\bar{k}_s)_{\|} - (\bar{k}_i)_{\|}$. The atomic position vector $\bar{r}_n$ can be expressed by:

$$\bar{r}_n = \bar{R}_n + (m_1 \cdot \bar{a}_1 + m_2 \cdot \bar{a}_2) \tag{2.3}$$

where $\bar{R}_n$ is the location of the atom within the unit cell, $\bar{a}_1$ and $\bar{a}_2$ are the primitive translation vectors of the surface, and m_1 and m_2 are integers. The equation (2.2) becomes:

$$A_s = A_o \cdot \{\sum_n f_n \cdot e^{i\bar{q}_{\|} \cdot \bar{R}_n}\} \cdot \sum_{m_1, m_2} e^{i\bar{q}_{\|} \cdot (m_1\bar{a}_1 + m_2\bar{a}_2)} \cdot e^{i\bar{k}_{sc} \cdot \bar{r}} \tag{2.4}$$

or

$$A_s = A_o \cdot \{\sum_n f_n \cdot e^{i\bar{q}_{\|} \cdot \bar{R}_n}\} \cdot \delta(\bar{q}_{\|} - \bar{G}) \cdot e^{i\bar{k}_{sc} \cdot \bar{r}} \tag{2.5}$$

where $\bar{G}$ is the reciprocal lattice vector in two dimensions parallel to the surface given by:

$$\bar{G} = h \cdot \bar{b}_1 + p \cdot \bar{b}_2 \tag{2.6}$$

where h and p are integers. The primitive translation vectors of the reciprocal lattice $\bar{b}_1$ and $\bar{b}_2$ are given by:

$$\vec{b}_1 = 2\pi \frac{\vec{a}_2 \times \hat{z}}{\vec{a}_1 \cdot (\vec{a}_2 \times \hat{z})} \quad \text{and} \quad \vec{b}_2 = 2\pi \frac{\hat{z} \times \vec{a}_2}{\vec{a}_2 \cdot (\hat{z} \times \vec{a}_2)} \tag{2.7}$$

From the equation (2.5), we can see that the diffraction peaks will occur whenever the two-dimensional Bragg condition is fulfilled:

$$\vec{q}_{\parallel} = (\vec{k}_s)_{\parallel} - (\vec{k}_i)_{\parallel} = \vec{G} \tag{2.8}$$

For normal-incident, the momentum transfer parallel to the surface is zero, leading the diffracted electrons to emerge with the parallel momenta equal to the reciprocal lattice vector in two dimensions (parallel to the surface). The diffraction spots (integer beams) are usually labeled by a pair of integers (h,p), as given in the equation (2.6). The diffraction pattern provides the information of the unit surface cell and reconstruction on the surface. The distance between the spots gives the information on the distance between the atoms. Now, if we introduce a thick slab consisting infinite layers which has the periodicity perpendicular to the surface, as shown in Figure 2.6 (b), then the amplitude of the diffracted electron can be written as the following, i.e., by modifying the equation (2.5):

$$A_s = A_o \cdot \{\sum_n f_n e^{i\vec{q}\cdot\vec{R}_n}\} \cdot \delta(\vec{q}_{\parallel} - \vec{G}) \cdot e^{i\vec{k}_{sz}\cdot\vec{r}} \tag{2.9}$$

where the vector $\vec{R}_n = (n-1)\vec{a}_3$, n is integers, and $\vec{a}_3 = \xi\vec{a}_1 + \eta\vec{a}_2 + d_o\hat{z}$ where d_o is the interlayer spacing, ξ and η represents the registry shift from one to the next atomic-plane. By assuming the scattering factor for each atom is the same and constant equal to f, the equation (2.9) becomes:

$$A_s = A_o \{\frac{f}{(1 - e^{i\vec{q}\cdot\vec{a}_3})}\} \delta(\vec{q}_{\parallel} - \vec{G}) \tag{2.10}$$

From this equation (2.10) we will have diffraction rods by plotting the intensity of each beam as a function of the energy. The diffraction peaks (Bragg peaks) will occur at the conditions:

$$\bar{q} \cdot \bar{a}_3 = 2\pi p \quad , \text{where } p = 1,2,3,... \tag{2.11}$$

For simplicity, in order to understand the process of the electron diffraction from surface, let's consider a space where one-half is vacuum and the other one-half is occupied by a crystal composed of semi-infinite row of identical atoms with the interlayer spacing equal to d_o. Assume that there is only one atom in each atomic-plane. The properties of the scattering potential of each atom can be expressed in the transmission (T) and reflection (R) coefficients. Let's assume that T is real and R is complex. The relation between T and R is given by:

$$T^*T + R^*R = 1 \quad \text{or} \quad R = i\sqrt{(1-T^2)} \tag{2.12}$$

In the kinematic limit (where the multiple scattering is neglected), the amplitude of the diffracted electron, as given in the equation (2.10), can be written as the following:

$$A_s = A_o\{\frac{i\sqrt{(1-T^2}}{1-e^{iqd_o}}\}e^{-ikx} \tag{2.13}$$

The intensity of the diffracted electron or reflected intensity is given by $|A_s|^2$. Figure 2.7 shows the plot of the intensity as a function of the kinetic energy of electrons for T=0.8 and d_o=2.5944 Å. The Bragg reflection peaks occur at the energy $E = (\hbar^2/2m)(\pi^2 p^2/d_o^2)$ where p=1,2,3, and so on, as suggested in the equation (2.11). As shown in Figure 2.7, the Bragg reflection peaks are infinitely sharp because the lifetime of electrons in the calculation has been assumed to be infinite. In fact in the real situation, the lifetime of electrons in the solids is finite, as shown in Figure 2.5. In most LEED I-V calculations, the lifetime of electrons (electron-attenuation or mean-free-path of the electrons) is included in the calculations via an optical-potential. This optical-potential has two parts: a real part (V_{or}) and an imaginary part (V_{oi}), which are related to the elastic-scattering and inelastic-scattering of electrons in solids, respectively.

The imaginary part of the optical-potential V_{oi} can be described by a slow function of the kinetic energy of electrons. Let's consider a space where one-half is a vacuum and

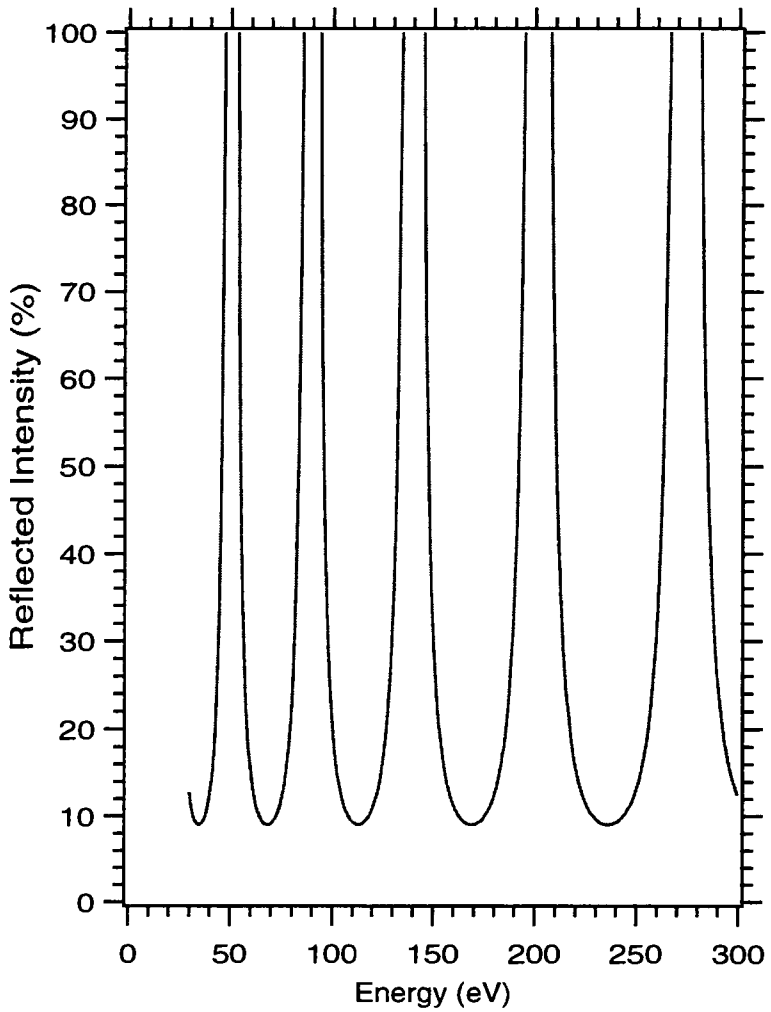


Figure 2.7: Calculated intensity as a function of the energy in the kinematic approximation by ignoring the lifetime of the electron for the model described in the text.

the other one-half is occupied by a crystal composed of a semi-infinite row of identical atoms and only one atom in each atomic plane, as was discussed above. The energy of electrons in the crystal can be written as the following (by ignoring the atomic-potential) [11]:

$$\frac{\hbar^2 k_s^2}{2m} = E + V_{or} + iV_{oi} \tag{2.14}$$

Now, k_s is complex and it can be written as $k_s = k_s^r + ik_s^i$. The equation (2.14) becomes:

$$\frac{\hbar^2}{2m}[(k_s^r)^2 - (k_s^i)^2 + i2k_s^i k_s^r] = E + V_{or} + iV_{oi} \tag{2.15}$$

or

$$E + V_{or} = \frac{\hbar^2}{2m}\{(k_s^r)^2 - (k_s^i)^2\} \text{ and } V_{oi} = 2(\frac{\hbar^2}{2m})(k_s^i)^2(k_s^r)^2 \tag{2.16}$$

By eliminating k_s^i in the equation (2.16), then we have:

$$E + V_{or} = \frac{\hbar^2 (k_s^r)^2}{2m} - \frac{V_{oi}^2}{4\left(\frac{\hbar^2 (k_s^r)^2}{2m}\right)^2} \tag{2.17}$$

Since $V_{oi}^2 << \left(\frac{\hbar^2 (k_s^r)^2}{2m}\right)^2$, the real part of the wave vector inside the crystal is given by:

$$(k_s^r) = \sqrt{\frac{E + V_{or}}{\hbar^2 / 2m}} \tag{2.18}$$

and the imaginary part is given by:

$$(k_s^i) = \frac{V_{oi}}{2(\hbar^2 / 2m)\sqrt{\frac{E + V_{or}}{\hbar^2 / 2m}}} \tag{2.19}$$

The wave function of the electrons inside the crystal is given by:

$$\psi_s = Be^{i(k_s^r + ik_s^i)x} = Be^{ik_s^r x} \cdot e^{-x/\lambda} \tag{2.20}$$

where λ is the mean free path of the electrons inside the crystal given by:

$$\lambda = 1/(k_s^i) = \frac{2(\hbar^2/2m)\sqrt{\frac{E+V_{or}}{\hbar^2/2m}}}{V_{oi}} \tag{2.21}$$

By choosing the imaginary part of the optical-potential

$$V_{oi} = C\left(\frac{E}{200/27.21 + Vor}\right)^{1/3} \tag{2.22}$$

then we can have the trend of the mean free path of the electrons used in the LEED calculations similar to the universal curve of the mean-free-path in solids. Figure 2.8 shows that the chosen imaginary part of the optical-potential described in equation (2.22) results in a reasonable mean-free-path in a solid for the energy range of the LEED *I-V* analysis (E=40 - 600 eV).

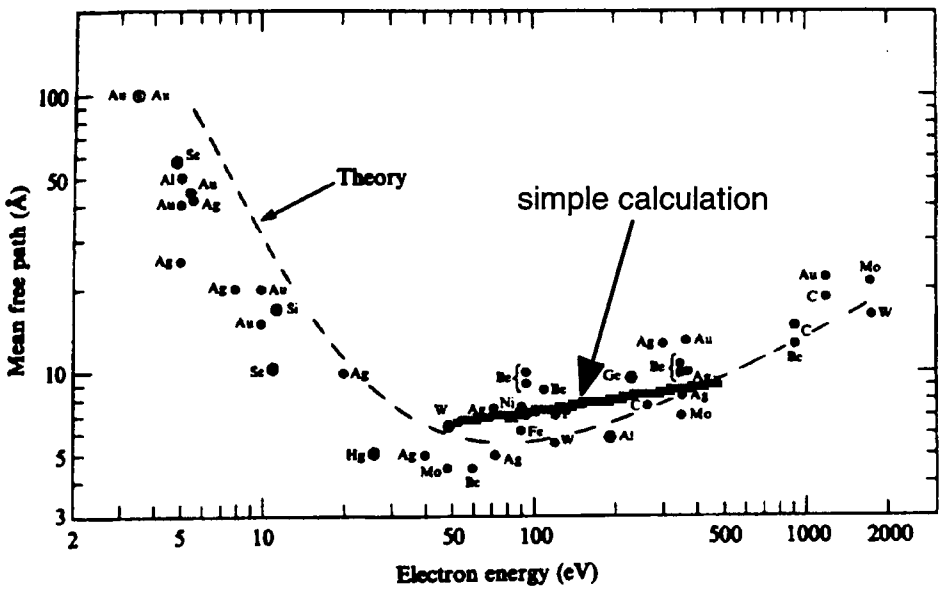


Figure 2.8: "Universal Curve" of electron mean-free path in various metals (dashed line and filled circles) [4] together with the electron mean-free path from a simple calculation (solid line).

Now let's include the attenuation of the electron via the optical-potential in the calculation of the intensity of the diffracted electrons for the model discussed above (a space where one-half is vacuum and the other one-half is occupied by a crystal composed of semi-infinite row of identical atoms with interlayer spacing equal to d_o and there is only one atom in each atomic plane). Figure 2.9 shows the intensity of the diffracted electrons as a function of the kinetic energy for T=0.8, d_o=2.5944 Å, V_{or}=0.0 eV, and V_{oi} as given in the equation (2.22) for the value of C=-3.0 eV (thick solid line), C=-5.0 eV (dashed line), and in the case of an infinite mean-free-path of electrons (thin solid line).

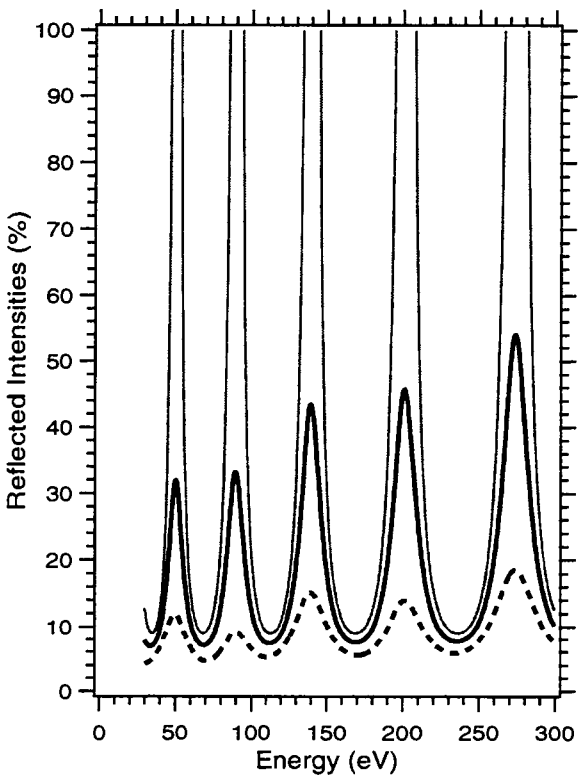


Figure 2.9: Reflected intensities for various imaginary parts of the optical potential and an infinite electron mean-free-path. Where T=0.8, d_o=2.5944 Å, V_{or}=0.0 eV, and V_{oi} as given in equation (2.22) for the value of C=-3.0 eV (thick solid line), C=-5.0 eV (dashed line), and in the case of the infinite mean-free path (thin solid line).

As shown in Figure 2.9 above, as the value of V_{oi} increases, the reflected intensities are reduced substantially and the width of the peak become larger. This behavior is related to the inelastic-scattering of electrons in a solid. The increasing of the value of V_{oi} means to enlarge the absorption in a solid, causing large energy losses of electrons. If the value of V_{oi} is very large, the reflected intensities will be zero and the width of the peak will be infinite, because all electrons are absorbed in the solid. The effect of the real part of the optical-potential V_{or} on the reflected intensities is shown in Figure 2.10 for V_{or} =5 eV (solid line) and V_{or} =10 eV (dashed line). It shows that the real part of optical-potential will shift the position of the peaks. It also changes the reflected intensities but it is not significant. The real part of the optical-potential V_{or} could be assumed to be independent from the energy of the electrons [9]; i.e., $V_{or} \approx -(E_F+\Phi)$, where E_F is the Fermi energy and Φ is the work function. In the LEED *I-V* calculations, both the real and imaginary parts of the optical-potential are optimized.

So far, we have discussed the LEED calculation in the kinematic approximation or single scattering by assuming the back-scattering is very weak. Now let's see the effect of the multiple scattering on the reflected intensities. Figure 2.11 illustrates the multiple scattering process in a simple case, as discussed above (a space where one-half is vacuum and the other one-half is occupied by a crystal composed of semi-infinite row of identical atoms with interlayer spacing equal to d_o and there is only one atom in each atomic plane). The surface is taken to be at a distance one half of the lattice constant from the last scattered atom. Let a^+ and a^- be amplitudes of the forward and backward-traveling waves. Assume a_0^+ is an amplitude traveling wave of an electron that scatters with the first atom. This electron will scatter to the second atom with amplitude a_1^+ but also back-scatter into the vacuum. The electron with amplitude a_1^+ will scatter with the third atom but also back-scatter and scatter with the second atom, etc. The amplitude of the reflected wave (see Pendry [9]) is given by the equation below:

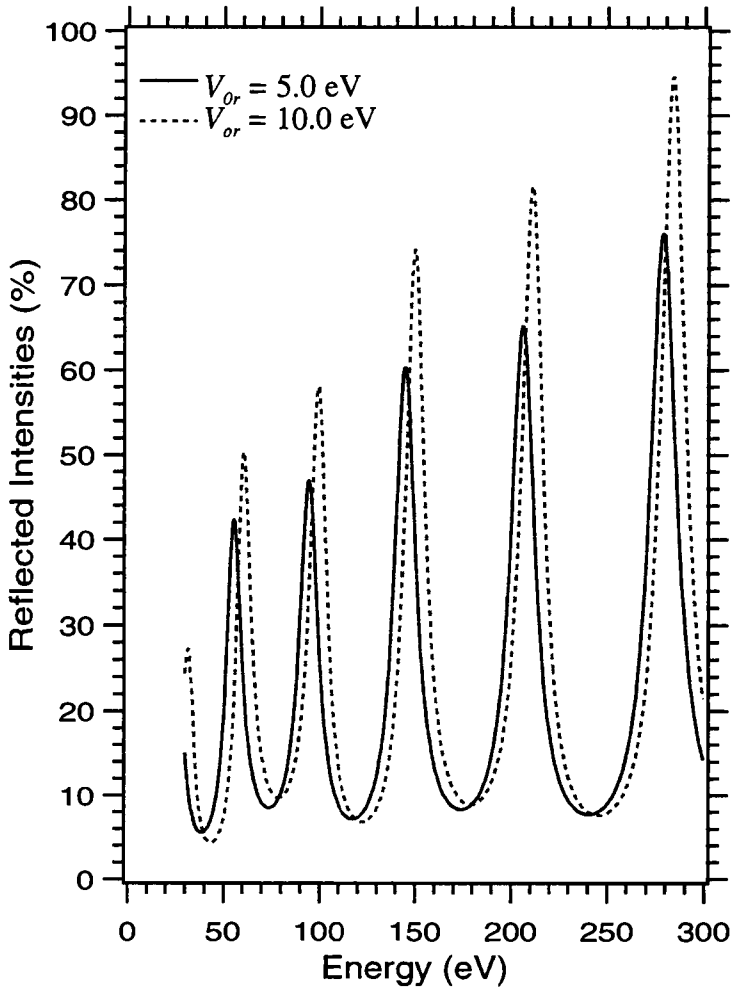


Figure 2.10: Reflected intensities for various real part of the optical potential. V_{or} =5 eV (solid line) and V_{or} =10 eV (dashed line).

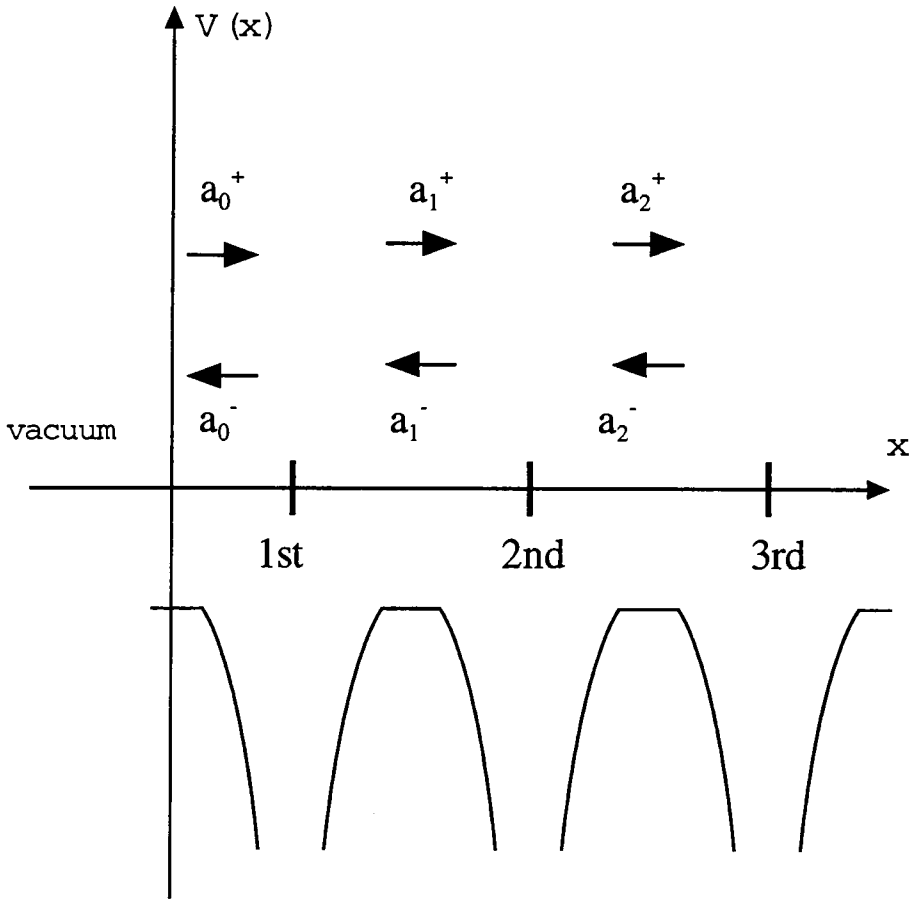


Figure 2.11: Schematic multiple scattering process for a simple.

$$C = \frac{k_i(1 + a_0^+ / a_0^-) + k_s(1 - a_0^+ / a_0^-)}{k_i(1 + a_0^+ / a_0^-) - k_s(1 - a_0^+ / a_0^-)} \qquad (2.23)$$

where,

$$a_0^+/a_0^- = \frac{i}{\sqrt{1-T^2}}\left(+i\sin(k_s d_0) \pm i(\sqrt{T^2 - \cos^2(k_s d_0)}\right) ; \text{ if } T^2 \rangle \cos^2(k_s d_0) \qquad (2.24)$$

and

$$a_0^+/a_0^- = \frac{i}{\sqrt{1-T^2}}\left(+i\sin(k_s d_0) \pm (\sqrt{\cos^2(k_s d_0) - T^2}\right) ; \text{ if } T^2 \langle \cos^2(k_s d_0) \qquad (2.25)$$

The comparison of the intensity of the diffracted electron as a function of its kinetic energy from the multiple scattering calculation (solid line) and kinematic approximation (doted line) is shown in Figure 2.12 for T=0.8, d_o=3.142 Å, V_{or}=0.0, and C=-3.0 eV. In this model, the multiple scattering has effects of reducing intensities and adjusting the width of the peaks from the kinematic approximation. There is no extra peak that appears in the multiple scattering calculation because there is only one atom in each atomic plane in the model. In the real situation where there are many atoms in each atomic plane, the electrons not only scatter with atoms in the atomic plane perpendicular to surface but also with the atoms in the atomic plane parallel to the surface. These will reduce the reflected intensities and produce extra peaks as shown in the Figure 2.13. The Bragg peaks (see the equation (2.11)) and extra peaks (due to multiple scattering) are indicated by thick lines and thin lines, respectively. Note, in the Figure 2.13, the reflected intensities are small at higher energy because of thermal effect (it will be discussed in the next section).

As was introduced in Chapter 1, as a consequence of the creation of a surface, the most commonly observed phenomenon is the interplanar relaxation, starting with a contraction or expansion of the interplanar spacing between the first and second layers. Figure 2.14 shows the reflected intensities of the (00) beam for two different cases: for the first interlayer spacing d_{12} is equal to d_o (the same as in the bulk) noted by dashed line, and d_{12} is equal to d_o-0.1 Å (solid line). When the first interlayer spacing has a small change

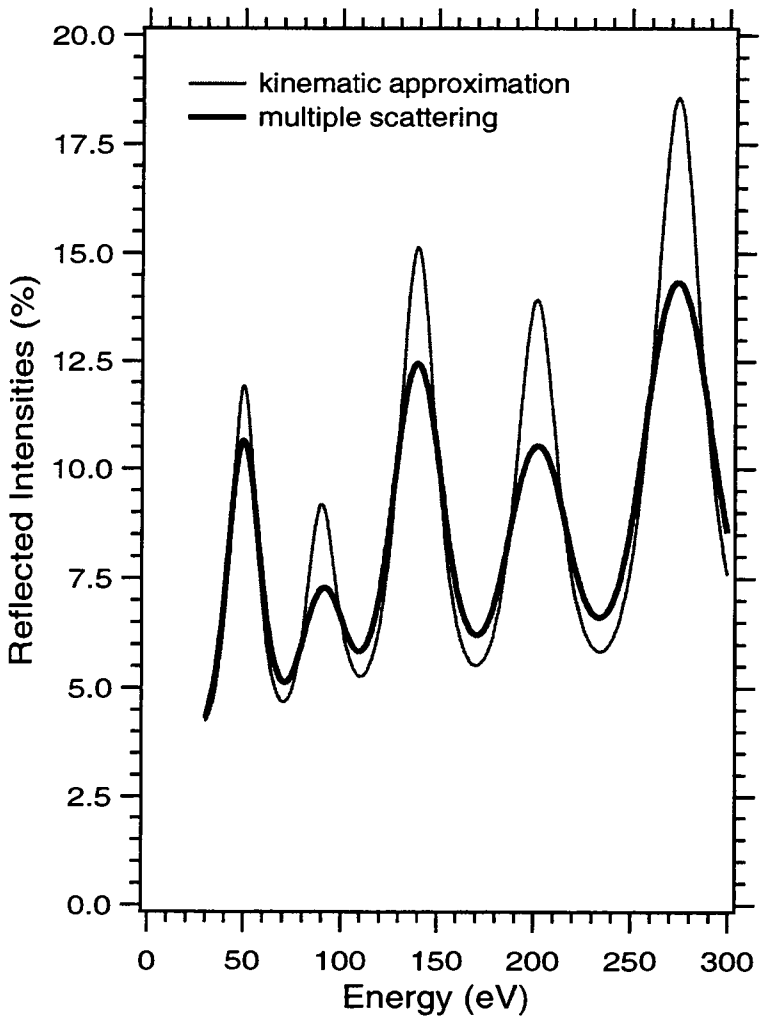


Figure 2.12: Reflected intensities for a simple model (see text) in the kinematic approximation (thin line) and multiple scattering (thick line).

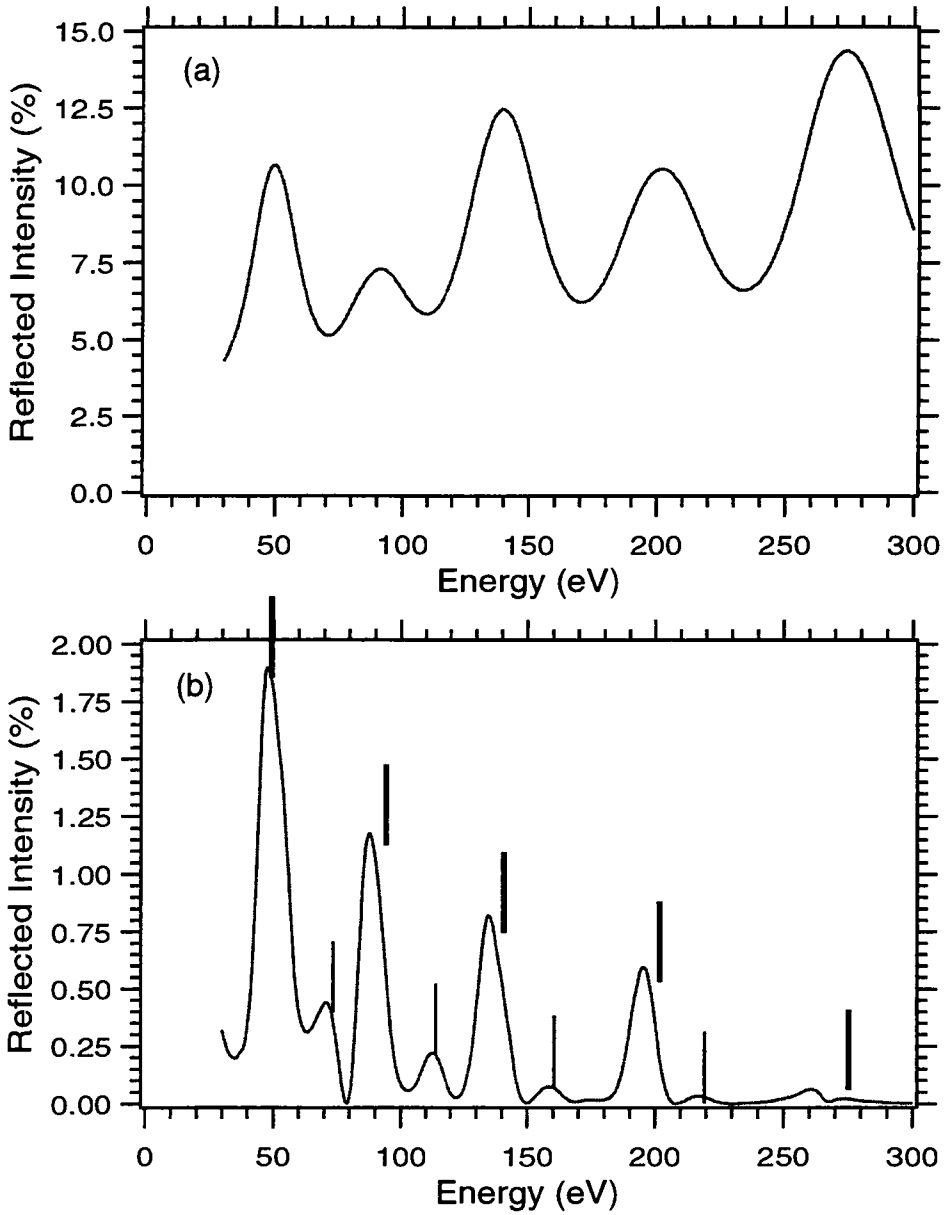


Figure 2.13: Reflected intensities from multiple scattering calculations: (a) a simple case as discussed in the text, and (b) in the real situation. Vertical thick and thin lines indicate the Bragg peaks and extra peaks due to multiple scattering, respectively.

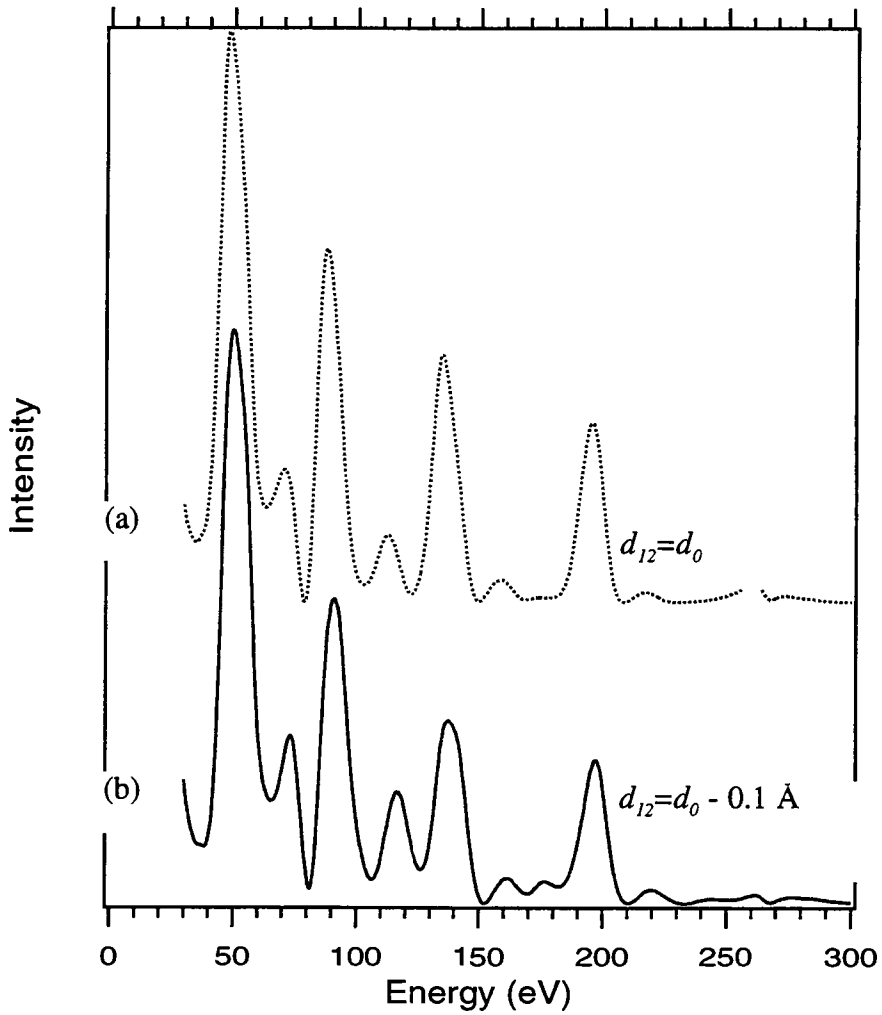


Figure 2.14: Reflected intensities from the (00) beam. (a) for the first interlayer spacing d_{12} is equal to d_o (the same as in the bulk) noted by dashed line, and (b) for the first interlayer spacing d_{12} is equal to d_o-0.1 Å (solid line).

from the bulk interlayer spacing, the position of the peaks shifts, the height of the intensities and the width of the peaks change, and it could produce small peaks. This tell us that the reflected intensities from the surface are different from the bulk. More importantly, the reflected intensities provide the information of the interlayer spacing or geometric structure near the surface region. The calculated spectra is compared to the experimental spectra in the LEED *I-V* analysis. The structural and non-structural parameters are optimized in order to have a best-fit between the calculated spectra and experimental spectra. When we have a best-fit, then the structural parameters can be considered to be the true geometric structure near the surface region. A comprehensive description of the LEED *I-V* for the determination of the atomic structure in the surface region has been derived by Pendry [9] and Van Hove *et al.* [11]. Nowadays, LEED *I-V* has become the most powerful tool in the surface crystallography. Until the end of 1997, there are 751 surface structure determinations which have been solved by the LEED *I-V* technique which is the technique used most in the surface crystallography, as shown in Figures 2.15 and 2.16 [10].

The electron scattering process in a solid is very complicated. The electrons can be scattered by a strong potential in the solid, undergo a loss of energy, and lower their kinetic energy as they enter into the potential well of the crystal. For simplicity, the muffin-tin approximation is used in the LEED *I-V* analysis [9,11]. In this approximation, the atoms in a solid are assumed as non-overlapping spheres with touching between one and another, as shown in Figure 2.17. In the muffin-tin approximation, the potential inside the sphere is spherically symmetric and the potential outside the sphere is constant, as shown in Figure 2.17. By using this approximation, then the electron scattering process inside the crystal is only an ion-core scattering process.

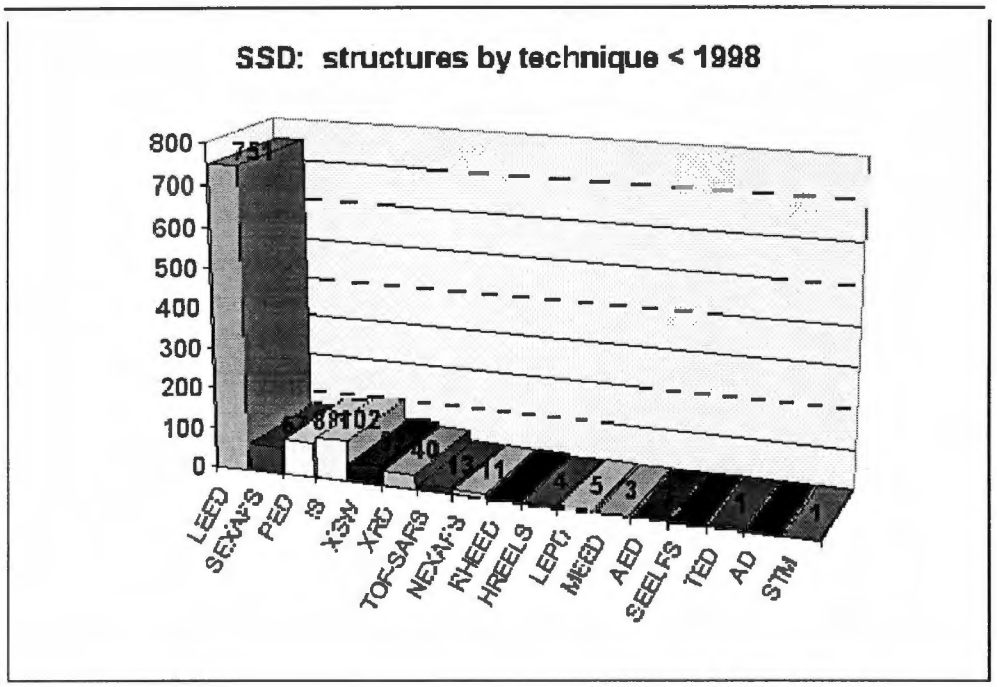


Figure 2.15: Surface structure determination by techniques until the end of 1997 [10]. List of technique acronyms, in plotting sequence (left to right or bottom to top): LEED - low-energy electron diffraction; SEXAFS - surface extended x-ray absorption fine structure; PED -photoelectron diffraction; IS - low-, medium- and high-energy ion scattering; XSW - x-ray standing wave; XRD -x-ray diffraction; TOF-SARS - time-of-flight scattering and recoiling spectrometry; NEXAFS - near-edge x-ray absorption fine structure; RHEED - reflection high-energy electron diffraction; HREELS - high-resolution electron energy loss spectroscopy; LEPD - low-energy positron diffraction; MEED - medium-energy electron diffraction; AED - Auger electron diffraction; SEELFS - surface extended energy loss fine structure; TED - transmission electron diffraction; AD - atom diffraction; STM - scanning tunneling microscopy.

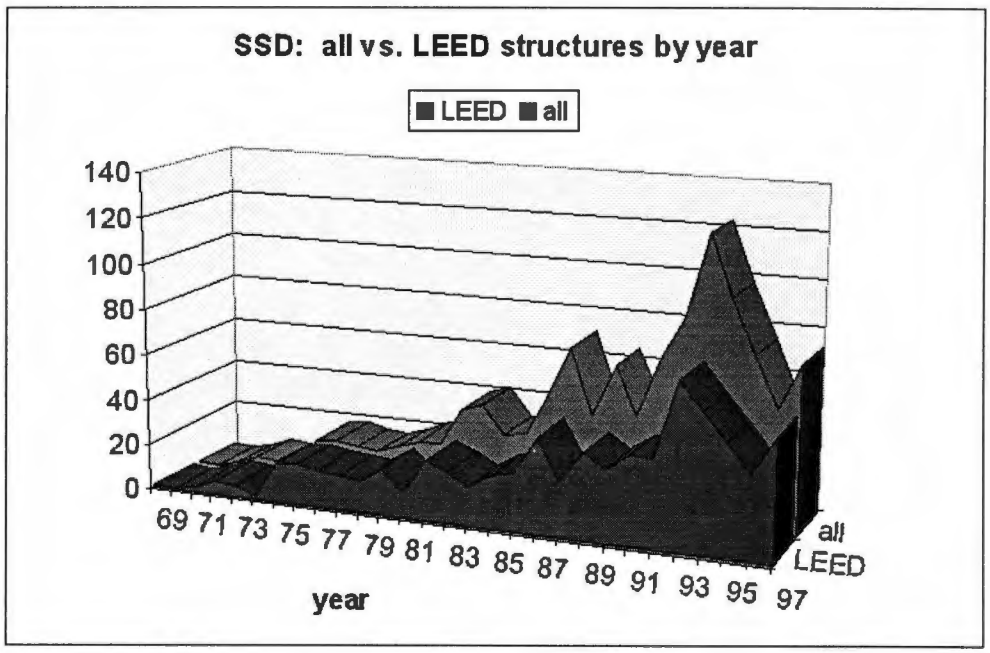
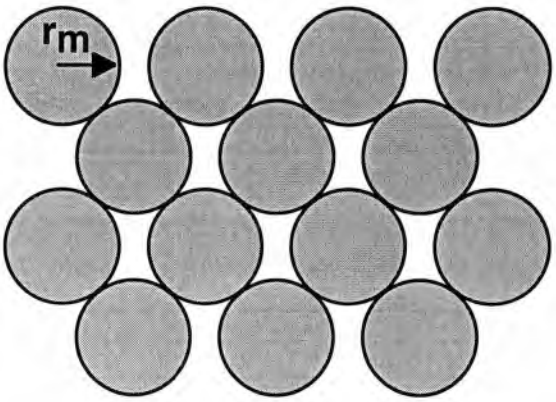


Figure 2.16: Number of surface structure determinations vs. year: by LEED and LEED plus other techniques (all) [10].

a) plan view



b) sectional view

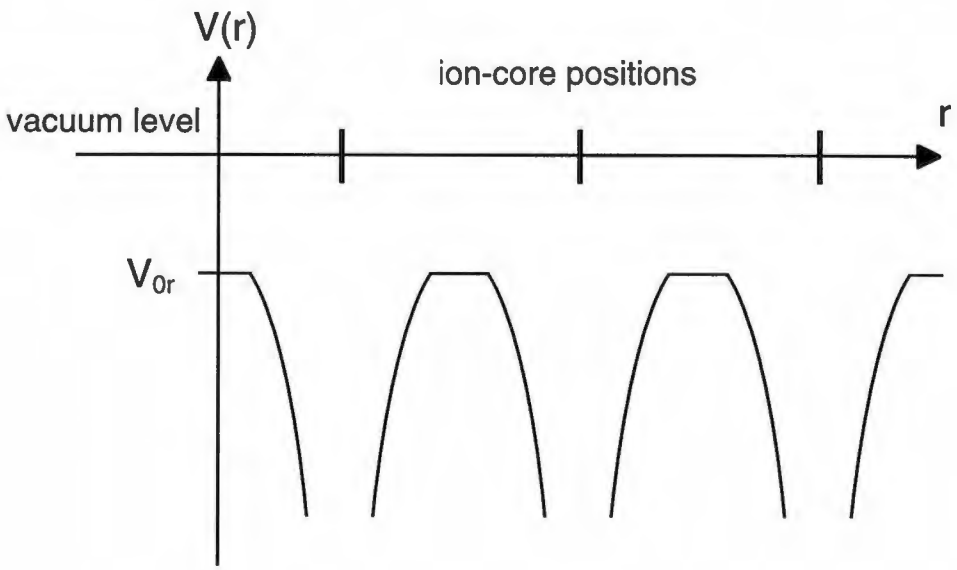


Figure 2.17: Muffin-tin potential: a) plan view, and b) sectional view.

2.3.1.1 Atomic Phase Shifts

Assume an electron with kinetic energy E and momentum $\boldsymbol{k}$ scatters with a single atom or a sphere with the muffin-tin potential $V(\boldsymbol{r})$ and a muffin-tin radius r_m. The time-independent Schrödinger equation is given by:

$$\left[-\frac{\hbar^2}{2m}\nabla^2 + V(\mathbf{r})\right]\psi(\mathbf{r}) = E\psi(\mathbf{r}) \tag{2.26}$$

In the large r region, the wave function $\psi(\mathbf{r})$ can be written in an asymptotic form [13]

$$\psi(\mathbf{r}) \xrightarrow[r\to\infty]{} e^{ikz} + f(k,\theta,\phi)\frac{e^{i\vec{k}\cdot\vec{r}}}{r} \tag{2.27}$$

where $f(k,\theta,\phi)$ is the scattering amplitude, θ is the polar angle (scattering angle) and ϕ is the azimuthal angle. By using the method of partial-wave, the wave function $\psi(\mathbf{r})$ and the scattering amplitude $f(k,\theta,\phi)$ can be expanded in a series of Legendre polynomials. The potential V(**r**) is completely symmetric such that the wave function and scattering amplitude do not depend on the azimuthal angle ϕ.

$$\psi(r,\theta) = \sum_{l=0}^{\infty} R_l(k,r)P_l(\cos\theta) \tag{2.28}$$

$$f(k,\theta) = \sum_{l=0}^{\infty} f_l(k)P_l(\cos\theta) \tag{2.29}$$

Equation (2.24) can be written as the following:

$$\left(-\frac{\hbar^2}{2m}\frac{1}{r^2}\frac{d}{dr}\left(r^2\frac{d}{dr}\right) + \frac{\hbar^2}{2m}\frac{l(l+1)}{r^2} + V(r)\right)R_l = E.R_l \tag{2.30}$$

The solution of the equation (2.30) in the region $r > r_m$ is given by:

$$R_l(k,r) = A_l(k)j_l(kr) + B_l(k)n_l(kr) \tag{2.31}$$

where j_l and n_l are the spherical Bessel and Neumann functions. In the large region, the equation (2.31) can be written as:

$$R_l(k,r) \xrightarrow[r\to\infty]{} C_l(k)\frac{1}{kr}\sin\left(kr-\frac{l\pi}{2}+\delta_l(k)\right) \tag{2.32}$$

Combining the equations (2.27), (2.28), (2.29), and (2.31), the scattering amplitude (known as t-matrix) can be written as:

$$f(k,\theta)=\frac{1}{i2k}\sum_{l=0}^{\infty}(2l+1)\left(e^{i2\delta_l}-1\right)P_l(\cos\theta) \tag{2.33}$$

It is clear that *the scattering amplitude depends only on the phase shifts* $\delta_l(k)$. These phase shifts $\delta_l(k)$ represent the atomic scattering potential of a single atom within the muffin-tin approximation.

It is clear that one of the most important ingredients in the LEED *I-V* calculations is the atomic phase shift $\delta_l(k)$. To calculate the phase shifts, we need to have the muffin-tin potential *V(r)* where it can be obtained from the Mattheiss' prescription [14,15], i.e., by performing a self-consistent Hartree-Fock calculation. In this calculation, the position of the atoms is assumed as in the bulk. The total potential-energy in each muffin-tin sphere is obtained by adding the electrostatic component computed by using the charge density distribution and a local Slater-like exchange term [19] given by:

$$V_{ex}(\mathbf{r})=-3\alpha\left(\frac{3\rho(\mathbf{r})}{8\pi}\right)^{1/3} \tag{2.34}$$

where the exchange parameter α is listed in the Table I of the ref. 16 for many elements.

When we have the total potential-energy in the muffin-tin sphere, we can obtain the atomic phase shifts $\delta_l(k)$ by applying the boundary condition (the wave functions inside and outside the muffin-tin sphere must be matched at the muffin-tin radius r_m) to the equation (2.30) and we have:

$$\tan\delta_l(k)=\left(\frac{kr_m j'_l(kr_m)-\beta_l j_l(kr_m)}{kr_m n'_l(kr_m)-\beta_l n_l(kr_m)}\right) \tag{2.35}$$

where

$$\beta_l = \left[\frac{r}{R_l(kr)} \frac{dR(kr)}{dr} \right]_{r=r_m} \tag{2.36}$$

and

$$j'_l(kr_m) = \left[\frac{dj_l(kr)}{d(kr)} \right]_{r=r_m} \quad \text{and} \quad n'_l(kr_m) = \left[\frac{dn_l(kr)}{d(kr)} \right]_{r=r_m} \tag{2.37}$$

The muffin-tin potentials and the phase shifts used in the LEED *I-V* calculations in the research presented in this thesis were generated by using the Barbieri-Van Hove phase shift package [17]. The plots of the muffin-tin potential and phase shifts for Mg are shown in Figures 2.18 and 2.19, respectively. The numerical values of the phase shifts for several elements or atoms (such as: Mg, Sn, and Ge) are tabulated in appendix A. Moruzzi *et al.* calculated the self-consistent band structure for many elements. The numerical values of the potential are tabulated in his book [18]. By using this potential, one can obtain the phase shifts by solving the equation (2.30).

The scattering amplitude given in the equation (2.33) is expanded in the Legendre polynomials, where the sum of the angular momentum l is from zero to infinity. The value of $(l+1)$ is equal to the number of the phase shifts included in the calculation. Now the question is, how many phase shifts that need to be included in the LEED calculation ? or what is the maximum value of l (l_{max}) ? A simple way to estimate the value of l_{max} is to use a classical analogous [9]. Consider a classical particle is moving with a linear momentum k and angular momentum l approaches the potential confined within a sphere of radius R_{mft}. The closest approach of the particle to the center of the sphere will be R_l where $l=kR_l$. If R_l were greater than R_{mft} the particle could not see the potential at all. So, the maximum of l is equal to kR_{mft} ($l_{max}= kR_{mft}$). Another way to determine the value of l_{max} is to calculate the scattering amplitude squared as a function of the energy (the same energy range with the experimental data) by varying the value of l_{max}, as shown in Figure 2.20 in the case of

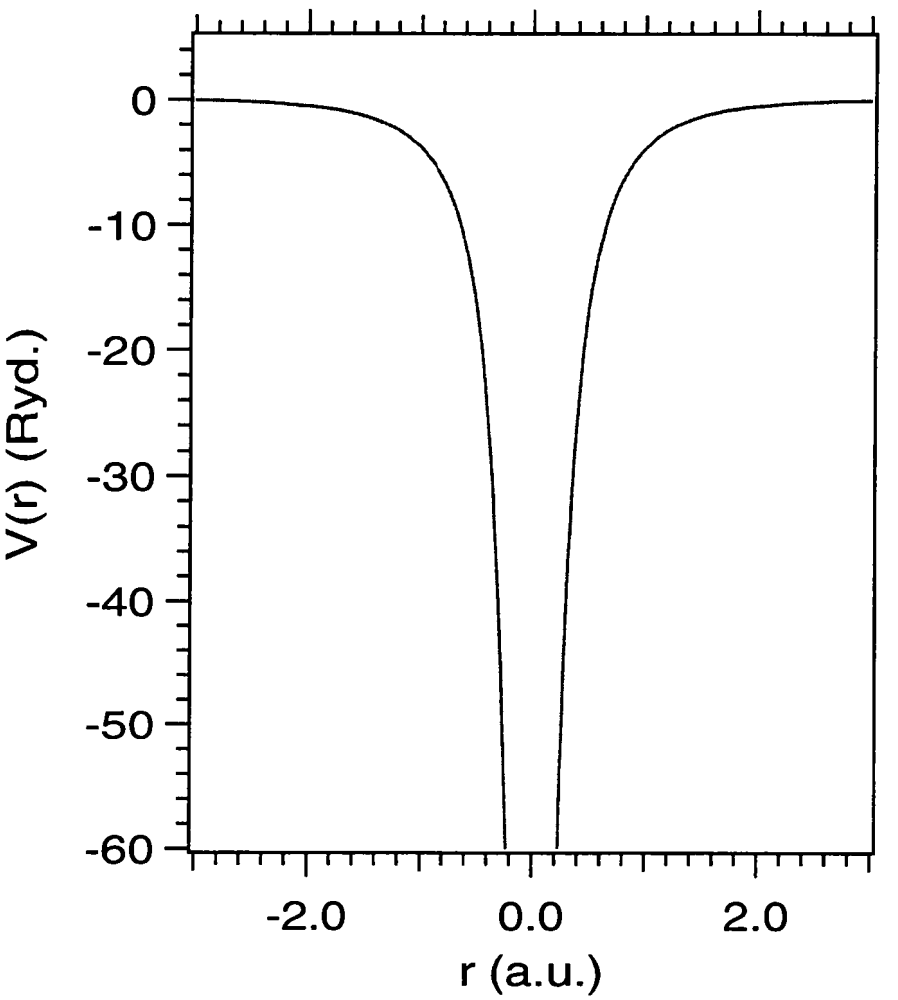


Figure 2.18: Muffin-tin potential for magnesium.

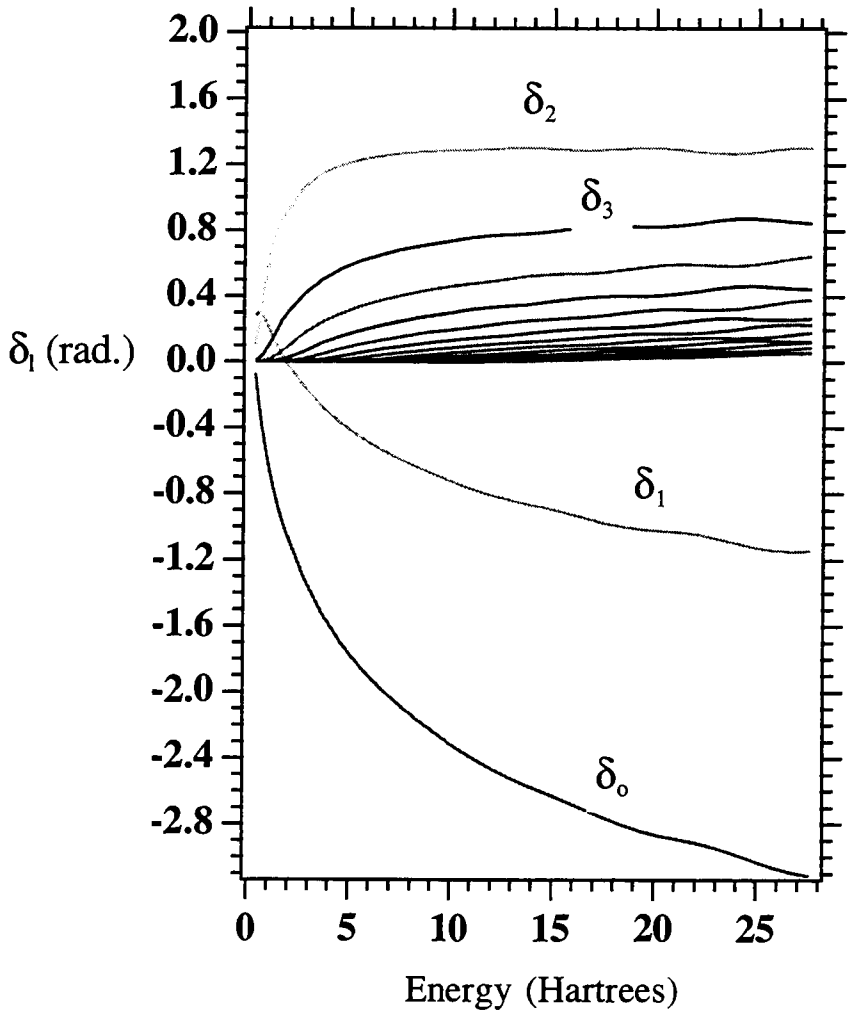


Figure 2.19: Atomic phase shifts (δ_l) as a function of the energy for magnesium.

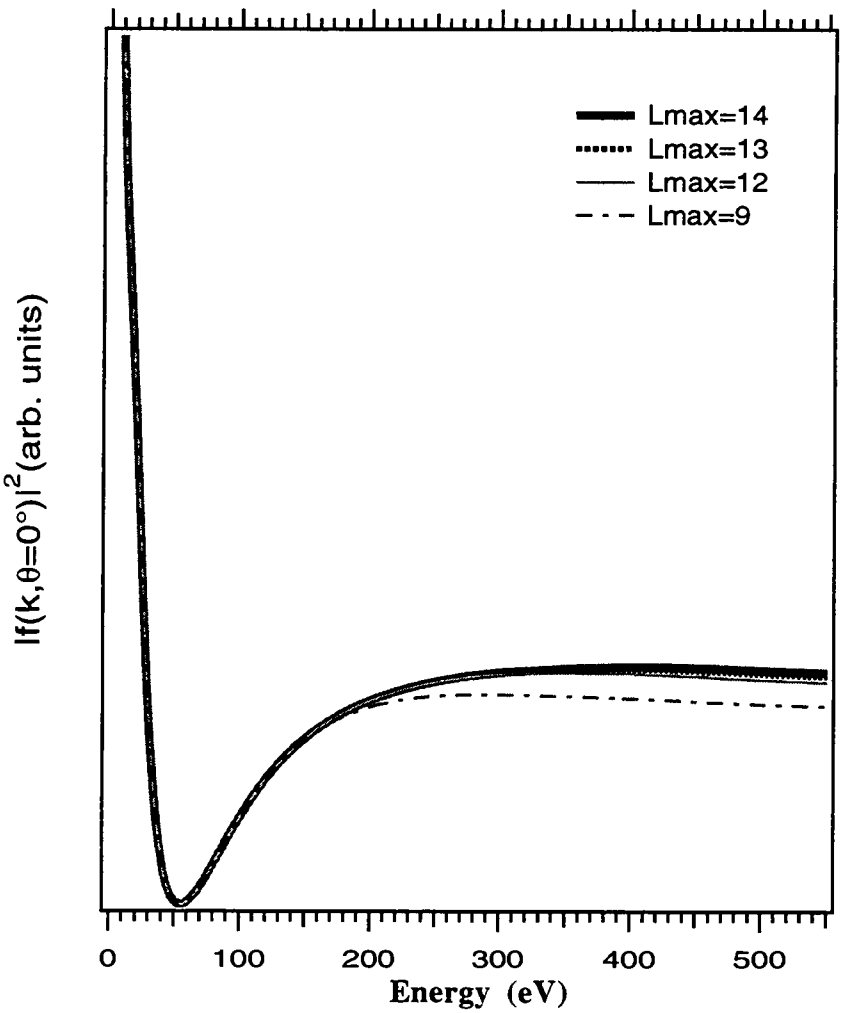


Figure 2.20: The scattering amplitude squared for l_{max}=9, 12, 13, and 14 as a function of the energy for magnesium.

magnesium. From Figure 2.20 above, we can see that the scattering amplitudes squared for l_{max}=12, 13, and 14 are about the same. So, the appropriate value of l_{max} is 12 or 13. In other words, we need to include at least 12 phase shifts in the LEED *I-V* calculations for magnesium.

2.3.1.2 Multiple Scattering

Multiple scattering calculation in the real crystal is very complicated and expensive in comparison to the kinematic approximation. Now the question is, do we need to do multiple scattering calculations to obtain the calculated LEED *I-V* spectra ? As we know, the kinematic approximation works well whenever the transmission coefficient *T* is about one (the back-scattering is very weak). To examine if the back-scattering is very weak or strong from a certain atom, we need to plot the scattering amplitude squared as a function of the polar angle, as shown in Figure 2.21. The forward-scattering is at the polar angle θ=0 and backward-scattering is at the polar angle θ=180° (π radian). In the case of magnesium, as shown in Figure 2.21, the scattering amplitude squared from the back-scattering is not weak, especially at the kinetic energy of the electron *E*=128 eV. This means that the kinematic approximation is not adequate, therefore multiple scattering calculations need to considered in the LEED *I-V* analysis for magnesium.

In principle, there are three steps in doing calculations of the LEED *I-V* spectra. First, calculate the scattering amplitude or t-matrix, as discussed above, for each element or atom. Second, calculate the layer-diffraction matrix for a single-layer (if there is one atom in the unit cell) or a composite layer (if there is more than one atom in the sublayer) by using the matrix inversion method [20], by using the result from the first step. Third, to perform multiple scattering calculations between the interlayer to obtain the total t-matrix (scattering amplitude). The calculations in the first and second steps are done in exact (without any perturbation). However, the calculations in the third step can be done by

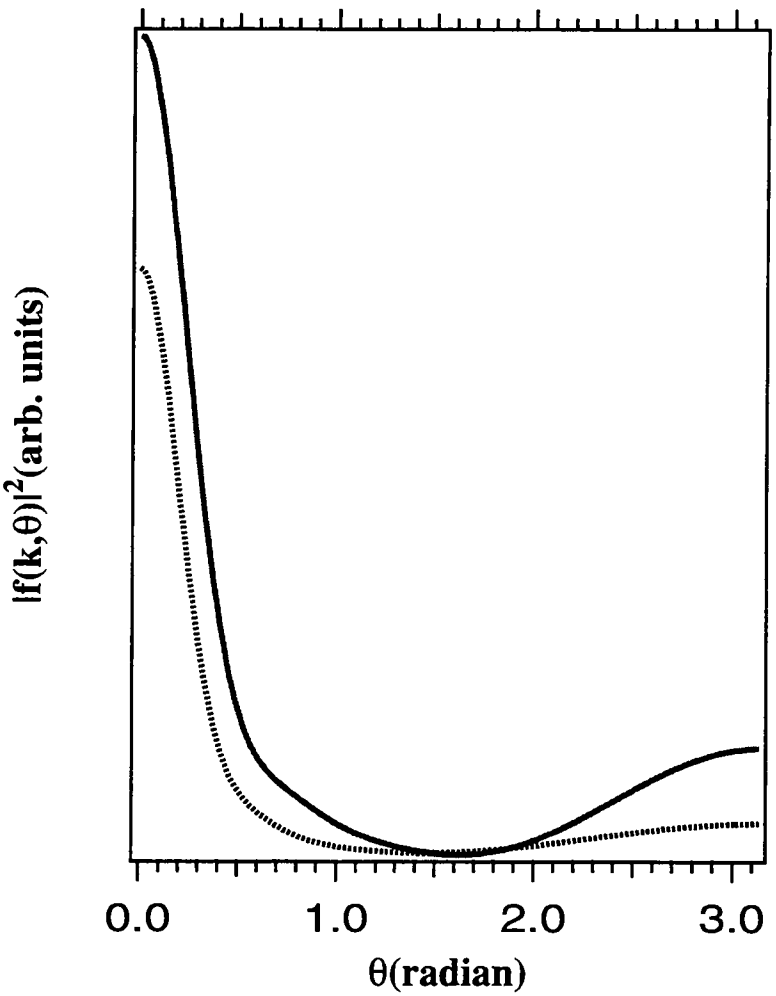


Figure 2.21: The scattering amplitude squared as a function of the polar-angle for magnesium. The forward scattering is at the polar-angle θ=0 and backward scattering is at the polar-angle θ=180° (π radian), solid line for the energy E=128 eV and dashed line for the energy E=200 eV.

using the perturbation approach, such as the renormalized forward scattering (RFS) perturbation method [9,11,12].

Figure 2.22 shows the mechanism of the renormalized forward scattering (RFS) perturbation method [12]. This RFS method is commonly used in the LEED *I-V* calculations. The solid vertical lines represent the single-layers or composite layers. Transmitted and reflected waves are indicated by **t** and **r**, respectively. In this method, it is assumed that the reflection scattering from any layer inside the crystal is weak. As shown in Figure 2.22, the incident electron is transmitted from the first layer to the second layer and reflected from the first layer. The electron transmitted from the first layer to the second layer is transmitted to the third layer and reflected from the second layer, etc. The total reflectivity from the surface is the summation of the number of reflections: 1st order, 2nd order, etc. The calculations of LEED *I-V* curve by using the RFS method are fast in comparison to the other method, such as the Layer Doubling method [9,11]. This is the main reason why the RFS method is used most in the LEED *I-V* calculations. The RFS method is valid whenever the back-scattering is weak. However, for the system in which the interlayer spacing is short (i.e., less than 1 Å), and where the back-scattering is strong, the RFS method is not valid. The strong intensity from the back-scattering will create the divergence in the calculation of the total reflected intensity. Nevertheless, we still can use the renormalized forward scattering method by combining the short interlayer spacing to become a composite layer or we can combine the short interlayers to be a *giant* composite layer which consists of many subplanes and many atoms. In this case, the renormalized forward scattering method is still valid but the calculations become very slow.

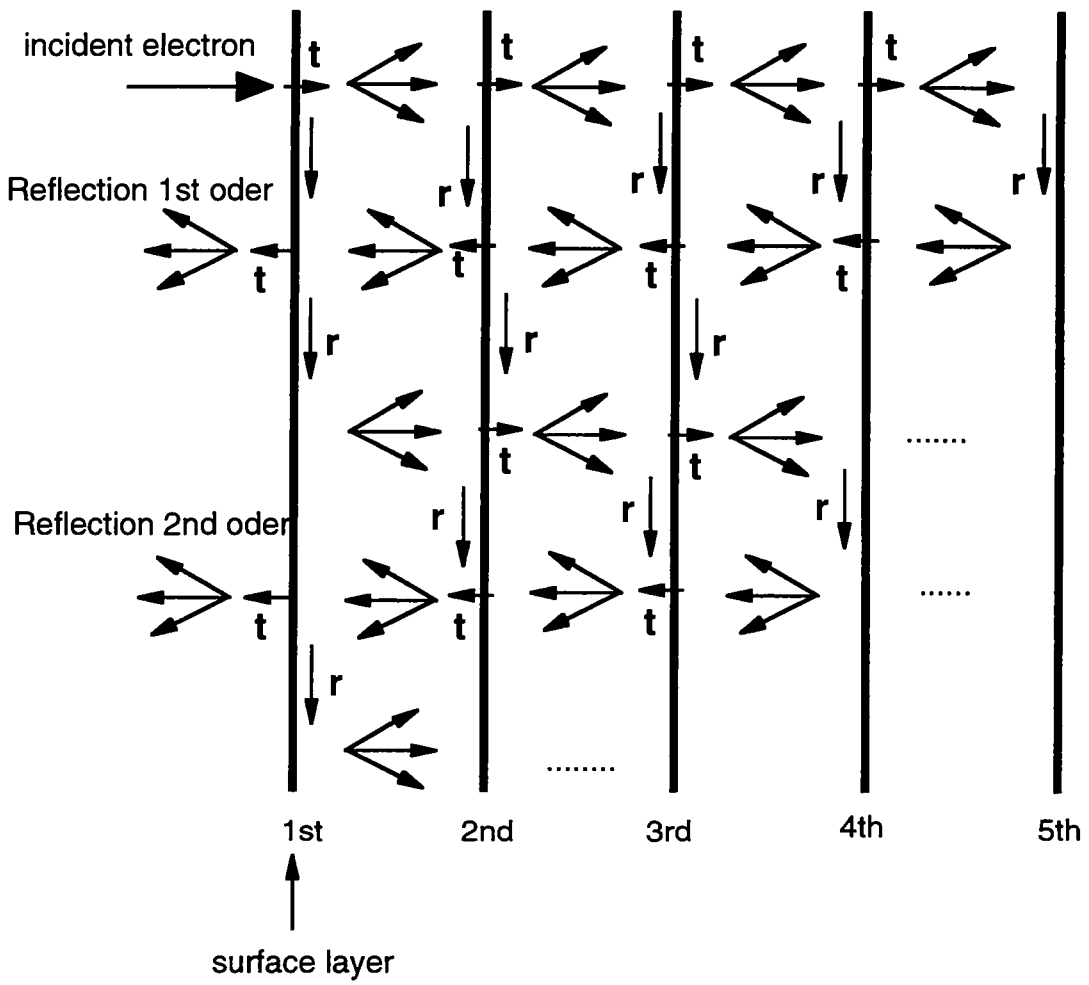


Figure 2.22: Mechanism of the renormalized forward scattering (RFS) perturbation method used in the LEED *I-V* calculations. Vertical thick line represent layers. **t** and **r** mean transmitted and reflected waves, respectively.

2.3.1.3 Structural and Non-structural Parameters

The structural parameters or geometric structure of the atoms in the surface region are varied in the LEED *I-V* calculations by a trial-and-error procedure in order to have the agreement between calculated and experimental data. If we think that the geometric structure of the recent study is similar to the previous experimental study or the theoretical prediction, then it is recommended to use this structure for a reference structure in the recent LEED *I-V* calculations. However, if the geometric structure is still unknown, we need to guess a certain structure or use the bulk values for a reference structure in the calculations. It is *not* easy to choose or guess a certain atomic structure for the reference structure, especially for a complex material containing a lot of atoms in the unit cell and having both vertical and in-plane relaxations.

The non-structural parameters in the LEED *I-V* calculations are an optical-potential and a Debye-temperature. As has been discussed in the earlier, the lifetime of electrons in a solid need to be included in the calculations, via an optical-potential. In the research presented in this thesis, the real part of the optical-potential (V_{or}) was chosen to be a constant (energy independent), but it was optimized in order to have the best-fit, while the imaginary part of the optical-potential (V_{oi}) was modeled as given in equation (2.29), where C is constant optimized manually.

When the temperature of a solid is increased, there are several obvious major changes in the apparent of the LEED *I-V* spectra: the intensities of the *I-V* spectra decrease (greater effect at high energy than at low energy), the width of the peaks become broad, and the background intensities increase. These effects are related to the surface roughness and the vibration of the surface atoms. The decreasing intensities are due to the destructive interference effects between the waves scattered by slightly disorder atoms at the surface. The width broadening is related to phonon energy losses, and the increasing of background intensities is related to the thermal diffuse scattering. Figure 2.23 shows the typical LEED

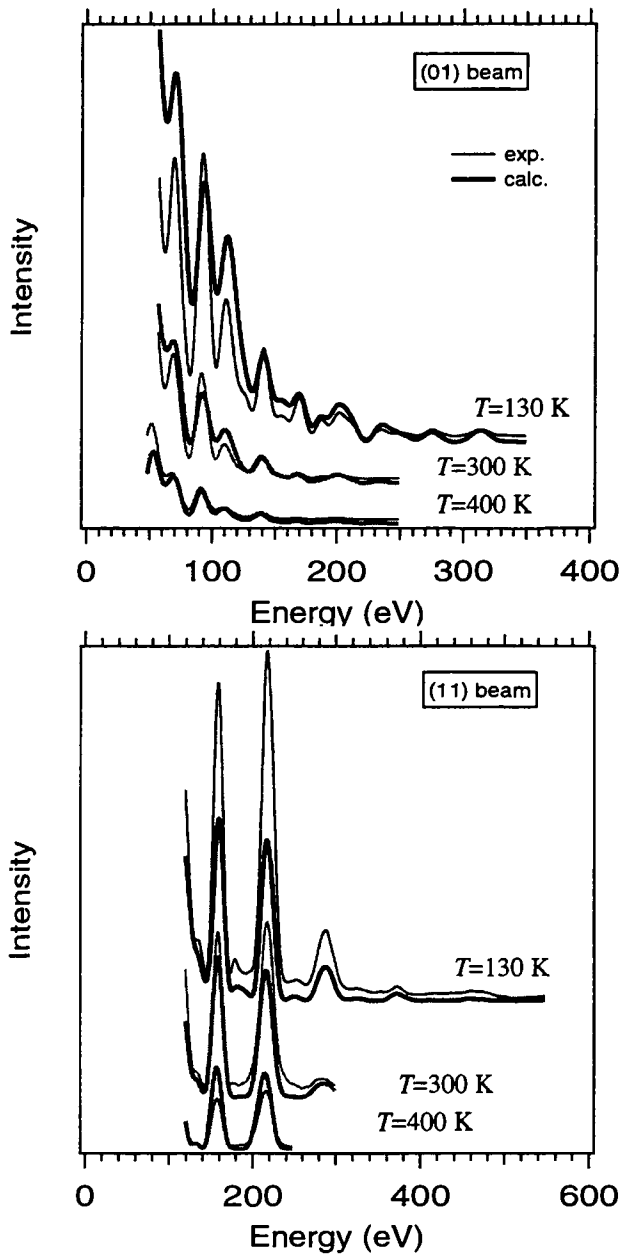


Figure 2.23: Typical LEED *I-V* spectra as a function of temperature. The baselines are shifted for clarity.

I-V spectra at three different temperatures, where the baselines are shifted for clarity. The thermal effects are treated in the LEED *I-V* calculations by multiplying the scattering t-matrix with the Debye-Waller factor e^{-M} [9,12].

$$t(k,\theta,T) = t(k,\theta)\cdot e^{-M} \tag{2.38}$$

where M is given by:

$$M = \frac{1}{2}\left\langle \left(\Delta\vec{k}\cdot\Delta\vec{r}\right)^2 \right\rangle_T = \frac{1}{6}\left|\Delta\vec{k}\right|^2 \left\langle (\Delta r)^2 \right\rangle_T \tag{2.39}$$

where T is the temperature of experimental data and $\Delta\vec{k} = \vec{k} - \vec{k}'$ is the momentum transfer. By assuming the vibration of the atoms is isotropic, then $\left\langle (\Delta r)^2 \right\rangle_T$ in equation (2.39) can be expressed as the following [9]:

$$\left\langle (\Delta r)^2 \right\rangle_T = \frac{9\hbar^2}{mk_B\Theta_D}\left[\frac{T^2}{{\Theta_D}^2}\int_0^{\frac{\Theta_D}{T}} \frac{x\,dx}{e^x - 1} + \frac{1}{4}\right] \tag{2.40}$$

where Θ_D is the Debye temperature that is related to the compressibility of a material: the higher Θ_D the harder material. The root-mean-square (rms) motion of an atom is given by $\sqrt{\left\langle (\Delta r)^2 \right\rangle_T}$. The equation (2.40) was implemented to treat the thermal effect in the LEED *I-V* calculations presented in this thesis, where the Debye temperature Θ_D is fitted manually.

2.3.1.4 Tensor LEED Approximation

As was discussed above, the determination of the position of atoms near the surface region in the LEED *I-V* analysis is actually a trial-and-error procedure. In conventional LEED *I-V* calculations, full dynamical calculations are performed for every trial structure; for example, we calculate the spectra for 1000 trial structures to find the best-fit structure. In this way, the determination of the position of atoms becomes very expensive and time

consuming, especially for a system that has more than one atom in the unit cell. Rous and Pendry [21-24] proposed the Tensor LEED approximation to overcome this problem.

The Tensor LEED approximation is a perturbative approach to calculate the LEED *I-V* spectra in which an initial reference trial structure is distorted in order to generate other trial structures. The atomic displacements (distortions from an initial-reference trial-structure) are assumed to be small; therefore, the effect of the distortion on the LEED *I-V* spectra can be calculated by using the perturbation theory. If an atom j is displaced (or distorted) by $\delta\vec{r}_j$, the effect of this displacement upon the scattering of electrons is given by:

$$\hat{t}^j = t^j + \delta t^j(\delta\vec{r}_j) \tag{2.41}$$

where δt^j is the change of the t-matrix due to the atomic displacement $\delta\vec{r}_j$. Let $\left|\phi(\vec{k}_{\parallel})\right\rangle$ be the exact LEED state of the undistorted system produced by an incident beam of parallel momentum $\vec{k}_{\parallel}$. Then, the change in the amplitude of electrons diffracted from the distorted atoms at the surface is given by:

$$\delta A = \sum_j \left\langle \phi(\vec{k}'_{\parallel}) \middle| \delta t^j \middle| \phi(\vec{k}_{\parallel}) \right\rangle \tag{2.42}$$

or

$$\delta A = \sum_j \sum_{lm,l'm'} T_{lm,l'm'}{}^j \cdot \delta t_{lm,l'm'}{}^j \tag{2.43}$$

where $lm, l'm'$ are the angular momentums. The tensor T depends only upon the scattering potential of the reference atoms and is independent from the atomic displacement; therefore T plays the role of a form factor. The intensity of the spectra can be written as the following:

$$I \propto |A + \delta A|^2 \tag{2.44}$$

where A is the amplitude of the electron diffracted from the undistorted surface (atoms). So, the t-matrix of a certain reference structure can be distorted in order to calculate new

spectra without performing a full dynamical calculation. This is the basic idea of the Tensor LEED approximation.

The validity of the Tensor LEED approximation has been verified, finding that this approximation holds up to the displacement of an atom by 0.4 Å [24]. The origin of the failure of the Tensor LEED approximation is the appearance of the multiple scattering correlation between displaced atoms. As the displacement becomes bigger, the multiple scattering between the displaced atoms begins to make a significant contribution to the scattered intensity.

2.3.1.5 Reliability Factor and Error-bar in the LEED *I-V* Calculations

The atomic structure near the surface region determined by the LEED *I-V* calculations depends highly on the optimization of the agreement between the calculated and experimental spectra. Therefore, it is not sufficient to judge the agreement between the calculated and experimental spectra visually. The agreement should be judged by a single number known as a reliability factor (or *R* factor), which is extremely sensitive to the atomic positions at the surface. There are several type of *R* factors which have been proposed in the LEED *I-V* calculations [11,25]. Each *R* factor has a certain feature, such as: sensitivity to the relative peak positions, shoulders, small peaks, etc. [25]. Nonetheless, there is no consensus in the surface crystallography community about which *R* factor should be used in the LEED *I-V* calculations.

In the research presented in this thesis, the Pendry *R* factor (R_P) was used to judge the agreement between the experimental and calculated spectra. This *R* factor is very sensitive to the relative peak positions and small peaks, where the peak positions and small peaks are very important because they are related to the geometric structure at the surface. The large peaks are also important; therefore, Pendry [26] proposed to treat all peaks and

minima with equal weight, which is based on the logarithmic derivative (L) of the I-V curves given by:

$$L = \frac{1}{I(E)} \frac{dI(E)}{dE} \tag{2.45}$$

where $I(E)$ is the intensity as a function of kinetic energy of the electron E (I-V curve). In order to avoid the singularities when the intensity is zero, Pendry defined a Y-function as the following:

$$Y = \frac{L}{1 + V_{oi}^{2} L^{2}} \tag{2.46}$$

where V_{oi} is the imaginary part of the optical-potential. The Rp factor equation for a certain beam is given by [26]:

$$R_P = \frac{\int \left(Y_{\exp} - Y_{cal}\right)^2 dE}{\int \left(Y^2{}_{\exp} + Y^2{}_{cal}\right) dE} \tag{2.47}$$

where Y_{exp} and Y_{cal} are the Y-functions of the experimental and calculated spectra, respectively. The total Rp factor for N inequivalent beams is given by:

$$(R_P)_T = \frac{\sum_{i=1}^{N} (\Delta E)_i \cdot (R_P)_i}{\sum_{i=1}^{N} (\Delta E)_i} \tag{2.48}$$

where $(\Delta E)_i$ is the energy range of beam i. If the Rp factor is equal to zero, this means the experimental and calculated spectra are identical, which is not possible. If the Rp factor is equal to one, then there is no correlation between the experimental data and calculated spectra.

In equation (2.48), the total Rp factor depends on the total range of the kinetic energy of electron and the number of inequivalent beams. So, the value of the total R factor in the LEED I-V calculation is not unique. There is no consensus about a certain value of the total Rp factor for an acceptable model. However, in general, for the system that has

few atoms in the unit cell, the total *Rp* factor below 0.25 is an acceptable model. The accuracy of the structural determination depends highly on the size of the data set. The more experimental data we have, the more accurate result will be. However, the capability of instruments and the temperature effect limit us to have a certain size of the data set.

In the LEED *I-V* calculations, the atomic structure near the surface region is determined by a trial-and-error approach from a variety of the possible geometries until the agreement between experimental and calculated spectra is satisfied. Consequently, we could have the value of the total *Rp* factor at a local minimum, not at a global minimum. To avoid this problem, we need to plot the total *Rp* factor as a function of the displacement of atoms or the interlayer spacing. For example, Figure 2.24 shows the plot of the total *Rp* factor as a function of the change in the first interlayer spacing Δd_{12} from the optimized position. The uncertainty or error-bar in the LEED *I-V* calculations is determined from the variance of the total *Rp* factor, as proposed by Pendry, and is given by [26]:

$$\sigma = (R_P)_{\min} x \sqrt{\frac{8 \cdot |V_{oi}|}{\Delta E}} \tag{2.49}$$

where ΔE is the total energy of range of the experimental data and $(Rp)_{min}$ is the total *Rp* factor at global minimum. The error-bar is given in the region between $(Rp)_{min}$ and $(Rp)_{min}+\sigma$, as shown in Figure 2.24, where the correlations between parameters are not considered.

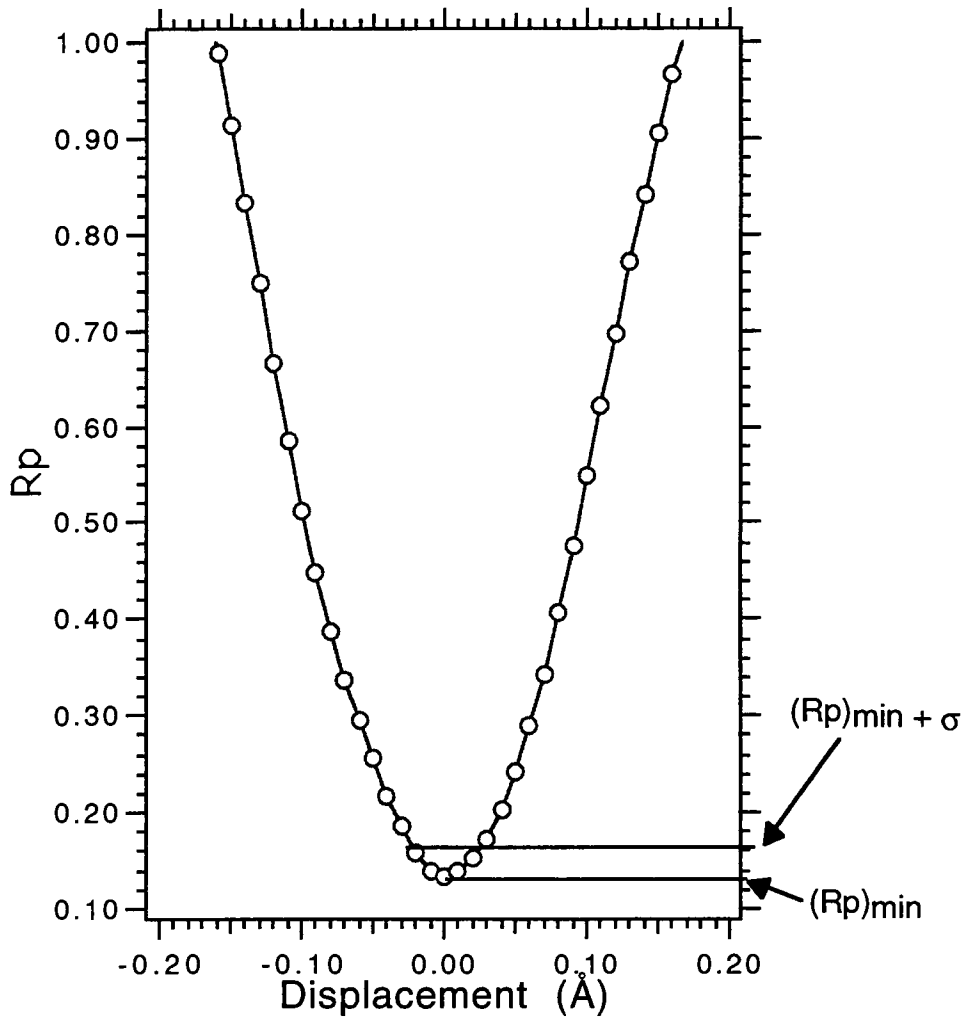


Figure 2.24: The *Rp* factor versus the displacement of the first interlayer spacing from the optimized position.

2.3.2 Computer Codes

We have used the Barbieri-Van Hove Tensor LEED package program [27] with some modifications — i.e., the rms motion of atom is given by equation (2.38) — in the structural determinations in the presented thesis. The program was described in a review article by Van Hove *et al.* [28]. The program was compiled by AIX XL FOTRAN 90 compiler version 3.2, using an IBM Power II RISC/6000-7030-3CT Workstation. There are two steps in the structural determinations. The first step is to perform a full dynamical-calculation for the reference structure by choosing a certain initial structural and non-structural parameters. Performing a full-dynamical calculation is time consuming. In general, it will take several hours. The t-matrix from a full dynamical calculation of reference structure is saved or stored in the disk. The second step is to choose an initial trial structure to calculate the *I-V* spectra by using the t-matrix from a full dynamical calculation of the reference structure via the Tensor LEED approximation. Usually this only takes several minutes. Evaluate the *Rp* factor from the calculated and experimental spectra and check if the *Rp* factor is at the minimum or not. Repeat step two until the *Rp* factor is at the minimum. Now check if the *Rp* factor is at the local minimum or global minimum. Redo steps one and two until the *Rp* factor is satisfied and at the global minimum. Figure 2.25 shows a flowchart for the structural determination used in this presented study.

2.3.3 LEED Experiment

A standard commercial 4-grids LEED optic is usually used in the LEED experiment. The electrons produced in a well collimated monoenergetic beam by an electron gun from a cold cathode electron source (LaB_6) are directed to the sample. These electrons will scatter with atoms near the surface region and back-scatter from the surface into the vacuum. These back-scattered electrons will travel through four hemispherical concentric grids and be viewed on the phosphorescent screen. All grids and the screen have a central hole

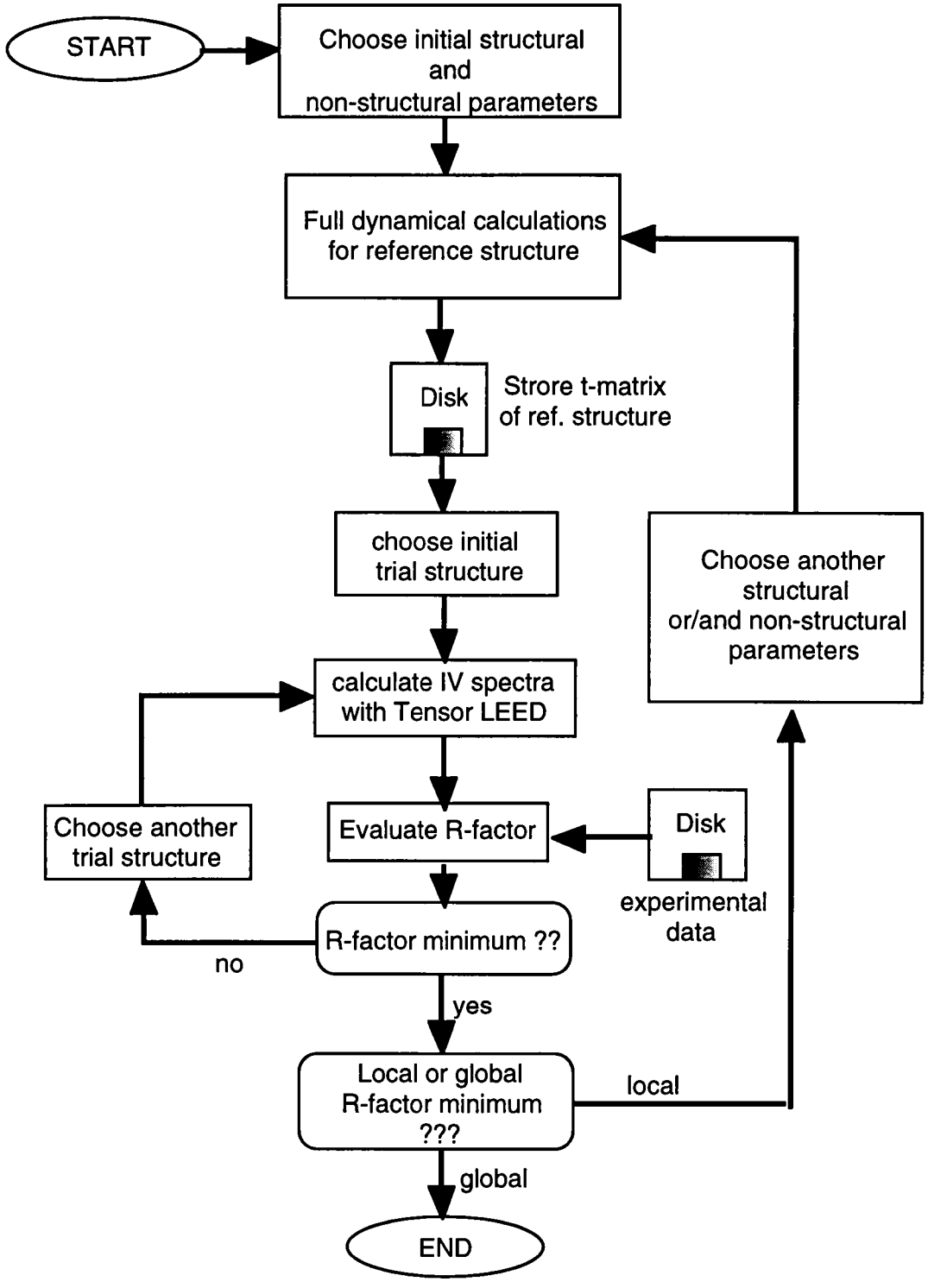


Figure 2.25: Flowchart for structural determination by LEED.

through in which the electron gun is inserted, as shown in Figure 2.26. The first grid is connected to the ground in order to provide a field free region between the grounded sample and the first grid. The second and third grids are suppressors applied a negative-potential to allow a narrow energy range of the elastically scattered electrons to be transmitted to the screen. The fourth grid is connected to the ground in order to reduce the field. The screen is applied a high-voltage 4 kV to render the diffraction electron beams visible. The LEED data in the research presented in this thesis were collected by using a standard commercial 4-grids LEED optic manufactured by the Omicron company. Figure 2.2 shows an example of a (1x1) LEED pattern at the kinetic energy of the electron E=50 eV for the Mg(0001) surface.

The domain size or coherence length of the sample can be predicted from the size of the diffraction spots. Pendry proposed the coherence length given by the equation [9]:

$$l_c = \frac{2\pi}{k[2\sin^2(\alpha)\cdot(\Delta\theta)^2 + \cos^2(\alpha)\cdot(\Delta E/E)^2]^{1/2}} \qquad (2.50)$$

where α is the angle between the scattering momentum wave vector and the parallel surface. E is the energy, and $(\Delta E)^2$ and $(\Delta\theta)^2$ are the mean square spread in energy and angular of the beam, respectively. In the case of the Mg(0001) surface, at energy E=92.5 eV, $\Delta E \approx 1.0$ eV, $\Delta\theta \approx 0.0083$ rad., and $\alpha \approx 45°$, then the coherence length is about 100 Å.

The information of the geometric structure near the surface region is contained in the diffraction intensity beams measured as a function of the kinetic energy of the electrons (I-V curves). A typical experimental set up to collect the LEED I-V data is shown in Figure 2.27. The sample was grounded and oriented such that the electron beam was at normal-incident perpendicular to the surface. The Auto LEED controller was connected to a CCD camera, LEED controller, video monitor, and computer. The computer software used to obtain the LEED I-V spectra was developed at the University of Erlangen, Germany [29]. Every diffracted beam (spot) was trapped by a window containing 15x15 pixels at a fixed

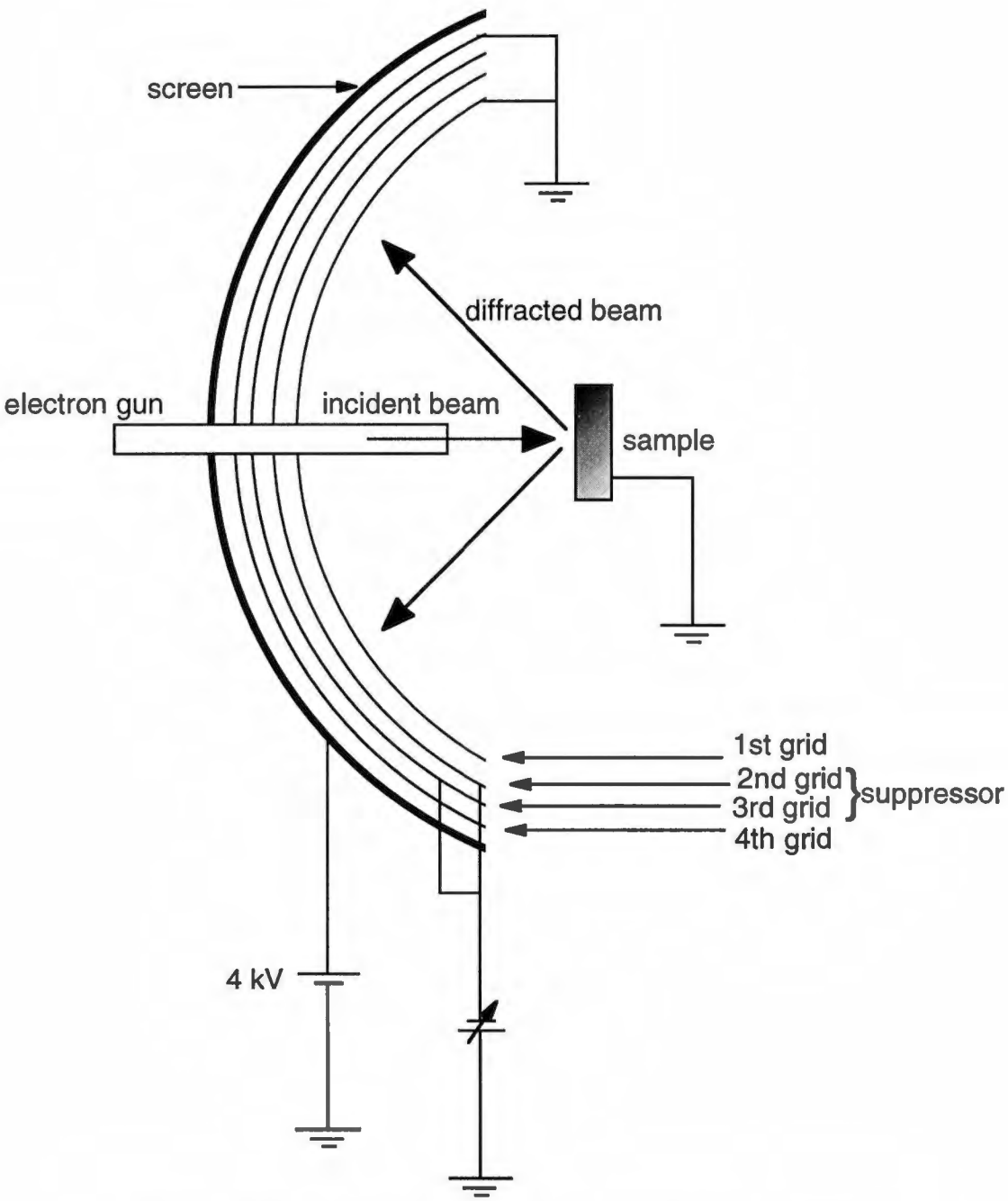


Figure 2.26: Schematic of a four grids LEED display system.

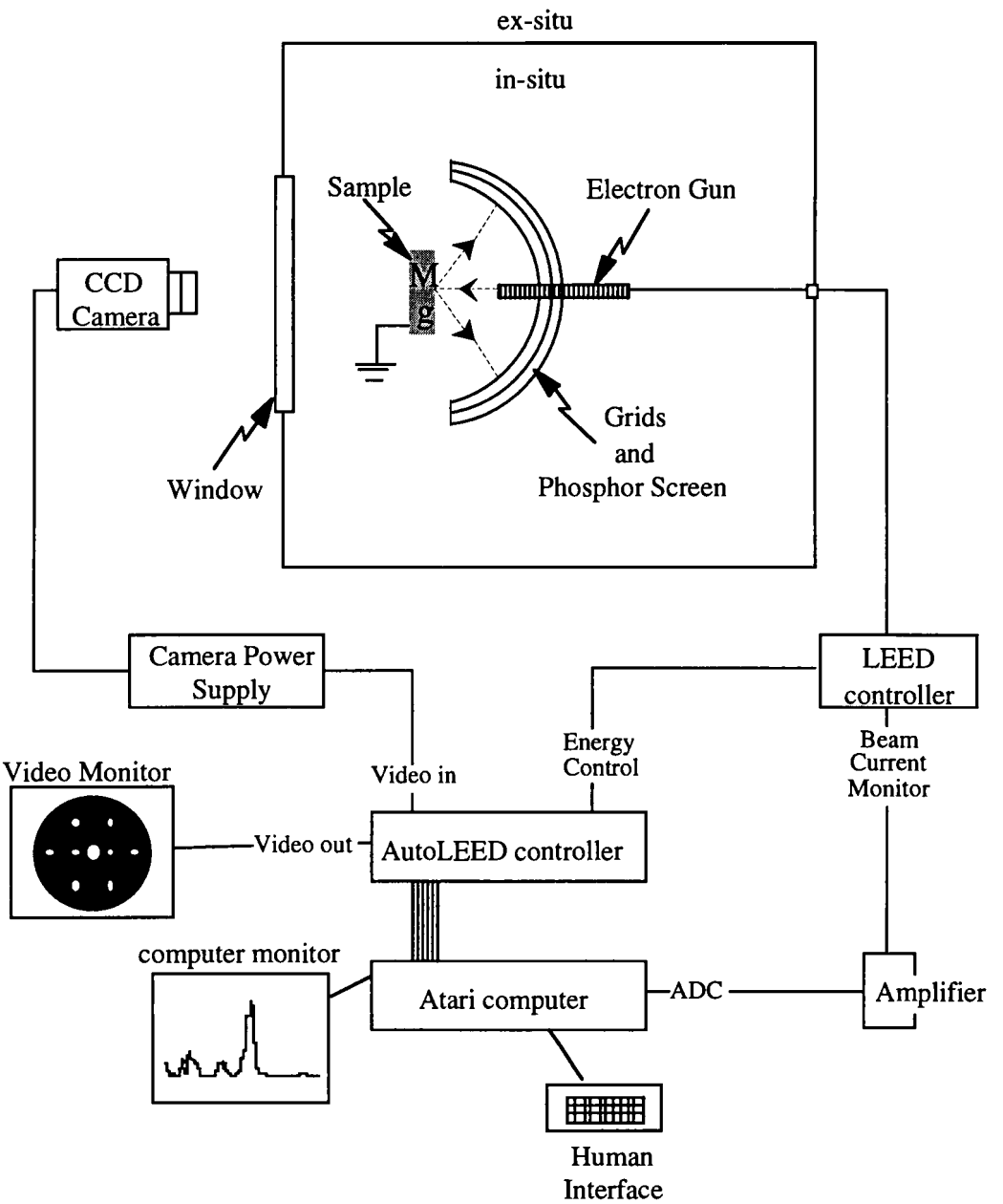


Figure 2.27: Schematic set up of LEED *I-V* experiment.

kinetic energy of the electron. As the energy was increased (step by step with 0.5 eV increments), the diffracted beams moved toward the center of the screen and at the same time the windows moved to follow the diffracted beams, therefore the diffracted beam was always inside the window. The intensity as a function of energy (*I-V* spectra) for all equivalent beams was recorded at the same time with energy increments of 0.5 eV. At each energy step, the background intensity inside the edge of the window was subtracted and the incident beam current as a function of energy was recorded.

For a normal-incident LEED *I-V* experiment, it is very important to have a correct alignment of the sample (polar angle $\theta \approx 0°$). Misalignment of the sample will shift the peak positions and even could produce small extra peaks, leading to poor quality of the experimental data. To avoid this problem, it is necessary to align the sample correctly. This can be done by adjusting the position of the sample until the *I-V* curves of the equivalent beams are almost identical; i.e., so that the *Rp* factor among the symmetrically equivalent beams is less than 0.1. Noonan and Davis proposed that the averaging technique of all accessible symmetry equivalent beams will improve the quality and accuracy of the experimental data [33]. However, the presence of the electron gun could limit us to take all symmetrically equivalent beams. The previous study showed that misalignments of polar angle up to 3° still yield a reasonable quality of the data [34].

The presence of magnetic field near the sample will shift the position of the peaks. Usually this happens at low energy; i.e., for kinetic energy less than 150 eV. Consequently, the *Rp* factor among the symmetrically equivalent beams can not be achieved less than or equal to 0.1. Care must be taken to eliminate this problem. The UHV chamber system needs to be shielded, such as by μ-metals or Helmholtz coils to compensate the Earth's fields. If we suspect the magnetic fields are from the sample holder then the sample holder needs to be demagnetized.

In the research presented here, all accessible equivalent beams are averaged and normalized by beam currents. Figure 2.28 shows our typical experimental data (*I-V* curves) of (01), (11), (02), and (21) beams of the Mg(0001) surface where the LEED pattern of this surface exhibits a six-fold symmetry: (a) the *I-V* spectra from all accessible symmetrically equivalent beams, (b) averaging of the *I-V* spectra from accessible symmetrically equivalent beams, and (c) normalized *I-V* spectra from (b) for raw data (doted lines) and smoothed data (solid lines).

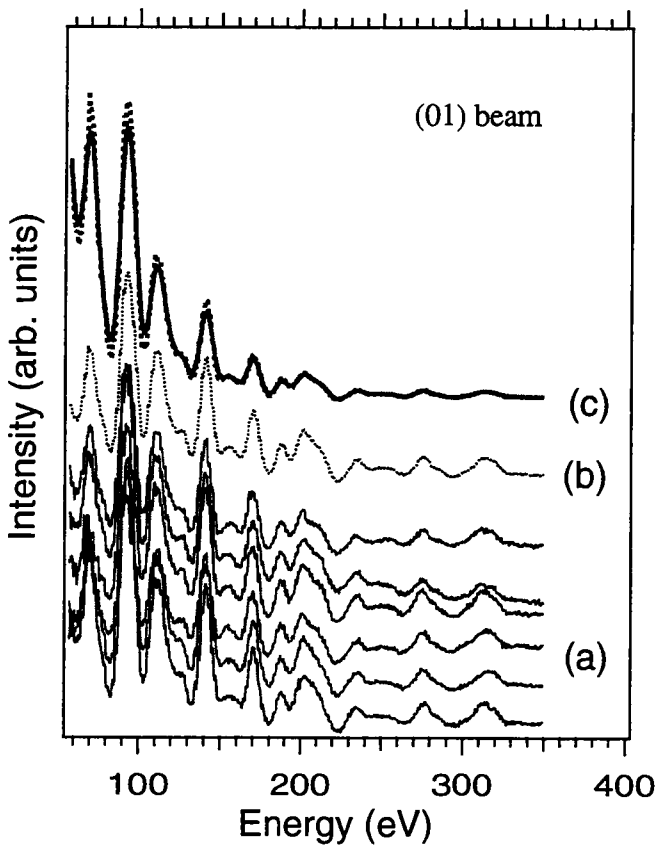


Figure 2.28: Measured LEED *I-V* spectra of the Mg(0001) surface: (a) *I-V* spectra of all symmetrically equivalent beams. (b) Average of *I-V* spectra of equivalent beams. (c) Normalized of the average of *I-V* spectra, raw data (dots) and smoothed data (solid line).

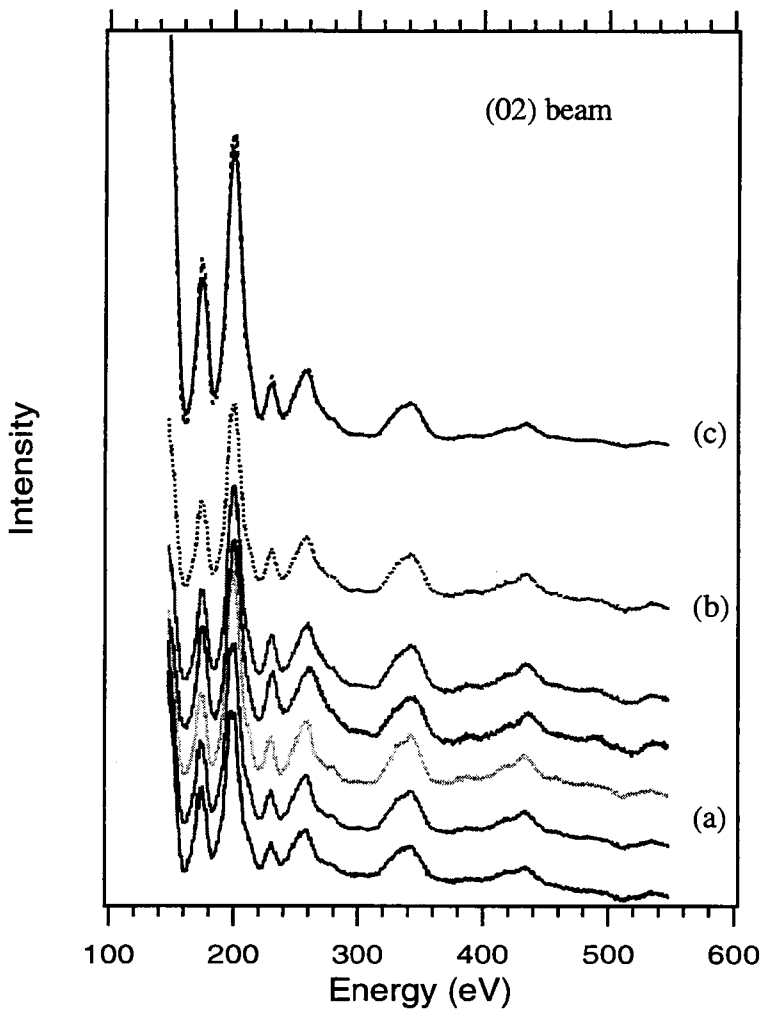


Figure 2.28: (continued)
Measured LEED *I-V* spectra of the Mg(0001) surface: (a) *I-V* spectra of all symmetrically equivalent beams. (b) Average of *I-V* spectra of equivalent beams. (c) Normalized of the average of *I-V* spectra, raw data (dots) and smoothed data (solid line).

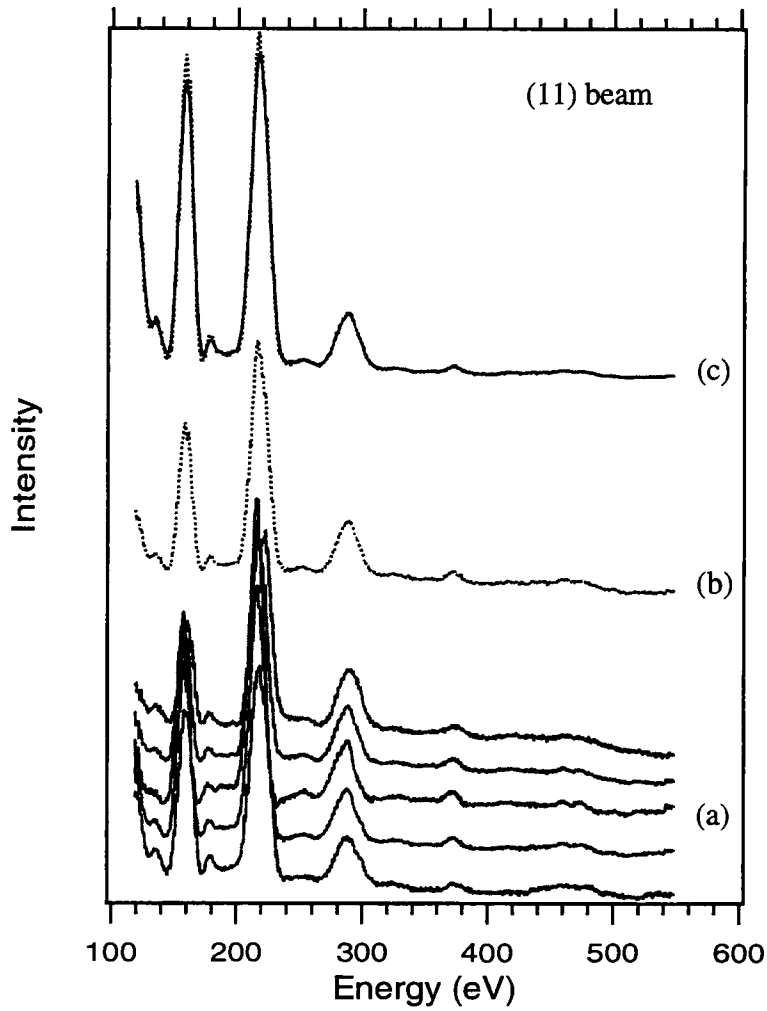


Figure 2.28: (continued)
Measured LEED *I-V* spectra of the Mg(0001) surface: (a) *I-V* spectra of all symmetrically equivalent beams. (b) Average of *I-V* spectra of equivalent beams. (c) Normalized of the average of *I-V* spectra, raw data (dots) and smoothed data (solid line).

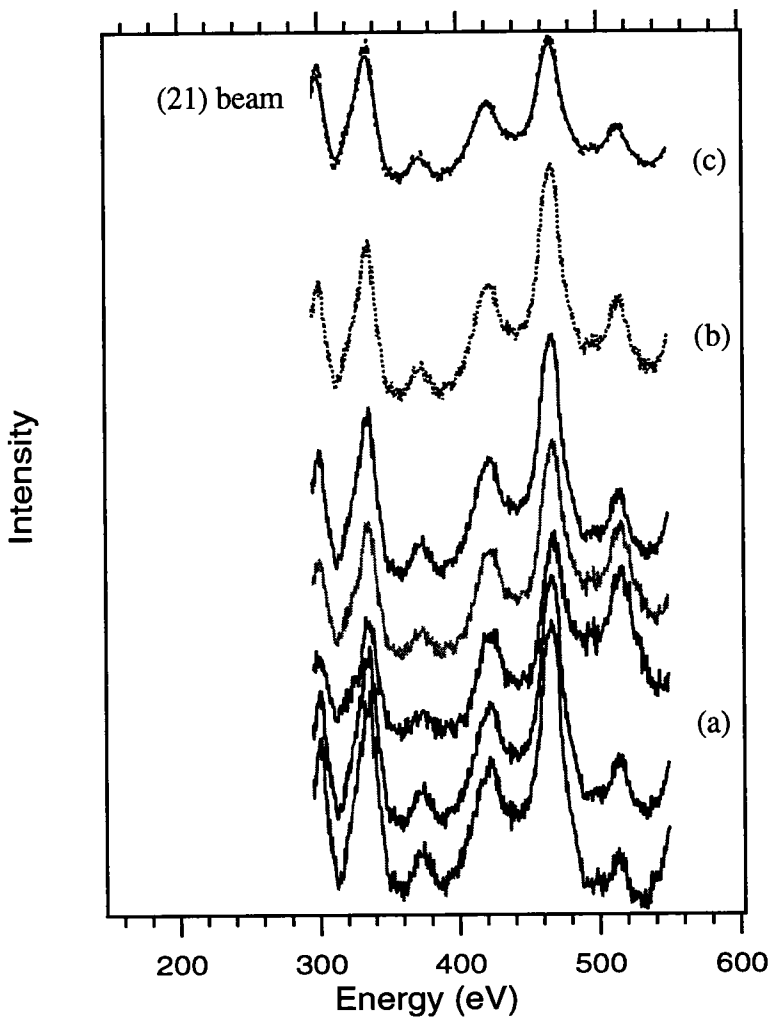


Figure 2.28: (continued)
Measured LEED *I-V* spectra of the Mg(0001) surface: (a) *I-V* spectra of all symmetrically equivalent beams. (b) Average of *I-V* spectra of equivalent beams. (c) Normalized of the average of *I-V* spectra, raw data (dots) and smoothed data (solid line).

2.4 Electron Energy Loss Spectroscopy (EELS)

Electron energy loss spectroscopy is used to measure the distribution of the electrons back-scattered inelastically from a surface [5]. By analyzing this electron distribution, one can obtain the direct information of the properties of the surface excitations, such as: adsorbate vibrations, lattice vibrations (phonons), and electronic excitations (interband transitions and surface plasmons). This technique is surface sensitive because the kinetic energy of the electron is chosen suitably in order to have a penetration depth of a few atomic layers.

Assume a highly monoenergetic electron with the kinetic energy E_i and momentum $\vec{k}_i$ is directed toward the surface of a solid (sample) with an incident angle θ_i with respect to normal of the surface, as shown in Figure 2.29. This electron will scatter inelastically with the atoms with an energy loss $\Delta E = \hbar\omega_v$ and a momentum transfer $\vec{q}$, and back-scatter into the vacuum with the energy E_s, momentum $\vec{k}_s$, and scattered angle θ_s. The energy of the electron is conserved in this process, therefore we have the relation as the following:

$$\Delta E = E_i - E_s \tag{2.51}$$

The energy loss ΔE is a vibrational frequency of the surface excitation that depends on the momentum transfer $\vec{q}$; thus the equation above becomes:

$$E_s(\vec{k}_s) = E_i(\vec{k}_i) - \hbar\omega_v(\vec{q}_{\parallel}) \tag{2.52}$$

and the momentum of the electron parallel to the surface is also conserved,

$$\vec{k}_{s\parallel} = \vec{k}_{i\parallel} - \vec{q}_{\parallel} \pm \vec{G} \tag{2.53}$$

where $\vec{G}$ is a two-dimensional reciprocal lattice vector that is parallel to the surface. From the equations (2.52) and (2.53), one can have a simple expression of the momentum transfer parallel to the surface:

$$\vec{q}_{\parallel} = \frac{\sqrt{2m}}{\hbar}\left(\sqrt{E_i}\sin\theta_i - \sqrt{E_i - \hbar\omega_v}\sin\theta_s\right) \pm \vec{G} \tag{2.50}$$

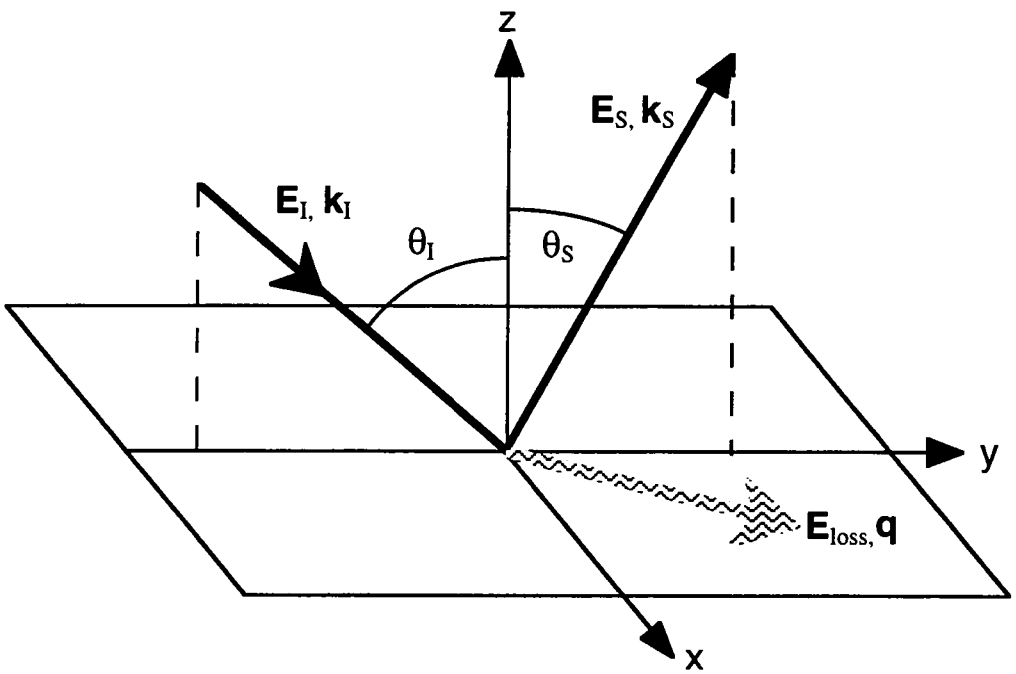


Figure 2.29: Scattering geometry in electron energy loss spectroscopy, y-z plane is called the scattering plane.

From equation (2.50), one can choose a certain value of the incident angle, scattered angle, and incident energy of the electron in order to have a desired parallel momentum transfer $\bar{q}_{\parallel}$. The vibrational energy at the surface is usually small; therefore, a high resolution instrument is required in order to be able to detect the surface vibrational losses.

There are two scattering regimes of the inelastic electron scattering process in the energy loss spectroscopy technique:

(i) The first is the dipole scattering regime where the vibrational mode at a surface is excited by a long-range dipolar field of an incident electron. This interaction is characterized by a small-angle scattering, where $\theta_S \approx \theta_i$. The mechanism of the dipole scattering can be explained by considering an adsorbed molecule with the dipole moment $\bar{\mu}$ that is placed on a clean surface material [30,31]. The incident electron and its image will create an electric field $\bar{E}$ at the adsorption site. The interaction between the incident electron and adsorbed molecule is given by $U = -\bar{\mu}.\bar{E}$. The scattering cross section for the transition from an incident state $|\psi_i\rangle$ to a final state $|\psi_s\rangle$ is given by [30,31]:

$$\frac{d\sigma}{d\Omega} = \left(\frac{4m\mu e}{\hbar^2}\right)\frac{v_s}{v_i}\frac{1}{\cos\theta_i}\left|2\pi^2\langle\psi_s|\frac{z}{|\bar{x}|^3}|\psi_i\rangle\right|^2 \qquad (2.51)$$

where $\mu = \langle f|\mu_z|0\rangle$ is the expectation value of the normal component of the dipole operator between the ground state $|0\rangle$ and the excited state $\langle f|$ of atoms, v_s and v_i are the velocities of scattered and incident electrons, and the term $z/|\bar{x}|^3$ is the dipolar field associated with the electron and its image at the adsorption site. The matrix element in equation (2.51) can be written as [31]:

$$\left|2\pi^2\langle\psi_s|\frac{z}{|\bar{x}|^3}|\psi_i\rangle\right|^2 = \left(\frac{q_{\parallel}}{(\bar{k}_{i,z}-\bar{k}_{s,z})^2+q_{\parallel}^2} - \frac{q_{\parallel}}{(\bar{k}_{i,z}+\bar{k}_{s,z})^2+q_{\parallel}^2}\right)^2 \qquad (2.52)$$

The plot of the dipole scattering cross section as a function of scattering angle (equations (2.51) and (2.52)) shows that the sharp dipole scattering cross section is at specular direction ($\Delta\theta = 0$); while for off-specular ($\Delta\theta \geq 2°$), the scattering cross section is almost zero [32]. From equation (2.51), the dipole scattering cross section will be zero whenever the z-component of the dipole is zero ($\mu_z = 0$), leading to the selection rule for the dipole scattering regime: *vibrational modes can only be excited if the dipole moment has a component normal to the surface.*

(ii) The second is the impact scattering regime or large-angle scattering. The mechanism in this scattering regime comes from the interaction of the electrons with the ion-cores in a solid that is similar to the mechanism of LEED. The scattering cross section for the impact scattering of a vibration mode Q_v is given [5]:

$$\left(\frac{d\sigma}{d\Omega}\right)_v = A\frac{mE_i\cos^2(\theta_s)}{2\pi^2\hbar^2\cos(\theta_i)}\left|M(\vec{k}_i,\vec{k}_s,Q_v)\right|^2 \tag{2.53}$$

where A is the surface area of the sample and M is the matrix element given by:

$$M(\vec{k}_i,\vec{k}_s,Q_v) = \sqrt{(1+n_v}\sqrt{\frac{\hbar}{2N\omega_v}}\left(\frac{\partial f}{\partial Q_v}\right) \tag{2.54}$$

where N is the number of atoms in the unit cell, n_v is the number of phonons present in the system, and

$$\frac{\partial f}{\partial Q_v} = \sum_{j,\alpha}\left(\frac{\partial f}{\partial R_{j,\alpha}}\right)_0 u_{j,\alpha}(Q_v) \tag{2.55}$$

where α is the Cartesian components, $R_{j,\alpha}$ is the atomic position of jth atom, and $u_{j,\alpha}(Q_v)$ is the displacement vector of the atom j^{th} associated with the mode Q_v. The equations (2.53) and (2.55) show that whether the scattering cross section in the impact scattering regime will be zero or non-zero depends upon the value of $(\partial f / \partial R_{j,\alpha})$. Therefore, the selection rule for the impact scattering regime arises from the symmetry of the atomic

displacements $u_{j,\alpha}(Q_v)$ associated with the vibration mode Q_v: *if the scattering plane coincides with a mirror plane (reflection plane) of a surface, then all modes with atomic motion odd with respect to that mirror plane can not be excited* because the symmetry of $(\partial f / \partial R_{j,\alpha})$ causes $(\partial f / \partial Q_v)$ to vanish. A comprehensive explanation for both dipole and impact scattering regimes is described in the textbook by Ibach and Mills [5].

All vibrational spectra in the research presented in this thesis were obtained by using a commercial HREELS (high resolution energy loss spectroscopy) HIB 1000 manufactured by the VSW company. The layout of the instrument is shown in Figure 2.30. The detailed information of this instrument is given in the textbook by Ibach [6]. The energy resolution of this instrument can be achieved up to 2.0 meV for the impact energy of the electron 2 - 10 eV. The specular direction is set with the scattering geometry $\theta_S = \theta_I =$ 45°. The monocromator can be rotated in the scattering plane in order to achieve the off-specular direction. Besides rotating the monocromator, the sample also can be rotated around the polar axis. For a large momentum transfer, besides rotating the monocromator and sample, we also need to increase the impact energy (kinetic energy) of the electron, (see equation (2.50)). Figure 2.31 shows an example of our typical EELS spectrum from the magnesium surface taken by using a commercial HREELS HIB 1000 instrument in the off specular direction. The dots are raw data, while the solid line is smoothed data. The energy loss is at the energy E=14.5 meV.

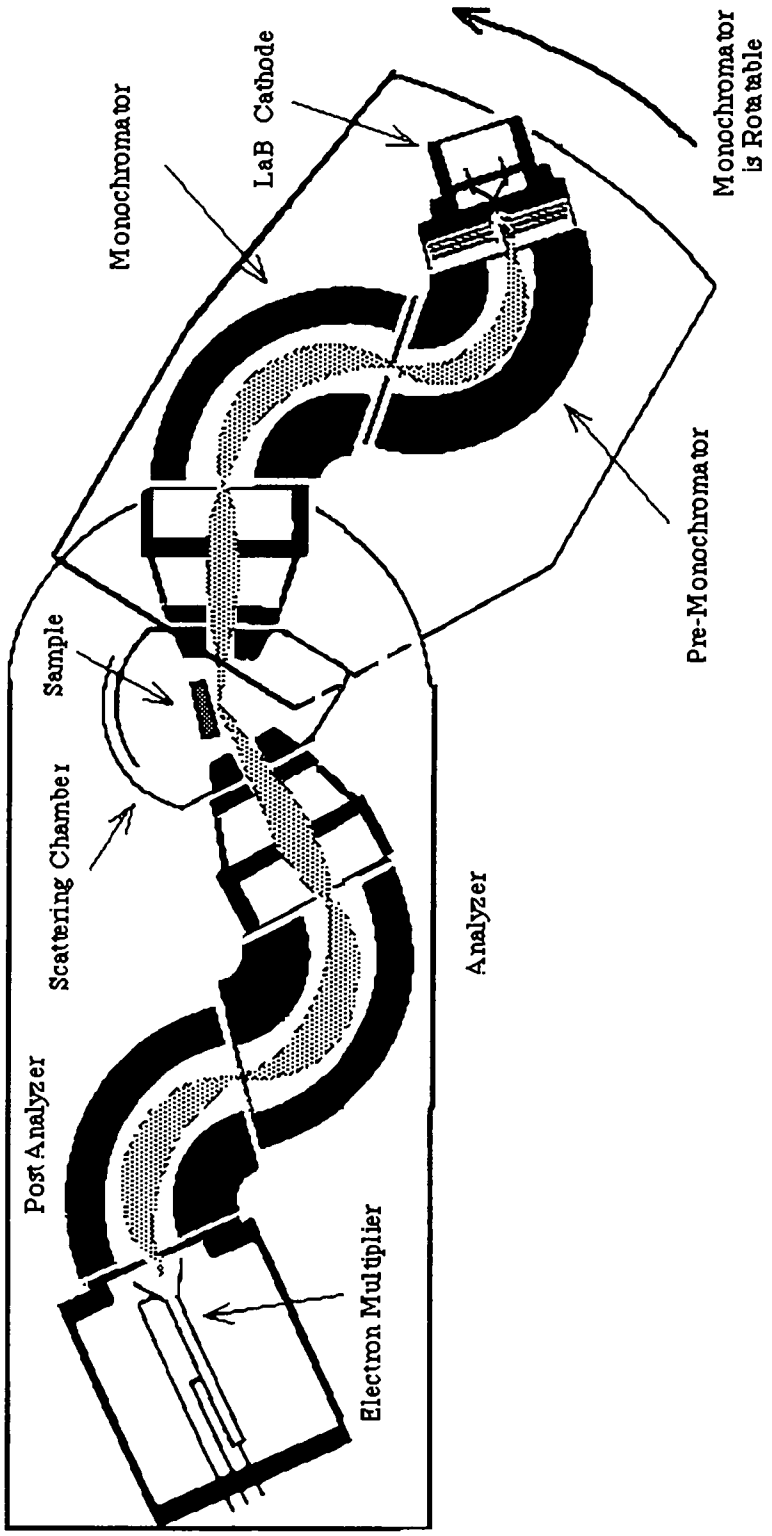


Figure 2.30: Layout of EELS spectrometer - HIB 1000 (VSW).

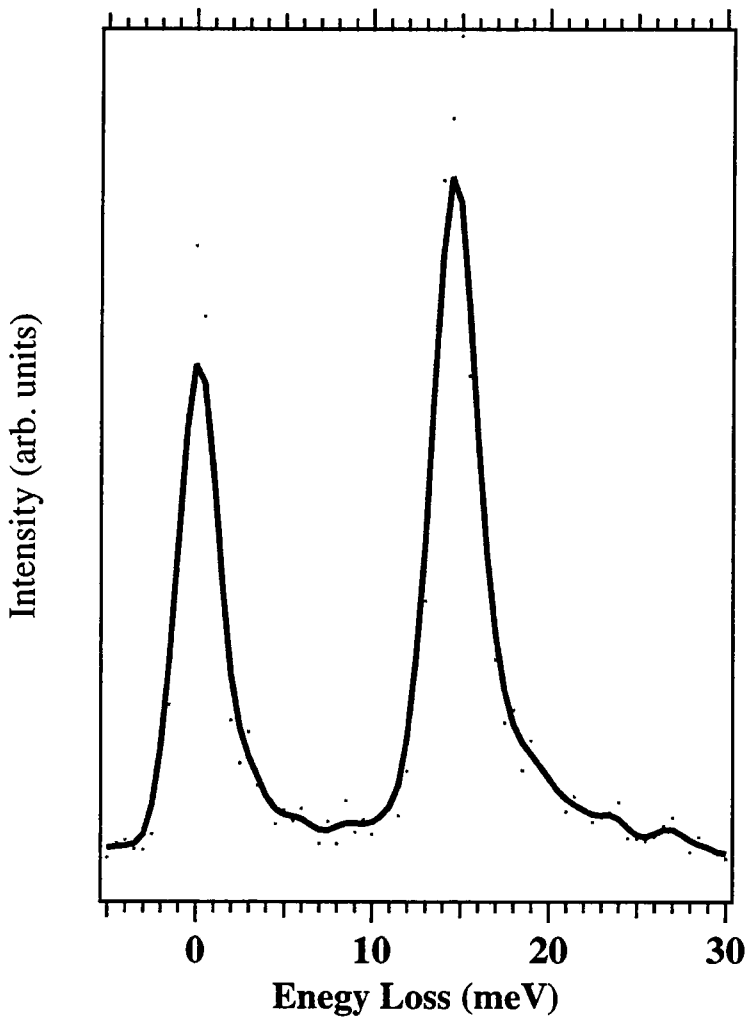


Figure 2.31: EELS spectrum at the Mg(0001) surface. Dots are raw data and solid line is smoothed data.

2.5 References

1. J.F. O'Hanlon: *A User's Guide to Vacuum Technology* (Wiley, New York, 1989).

2. D.M. Hoffman, B. Singh, and J.H. Thomas, *Handbook of Vacuum Science and Technology* (Academic Press, San Diego, 1998).

3. Phillip T. Sprunger, Ph.D. Thesis, Department of Physiscs, Univeristy of Pennsylvania, 1993.

4. A. Zangwill: *Physics at Surfaces* (Cambridge University Press, Cambridge, 1988).

5 H. Ibach and D.L. Mills: *Electron Energy Loss Spectroscopy* (Academic Press, New York, 1982).

6. H. Ibach: *Electron Energy Loss Spectrometers - The Technology of High Performance* (Springer, Heidelberg, 1991).

7. C. Davisson and L.H. Germer, Phys. Rev. **30**, 705 (1927).

8. R.L. Park and H.E. Farnsworth, Surf. Sci. **2**, 527 (1964).

9. J.B. Pendry: *Low Energy Electron Diffraction* (Academic, London, 1974).

10. M.A. Van Hove, private communication.

11. M.A. Van Hove, W.H. Weinberg, and C.-M. Chan: *Low-Energy Electron Diffraction* (Springer, Berlin, 1986).

12. M.A. Van Hove and S.Y. Tong: *Surface Crystallography by LEED* (Springer, Berlin, 1979).

13. J.J. Sakurai: *Modern Quantum Mechanics* (Addison-Wesley, New York, 1985).

14. L.F. Mattheiss, Phys. Rev **133**, A1399 (1964).

15. T. Loucks: *Augmented Plane Wave Method* (Benjamin, New York, 1967).

16. K. Schwarz, Phys. Rev. B **5**, 2466 (1972).

17. A. Barbieri and M.A. Van Hove, private communication.

18. V.L. Moruzzi, J.F. Janak, and A.R. Williams: *Calculated electronic properties of metals* (Pergamon, New York, 1978).

19. J.C. Slater: *Insulators Semiconductors and Metals* (McGraw Hill, New York, 1967).

20. J.L. Beeby, J. Phys. C **1**, 82 (1968).

21. P.J. Rous, J.B. Pendry, D.K. Saldin, K. Heinz, K. Müller, and N. Bickel, Phys. Rev. Lett. **57**, 2951 (1986).

22. P.J. Rous and J.B. Pendry, Surf. Sci. **219**, 355 (1989).

23. P.J. Rous and J.B. Pendry, Surf. Sci. **219**, 373 (1989).

24. P.J. Rous, Progr. Surf. Sci. **39**, 3 (1992).

25. M.A. Van Hove and R.J. Koestner, in *Determination of Surface Structure by LEED,* edited by P.M. Marcus and F. Jona, The IBM Research Symposia Series (Plenum, New York, 1984).

26. J.B. Pendry, J. Phys. C **4**, 2514 (1971).

27. A. Barbieri and M.A. Van Hove: *Symmetrized Automated Tensor LEED* package, Version 4.1, available from M.A. Van Hove.

28. M.A. Van Hove, W. Moritz, H. Over, P.J. Rous, A. Wander, A. Barbieri, N. Materer, U. Starke, and G.A. Samorjai, Surf. Sci. Rep. **19**, 191 (1993).

29. K. Müller and K. Heinz, in The Structure of Surface, edited by S.Y. Tong and M. A. Van Hove, Springer Series in Surface Science Vol. 2, pp. 105-112 (Springer, Berlin, 1985).

30. B.N.J. Persson, Solid State Comm. **24**, 573 (1977).

31. B.N.J. Persson, Surf. Sci. **92**, 265 (1980).

32. J.B. Hannon, Ph.D. Thesis, University of Pennsylvania (1994).

33. J.R. Noonan and H.L. Davis, Science **234**, 310 (1986).

34. K. Heinz, Surf. Sci. **229/300**, 433 (1994).

Chapter 3

Thermal Effects on the Surface Structure of Mg(0001) and Mg(10$\bar{1}$0)

If the interatomic potential in solids were purely harmonic, the mean positions of the atoms in solids would not change as the temperature increases, even though the amplitude of atomic vibration is large. However, the interatomic potential in solids is anharmonic. A small change in the ionic potential energy will accompany an increase in the separation of ionic positions in a solid. Therefore, it is well known that the thermal expansion is directed by the nature of anharmonicity of the interatomic force in a solid, as has been discussed in Chapter 1.

As a surface is created, the number of nearest-neighbors of atoms at the surface is reduced and the atoms near the surface region relax, which cause the interlayer potential to become more asymmetric at the surface than in the bulk. Consequently, the anharmonicity at the surface will be larger than the bulk. Baddorf and Plummer have demonstrated evidence of enhanced surface anharmonicity at a metal surface by using high resolution electron energy loss spectroscopy [1]. Their measurements showed that the surface anharmonicity is much larger than in the bulk [1]. Consequently, the thermal expansion at the surface should be larger than in the bulk. There have been several reports of *anomalous thermal expansion at metal surfaces* [2-7]. The first observation in 1987 was for Pb(110), using double alignment ion scattering. A gradual increase in the surface thermal expansion coefficient relative to the bulk was observed in the temperature range of 29 K to ~460 K, but a precipitous increase occurred at 485 K in the premelting regime [2]. A kinematic analysis of electron diffraction data from Ni(100) in 1990 showed a rapid increase in the surface thermal expansion compared to the bulk above 900 K, reaching a value ~20 times larger than the bulk expansion [3]. X-ray reflectivity measurements (in 1993) on Cu(110)

in the temperature range of 300 K to 900 K showed an enhanced surface thermal expansion (2-3 times the bulk value) [5], but as in the case of Pb(110), the surface was contracted with respect to the bulk at all temperatures studied. A double alignment ion scattering study of Ag(111) in 1994 revealed an anamolously large surface thermal expansion for temperatures above ~600 K [6]. As the temperature of solid is increased, the surface anharmonicity increases as well. This will lead to a very large anisotropic vibration, causing disordering and melting of the surface region [8-10]. For example, molecular dynamics simulations showed that the Ni(110) surface became disordered at the temperature 1450 K through the generation of vacancies accompanied by the formation of an adlayer [10].

Early free energy calculations showed that large thermal expansion at a surface was governed by a large anharmonicity perpendicular to the surface [8,11,12], as was discussed above. However, a new mechanism of thermal expansion at a surface proposed by Narasimham and Scheffler [13] contradicts this picture. In their model the phonon frequencies are obtained from *ab initio* total energy calculations. Anharmonic effects are treated within the quasiharmonic approximation. At a finite temperature the equilibrium structure is determined by the minimum of the free energy with respect to the structural parameters, where both the electrons and the phonons are important in determining the structure. They suggest that a large thermal expansion at a metal surface can be attributed to a rapid softening of the *in-plane* phonon frequencies with increasing temperature rather than anharmonicity in the out-of-plane modes [13]. Another new mechanism for the surface thermal expansion at a metal surface was proposed by Marzari *et al.* [14]. By using a finite temperature density functional molecular dynamic simulation, they found a thermal contraction in the first layer of the Al(110) surface, as a consequence of strongly anharmonic mean-square-displacement of atoms in the *second* layer (*not* in the surface

layer) perpendicular to the surface [14]. Clearly, studying the thermal effects on the surface structure of a metal surface is an interesting subject.

3.1 The Mg(0001) Surface

3.1.1 Introduction

Temperature dependence measurements of the Rayleigh wave on the Be(0001) surface by Hannon showed no enhanced surface anharmonicity at this surface [15], suggesting that the surface thermal expansion on Be(0001) is similar to the bulk. However, measurements showed a large thermal surface expansion in the first interlayer of Be(0001), i.e., six times larger than in the bulk [7]. This observation was supported by the density-functional calculations for the surface thermal expansion from the minimum in the free energy within the quasiharmonic approximation, where the free energy was obtained from sampling vibrational modes. This calculation suggested that the enhanced thermal expansion at the Be(0001) surface was caused primarily by a softening of the *in-plane* vibrations [7,13]. This conclusion, however, has been dramatically challenged by an *ab initio* study of the surface thermal expansion within the quasiharmonic approximation, where the free energy was obtained from *full* vibrational dispersions computed by density-functional perturbation theory by Lazzeri and de Gironcoli [16]. They claimed that there was no an anomalously large thermal expansion at the Be(0001) surface and the experiments might be a consequence of the surface morphology [16].

From the experimental view, one might need to address two possible reasons for this confusion:

(1) LEED *I-V* Analysis

LEED *I-V* is one of the most powerful tools in surface crystallography, and it has been applied for many cases (for normal-incident) [17-18]. Its accuracy is reasonably well, especially for the vertical displacement of the top surface layer because the

momentum transfer perpendicular to the surface is large. However, the accuracy depends primarily on the size of the experimental data set. In the case of the Be(0001) surface [7], at temperatures T=110 K and T=300 K, the experimental data sets contain three inequivalent beams with the total energy ranges of ΔE=970 eV (T=110 K) and of ΔE=870 eV (T=300 K). While at temperature T=700 K, the experimental data set contains *only one* inequivalent beam with the total energy range of ΔE=220 eV. The values of *Rp* factors are quite good for all there temperatures studied, meaning the models are supposed to be very confident. However, because the size of the data set at T=700 K is small, the accuracy of LEED is poor at this temperature.

(2) Surface Morphology.

Lazzeri and de Gironcoli [16] claimed that poor agreement between the experimental data and their calculations was related to some degree of the structural disorder present in the actual Be(0001) surface, reflecting in the poor agreement between the theoretical and experimental (fitting parameters) rms vibrational displacements of the surface layer. They suggested that the actual Be(0001) surface could have a fcc(111) termination, i.e., a complete fcc(111) Be adlayer [16]. Pohl investigated the possibility of a fcc(111) termination of the hcp(0001) surface of Be (as suggested by Lazzeri and de Gironcoli) via LEED *I-V* analysis. However, he found that the agreement between the calculated and experimental spectra is poor, meaning this model (a fcc(111) termination) needs to be rejected [19]. This shows that an anomalously large thermal expansion at the Be(0001) surface as a consequence of the surface morphology suggested by Lazzeri and de Gironcoli [16] is *not* the case.

From the theoretical side, Lazzeri and de Gironcoli have demonstrated that the first interlayer thermal expansion determined within the quasiharmonic approximation depends on the sampling of the vibrational modes in the Brillouin zone [16]. In principle, full sampling in the Brillouin zone should give an accurate result. For the Be(0001) surface, at

temperature T=110 K the agreement between the results from the calculations within the quasiharmonic approximation (using full sampling in the Brillouin zone) and experimental data is excellent. However, the agreement at the other temperatures (T=300 K and T=700 K) is poor. It is very surprising that even at temperature T=300 K the agreement between theory and experiment is poor, while the size of the experimental data set at temperature T=300 K is almost the same as that of at temperature T=110 K. This immediately raises a question of whether the quasiharmonic approximation is valid for all temperatures or not. If it is not, then at what range of temperatures, does the quasiharmonic approximation is valid ? As we already know that in the quasiharmonic approximation, the first interlayer distance d_{12} at a finite temperature is obtained by minimizing the free energy for the surface with d_{12}, while *all other interlayer distances are assumed the same as in the bulk.* This assumption will produce a less accurate result of the thermal expansion in the first interlayer for a system where the thermal expansion in the second interlayer (d_{23}) is significantly different than in the bulk.

I have conducted the study of the thermal effects on the surface structure of Mg(0001). Magnesium (Mg) is a two valence *s-p* bonded metal with a hexagonal close-packed (hcp) structure, the same as Be. In contrast to Be, the *c/a* ratio for Mg is almost ideal (1.623) [20], and the density of states (DOS) of bulk Mg is nearly free-electron-like [21]. The electronic properties of Mg(0001) are free-electron like [22-24], but the density of surface states is significantly less than on Be(0001) [22]. The previous experimental study at T=100 K showed that the first interlayer spacing for the Mg(0001) surface is expanded by 1.9% with respect to the bulk, while the interplanar relaxations in the deep layers are almost zero [25]. Therefore, the study of the thermal expansion of the Mg(0001) surface is an ideal test for calculations within the quasiharmonic approximation.

3.1.2 Experiment and Analysis

Experiments were performed by using a standard ultra high vacuum chamber. The sample preparation was followed as was described in Chapter 2.2. The cleanliness of the sample was monitored by Auger electron spectroscopy (AES) and electron energy loss spectroscopy (EELS). A sharp (1x1) LEED pattern was observed, indicating no reconstruction on this surface. The photo of the diffraction pattern of Mg(0001) atoms for the incident energy E=50 eV at room-temperature is shown in Figure 3.1. The intensities of the diffracted electrons for normal-incidence as a function of the incident electron energy were recorded at the temperatures of the sample of 130 K, 300 K, and 400 K, where the procedure was described in Chapter 2.3.3.

The structural model of the bulk truncation of Mg(0001) is shown in Figure 3.2. The primitive translation vectors of direct and reciprocal of the Mg(0001) surface are given below:

$$\vec{a}_1 = \frac{a}{2}\left(-\sqrt{3}\,\hat{x} + \hat{y}\right) \qquad ;\vec{a}_2 = \frac{a}{2}\left(\sqrt{3}\,\hat{x} + \hat{y}\right) \tag{3.1}$$

$$\vec{b}_1 = \frac{2p}{a}\left(-\frac{1}{\sqrt{3}}\,\hat{x} + \hat{y}\right) \quad ; \qquad \vec{b}_2 = \frac{2p}{a}\left(\frac{1}{\sqrt{3}}\,\hat{x} + \hat{y}\right) \tag{3.2}$$

The two dimensional reciprocal lattice vectors (parallel to the surface) are defined by

$$\vec{G} = h\,\vec{b}_1 + k\,\vec{b}_2 \tag{3.3}$$

where h and k are integers assigned for the beams in the LEED pattern. Figure 3.3 shows the beam assignment for the LEED pattern of the Mg(0001) surface by using equation (3.3).

As shown in Figure 3.2, the Mg(0001) surface exhibits a three-fold rotational symmetry with a stacking sequence of ABAB. There are two possible bulk terminations (A

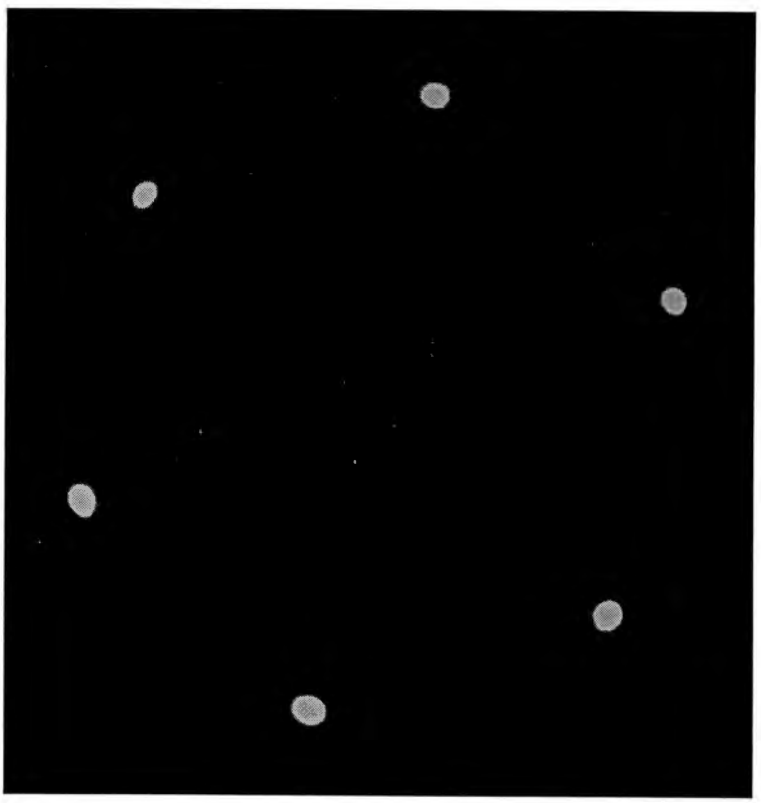


Figure 3.1: LEED photo from Mg(0001) at energy E=50 eV at room temperature.

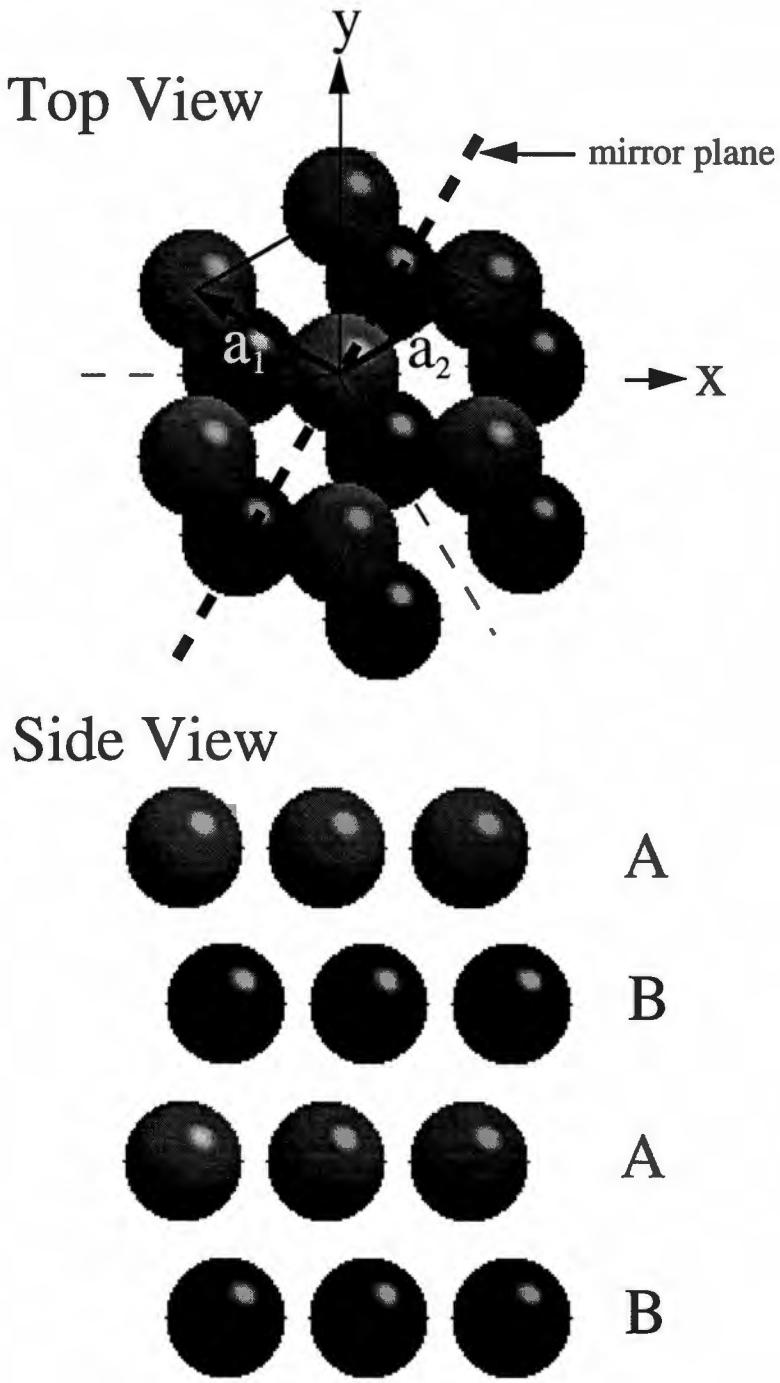


Figure 3.2: Bulk truncated model of the Mg(0001) surface.

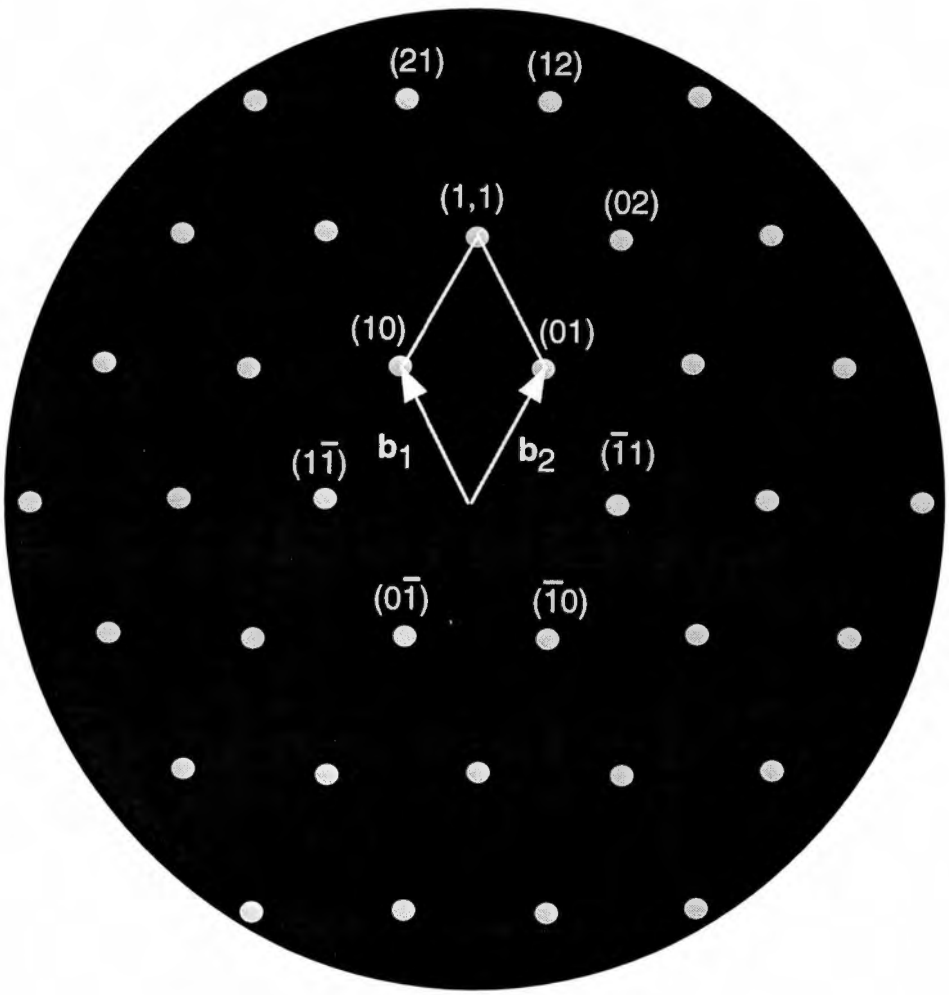


Figure 3.3: Beam assignments for LEED pattern of the Mg(0001) surface.

or B) of the 'ideal' hcp(0001) surface. Consequently, the diffraction pattern or a (1x1) LEED pattern for the Mg(0001) surface is expected to be a three-fold symmetry. However, the observed (1x1) LEED pattern of Mg(0001) exhibited a six-fold symmetry, as has been observed for the other hcp(0001) surfaces [7], indicating a natural averaging over the two possible bulk terminations (A and B) of the 'ideal' Mg(0001) surface or a fcc(111) termination with a complete Mg adlayer. Consequently, the number of inequivalent beams (the size of the data set) for Mg(0001) is reduced significantly by a factor of two in comparison to a fcc(111) surface. We have four inequivalent beams {(01), (11), (02), and (21)} with the total energy ΔE = 1425 eV at the temperature T=130 K; three inequivalent beams {(01), (11), and (02)} with the total energy ΔE = 740 eV at the temperature T=300 K, and two inequivalent beams {(01), and (11)} with the total energy ΔE = 560 eV at the temperature T=400 K. There are obvious changes in the diffraction pattern as the temperature increases: the beam spots broaden, the diffuse background between the spots increases, and the spot intensities drop significantly, especially at higher energy. Magnesium is a soft material where the Debye temperature is about 400 K. This leads to the reduction in the data set significantly with an increasing of the temperature, as shown in Figure 3.4, which is the consequence of the Debye-Waller attenuation at higher beam energies, as was discussed in Chapter 2. For example, the intensity at energy E=111 eV of the (01) beam decays exponentially with the increasing temperature (T), following the equation $I(T) \sim I_0\, e^{-K.T}$ with K of 0.00216, as shown in Figure 3.5. If this number is converted into the Debye-Waller factor, as given in Chapter 2, we find that the rms displacement of atoms $\langle u \rangle = 7.454 \times 10^{-3} \times \sqrt{T}$ Å for the Mg(0001) surface. At T=130 K, we have $\langle u \rangle$ = 0.085 Å, while the rms displacement of atoms in the bulk is about 0.113 Å (fitting parameters in the LEED I-V calculations). The value of rms deduced from the intensities ratio discussed above depends upon the beam and energy. Therefore, if we only

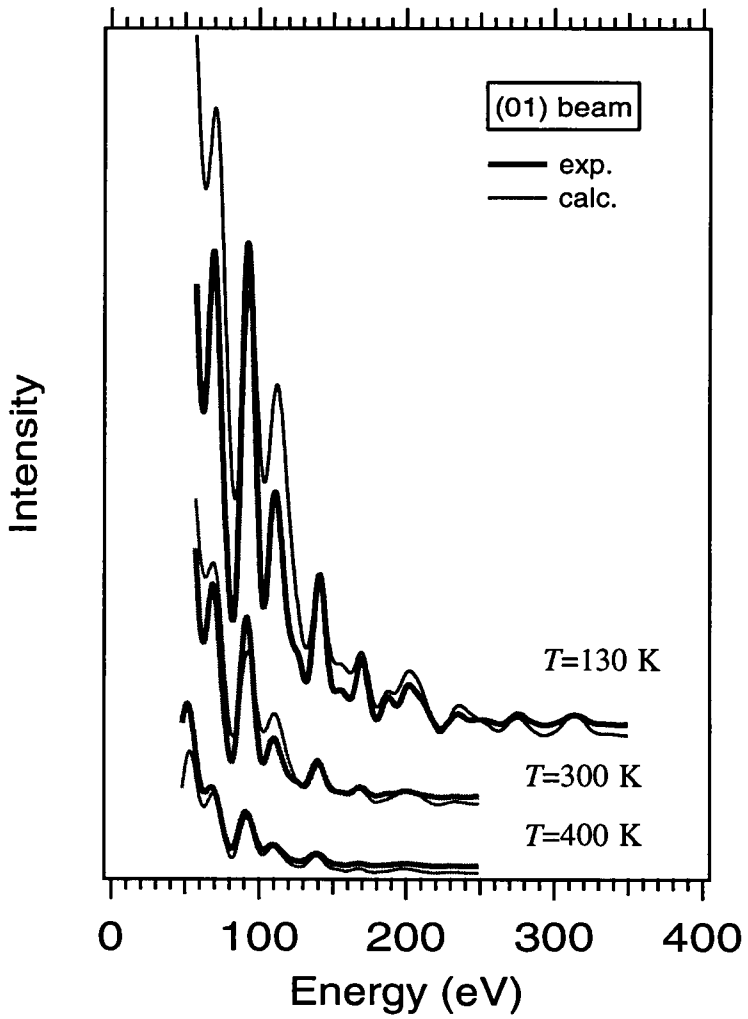


Figure 3.4: Measured and calculated LEED *I-V* spectra for the optimized structures of Mg(0001) at the temperatures *T*=130 K, 300 K, and 400 K.

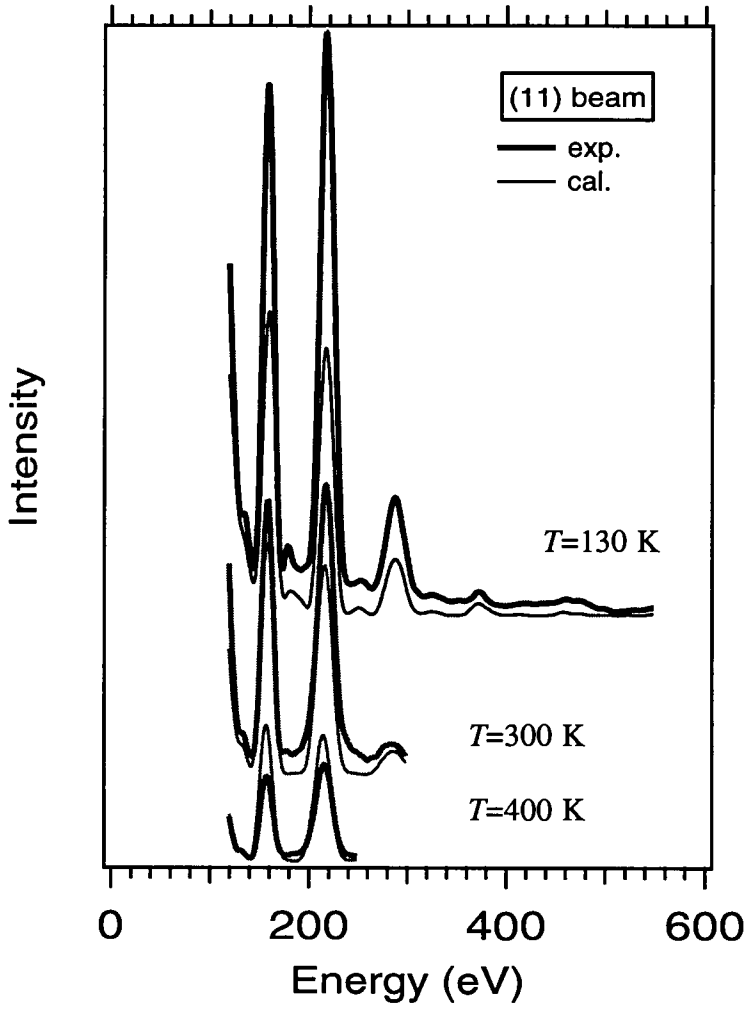


Figure 3.4: (continued)
Measured and calculated LEED *I-V* spectra for the optimized structures of Mg(0001) at the temperatures *T*=130 K, 300 K, and 400 K.

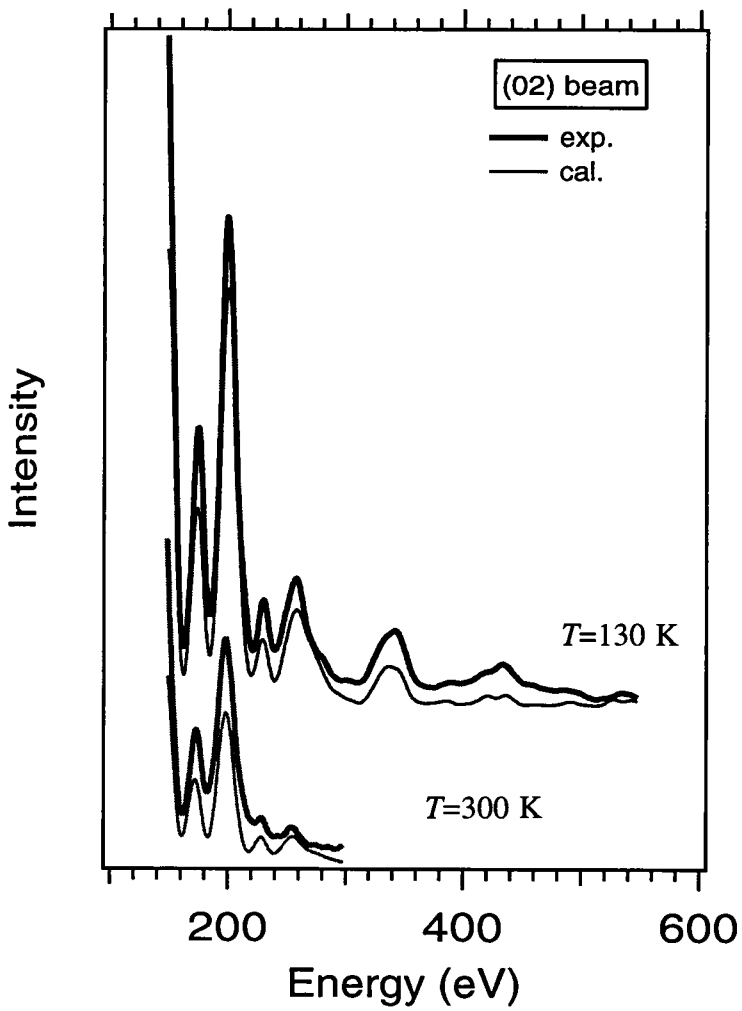


Figure 3.4: (continued)
Measured and calculated LEED *I-V* spectra for the optimized structures of Mg(0001) at the temperatures *T*=130 K, 300 K, and 400 K.

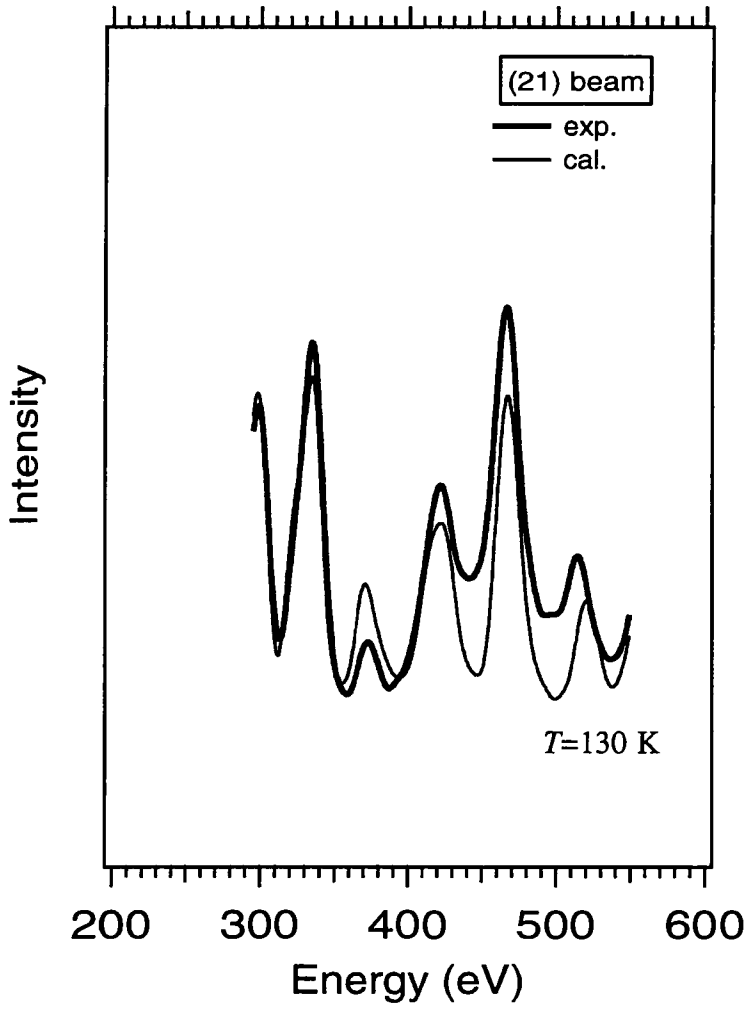


Figure 3.4: (continued)
Measured and calculated LEED *I-V* spectra for the optimized structures of Mg(0001) at the temperatures T=130 K, 300 K, and 400 K.

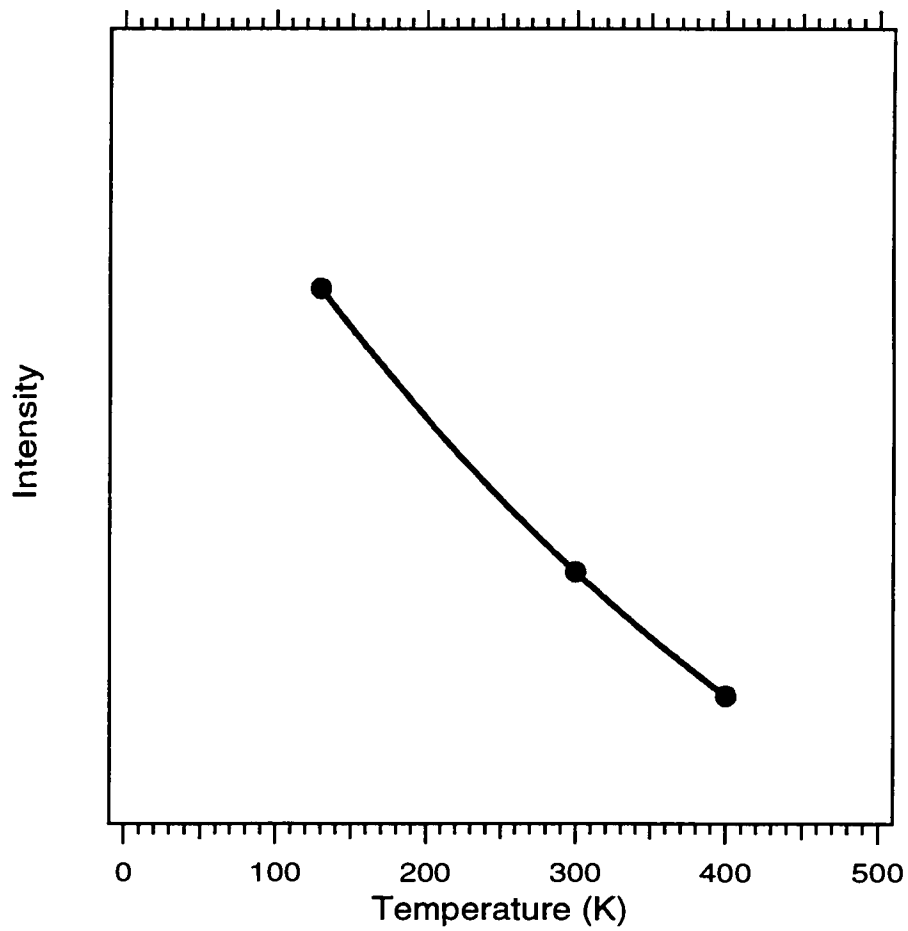


Figure 3.5: The intensities of the (01) beam at energy E=111 eV as a function of temperature at the Mg(0001) surface (filled circles). The solid line is the fit by an exponential function.

consider a certain energy of a certain beam, the accuracy of the rms displacement of atoms from analysis of ratio intensity is rather poor, i.e., within ±25% from the "correct" value. However, it is very useful for the starting point in the LEED *I-V* calculations for an element where its Debye temperature is still unknown.

The analysis of LEED *I-V* spectra was carried out by using standard multiple scattering algorithms combined with the Tensor-LEED, as was discussed in Chapter 2. A full dynamical calculation for the initial reference structure was performed by using the Beeby matrix inversion scheme, where multiple scattering within the layer was treated exactly, and the renormalized forward scattering (RFS) method was used for stacking layers [17,18]. Fourteen atomic phase shifts of magnesium were employed in our calculations, which we derived from the muffin-tin potential approximation with the muffin-tin radius of Mg is 2.9698 a.u. [21]. The electron attenuation was described by an optical-potential, where the real-part of the optical-potential (V_{or}) was energy independent and optimized during the search for all three temperatures studied, while the imaginary part (V_{oi}) was modeled by an equation below, as was discussed in Chapter 2:

$$V_{oi} = C\{\frac{E}{(200/27.21 + V_{or})}\}^{1/3} \ eV \qquad (3.4)$$

where E is the electron energy (eV) and C is a constant optimized during the search. The temperature effect was included through thermal vibrations using a Debye temperature converted into the isotropic root-mean-square (rms) displacements $\langle u \rangle_1$ (first layer), $\langle u \rangle_2$ (second layer), and $\langle u \rangle_b$ (bulk) (as was described in Chapter 2). These rms displacements were optimized manually by changing the Debye temperature. The bulk lattice constants used in the calculations are tabulated in Table 3.1. Since the observed LEED pattern exhibited a six-fold symmetry, indicating an averaging over the two possible bulk terminations (A and B), the calculations were performed for both terminations (A and B). The calculated intensities from A and B terminations were averaged and compared to the

experimental spectra to search a minimum *Rp* factor by using the automated search algorithm in order to obtain the determination of the surface structures [26-29]. No in-plane relaxations were considered in the calculations.

Table 3.1: Lattice constants of bulk magnesium and the interlayer distance (d_0) of the Mg(0001) surface [20] for three temperatures studied.

	T=130 K	T=300 K	T=400 K
a_o(Å)	3.1970	3.2094	3.2183
c (Å)	5.1888	5.2105	5.2254
c/a_o	1.6230	1.6235	1.6237
d_0(Å)	2.5944	2.6053	2.6127

3.1.3 Results and Discussion

The observed (1x1) LEED pattern indicates no reconstruction on the Mg(0001) surface from the temperatures T=130 K to T=400 K, as predicted by T=0 K calculations [30]. Figure 3.4 shows the comparison between the experimental and the best-fit spectra for all three temperatures studied. The agreement between the experimental data and the best-fit spectra are excellent, reflected in the Pendry *R* factor (*Rp*); at T=130 K *Rp* of 0.13, at T=300 K *Rp* of 0.11 and at T=400 K *Rp* of 0.10. The *Rp* factors at T=300 K and 400 K are quite good; however since the size of the data set are small, the error-bars at these temperatures are rather large. Table 3.2 lists the optimized values of structural parameters (the first three interlayer spacings) and non-structural parameters of the Mg(0001) surface for all three temperatures investigated. Our temperature measurements of the first interlayer relaxation are: $\Delta d_{12}/d_0 = +2.0\ (\pm 0.5)\%$ at T=130 K, $\Delta d_{12}/d_0 = +2.3\ (\pm 0.7)\%$ at T=300 K, and $\Delta d_{12}/d_0 = +2.5\ (\pm 1.1)\%$ at T=400 K.

Table 3.2: Geometric parameters extracted from the best-fit spectra to the LEED *I-V* data of Mg(0001) as a function of temperature.

Temperature	T=130 K	T=300 K	T=400 K
structural parameters:			
$\Delta d_{12}/d_o$(%)	+2.0(±0.5)	+2.3(±0.7)	+2.5(±1.1)
$\Delta d_{23}/d_o$(%)	+0.2(±0.6)	+0.1(±1.1)	+0.5(±1.4)
$\Delta d_{34}/d_o$(%)	+0.0(±0.9)	+0.1(±1.3)	+0.2(±1.5)
non-structural parameters:			
$\langle u \rangle_1$(Å)	0.195	0.285	0.327
$\langle u \rangle_2$(Å)	0.140	0.197	0.226
$\langle u \rangle_{bulk}$(Å)	0.113	0.152	0.173
V_{oi} ; C(eV)	-5.0	-5.0	-5.0
V_{or} (eV)	3.02	3.24	3.44
R_P	0.13	0.11	0.10

The relaxation in the deep layers ($\Delta d_{23}/d_0$ and $\Delta d_{34}/d_0$) are almost zero, i.e., the interlayer spacings of d_{23} and d_{34} are almost the same as in the bulk. The rms vibrational displacements at low-temperature (T=130 K) are 0.113 Å in the bulk, 0.140 Å in the second layer, and 0.195 Å in the surface (top) layer. At this temperature (T=130 K), the rms vibrational displacements in the surface layer is about 1.7 times the bulk value. The rms vibrational displacements become larger as the temperature increases. At T=400 K, the rms vibrational displacements are 0.173 Å in the bulk, 0.226 Å in the second layer, and 0.327 Å in the surface (top) layer. So the rms vibrational displacement in the surface layer at T=400 K is about 1.9 times the bulk value. It is understood why the rms vibrational displacements in the surface layer are larger than in the bulk, the reduced coordinations of atoms at the surface cause a significant softening of the phonons at the surface. The optical-potential also changes as the temperature increases, but it is not significant. To ensure that our optimized structural parameters are not at a local minimum but at a global minimum, we plot the Rp factor as a function of the first interlayer spacing for all three temperatures as shown in Figure 3.6, while the other parameters are fixed at the optimized values listed in Table 3.2.

The previous experimental study of surface structure of Mg(0001) at T=100 K (LEED I-V analysis) by Sprunger *et al.* [25] reported that $\Delta d_{12}/d_0$ = + 1.90 (±0.3)%, $\Delta d_{23}/d_0$ = + 0.8 (±0.4)%, and $\Delta d_{12}/d_0$ = - 0.4 (±0.5)%. These values are in excellent agreement with our experimental data at T=130 K, where $\Delta d_{12}/d_0$ = + 2.0 (±0.5)%, $\Delta d_{23}/d_0$ = + 0.2 (±0.7)%, and $\Delta d_{12}/d_0$ = + 0.0 (±0.9)%.

Wright *et al.* [31] performed first-principles calculations based on the local density approximation for surface structure of Mg(0001) at T=0 K. The surface relaxations were determined by calculating Hellman-Feyman forces acting on the atoms and allowing the layers to move along the forces until the magnitude of the forces became smaller than 0.01 mRy/bohr or 4×10^{-10} N. They reported that the first three interlayer spacing of Mg(0001) is

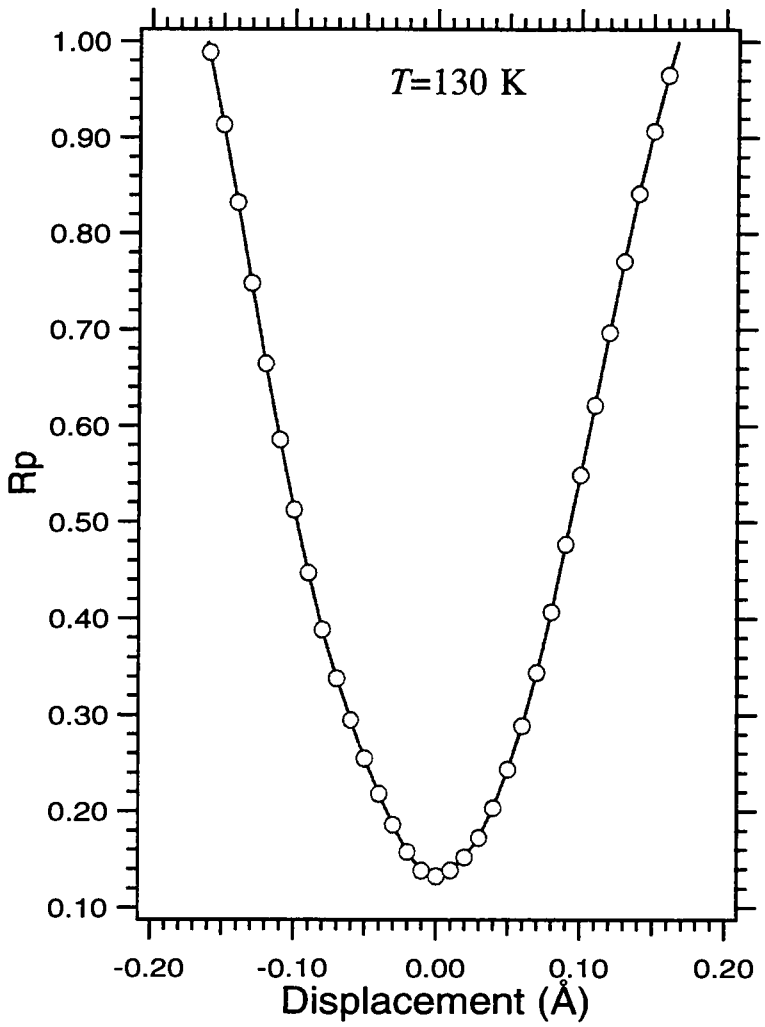


Figure 3.6: Displacement of the first interlayer spacing from the optimized value, while the other parameters are fixed at the optimized values given in Table 3.2.

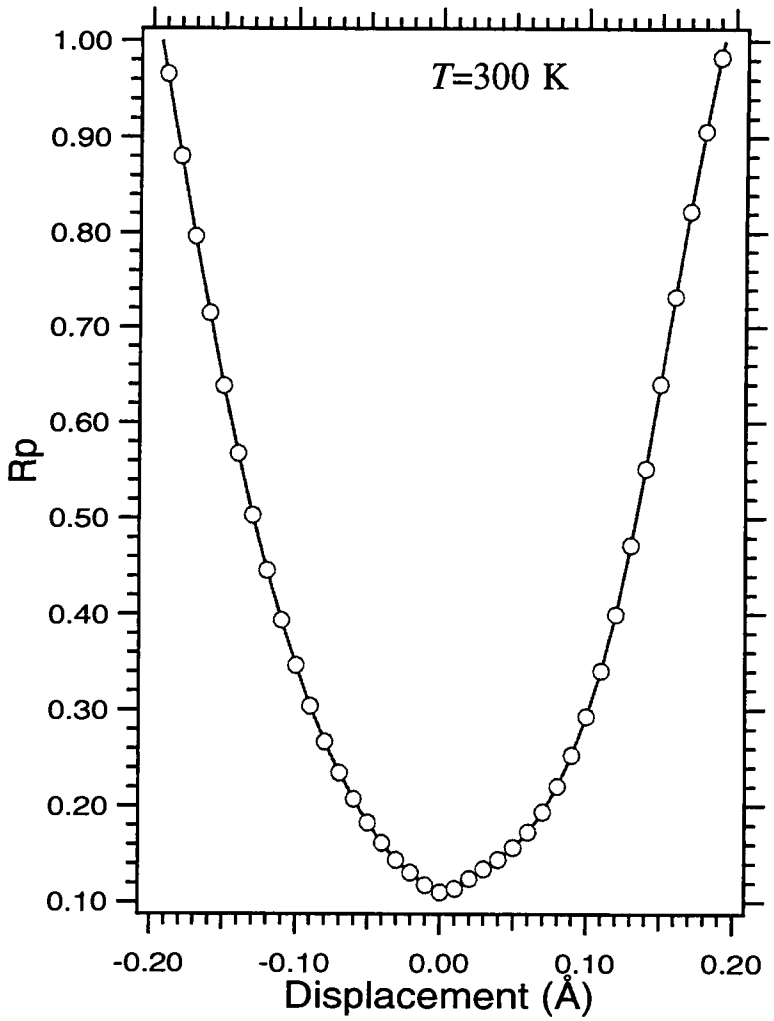


Figure 3.6: (continued)
Displacement of the first interlayer spacing from the optimized value; while the other parameters are fixed at the optimized values given in Table 3.2.

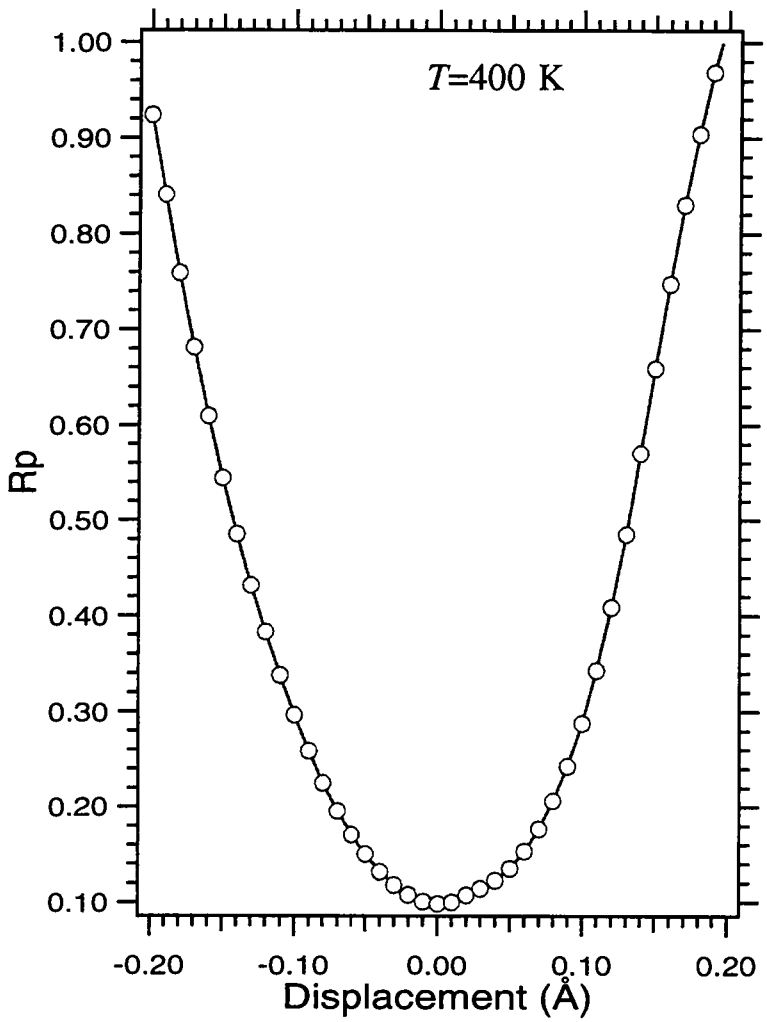


Figure 3.6: (continued)
Displacement of the first interlayer spacing from the optimized value; while the other parameters are fixed at the optimized values given in Table 3.2.

expanded with respect to the bulk by 1.5%, 0.5%, and 0.1% [31]. Similar calculations using an *ab initio* approach based on density functional theory in the local density approximation, where the interlayer relaxations were found by calculating the Hellmann-Feynman forces acting on the atoms and allowing the atomic layers to move along the forces until these forces became less than 1 *mRy/Bohr*, by Staikov and Rahman found that the first three interlayer relaxations for the Mg(0001) surface with respect to the bulk are +1.8%, +0.2%, and -0.3% [30]. Other recent *ab initio* calculations by Bungaro, where non-linear core corrections were included in the calculations, showed that interlayer relaxations for the Mg(0001) surface with respect to the bulk are +1.8(±0.3)%, +0.3(±0.3)%, and -0.5(±0.3)% [32]. Figure 3.7 shows the plot of our temperature dependent measurements of the first interlayer relaxation (filled circles) together with the previous experimental study (unfilled circle) [25], and recent theoretical studies [30-32].

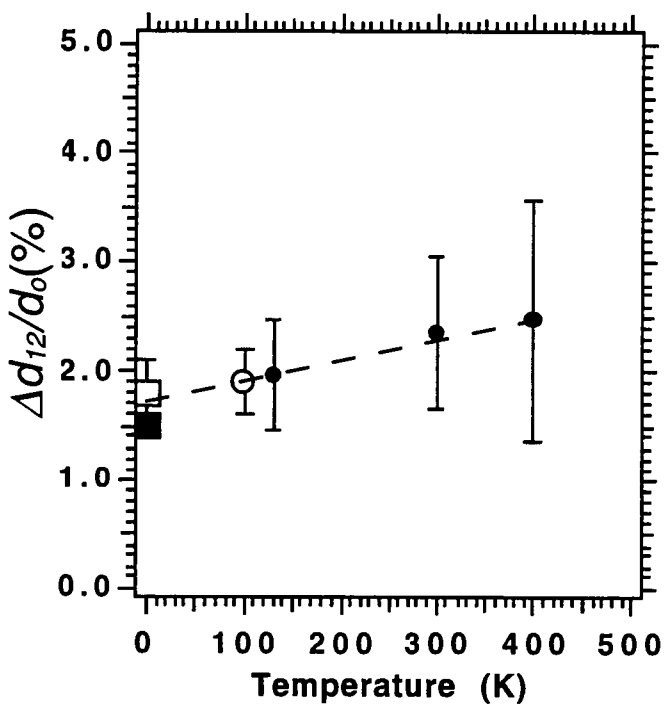


Figure 3.7: Measured (circles) interplanar relaxations as a function of temperature for Mg(0001) together with the previous the previous studies. The experimental study (unfilled circle) [ref. 25], theoretical studies at T=0 K; filled square [ref. 31] and unfilled square [ref. 30,42].

When our temperature dependent measurements of the first interlayer spacing of the Mg(0001) surface with respect to the bulk $\Delta d_{12}/d_0$ (%) are extrapolated to T= 0 K (dashed line in Figure 3.7), we find that the first interlayer spacing at zero temperature is expanded by +1.7% with respect to the bulk and it is in *excellent* agreement with the T=0 K calculations as listed in Table 3.3 below.

Table 3.3: Comparison of the first interlayer relaxation for the Mg(0001) surface between calculations and our experimental results (extrapolated to T=0 K).

	$\Delta d_{12}/d_0$ (%)
Theory (ref. 31)	+1.5
Theory (ref. 30)	+1.8
Theory (ref. 32)	+1.8
Experiment (this study)	+1.7

The small expansion in the first interlayer spacing of the Mg(0001) surface is expected since this surface is a close metal surface, where the charge smoothing effect is very small and there is charge that "spills out" into the vacuum due to the presence of the surface, which drives an expansion of the first interlayer spacing (due to the outward pressure of the conduction electrons) [33]. This behavior is similar to the case of the Al(111) surface, where the first interlayer relaxation is expanded by +1.7% [34]. The magnitude of the first interlayer relaxation of Mg(0001) is comparable to that of Al(111) but not to Be(0001). The first interlayer spacing of the Be(0001) surface is rather large, i.e., +3.1% [7]. One of possible reasons for large outward expansion of the first interlayer spacing of Be(0001) is because the Be(0001) surface is much more metallic than the bulk, due to the surface states, therefore the *c/a* ratio in the vicinity of surface would like to be

closer to the ideal isotropic value of 1.63, as suggested by Stumpf *et al.* [35]. The other possible reason is because Be is a high electron density metal, i.e., r_s = 1.87 [36]; while for Mg, r_s is equal to 2.66 [36]. Therefore, a creation of the Be(0001) surface causes more charge "spill out" into the vacuum than that of Mg(0001). Consequently, the expansion of the first interlayer spacing at the Be(0001) surface is larger than at the Mg(0001) surface.

A surface thermal expansion coefficient is defined as the following:

$$\alpha_S = \frac{1}{d_{12}}\left(\frac{\partial d_{12}}{\partial T}\right) \tag{3.5}$$

where d_{12} is the interlayer spacing in the first layer and T is the temperature. Our results show that the surface thermal expansion for the first interlayer spacing d_{12} of the Mg(0001) surface is $\alpha_s \approx +1.8 \times \alpha_B$, where $\alpha_B = 25\text{x}10^{-6}$ K^{-1} (bulk thermal expansion [36]). Unfortunately, our error-bars are rather large at higher temperatures. This is the consequence of the size of data sets because of the Debye-Waller attenuation at higher beam energies. If we consider the error bars, however, the surface thermal expansion of the Mg(0001) surface is the same as in the bulk.

Figure 3.8 shows the temperature dependent for the first two interlayer relaxations for the Mg(0001) and Be(0001) surfaces. Even if we neglect the error-bars, the surface thermal expansion in the first interlayer at the Mg(0001) surface (1.8 times bulk thermal expansion) is still significantly different than at the Be(0001) surface, i.e., the thermal expansion of Be(0001) is 6 times larger than in the bulk [7]. The surface thermal expansion in the second interlayer of the Be(0001) surface is also large in comparison to that of the Mg(0001) surface. In conclusion, the surface thermal expansion at the Mg(0001) surface is significantly different than at the Be(0001) surface. As was discussed by Kevan [37], the surface states might be expected to play an important role in understanding the unusual surface phenomena. Therefore, the unusual surface thermal expansion behavior at the

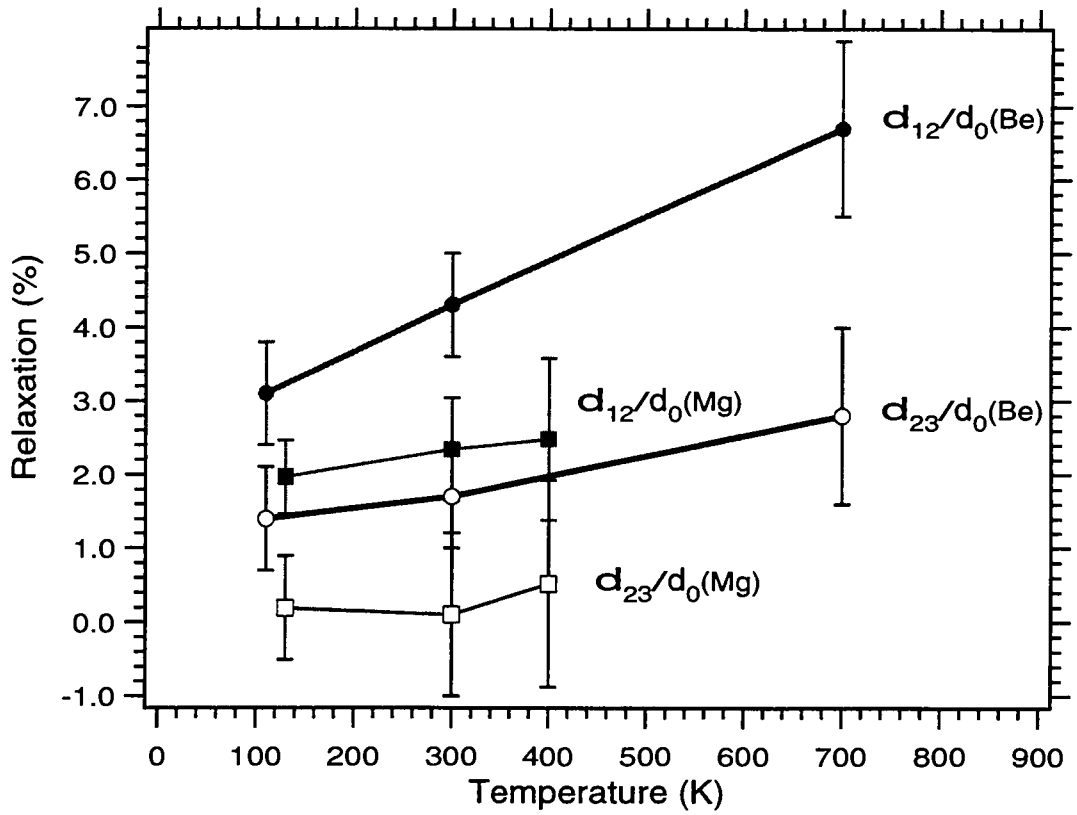


Figure 3.8: The first and second interlayer relaxations with respect to the bulk as a function of temperatures for Be(0001) [7] and Mg(0001) [this study].

Be(0001) surface might be related to the significant contribution of the surface states, i.e., the electronic properties of Be(0001) are dominated by the surface states.

No enhanced surface thermal expansion at the Mg(0001) surface can be confirm by studying the thermal expansion of the Al(111) surface. Both bulk Al and Mg are free-electron-like metals and their surface electronic properties are similar, i.e., less significant contribution of the surface states.

3.1.4 Conclusions

In summary, we have utilized electron diffraction to study the thermal effects on the surface structure of Mg(0001). The observed (1x1) LEED pattern indicated no reconstruction on the Mg(0001) surface. Our results at T=130 K are in excellent agreement with the previous experimental study [25]. When our temperature dependent data are extrapolated to T=0 K, they are in *excellent* agreement with the calculations at T=0 K. We found that the thermal expansion at the Mg(0001) surface is similar to the bulk, which is significantly different than in the case of Be(0001) [7]. Large thermal expansion at the Be(0001) surface could be due to presence of the surface states or small value of r_s in comparison to the Mg(0001) surface.

3.2 The Mg(10$\bar{1}$0) Surface

3.2.1 Introduction

The (10$\bar{1}$0) surface of hexagonal close-packed (hcp) is an open surface, having higher corrugation than the hcp(0001) surface. This hcp (10$\bar{1}$0) surface has two possible surface terminations: *short termination* and *long termination*, as illustrated in Figure 3.9. In *short termination*, the first interlayer spacing d_{12} is shorter than the second interlayer spacing d_{23} and each atom on the top surface layer is surrounded by six nearest neighbors (four atoms in the second layer and two atoms in the third layer). However, in *long*

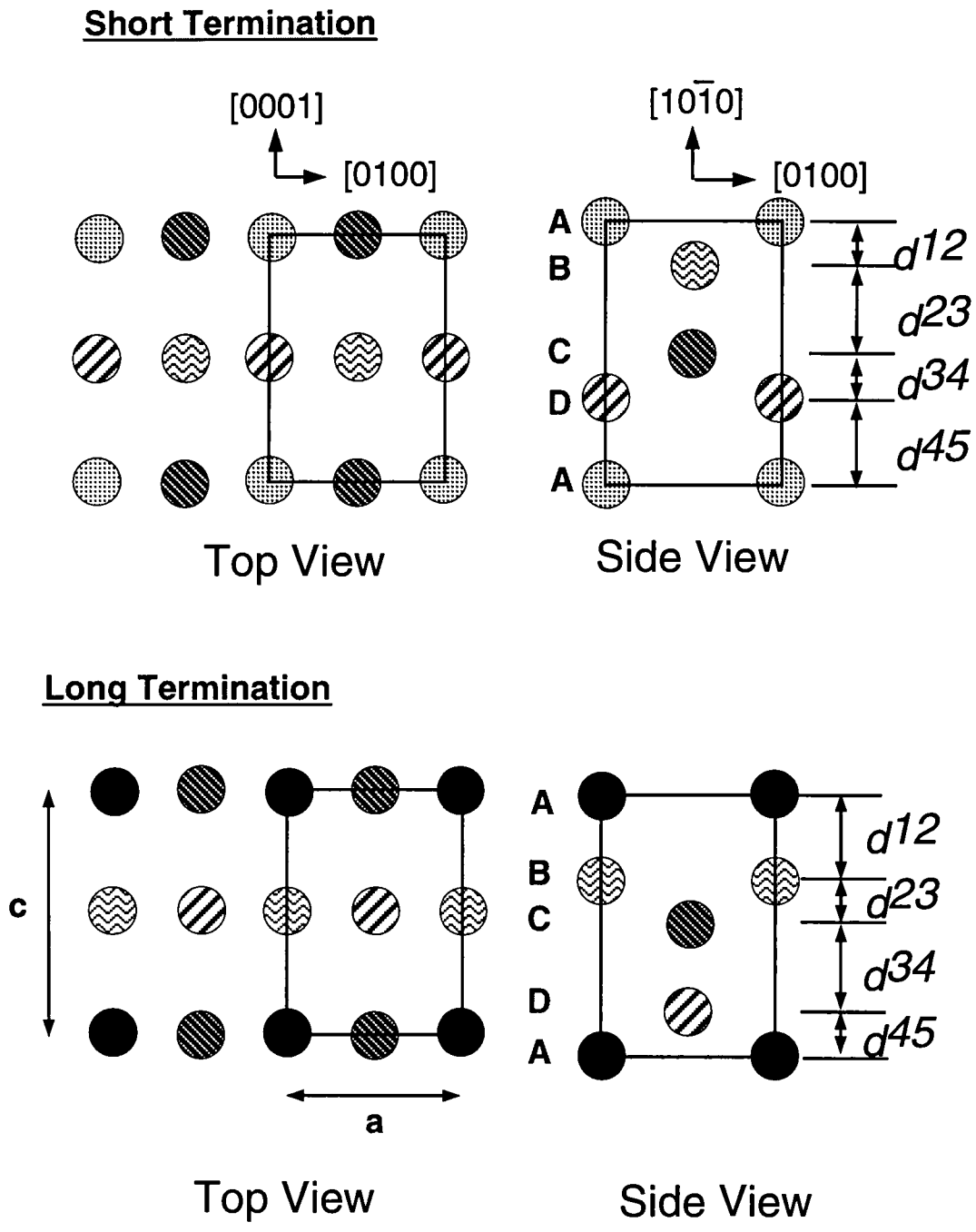


Figure 3.9: Structural model for the Mg(10$\bar{1}$0) surface; the top and side views for the long termination and short termination.

termination, the interlayer spacing d_{12} is longer than d_{23} and each atom on the top surface layer is surrounded by only four nearest neighbors (two atoms in the second layer and two atoms in the third layer). In *short termination*, the first interlayer may be thought of as a bilayer and the crystal may be thought of as a stack of such bilayers. The interlayer spacing of this surface is rather short; i.e., d_{12} is 0.923 Å and d_{23} is 1.846 Å (about 0.87 planes/Å), allowing one to observe the effects of damped oscillatory behavior into deep layers since the probing depth of LEED is about 8 - 10 Å from the top layer or surface layer.

As was discussed in Chapter 1, for open metal surfaces, in general, the first interlayer spacing is contracted, the second interlayer spacing is expanded, the third interlayer spacing is contracted, etc. The relaxation pattern is of an oscillatory character with the alternating contraction and expansion following the trend - + - + -, and the interlayer relaxations usually occur up to the fourth or fifth atomic planes. Therefore, it is very interesting to observe the temperature dependent of the interlayers.

3.2.2 Experiment and Analysis

The Mg($10\bar{1}0$) sample was cut and mechanically polished in Oak Ridge National Laboratory. The experiment was performed in an ultra high vacuum (UHV) chamber with base pressure is better than 10^{-10} Torr. The sample preparation was followed as described in Chapter 2.2. The LEED pattern (1x1) at temperatures T=120 K to 400 K was observed, indicating that there is no reconstruction at the Mg($10\bar{1}0$) surface. The photo of diffraction pattern of Mg($10\bar{1}0$) atoms observed at energy 50 eV at room-temperature is shown in Figure 3.10.

The primitive translation vectors of direct and reciprocal of the Mg($10\bar{1}0$) surface are given below:

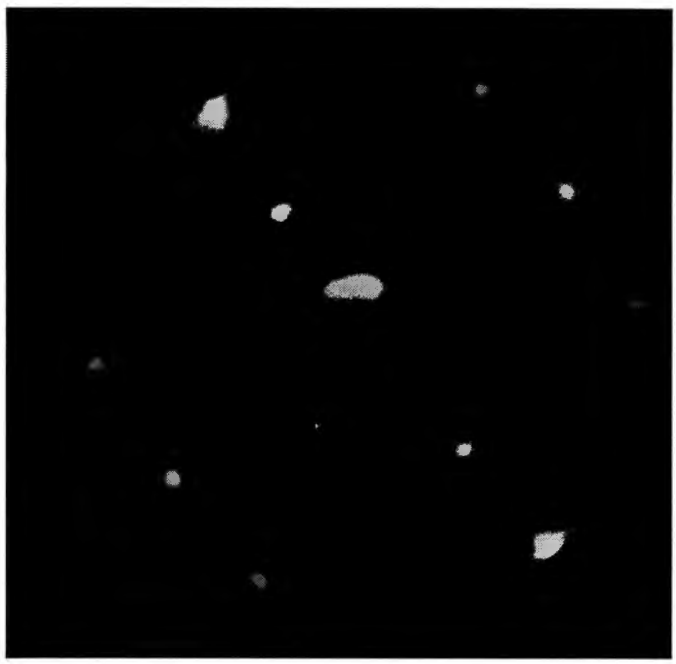


Figure 3.10: LEED pattern of Mg($10\bar{1}0$) at E=50 eV at room-temperature.

$$a_1 = a\,\hat{y} \quad ; \quad a_2 = c\,\hat{z} \tag{3.6}$$

$$b_1 = \frac{2\pi}{a}\,\hat{y} \quad ; \quad b_2 = \frac{2\pi}{c}\,\hat{z} \tag{3.7}$$

The two dimensional reciprocal lattice vectors are defined from equations (3.3) and (3.7), where h and k are integers assigned as the beams in the LEED pattern. Figure 3.11 shows the beam assignments for the LEED pattern of the Mg(10$\bar{1}$0) surface.

The intensities of the diffracted beams as a function of the incident electron energy were measured with the sample temperatures of 120 K, 300 K, and 400 K, where the procedure was described in Chapter 2. We have seven inequivalent beams {(10), (01), (11), (02), (12), (03), and (13)} with the total energy ΔE = 1600 eV at temperature T=120 K, six inequivalent beams {(10), (01), (11), (02), (12), and (03)} with the total energy ΔE = 740 eV at temperature T=300 K, and five inequivalent beams {(10), (01), (11), (02), and (12)} with the total energy ΔE = 560 eV at temperature T=400 K.

Similar to the case of Mg(0001), where the reduction of the total energy range in the data set with increasing temperature is the consequence of Debye-Waller attenuation at higher beam energies. The intensities decay exponentially with increasing temperature (T), following $I \sim I_o\, e^{-K.T}$. For the (01) beam at energy E=116.5 eV, we find K=0.0017, as shown in Figure 3.12. If this number is converted into the Debye-Waller model, we find the rms displacement of atoms $\langle u \rangle = 6.612 \times 10^{-3} \times \sqrt{T}$ Å. At T=120 K, we have the rms $\langle u \rangle$ = 0.073 Å that is smaller than the value from the LEED I-V calculations. The accuracy is rather low because the value of rms deduced from the intensities ratio depends upon the beam and energy. Figure 3.12 shows that the Mg(0001) surface is rather softer than the Mg(10$\bar{1}$0) surface, which might be related to the stacking sequence.

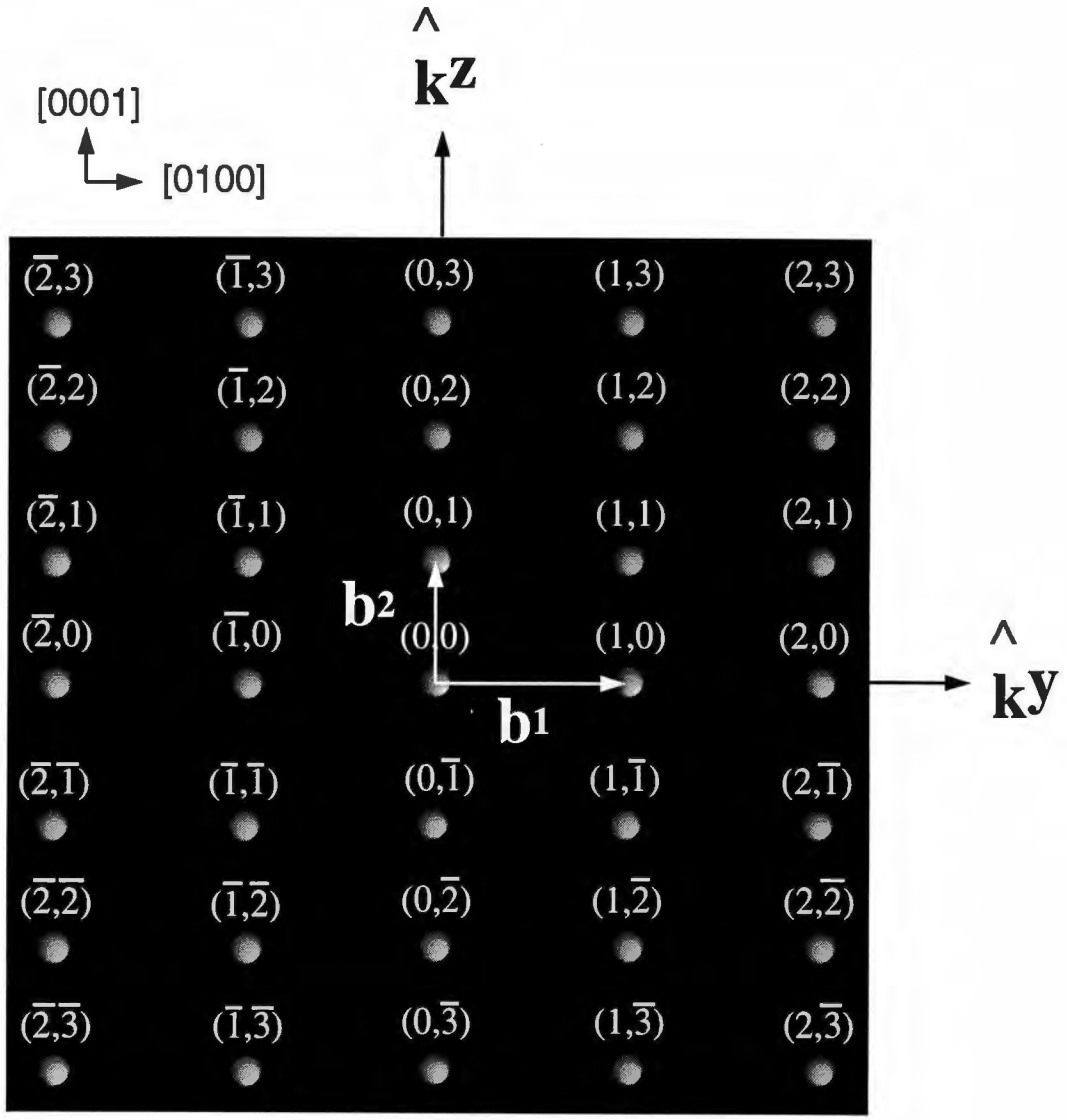


Figure 3.11: Reciprocal vectors and beams assignment for the Mg(10$\bar{1}$0) surface.

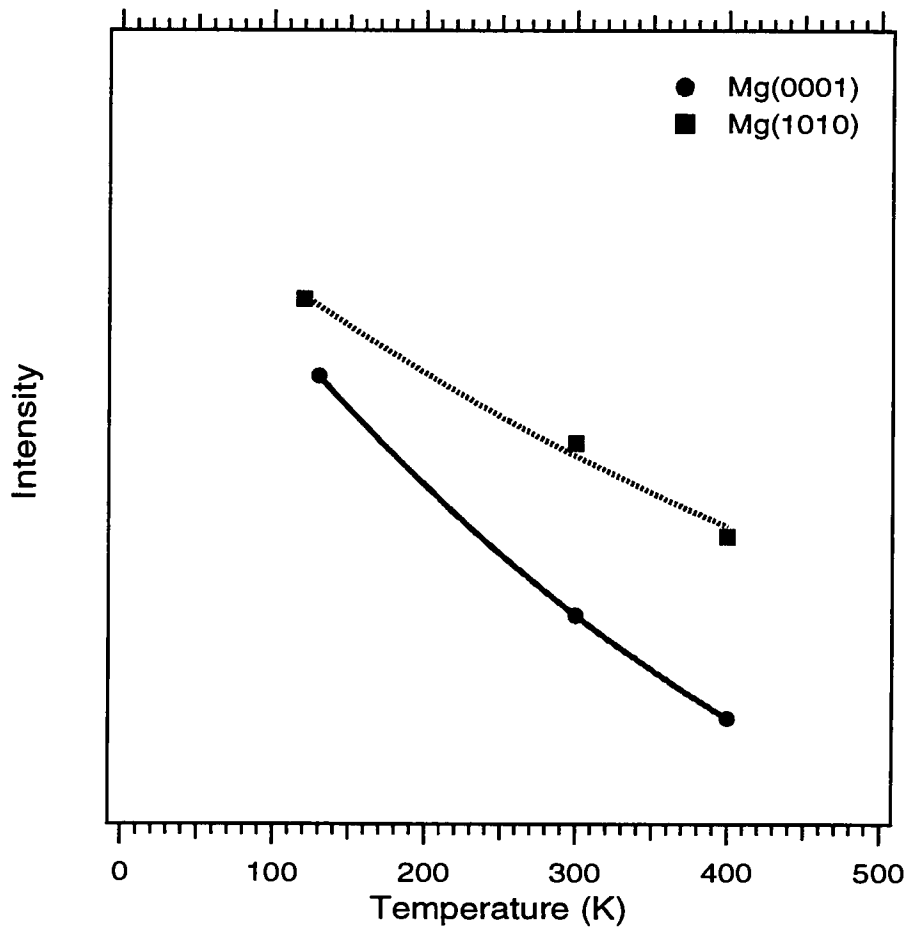


Figure 3.12: The intensities of the (01) beams at E=111 eV for the Mg(0001) surface (filled circles) and at E=116.5 eV for the Mg(10$\bar{1}$0) surface (filled squares) as a function of temperature together with the fit by exponential functions (solid and dashed lines).

The analysis of LEED *I-V* spectra is the same as mentioned in section 3.1, except a composite layer was introduced for short interlayer spacings (less than 1 Å) in order to avoid the divergence in the calculations. In order to see the effect of damped oscillatory relaxations, we performed the LEED *I-V* calculations for several models, called model I - VI, i.e., we varied only the first layer in model I, the first and second layers in model II, the first, second, and third layers in model III, etc. There was no in-plane relaxation considered in the calculations. The bulk lattice constants used in the calculations are tabulated in Table 3.1.

3.2.3 Results and Discussion

An ideal Mg(10$\bar{1}$0) surface has a stacking consequence of ABCDABCD. For short termination, AB and CD are the *short* interlayer spacing; while BC and DA are the longer one. However, for long termination, AB and CD are the *long* interlayer spacing; while BC and DA are the shorter one, see Figure 3.9. Both terminations have a two-fold symmetry and produce the same (1x1) LEED pattern. Our observed (1x1) LEED pattern indicates no reconstruction on the Mg(10$\bar{1}$0) surface from temperatures T=120 K to T=400 K, as shown in Figure 3.10, which is in agreement with the other previous studies of the hcp(10$\bar{1}$0) surfaces (Re [38], Ti [39], Co [40,41], and Be [42]), even though calculations predicted a possibility of the reconstruction on the Mg(10$\bar{1}$0) surface [30].

We performed the LEED *I-V* calculations for both terminations of an ideal Mg(10$\bar{1}$0) surface. Our results show that the preferred termination is the short termination for all three temperatures studied, reflected in the Pendry *Rp* factors. For long termination (model VI): *Rp*(120 K)=0.34, *Rp*(300 K)=0.31, and *Rp*(400 K)=0.37. However, for short termination (model VI): *Rp*(120 K)=0.15, *Rp*(300 K)=0.14, and *Rp*(400 K)=0.16. The mixture between long termination and short termination domains does not improve the

Rp factor. Our results are in agreement with all the previous studies of hcp($10\bar{1}0$) surfaces [38-42], showing that the surface terminates with *short termination*. It can be understood why the hcp($10\bar{1}0$) surface is terminated by short termination. To create a long termination domain, the first layer atom will lose six nearest neighbor atoms. However, to create a short termination domain, the first layer atom will lose only four nearest neighbor atoms. This one of the reasons why the hcp($10\bar{1}0$) surface is terminated by short termination. Another reason is the kinetic energy of electrons of short termination is lower than that of long termination, because for the short termination, the corrugation is smaller and the electronic wave functions are smoother. The comparison between our structure of Mg($10\bar{1}0$) at T=120 K (model VI) and the previous structural studies of the hcp($10\bar{1}0$) surfaces [38-42] is listed in Table 3.4.

Table 3.4: Comparison between the structure of Mg($10\bar{1}0$) at T=120 K and the previous structural studies of hcp($10\bar{1}0$).

Elements	Termination	Δd_{12}(%)	Δd_{12}(%)	Δd_{12}(%)	Δd_{12}(%)
Re(Ref. 38)	Short	-17	---	---	---
Co(Ref. 41)	Short	-6.5	+1.0	---	---
Co(Ref. 40)	Short	-12.8	+0.8	---	---
Ti(Ref. 39)	Short	-6	---	---	---
Be(Ref. 42)	Short	-25	+5	-11	+2
Mg(this study)	Short	-16.4	+7.8	-10.5	+3.8

All of the previous and recent structural studies of hcp(10$\bar{1}$0) have a contraction in the first interlayer spacing, as suggested by Finis - Heine's model based on the Smoluchowski charge smoothing mechanism [43-44]. The second interlayer spacing is expanded for all cases, except for Re and Ti since the second interlayer spacing was fixed at bulk position in the calculations. The third interlayer spacing for Mg(10$\bar{1}$0) was contracted. and this behavior is in agreement with Be. However, for the other surfaces (Re, Co, and Ti), the third interlayer spacing was fixed at bulk position in the calculations. Both Mg and Be showed clearly that the relaxation pattern is of an oscillatory character with the alternating contraction and expansion following the trend - + - + - + that might be a general rule for the hcp(10$\bar{1}$0) surfaces.

The measured and calculated relaxations of *simple metal* surfaces is shown in Figure 3.13. The agreement between the experimental data and the calculations is very good. The change in the first interlayer spacing from the bulk truncated (Δd_{12}) has a linear function of the inverse area per unit cell (normalized to the volume per bulk atom), as shown in Figure 3.13(a). For a close surface metal, the first interlayer spacing is expanded; while for an open surface metal the first interlayer spacing is contracted. The first interlayer spacing (d_{12}) of the Mg(10$\bar{1}$0) surface is "normal" as expected for a simple metal surface. Figure 3.13(b) shows the plot between the change in interlayer spacing of the second and third layers (Δd_{23}) as a function of the inverse area per unit cell for simple metals. It shows that the relationship between the change in the interlayer spacing of the second and third layers (Δd_{23}) and the inverse area per unit cell is also linear, but it is the opposite sign from the trend of the change in first interlayer spacing (Δd_{12}). For a close surface metal, the interlayer spacing of the second and the third layers (d_{23}) is almost the same as in the bulk. But for an open surface metal, the interlayer spacing of the second and the third layers (d_{23}) is expanded. Figure 3.13(c) shows the relationship between the change in the interlayer

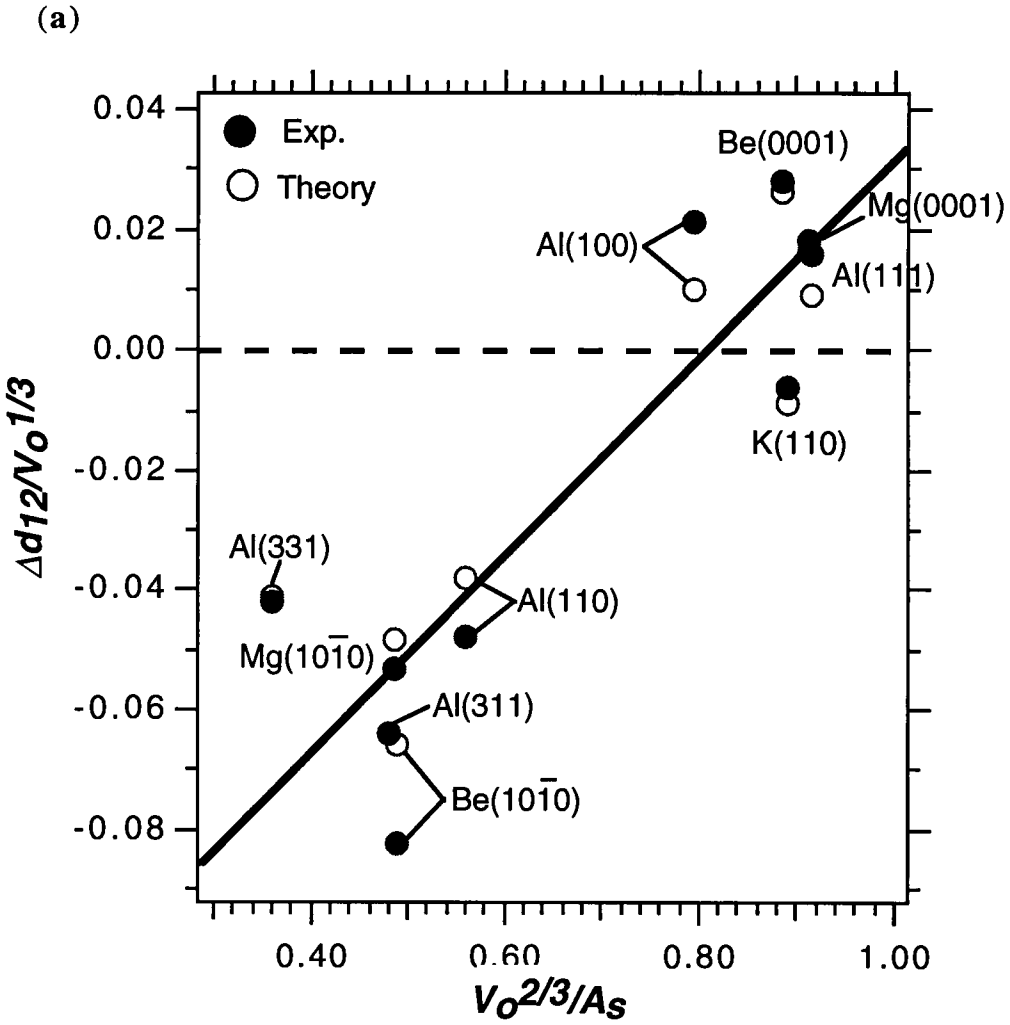


Figure 3.13: Measured and calculated relaxations of simple metal surfaces. Solid line is a linear fit of the data. The references for the points are: Be(0001) [ref. 7], Mg(0001) th. [ref. 32], exp. [this study], Al(111) th. [ref. 49], exp. [ref. 34], K(110) th. [ref. 50], exp. [ref. 51], Al(100) th. [ref. 52], exp. [ref. 53], Al(110) th. [ref. 45], exp. [ref. 54], Be(10$\bar{1}$0) [ref. 42], Mg(10$\bar{1}$0) th. [ref. 47], exp. [this work], Al(331) th. [ref. 55], exp. [ref. 56], and Al(311) [ref. 57].

(b)

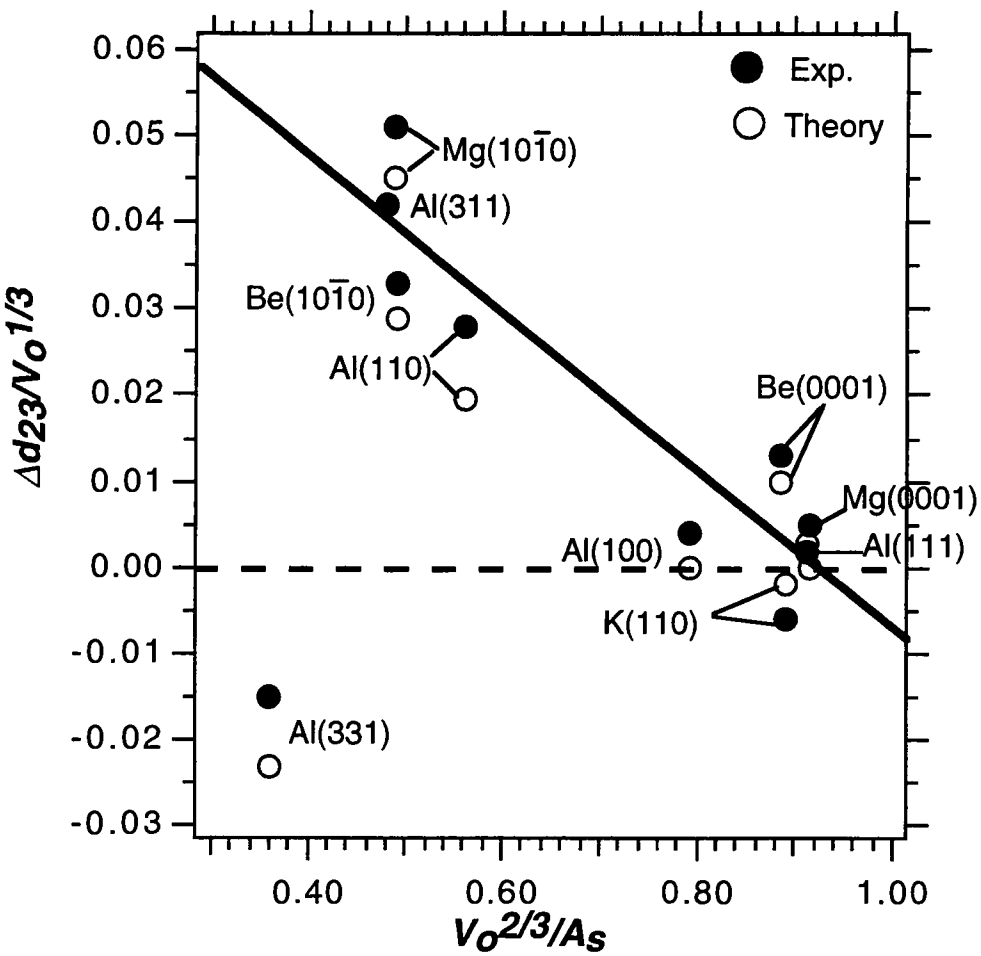


Figure 3.13: (continued)
Measured and calculated relaxations of simple metal surfaces. Solid line is a linear fit of the data, where the data of Al(331) are excluded. The references for the points are: Be(0001) [ref. 7], Mg(0001) th. [ref. 32], exp. [this study], Al(111) th. [ref. 49], exp. [ref. 34], K(110) th. [ref. 50], exp. [ref. 51], Al(100) th. [ref. 52], exp. [ref. 53], Al(110) th. [ref. 45], exp. [ref. 54], Be(10$\bar{1}$0) [ref. 42], Mg(10$\bar{1}$0) th. [ref. 47], exp. [this work], Al(331) th. [ref. 55], exp. [ref. 56], and Al(311) [ref. 57].

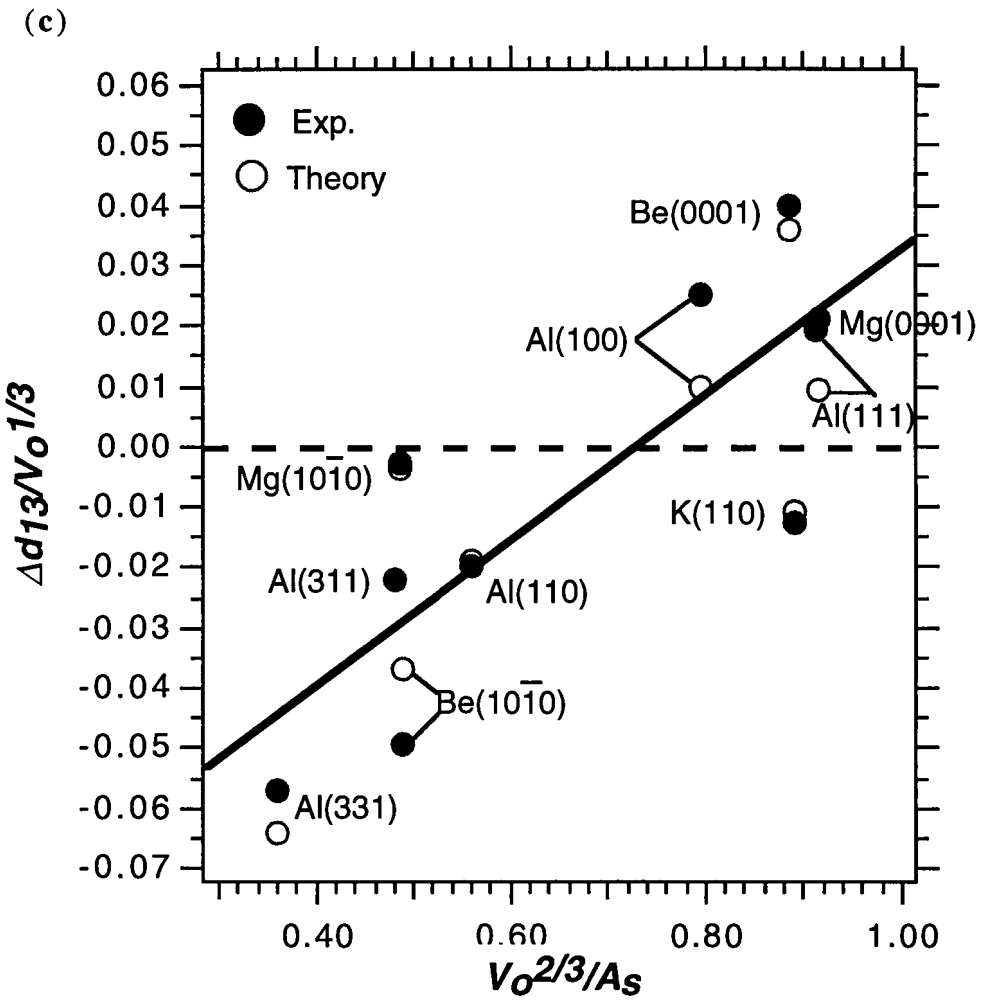


Figure 3.13: (continued)
Measured and calculated relaxations of simple metal surfaces. Solid line is a linear fit of the data. The references for the points are: Be(0001) [ref. 7], Mg(0001) th. [ref. 32], exp. [this study], Al(111) th. [ref. 49], exp. [ref. 34], K(110) th. [ref. 50], exp. [ref. 51], Al(100) th. [ref. 52], exp. [ref. 53], Al(110) th. [ref. 45], exp. [ref. 54], Be(10$\bar{1}$0) [ref. 42], Mg(10$\bar{1}$0) th. [ref. 47], exp. [this work], Al(331) th. [ref. 55], exp. [ref. 56], and Al(311) [ref. 57].

spacing of the first and third layers (Δd_{13}) and the inverse area per unit cell for simple metals. Its trend is similar to the trend of Δd_{12}, i.e., the interlayer spacing of the first and third layers is expanded for open surface simple metals, while the interlayer spacing of the first and third layers is contracted for a close surface. Figures 3.13(a) - (c) shows a very interesting feature of surface relaxations at simple metal surfaces, where *the relaxations at a metal surface might be controlled to a desired value* by engineering a certain material. For example, if we would like to have the first interlayer as in the bulk, i.e., Δd_{12}=0, then we need to engineer a certain face of a simple metal such that the value of $V_0^{2/3}/A_s$ is equal to about 0.8, where V_0 is the volume of bulk unit cell per atom and A_s is the area of surface unit cell. Similarly, if we would like to have the spacing of the first and third layers the same as in the bulk, i.e., Δd_{13}=0, then we need to engineer a certain face of a simple metal such that the values of $V_0^{2/3}/A_s$ are about 0.72 and so on.

The geometric parameters extracted from the best-fit to the LEED *I-V* data of the Mg(10$\bar{1}$0) surface for model I (vary only the first top layer in the calculations, but the other are fixed at bulk positions) are tabulated in Table 3.5. The first interlayer spacings for all temperature studied are contracted with respect to the bulk; $\Delta d_{12}/d_0$=-7.3% at T=120 K, $\Delta d_{12}/d_0$=-13.1% at T=300 K, and $\Delta d_{12}/d_0$=-20.3% at T=400 K. It is very surprising that the interlayer spacings become shorter as the temperature increases, leading to *thermal contraction* at the Mg(10$\bar{1}$0) surface. The surface thermal expansion in the first interlayer is about -12 times the bulk, i.e., $\alpha_{ij}=\Delta d_{ij}(T)/\Delta T \cdot d_{ij}) \times \alpha_B$, where $\alpha_B \approx 25\times10^{-6}$ K^{-1} (bulk thermal expansion of Mg). However, the *Rp* factors of this model are rather high, i.e., *Rp*(120 K)=0.382, *Rp*(300 K)=0.291, and *Rp*(400 K)=0.283. Consequently, this model must be rejected immediately, leading us to model II. The geometric parameters extracted from the best-fit for model II are tabulated in the Table 3.6. In this model, again the first interlayer spacing for all temperatures are contracted with respect to the bulk and they

Table 3.5: Geometric parameters extracted from the best-fit spectra to the LEED *I-V* data of model I (only one layer was varied in the calculations) for Mg(10$\bar{1}$0) as a function of temperature.

Temperature	120 K	300 K	400 K
$\Delta d_{12}/d_{12}^{bul}(\%)$	-7.3	-13.1	-20.3
$\Delta d_{23}/d_{23}^{bulk}(\%)$	+0.0	+0.0	+0.0
$\Delta d_{34}/d_{12}^{bulk}(\%)$	+0.0	+0.0	+0.0
$\Delta d_{45}/d_{23}^{bulk}(\%)$	+0.0	+0.0	+0.0
$\Delta d_{56}/d_{12}^{bulk}(\%)$	+0.0	+0.0	+0.0
$\Delta d_{67}/d_{23}^{bulk}(\%)$	+0.0	+0.0	+0.0
Bulk parameters:			
d_{12}^{bulk}(Å)	0.9229	0.9265	0.9290
d_{23}^{bulk}(Å)	1.8458	1.8529	1.8580
LEED non-structural parameters:			
$\langle u \rangle_1$(Å)	0.167	0.248	0.304
$\langle u \rangle_2$(Å)	0.139	0.193	0.232
$\langle u \rangle_{bulk}$(Å)	0.104	0.147	0.173
V_{oi} ; C(eV)	-3.0	-3.0	-3.0
V_{or} (eV)	5.00	6.74	7.16
R_P	0.382	0.291	0.283

Table 3.6: Geometric parameters extracted from the best-fit spectra to the LEED *I-V* data of mode II (only two layers were varied in the calculations) for Mg(10$\bar{1}$0) as a function of temperature.

Temperature	120 K	300 K	400 K
$\Delta d_{12}/d_{12}^{bul}(\%)$	-15.5	-18.6	-19.9
$\Delta d_{23}/d_{23}^{bulk}(\%)$	+6.1	+6.0	+5.8
$\Delta d_{34}/d_{12}^{bulk}(\%)$	+0.0	+0.0	+0.0
$\Delta d_{45}/d_{23}^{bulk}(\%)$	+0.0	+0.0	+0.0
$\Delta d_{56}/d_{12}^{bulk}(\%)$	+0.0	+0.0	+0.0
$\Delta d_{67}/d_{23}^{bulk}(\%)$	+0.0	+0.0	+0.0
Bulk parameters:			
d_{12}^{bulk}(Å)	0.9229	0.9265	0.9290
d_{23}^{bulk}(Å)	1.8458	1.8529	1.8580
LEED non-structural parameters:			
$\langle u \rangle_1$(Å)	0.167	0.256	0.285
$\langle u \rangle_2$(Å)	0.139	0.193	0.232
$\langle u \rangle_{bulk}$(Å)	0.104	0.147	0.173
V_{oi} ; C(eV)	-3.0	-3.0	-3.0
V_{or} (eV)	4.07	3.24	3.44
R_P	0.250	0.192	0.184

become shorter as the temperature increases, i.e., *thermal contraction.* The thermal expansion in the first interlayer is about -6.6 times the bulk for this model. The second interlayer spacing is expanded for all temperatures, where the thermal expansion is almost the same as in the bulk. The *Rp* factors for this model are still high, especially at T=120 K. For model III, the geometric parameters extracted from the best-fit spectra are tabulated in Table 3.7. The first interlayer spacings for all temperatures are contracted with respect to the bulk, and they become shorter as the temperature increases, with the thermal expansion coefficient in the first interlayer of about -6.3 times the bulk, which is similar to model II. However, in this model, the second interlayer spacings are expanded for all temperature with the thermal expansion of +2.3 times the bulk. It is really surprising that the third interlayer spacings become shorter as the temperature increases! The thermal expansion coefficient in the third interlayer is about -6.0 times the bulk, the same as the thermal expansion coefficient in the first interlayer. The *Rp* factors for this model are already acceptable, even though the *Rp* factor at T=120 K is still a bit high, i.e., *Rp*(120 K)=0.195, *Rp*(300 K)=0.174, and *Rp*(400 K)=0.178.

We go on to model IV in order to see what happens in the fourth interlayer where the geometric parameters extracted from the best-fit spectra are tabulated in Table 3.8. For this model, the first interlayer spacings for all temperatures are contracted with respect to the bulk and they become shorter as the temperature increases with thermal expansion coefficient in the first interlayer of about -6.6 times the bulk, which is similar to models II and III. The second interlayers are expanded for all temperatures with the thermal expansion of +4.6 times the bulk, which is larger than that of models II and III. In the third interlayer, the thermal expansion coefficient is about -6.8 times the bulk, which is almost the same as that of model III. The thermal expansion coefficient in the fourth layer is +2.4 greater than in the bulk. The *Rp* factors for this model are already acceptable for all temperatures, i.e., *Rp*(120 K)=0.170, *Rp*(300 K)=0.150, and *Rp*(400 K)=0.170. We

Table 3.7: Geometric parameters extracted from the best-fit spectra to the LEED *I-V* data of model III (only three layers were varied in the calculations) for Mg($10\bar{1}0$) as a function of temperature.

Temperature	120 K	300 K	400 K
$\Delta d_{12}/d_{12}^{bul}(\%)$	-16.9	-19.9	-21.1
$\Delta d_{23}/d_{23}^{bulk}(\%)$	+7.5	+8.5	+8.5
$\Delta d_{34}/d_{12}^{bulk}(\%)$	-8.7	-11.6	-13.3
$\Delta d_{45}/d_{23}^{bulk}(\%)$	+0.0	+0.0	+0.0
$\Delta d_{56}/d_{12}^{bulk}(\%)$	+0.0	+0.0	+0.0
$\Delta d_{67}/d_{23}^{bulk}(\%)$	+0.0	+0.0	+0.0
Bulk parameters:			
d_{12}^{bulk}(Å)	0.9229	0.9265	0.9290
d_{23}^{bulk}(Å)	1.8458	1.8529	1.8580
LEED non-structural parameters:			
$\langle u \rangle_1$(Å)	0.167	0.248	0.285
$\langle u \rangle_2$(Å)	0.137	0.193	0.232
$\langle u \rangle_{bulk}$(Å)	0.104	0.147	0.187
V_{oi} ; C(eV)	-3.0	-3.0	-3.0
V_{or} (eV)	6.30	4.09	6.86
R_P	0.195	0.174	0.178

Table 3.8: Geometric parameters extracted from the best-fit spectra to the LEED *I-V* data of model IV (four layers were varied in the calculations) for Mg(10$\bar{1}$0) as a function of temperature.

Temperature	120 K	300 K	400 K
$\Delta d_{12}/d_{12}^{bul}(\%)$	-15.9	-20.2	-20.3
$\Delta d_{23}/d_{23}^{bulk}(\%)$	+7.5	+9.2	+10.2
$\Delta d_{34}/d_{12}^{bulk}(\%)$	-9.4	-14.0	-14.3
$\Delta d_{45}/d_{23}^{bulk}(\%)$	+2.1	+3.9	+3.1
$\Delta d_{56}/d_{12}^{bulk}(\%)$	+0.0	+0.0	+0.0
$\Delta d_{67}/d_{23}^{bulk}(\%)$	+0.0	+0.0	+0.0
Bulk parameters:			
d_{12}^{bulk} (Å)	0.9229	0.9265	0.9290
d_{23}^{bulk} (Å)	1.8458	1.8529	1.8580
LEED non-structural parameters:			
$<u>_1$ (Å)	0.1668	0.2328	0.2590
$<u>_2$ (Å)	0.1397	0.2023	0.2316
$<u>_{bulk}$ (Å)	0.1073	0.1467	0.2256
V_{oi} ; C(eV)	-3.0	-3.0	-3.0
V_{or} (eV)	5.00	5.11	4.10
R_P	0.170	0.150	0.170

continue to models V and VI in order to see the thermal expansion behavior in deep layers. For these models, the geometric parameters extracted from the best-fit spectra are tabulated in Tables 3.9 and 3.10, respectively. For model V, we find that the thermal expansion coefficient in the first interlayer is about -6.6 times the bulk, which is similar to models II to IV. The second interlayers are expanded for all temperatures with the thermal expansion +4.7 larger than in the bulk, which is the same as that of model IV. However, in the third interlayer, the thermal expansion coefficient becomes about -8.7 times the bulk. The thermal expansion coefficient in the fourth and fifth layers are +1.4 and -3.3 times the bulk. While for model VI, the thermal expansion coefficient in the first interlayer is about -7.0 times the bulk, which is similar to models II to V. The second interlayers are expanded for all temperatures with the thermal expansion +5.0 larger than in the bulk, which is the same as that of models IV and V. The thermal expansion coefficient in the third interlayer is about -10.0 times the bulk. The thermal expansion coefficient in the fourth layer is +2.0 times the bulk. In the fifth and sixth layers, the thermal expansion are -1.0 and +3.0 times the bulk. The magnitude of surface relaxations for models V and VI are actually the same, i.e., in the experimental error-bars, as shown in Table 3.10. The comparison between the measured and calculated spectra for the optimized parameters for model VI is shown in Figure 3.14. The non-structural parameters were optimized in the calculations for all models (models I-VI) for all three temperatures studied. However, they are not very sensitive to models. The values of *Rp* factors for all models for three temperatures studied are listed in Table 3.11; while the coefficient of surface thermal expansion of Mg($10\bar{1}0$) with respect to the bulk for all models are listed in Tables 3.12. Figure 3.15 shows the plot of surface relaxations versus the normal distance from the surface toward the bulk for models I-VI at T=120 K. These clearly tell us that *the oscillatory relaxations can be observed if sufficient layers are varied in the calculations.*

Table 3.9: Geometric parameters extracted from the best-fit spectra to the LEED *I-V* data of model V (five layers were varied in the calculations) for Mg(10$\bar{1}$0) as a function of temperature.

Temperature	120 K	300 K	400 K
$\Delta d_{12}/d_{12}^{bul}(\%)$	-16.1	-21.1	-20.5
$\Delta d_{23}/d_{23}^{bulk}(\%)$	+7.8	+9.2	+10.6
$\Delta d_{34}/d_{12}^{bulk}(\%)$	-10.8	-16.2	-16.8
$\Delta d_{45}/d_{23}^{bulk}(\%)$	+3.7	+4.6	+4.0
$\Delta d_{56}/d_{12}^{bulk}(\%)$	-5.2	-10.5	-5.2
$\Delta d_{67}/d_{23}^{bulk}(\%)$	+0.0	+0.0	+0.0
Bulk parameters:			
d_{12}^{bulk}(Å)	0.9229	0.9265	0.9290
d_{23}^{bulk}(Å)	1.8458	1.8529	1.8580
LEED non-structural parameters:			
$<u>_1$(Å)	0.167	0.240	0.259
$<u>_2$(Å)	0.139	0.197	0.232
$<u>_{bulk}$(Å)	0.108	0.147	0.227
V_{oi} ; C(eV)	-3.0	-3.0	-3.0
V_{or} (eV)	5.25	5.99	4.88
R_P	0.155	0.147	0.168

Table 3.10: Geometric parameters extracted from the best-fit spectra to the LEED *I-V* data of model VI (six layers were varied in the calculations) for Mg(10$\bar{1}$0) as a function of temperature.

Temperature	120 K	300 K	400 K
$\Delta d_{12}/d_{12}^{bul}(\%)$	-16.4(±2.0)	-21.1(±2.0)	-20.6(±2.7)
$\Delta d_{23}/d_{23}^{bulk}(\%)$	+7.8(±1.0)	+9.4(±1.4)	+10.6(±1.6)
$\Delta d_{34}/d_{12}^{bulk}(\%)$	-10.5(±3.0)	-15.3(±3.0)	-17.5(±4.0)
$\Delta d_{45}/d_{23}^{bulk}(\%)$	+3.8(±1.6)	+4.9(±2.0)	+4.3(±2.0)
$\Delta d_{56}/d_{12}^{bulk}(\%)$	-5.5(±3.0)	-12.1(±4.0)	-6.9(±5.0)
$\Delta d_{67}/d_{23}^{bulk}(\%)$	+0.6(±2.0)	+2.9(±2.5)	+2.0(±3.5)
Bulk parameters:			
d_{12}^{bulk} (Å)	0.9229	0.9265	0.9290
d_{23}^{bulk} (Å)	1.8458	1.8529	1.8580
LEED non-structural parameters:			
$\langle u \rangle_1$ (Å)	0.167	0.233	0.259
$\langle u \rangle_2$ (Å)	0.139	0.202	0.232
$\langle u \rangle_{bulk}$ (Å)	0.108	0.147	0.226
V_{oi} ; C(eV)	-3.0	-3.0	-3.0
V_{or} (eV)	5.25	5.25	5.17
R_P	0.150	0.140	0.160

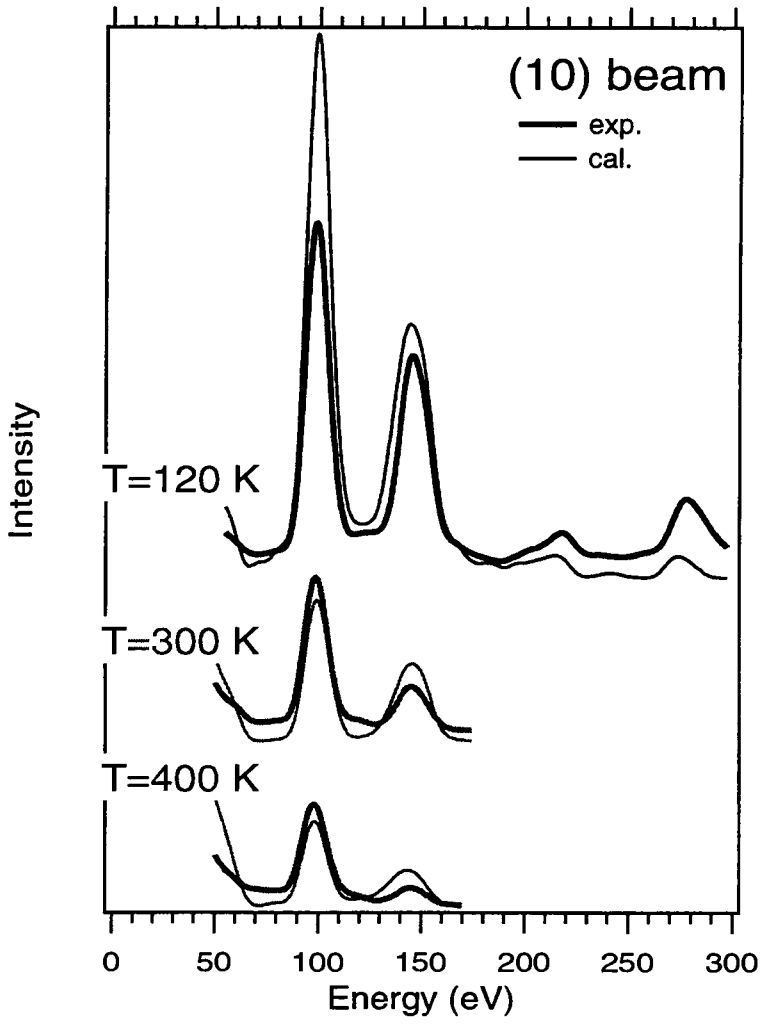


Figure 3.14: Measured and calculated LEED *I-V* spectra for the optimized structures of Mg(10$\bar{1}$0) at temperatures *T*=120 K, 300 K, and 400 K.

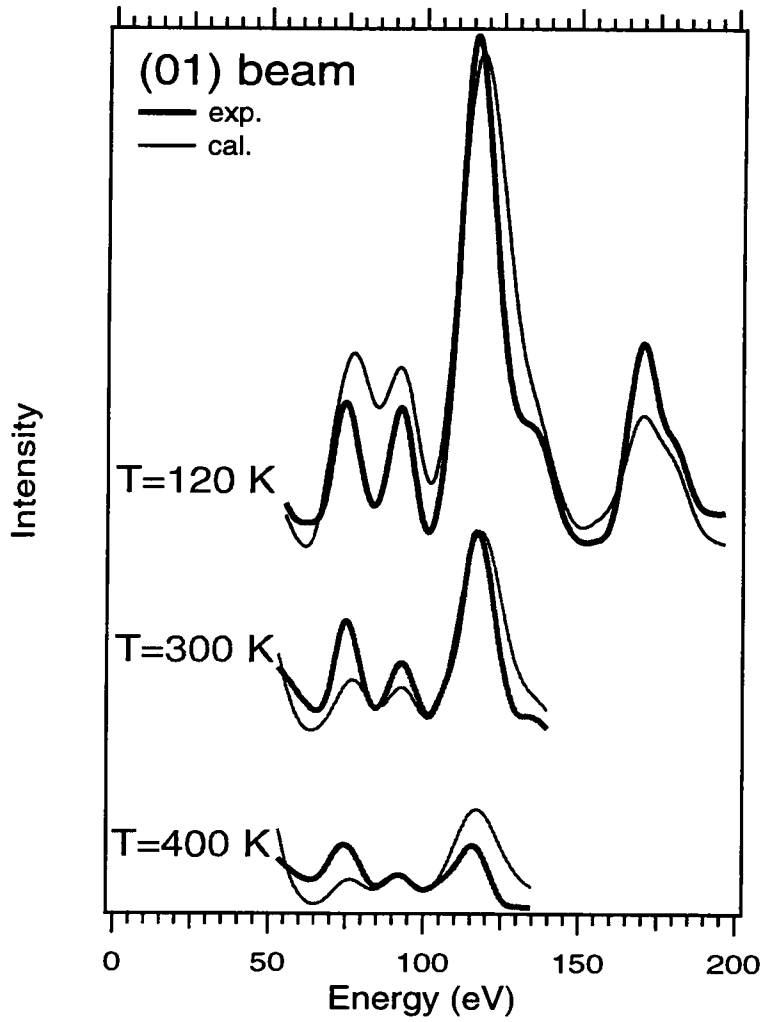


Figure 3.14: (continued)
Measured and calculated LEED *I-V* spectra for the optimized structures of Mg(10$\bar{1}$0) at temperatures *T*=120 K, 300 K, and 400 K.

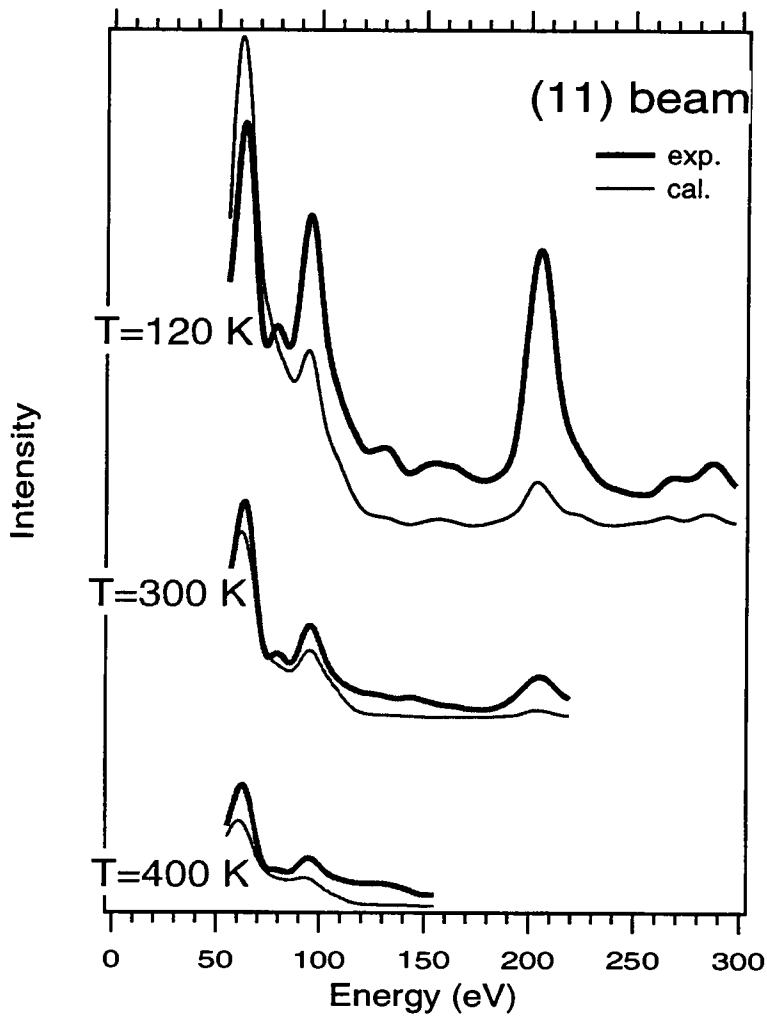


Figure 3.14: (continued)
Measured and calculated LEED *I-V* spectra for the optimized structures of Mg(10$\bar{1}$0) at temperatures *T*=120 K, 300 K, and 400 K.

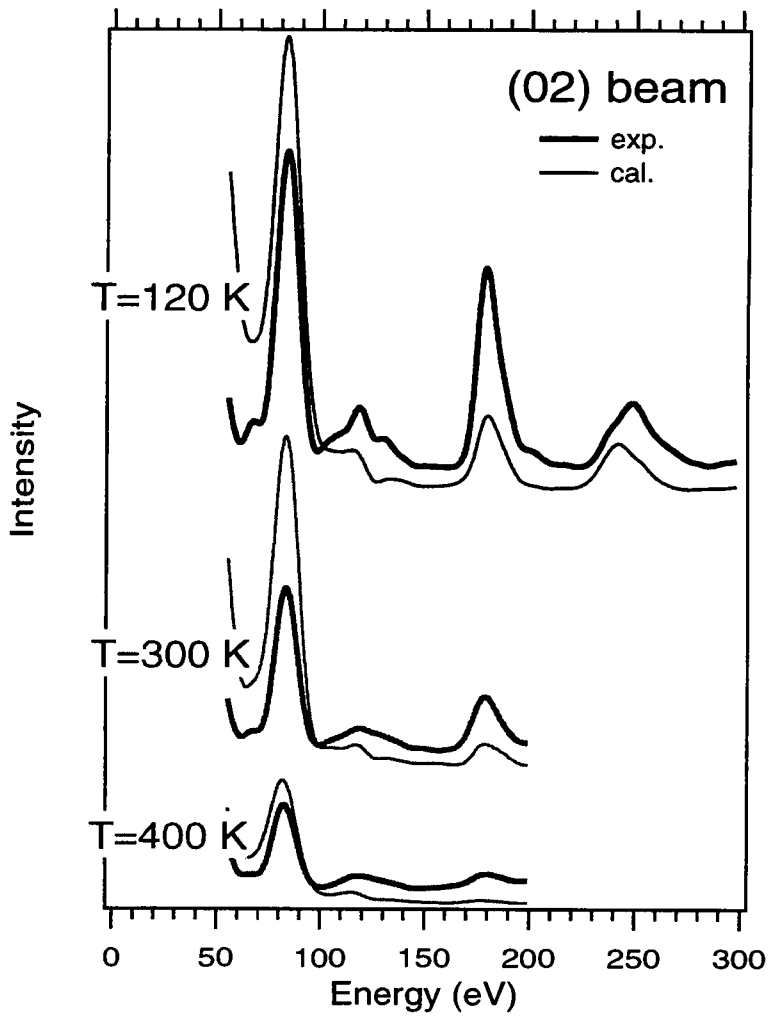


Figure 3.14: (continued)
Measured and calculated LEED *I-V* spectra for the optimized structures of Mg(10$\bar{1}$0) at temperatures *T*=120 K, 300 K, and 400 K.

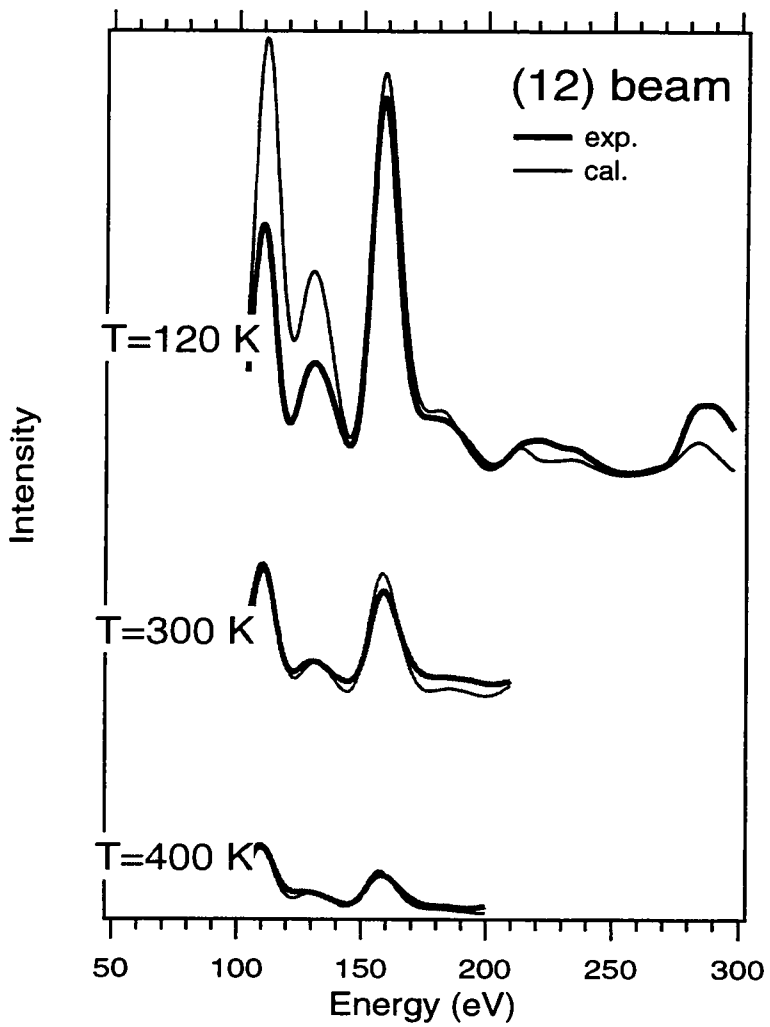


Figure 3.14: (continued)
Measured and calculated LEED *I-V* spectra for the optimized structures of Mg(10$\bar{1}$0) at temperatures *T*=120 K, 300 K, and 400 K.

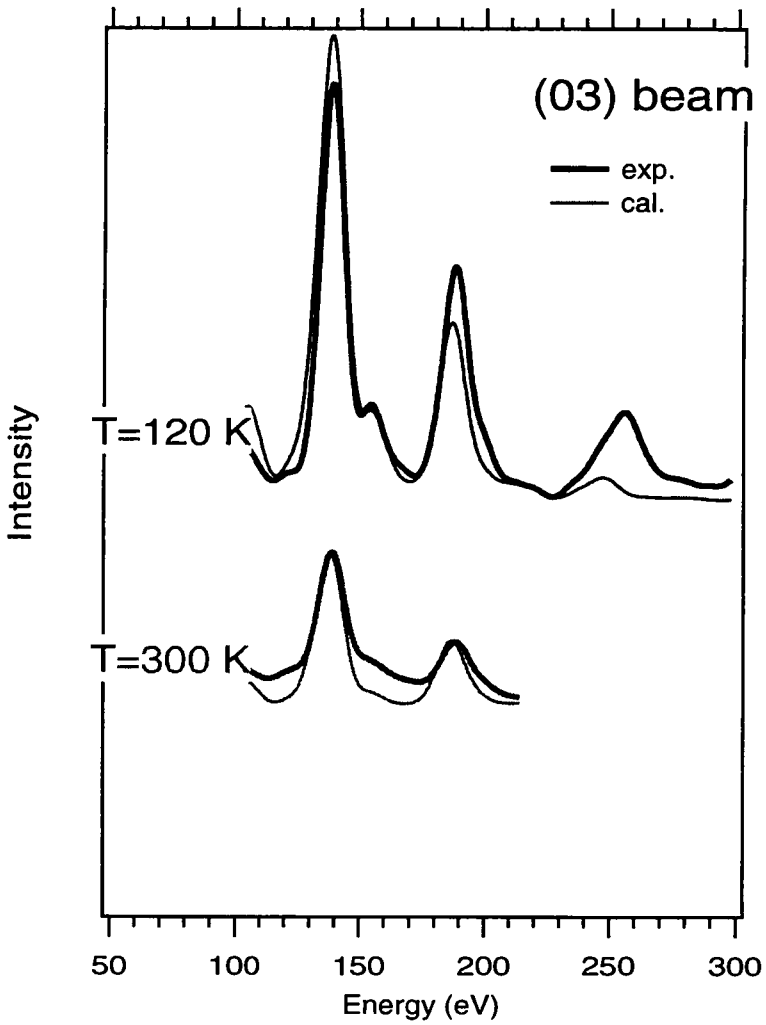


Figure 3.14: (continued)
Measured and calculated LEED *I-V* spectra for the optimized structures of Mg(10$\bar{1}$0) at temperatures *T*=120 K, 300 K, and 400 K.

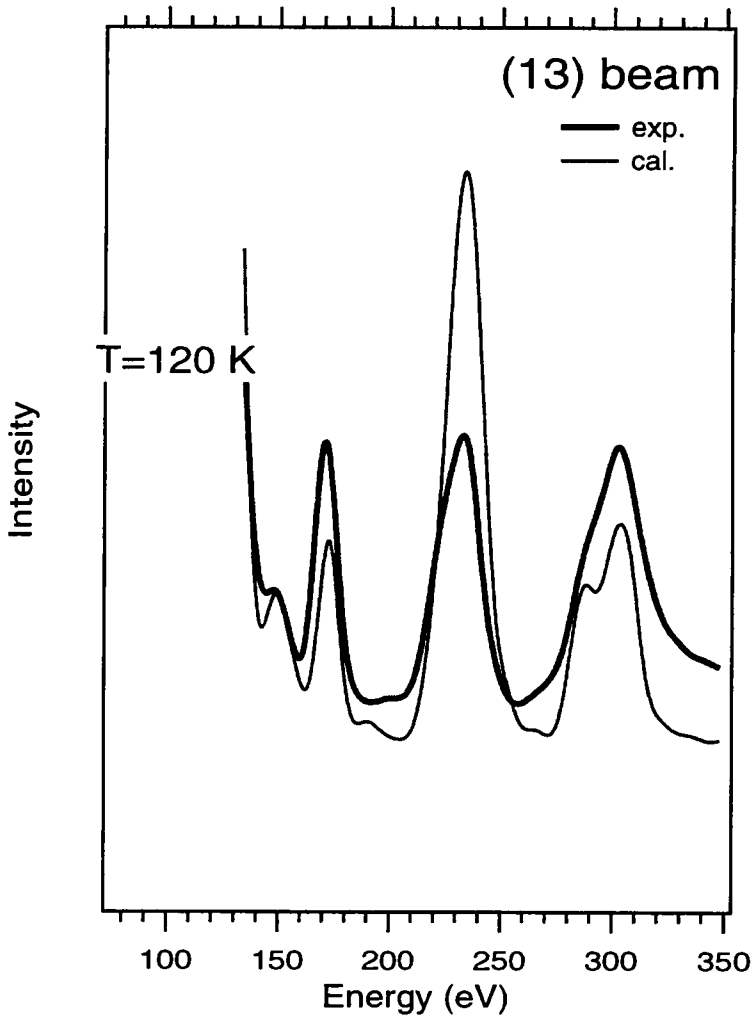


Figure 3.14: (continued)
Measured and calculated LEED *I-V* spectra for the optimized structures of Mg(10$\bar{1}$0) at temperatures *T*=120 K, 300 K, and 400 K.

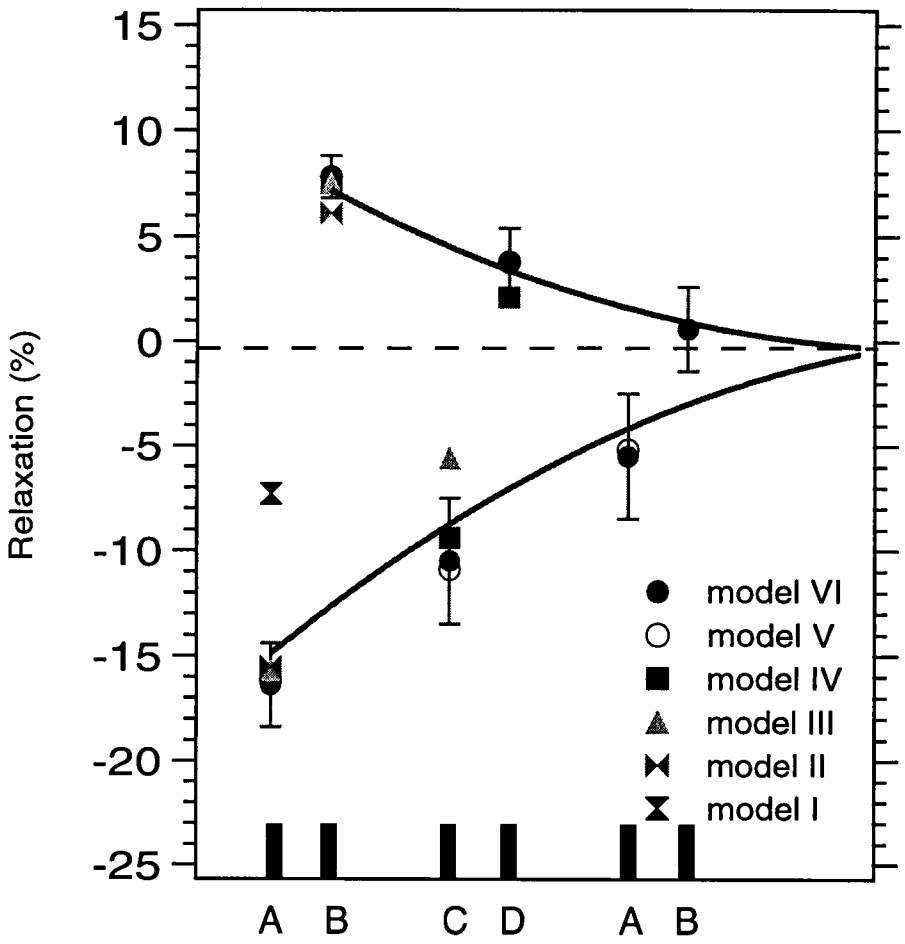


Figure 3.15: Surface relaxations for the Mg(10$\bar{1}$0) surface versus the normal distance from the surface toward the bulk for models I-VI at temperature T=120 K. A, B, C, and D indicate the layers. Solid lines are polynomial fitting curves.

Table 3.11: *Rp* factors for models I - VI for all three temperatures studied.

	Model					
	I	II	III	IV	V	VI
120 K	0.382	0.250	0.195	0.170	0.155	0.150
300 K	0.291	0.192	0.174	0.150	0.147	0.140
400 K	0.283	0.184	0.178	0.170	0.168	0.160

Table 3.12: Surface thermal expansion of Mg($10\bar{1}0$) with respect to the bulk for models I - VI, i.e., $\alpha_{ij}=\Delta d_{ij}(T)/\Delta T \cdot d_{ij})/\alpha_B$, where $\alpha_B \approx 25 \times 10^{-6}$ K^{-1} (bulk thermal expansion of Mg).

	Model					
	I	II	III	IV	V	VI
α_{12}	-12.0	-6.6	-6.3	-6.6	-6.6	-7.0
α_{23}	+1.0	+0.5	+2.3	+4.6	+4.7	+5.0
α_{34}	+1.0	+1.0	-6.0	-6.8	-8.7	-10.0
α_{45}	+1.0	+1.0	+1.0	+2.4	+1.4	+2.0
α_{56}	+1.0	+1.0	+1.0	+1.0	-3.3	-1.0
α_{67}	+1.0	+1.0	+1.0	+1.0	+1.0	+3.0

Despite the models (models I - VI), negative thermal expansion (or thermal contraction) in the first interlayer of the Mg(10$\bar{1}$0) surface was always observed. A kinematic analysis of electron diffraction from the Al(110) surface indicated a possibility of the negative thermal expansion in the first interplanar spacing in the temperature range of 40 K to 450 K, with the surface thermal expansion coefficient equal to -1 times the bulk thermal expansion coefficient [4]. This observation was supported by a very recent theoretical study by using finite temperature molecular dynamics simulations, suggesting that the thermal contraction at the Al(110) surface is a consequence of strongly anharmonic vibration of atoms in the second layer (not in the surface layer) perpendicular to the surface [14]. Since both Al and Mg are nearly free-electron-like metals, the mechanism of the thermal expansion at the Al(110) surface could be applied to the thermal contraction in the first interlayer of the Mg(10$\bar{1}$0) surface. However, as was shown above, the Mg(10$\bar{1}$0) surface revealed that the interlayer spacings, $d_{i,i+1}$, exhibit *remarkable oscillatory thermal relaxation.* As the temperature increases, the short interplanar spacings $d_{1,2}$, $d_{3,4}$, and $d_{5,6}$ contract while the long interplanar spacings $d_{2,3}$, $d_{4,5}$, and $d_{6,7}$ expand.

So far, there is no theoretical result available for the temperature dependence of the interlayer spacing or the thermal expansion coefficient at the Mg(10$\bar{1}$0) surface. Theory for a *s-p* bonded metal is remarkably accurate; therefore we extrapolate our temperature dependent data to *T=0* K to compare with the calculations at T = 0 K by Cho *et al.* (where the electron-screening was included in the calculations) [47,48] and Staikov *et al.* (electrostatics) [30], as listed in Table 3.13. Both calculations agree for the short termination domain. The comparison between calculations and the experimental data is displayed in Figure 3.16. The agreement between experimental data and theoretical result is excellent, showing damped oscillatory relaxations down to the sixth layer. Figure 3.16 shows that as the temperature increases, the interlayer spacing of bilayers become shorter; while the separations between the bilayers become larger. Cho *et al.* performed a set of *T*=0

Table 3.13: Comparison of the experimental data extrapolated to T=0 K for the Mg(10$\bar{1}$0) surface with the T=0 K calculations.

	experiment (this work)	theory [47]	theory [30]
$\Delta d_{12}/d_{12}^{bul}(\%)$	-14.5	-14.9	-14.9
$\Delta d_{23}/d_{23}^{bulk}(\%)$	+6.5	+6.9	+5.6
$\Delta d_{34}/d_{12}^{bulk}(\%)$	-7.5	-7.5	-8.2
$\Delta d_{45}/d_{23}^{bulk}(\%)$	+3.0	+1.7	+2.8
$\Delta d_{56}/d_{12}^{bulk}(\%)$	-5.0	-4.7	-3.8

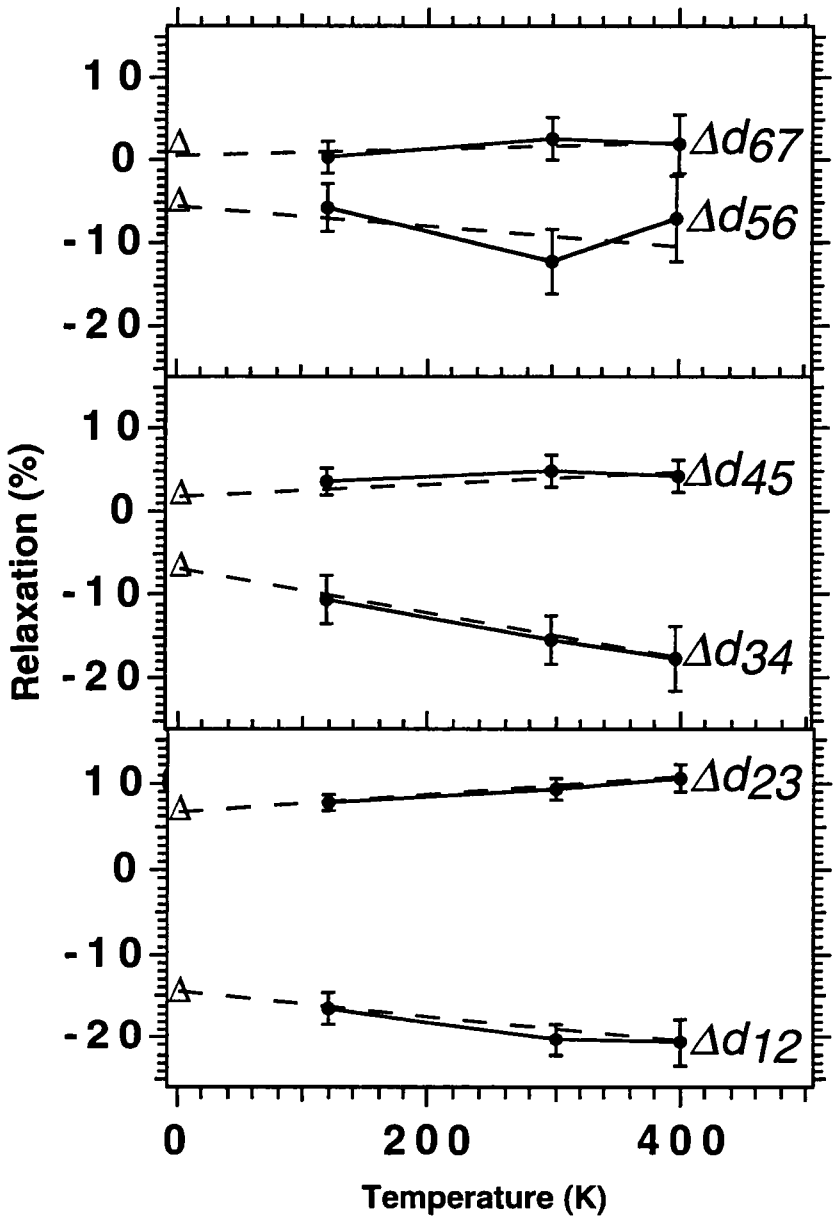


Figure 3.16: Relaxations of the Mg(10$\bar{1}$0) surface as a function of temperatures. Unfilled triangles are calculations by Cho [47] and filled circles are experimental data.

K calculations emulating the behavior of this surface at elevated temperatures [48]. The coupling between the contraction of d_{12} and the expansion of d_{23} was explored by calculating the fully relaxed value of d_{12} as a function of an inputted d_{23} spacing (all deeper planes being fixed) [48]. Figure 3.17 shows the result of this calculation compared to the relationship between d_{12} and d_{23} as determined experimentally by changing the temperature. Obviously, the first two interplanar spacings are intimately coupled, but a similar calculation using experimental values for d_{12} and d_{23} produces the tendency shown experimentally, a contraction of d_{34}. An extreme situation was explored theoretically [48] by optimizing the structure of an isolated bilayer, i.e., $d_{23}\rightarrow\infty$. A total energy calculation of d_{12} for the bilayer restraining the lateral structure to be bulk-like yields an equilibrium spacing d_1=0.22Å. This is a 75% reduction in the bulk value. If the two layers collapse into a single layer the areal density of Mg atoms would be 0.127/Å^2 compared to 0.118/Å^2 for the close packed (0001) plane, i.e., a 7% density increase. If the lateral restrictions are removed in the calculation, the lowest energy configuration is in fact a single hexagonal layer (100% contraction in d_{12}), with a density of 0.128/Å^2. The single hexagonal plane is therefore more stable (by -11 meV per atom) than the constrained bilayer. The results of these calculations for the bilayer is presented in the insert of Figure 3.17. An interesting possibility arises from the results shown in Figure 3.17. As the temperature increases, the bilayer reduces its interplanar spacing. If the first bilayer becomes sufficiently decoupled from the next bilayer, it might convert to a single incommensurate hexagonal layer. Thus at certain critical temperature T_C, where d_{23} is large enough (d_{12} small enough), the stable configuration of the first bilayer will be a single incommensurate hexagonal layer [48].

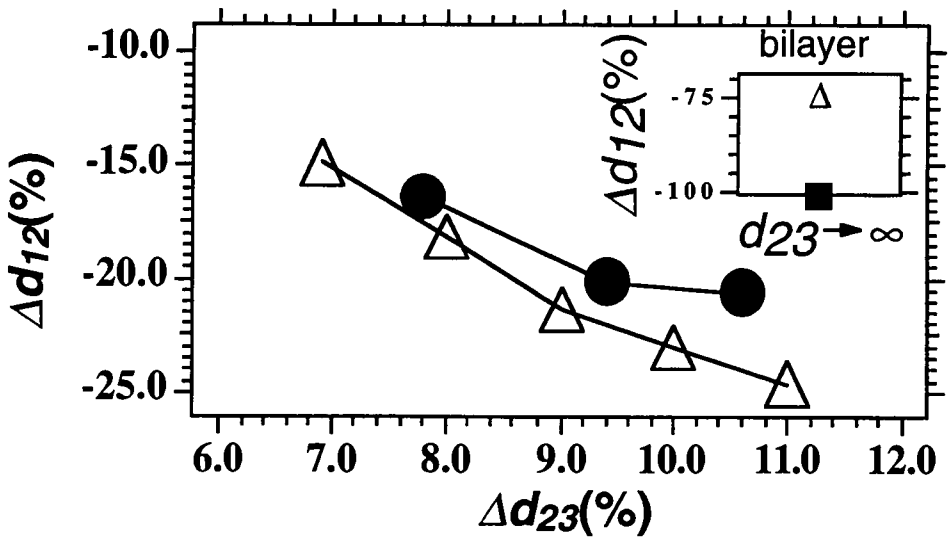


Figure 3.17: Calculated dependency of d_{12} with varying d_{23} by keeping all other layers fixed at the relaxed values for T=0 K (triangles) [48]. The experimental data (circles) are taken from the temperature dependence for d_{12} and d_{23} shown in Figure 3.16. The insert shows the calculation for an isolated bilayer. The triangle is for a lateral structure restrained to be bulk-like and the filled square is for a relaxed lateral structure, resulting in a single hexagonal plane.

3.2.4 Conclusions

In summary, we have presented the experimental observation of damped oscillatory interplanar thermal expansion at the Mg($10\bar{1}0$) surface. Despite the models (models I - VI), negative thermal expansion (thermal contraction) is always observed in the first interlayer. More importantly, the oscillatory relaxations and oscillatory thermal expansion at a metal surface can be observed if sufficient layers are varied in the calculations. At T=0 K there is an oscillatory interplanar relaxation, but it is more remarkable at a finite temperature, where the oscillatory interplanar thermal expansion was observed at a finite temperature. The surface thermal expansion for the first short interlayer spacing d_{12} is negative, $(\Delta d_{12}(T)/\Delta T \cdot d_{12})$ is -7 x α_B, where $\alpha_B \approx 25\text{x}10^{-6}$ K^{-1} (bulk thermal expansion). The first long interlayer spacing d_{23} is expanded by 6.5% at T=0 K and exhibits a large thermal expansion compared to the bulk, $(\Delta d_{23}(T)/\Delta T \cdot d_{23})$=+5 x α_B. The second short interlayer spacing d_{34} is contracted at T=0 K and displays a negative thermal expansion of -10 x α_B, larger than the negative thermal expansion observed for d_{12}. The second long interlayer spacing d_{45} is expanded at T=0 K and shows a positive thermal expansion of 2 x α_B. d_{56} is contracted at T=0 K and shows a tendency for negative thermal expansion (-1 x α_B). d_{67} is expanded at T=0 K and shows a tendency for positive thermal expansion (+3 x α_B). The net thermal expansion of the whole surface region, defined as the spacing between plane 1 and 7 is about the same as for the bulk!

This system consists of stacked bilayers, and an increase in temperature causes the interlayer spacing of a bilayer near the surface to decrease, while the separation between two neighboring bilayers increases. First-principles density-functional calculations at zero temperature [48] suggested that a bilayer close to the surface where symmetry is reduced naturally wants to shrink its interlayer spacing if its coupling to neighboring bilayer(s) is weakened [48]. Furthermore, a completely isolated bilayer ultimately prefers to collapse

into a single layer with a new (hexagonal) geometry [48]. The mechanism of the thermal contraction at the Al(110) surface [14] might be applied to the bilayers (short layers) at the $Mg(10\bar{1}0)$ surface where the thermal contraction is a consequence of strongly anharmonic vibration of atoms in the bilayers perpendicular to the surface. A better understanding of the thermal contraction at the $Mg(10\bar{1}0)$ surface could be achieved from a finite temperature calculation.

3.3 References

1. A. P. Baddorf and E. W. Plummer, Phys. Rev. Lett. **66** (1991), 2770.

2. J.W.M. Frenken, F. Huussen, and J.F. van der Veen, Phys. Rev. Lett. **58**, 401 (1987).

3. Y. Cao and E. Conrad, Phys. Rev. Lett. **65**, 2808 (1990).

4. H. Göbel and P. von Blanckenhagen, Phys. Rev. B **47**, 2378 (1993).

5. G. Helgesen, D. Gibbs, A.P. Baddorf, D.M. Zehner, and S.G.J. Mochrie, Phys. Rev. **48**, 15320 (1993).

6. P. Statiris, H.C. Lu, and T. Gustafsson, Phys. Rev. Lett. **72**, 3574 (1994).

7. K. Pohl, J. -H. Cho, K. Terakura, M. Scheffler, and E. W. Plummer, Phys. Rev. Letter. **80**, 2853 (1998).

8. C. S. Jayanthi, E. Tosatti, and L. Pietronero, Phys. Rev. B **31** (1985), 3456.

9. R.N. Barnett and Uzi Landman, Phys. Rev. B **44**, 3226(1991).

10. E.T. Chen, R.N. Barnett, and Uzi Landman, Phys. Rev. B **41**, 439(1990).

11. R. E. Allen and F. W. de Wette, Phys. rev. **179** (1969), 873.

12. S. K. S. Ma, F. W. de Wette, and G. P. Alldredge, Surf. Sci. **78** (1978), 598.

13. S. Narasimhan and M. Scheffler, Z. Phys. Chem. **202** (1997), 253.

14. N. Marzari, D. Vanderbilt, A. De Vita, and M. C. Payne, Phys. Rev. Lett. **82**, 3296 (1999).

15. J. B. Hannon, Ph.D. Thesis, University of Pennsylvania (1994).

16. M. Lazzeri and Stefano de Gironcoli, Phys. Rev. Lett. **81**, 2096 (1998).

17. J. B. Pendry, *Low Energy Electron Diffraction* , Academic Press., London, 1974.

18. M. A. V. Hove and S. Y. Tong, *Surface Crystallography by LEED* , Springer, Berlin, 1979.

19. K. Pohl, Ph.D. Thesis, University of Pennsylvania (1997).

20. *International Tables for X-Ray Crystallography* Vol. III, The Kynoch Press, Birmingham, England, 1962. *Thermal Expansion: Metallic Elements and Alloys*, edited by Thermophysical Properties Research Center at Perdue University, Thermophysical Properties of Matter Vol. 12, (IFI/Plenum New York, 1970).

21. V. L. Moruzzi, J. F. Janak, and A. R. Williams, *Calculated Electronic Properties of Metal,* Plenum, New York, 1978.

22. E. V. Chulkov, V. M. Silkin, and E. N. Shirykalov, Surf. Sci. **188** (1987), 287.

23. R.A. Bartynski, E. Jepsen, T. Gustafsson, and E. W. Plummer, Phys. Rev. B **32** (1985), 1921.

24. E.V. Chulkov and V.M. Silkin, Solid State Comm. **58** (1986), 273.

25. P.T. Sprunger, K. Pohl, H.L. Davis, and E.W. Plummer, Surf. Sci. **297** (1993), L48.

26. P.J. Rous, J.B. Pendry, D.K. Saldin, K. Heinz, K. Müller, and N. Bickel, Phys. Rev. Lett. **57**, 2951 (1986).

27. P.J. Rous and J.B. Pendry, Surf. Sci. **219**, 355 (1989).

28. P.J. Rous and J.B. Pendry, Surf. Sci. **219**, 373 (1989).

29. P.J. Rous, Progr. Surf. Sci. **39**, 3 (1992).

30. Pavlin Staikov and Talat S. Rahman, To be published.

31. Alan F. Wright, P. J. Feibelman, Susan R. Atlas, Surf. Sci. **302**, 215 (1994).

32. Ismail, Ph. Hofmann, E. W. Plummer, Claudia Bungaro, and W. Kress, To be published.

33. N. D. Lang and W. Kohn, Phys. Rev. B **1** (1970), 4555.

34. J.R. Noonan and H.L. Davis, J. Vac. Sci. Tech. A **8**, 2671(1990).

35. R. Stumpf, J.B. Hannon, P.J. Feibelman, and E.W. Plummer, in *Electronic Surface and Interface States on Metalic Systems,* edited by E. Bertel and M. Donath, pp. 151 (World Scientific, Singapore, 1995).

36. N. W. Ashcroft and N. D. Mermin, *Solid State Physics*, Holt, Rinehart, and Winston, 1976.

37. S.D. Kevan, in *Electronic Surface and Interface States on Metallic Systems*, edited by E. Bertel and M. Donath, page 1-11 (World Scientific, Singapore, 1995).

38. H.L. Davis and D. M. Zehner, J. Vac. Sci. Technol. **17** (1980), 190.

39. J. Mischenko III and P. R. Watson, Surf. Sci. **220** (1989), L667.

40. H. Over, G. Kleinle, G. Ertl, W. Moritz, K. -H. Ernst, H. Wohlgemuth, K. Christmann, and E. Schwarz, Surf. Sci. **254** (1991), L469.

41. M. Lindroos, C. J. Barnes, P. Hu, and D. A. King, Chem. Phys. Lett. **173** (1990), 92.

42. Ph. Hofmann, K. Pohl, R. Stumpf, and E.W. Plummer, Phys. Rev. B **53** (1996), 13715.

43. M. W. Finnis and V. Heine, J. Phys. F **4** (1974), L37.

44. R. Smoluchowski, Phys. Rev. **60** (1941), 661.

45. K. M. Ho and K. P. Bohnen, Phys. Rev. B **32** (1985), 3446.

46. A. G. Eguiluz, Phys. Rev. B **35** (1987), 5473.

47. J.-H. Cho, Ismail, Z. Zhang and E. W. Plummer, Phys. Rev. B **59**, 1677 (1999).

48. Ismail , J.-H. Cho, Z. Zhang and E. W. Plummer, To be published.

49. R.J. Needs, Phys. Rev. Lett. **58**, 53 (1987).

50. B.S. Itchkawitz, A.P. Baddorf, H.L. Davis, and E.W. Plummer, Phys. Rev. Lett. **68**, 2488 (1992).

51. Alan F. Wright and D.C. Chrzan, Phys. Rev. Lett. **70**, 1964 (1993).

52. K. M. Ho, and K. P. Bohnen, Phys. Rev. B **32**, 3446 (1985).

53. W. Berndt, D. Weick, C. Stampfl, A.M. Bradshaw, and M. Scheffler, Surf. Sci. **330**, 182 (1995).

54. J.N. Andersen, H.B. Nielsen, L. Petersen, and D.L. Adams, J. Phys. C **17**, 173 (1984).

55. J.S. Nelson and P.J. Feibelman, Phys. Rev. Lett. **68**, 2188 (1992).

56. D.L. Adams and C.S. Sørensen, Surf. Sci. **166**, 495 (1986).

57. J.R. Noonan, H.L. Davis, and W. Erley, Surf. Sci. **152/153**, 142 (1985).

Chapter 4

Surface Lattice Dynamics of Mg(0001) and Mg(10$\bar{1}$0)

4.1 Introduction

The creation of a surface from a bulk material leads to the existence of surface vibrational states, which are localized near the surface region and decay into the bulk perpendicular to the surface. The most commonly observed of the surface vibrational states is a Rayleigh mode or Rayleigh wave (RW). In the long wavelength limit (small wavevector), the dispersion of Rayleigh wave can be expressed in terms of the macroscopic elastic properties of the medium, where the displacement pattern of this mode usually extends farther into the bulk and its energy is a linear function of momentum wavevector. At large wavevector, this mode lies below the projection of bulk phonon modes onto the surface and its energy is related to the shape of the interatomic potential at the surface region. Therefore, the bonding between atoms in a solid is reflected in the dispersion of vibrational modes. Since the atoms near the surface region lose some of their coordinations, the potential near the surface region becomes more asymmetric than in the bulk. Therefore, the interatomic force constants near the surface region are different than in the bulk. These lead to enhanced surface anharmonicity and soft phonon modes, as was discussed in Chapter 1.

As a surface is created, the electrons near the surface region adjust themselves in order to lower their kinetic energies due to a local charge imbalance, which is known as the phenomenon of screening. These charge rearrangements at the surface region lead the surface force constants to be different than in the bulk. Self-consistent calculations, where the screening was taken into account, showed that the net restoring force on an atom at the surface is *not* in the nature of a sum over pair potentials but it has a significant effect due to

the surface anisotropic-electronic environment, leading to inherently anisotropic screening and enhanced non-central force constants at the surface [1].

The surface phonon measurements were initiated by Toennies and his collaborators by using the inelastic-He-scattering technique [2]. Subsequently, Ibach and his co-workers employed electron energy loss spectroscopy to measure the dispersion relation of the surface phonons [3]. Since then, both these techniques have been used widely to study the lattice dynamics of many surfaces. Nonetheless, we have learned very little about the interplay between the lattice dynamics, the electronic structure, and the geometric structure, especially at a finite temperature.

Phonons are the signature of lattice dynamics, and it seems that there should be an intimate relationship between the lattice dynamics, the electronic structure, and the temperature dependent lattice structure. The question is, can we establish this relationship ? In other words, can we relate the surface phonon dispersions to the electronic and structural properties at the surface ? Qualitatively, this complex-interplay has been shown by recent measurements and calculations for the (0001) surface of Be, where the surface electronic and vibrational properties as well as thermal expansion are quite different compared to the equivalent bulk [4-8]. Hannon *et al.* reported that the measured surface phonon dispersion at the Be(0001) surface was significantly different than expected from the bulk-truncated model (the dispersion of the Rayleigh wave cannot be described in terms of the bulk force constants) [4], as shown in Figure 4.1. Most significantly, the trend of the Rayleigh wave dispersion of Be(0001) along the zone boundaries $\overline{K}$ - $\overline{M}$ can only be modeled by reducing the non-central forces present in the bulk substantially. Hannon *et al.* speculated that this feature was caused by the unique electronic properties of the Be(0001) surface; whereas the bulk of Be is nearly semiconductor, but the surface is a high-density free-electron metal [5]. They speculated that the free-electron behavior at the surface would lead to central interatomic forces at the surface. This is an example where the surface phonon dispersion

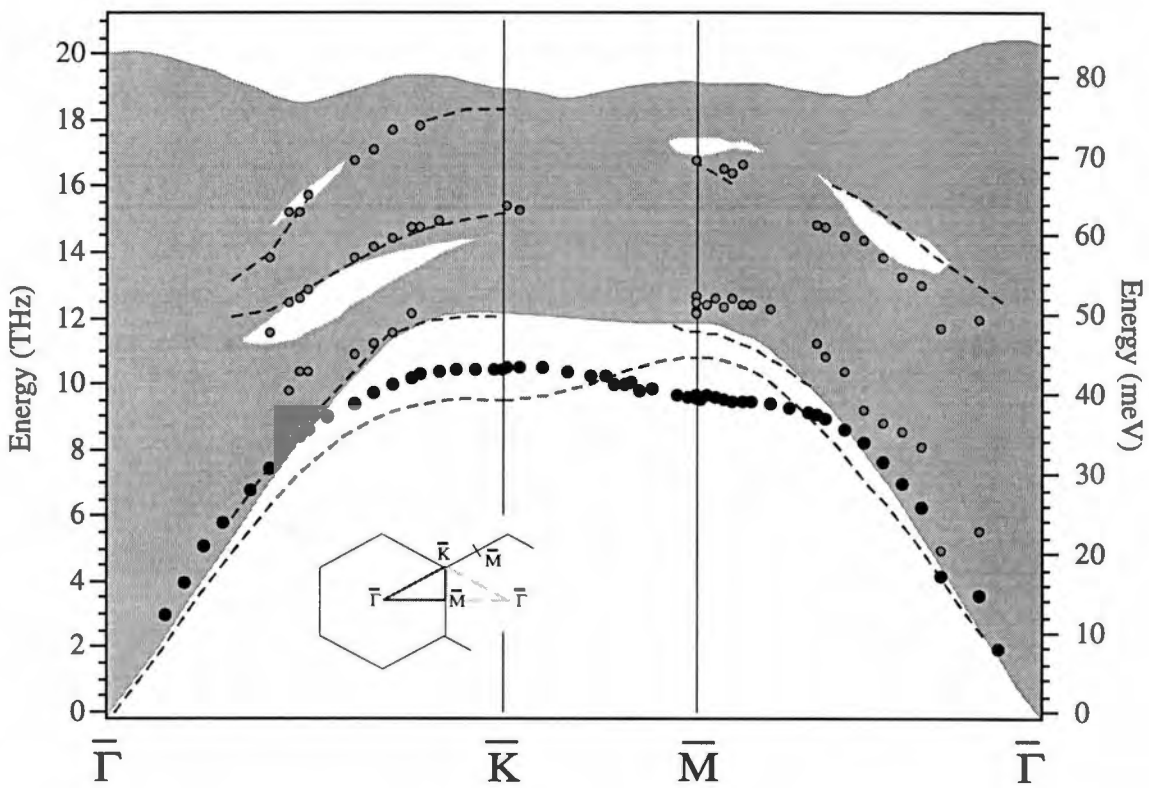


Figure 4.1: Dispersion of vibrational modes at the Be(0001) surface. The large (small) filled circles indicate intense (weak) features in the measured dispersion. Dotted lines indicate the surface modes for a bulk-terminated calculations by using the bulk force constants [6].

has been related to the surface electronic properties. Subsequently, Lazzeri and Gironcoli performed *ab initio* calculations (T=0 K) of the surface lattice dynamics for this surface [8]. Their results are in excellent agreement with the experimental data by Hannon [4]. They found that there are only three layers involved in the surface dynamics and *the surface forces continue to have a strong non-central component.* In addition, they predicted two additional modes below the bulk band edge which have never been observed experimentally. These additional modes are peaked in the subsurface layers and have both in-plane and out-of-plane components, which could be difficult to be detected experimentally. Unfortunately, these authors did not relate the strong non-central forces at the surface with the electronic properties.

Temperature dependent measurements of the Rayleigh modes at the zone boundaries $\overline{K}$ and $\overline{M}$ points of the Be(0001) surface by Hannon showed very little anharmonicity [6]. Thus, the surface thermal expansion of Be(0001) is expected to be similar to the bulk. Nonetheless, by using low energy electron diffraction (LEED) with multiple scattering analysis at temperatures 110 K to 700 K, Pohl *et al.* showed an anomalously large thermal expansion at the Be(0001) surface, i.e., 6 times larger than in the bulk [7]. It is quite surprising. The enhanced thermal expansion of Be(0001) was suggested by a primarily softening of the *in-plane* in stead of out-of-plane vibrations [7,9]. However, this conclusion has been challenged by an *ab initio* study of the surface thermal expansion within the quasiharmonic approximation, where the free energy is obtained from *full* vibrational dispersions computed by the density-functional perturbation theory [10]. It is very surprising that even at room-temperature, the agreement between this calculations and the experimental observation is poor.

The kinematic analysis of the electron diffraction from the Al(110) surface indicated a *negative* thermal expansion of the surface interplanar spacing in the temperatures range of 40 K to 450 K, with the surface thermal expansion coefficient equal to -1 times the bulk

thermal expansion coefficient [11]. This finding was supported by a very recent theoretical investigation by using finite-temperature density-functional molecular dynamic simulations that revealed a thermal contraction in the first interlayer (the interlayer spacing becomes shorter as the temperature increases) as a consequence of the strongly anharmonic mean-square-displacements of the atoms *in the second layer* (not in the surface layer) perpendicular to the surface [12].

Our temperature-dependent low energy electron-diffraction (LEED) *I-V* measurements of the Mg(10$\bar{1}$0) surface revealed *a remarkable oscillatory thermal relaxation.* As the temperature increases, the short interplanar spacings $d_{1,2}$, $d_{3,4}$, and $d_{5,6}$ contract, while the long interplanar spacings $d_{2,3}$, $d_{4,5}$, and $d_{6,7}$ expand, following the trend - + - +. The first short interlayer spacing d_{12} is negative, $(\Delta d_{12}(T)/\Delta T \cdot d_{12})$ is -7 x α_B, where $\alpha_B \approx 25 \times 10^{-6}$ K^{-1} (bulk thermal expansion), the first long interlayer spacing d_{23} exhibits a large thermal expansion compared to the bulk, $(\Delta d_{23}(T)/\Delta T \cdot d_{23})$=+5 x α_B, etc. The net thermal expansion of the whole surface region, defined as the spacing between plane 1 and 7 is about the same as in the bulk.

In an attempt to relate the surface phonon dispersions to the electronic and structural properties at the metal surface, we have chosen the magnesium surfaces in our study, i.e., the Mg(0001) and Mg(10$\bar{1}$0) surfaces, because magnesium is a simple metal where its electronic properties are nearly free electron-like [13,23]. Therefore, by choosing the magnesium surfaces, we hope that the analysis will be simpler and it is an ideal test for first principles calculations. In order to understand the nature of the surface force constants, the experimental data are compared with the bulk truncated calculations (by using bulk force constants) for all cases. We compare the surface lattice dynamics of Mg(0001) with those of Be(0001) and Al(111) since both Be(0001) and Al(111) are nearly free electron-like metals [24] in order to see whether the surface lattice dynamics of magnesium surfaces are

similar to those of other simple metal surfaces or not. Similar to the case of the Mg(10$\bar{1}$0) surface, we compare the surface lattice dynamics of Mg(10$\bar{1}$0) with those of Be(10$\bar{1}$0) and Al(110).

4.2 Surface Phonons of Mg(0001)

4.2.1 Experimental Data

The sample preparation was followed as described in Chapter 2. The sample (scattering plane) was oriented to the high-symmetry $\bar{\Gamma}$-$\bar{K}$-$\bar{M}$ and $\bar{\Gamma}$-$\bar{M}$ directions of the (0001) face by using LEED and laser. The geometry of bulk truncated model of hcp(0001) and its surface Brillouin zone (SBZ) are shown in Figure 4.2; where the $\bar{\Gamma}$-$\bar{M}$ direction is coincided within the mirror plane (dashed line in Figure 4.2(a)). The surface phonon dispersion of Mg(0001) were measured at room-temperature by using a HIB 1000 HREELS spectrometer , as was discussed in Chapter 2, with the energy resolutions of 3 - 5 meV. The impact energy was varied from 70 eV to 100 eV in order to obtain the highest phonon cross sections (loss intensities) at the zone boundaries. We found that the impact energy 80 eV produced the highest phonon cross sections at $\bar{K}$ point (q=1.304 Å^{-1}) along the $\bar{\Gamma}$-$\bar{K}$-$\bar{M}$ direction of the surface Brillouin zone with the scattering-geometry of incident angle θ_i=71.0° and scattering angle θ_s=41.5°, as shown in Figure 4.3. The quasi-elastic peak is at the energy loss equal to zero. The presence of the quasi elastic peak in the off-specular direction is due to the diffusive elastic scattering of electrons from the imperfections at the surface. The intense feature in the spectrum with energy loss 14.5 meV is the Rayleigh mode with the energy resolution full width half maximum (FWHM) of 4.2 meV. The dots are raw data and the solid line is the Lorentzian line shape convolved with the elastic peak with the intrinsic width of 1.3 meV.

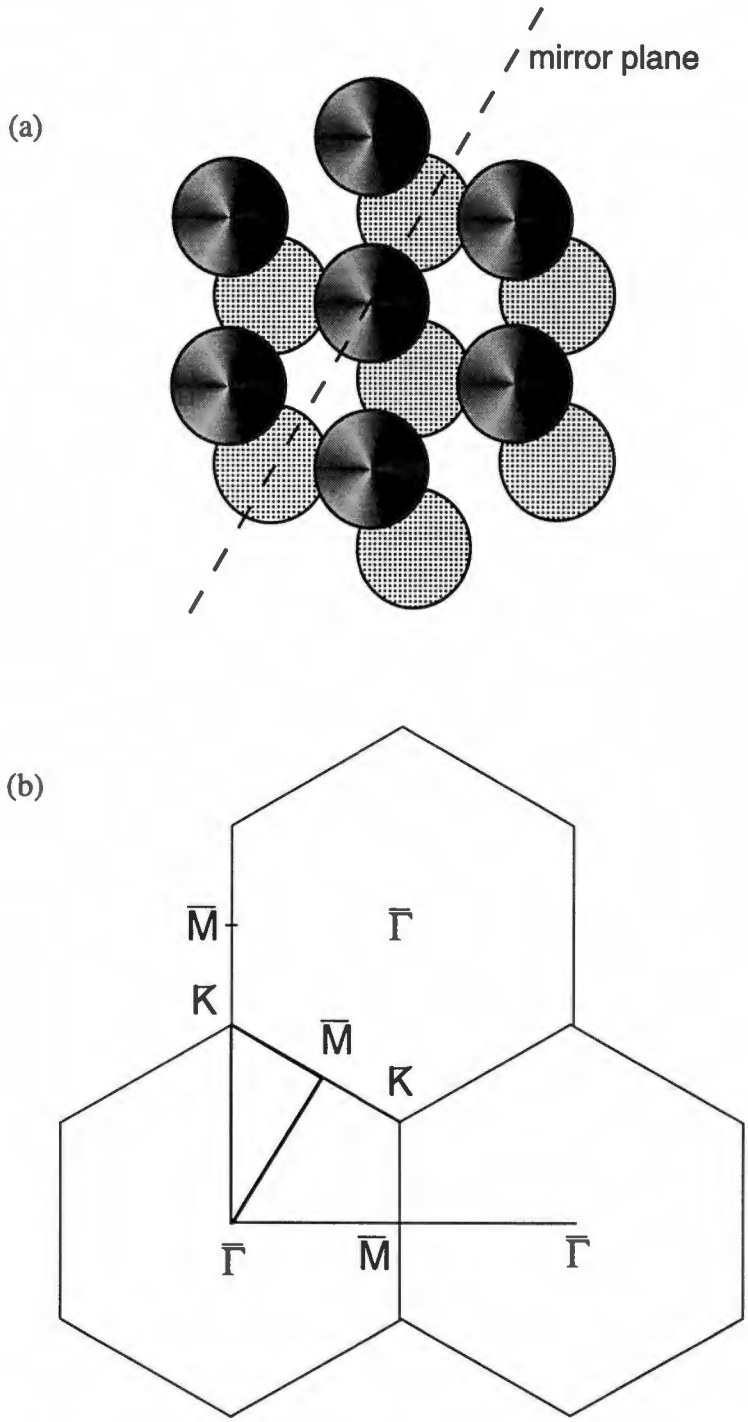


Figure 4.2: (a) The geometry of bulk truncated model of the hcp(0001) surface and (b) its surface Brillouin zone.

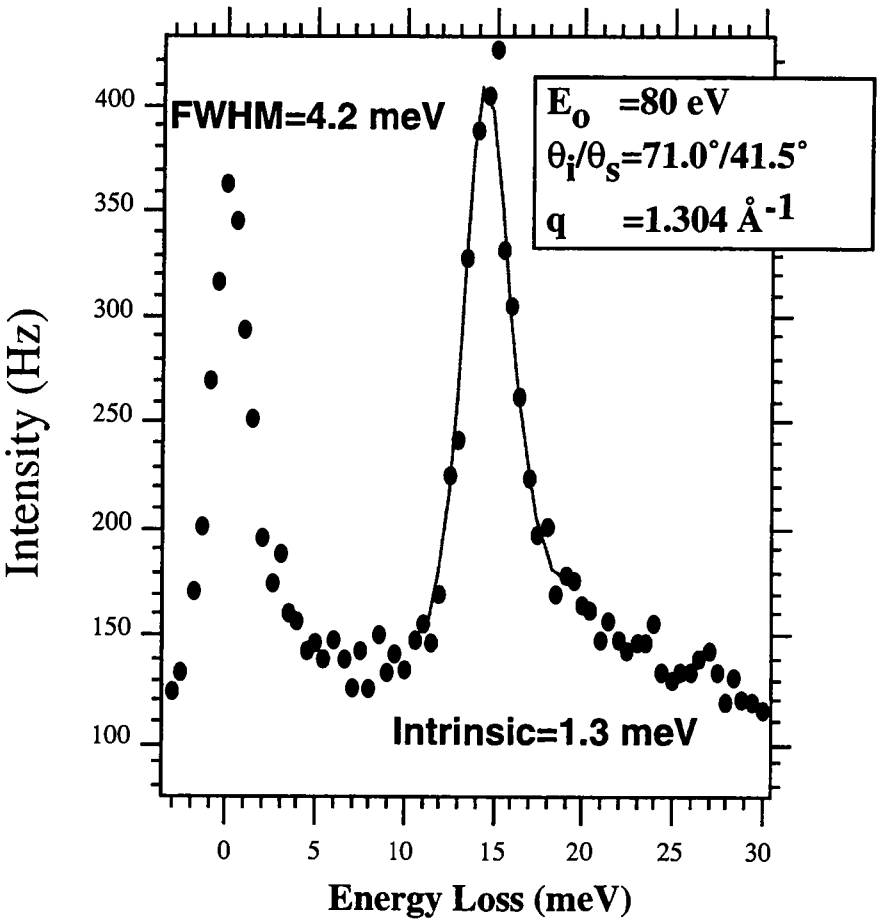


Figure 4.3: EELS spectrum from the Mg(0001) surface at $\overline{K}$(q=1.304 Å^{-1}) along the $\overline{\Gamma}$-$\overline{K}$-$\overline{M}$ direction with the energy resolution FWHM of 4.2 meV. The solid line is the Lorentzian line shape convoled with the elastic peak, with the intrinsic width of 1.30 meV.

A series of EELS spectra was measured along the $\overline{\Gamma}$-$\overline{K}$-$\overline{M}$ and $\overline{\Gamma}$-$\overline{M}$ (mirror plane) directions of the surface Brillouin zone (SBZ). Some of our typical EELS spectra are shown in Figure 4.4 with the energy resolutions of 3 - 5 meV. The dots are raw data and the solid lines are smoothed data. The energy of a Rayleigh mode is assigned by the peak position indicated by a vertical line. We did measurements at the $\overline{K}$ point of the SBZ for three different geometries: a) θ_i/θ_s = 71.0°/41.5°, b) θ_i/θ_s = 61.3°/36.5°, and c) θ_i/θ_s = 56.5°/33.5° (θ_i is incident angle and θ_s is scattering angle), as shown in Figure 4.5. We found that there are three modes at $\overline{K}$ point, which are labeled as K_1, K_2, and K_3 with the energies of 14.50 meV(K_1), 16.5 meV(K_2), and 23.50 meV(K_3). The $\overline{\Gamma}$-$\overline{M}$ direction coincides with a mirror plane of the surface; therefore the modes which are odd with respect to the reflection in the scattering plane can not be excited. However, these modes can be observed by looking at the $\overline{M}$ point along the $\overline{\Gamma}$-$\overline{K}$-$\overline{M}$ directions [4,6] (see Figure 4.2). Thus, the modes at $\overline{M}$ point were measured in two different directions, as shown in Figure 4.6: a) the spectra was measured at the $\overline{M}$ point along the $\overline{\Gamma}$-$\overline{K}$-$\overline{M}$ directions and b) the spectra was measured at $\overline{M}$ point along the $\overline{\Gamma}$-$\overline{M}$ direction. There are four modes observed experimentally at $\overline{M}$ which are labeled as M_1, M_2, M_3, and M_4 with the energies of 13.50 meV(M_1), 17.00 meV(M_2), 18.50 meV(M_3), and 27.50 meV(M_4).

We performed slab calculations by using the Born-von Kármán formalism for the Mg(0001) surface with a bulk truncated (BT) termination, as was described by Allen *et al.* [14] and implemented by Hannon [4,6] and Hofmann [15]. In this method, the dynamical matrix for a finite-thickness slab in two-dimensional periodicity is evaluated from the interatomic force constant matrices by summing over nearest-neighbor shells up to a certain cut-off. In our calculations, we have included a 150 layer-slab of Mg and force constants for up to seventh nearest neighbor interactions; where the force constants were determined by a fit to the bulk phonons of Mg measured by neutron scattering [16]. The bulk force

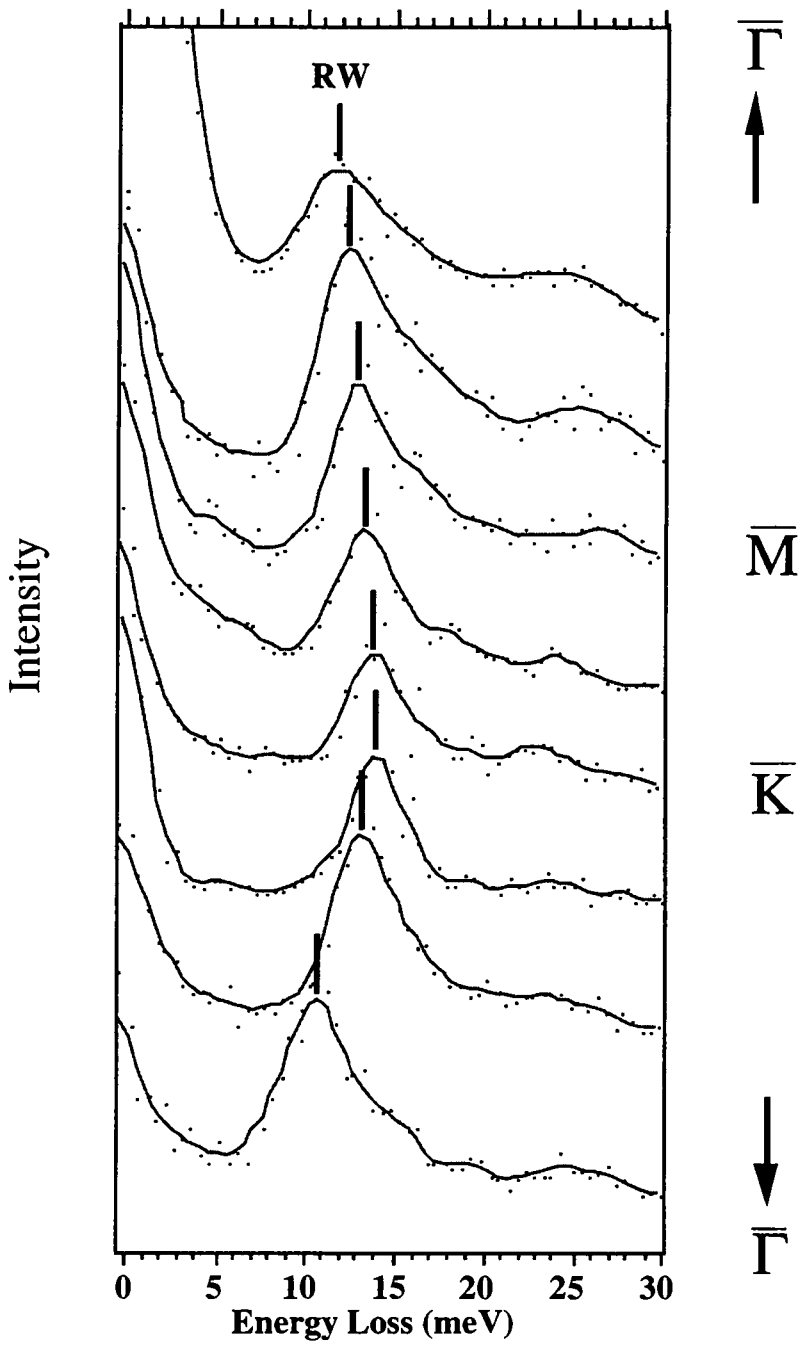


Figure 4.4: A series of EELS spectra from the Mg(0001) surface along the $\overline{\Gamma}$-$\overline{K}$-$\overline{M}$ and $\overline{\Gamma}$-$\overline{M}$ directions (see Figure 4.2). The dots are the raw data and the solid lines are the smoothed data. The Rayleigh modes are assigned from the peak positions indicated by vertical lines.

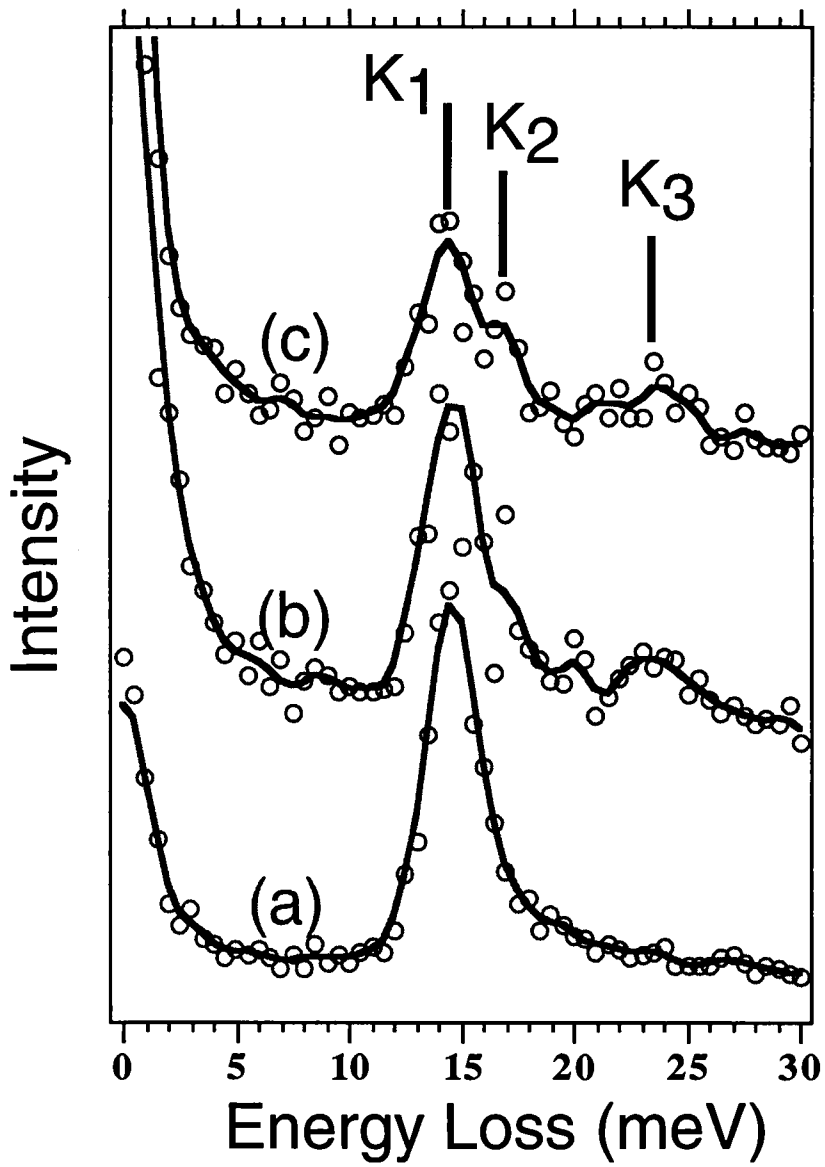


Figure 4.5: EELS spectra at $\overline{K}$ at three different geometries: a) $\theta_i/\theta_s = 71.0°/41.5°$, b) $\theta_i/\theta_s = 61.3°/36.5°$, and c) $\theta_i/\theta_s = 56.5°/33.5°$ (θ_i is incident angle and θ_s is scattering angle).

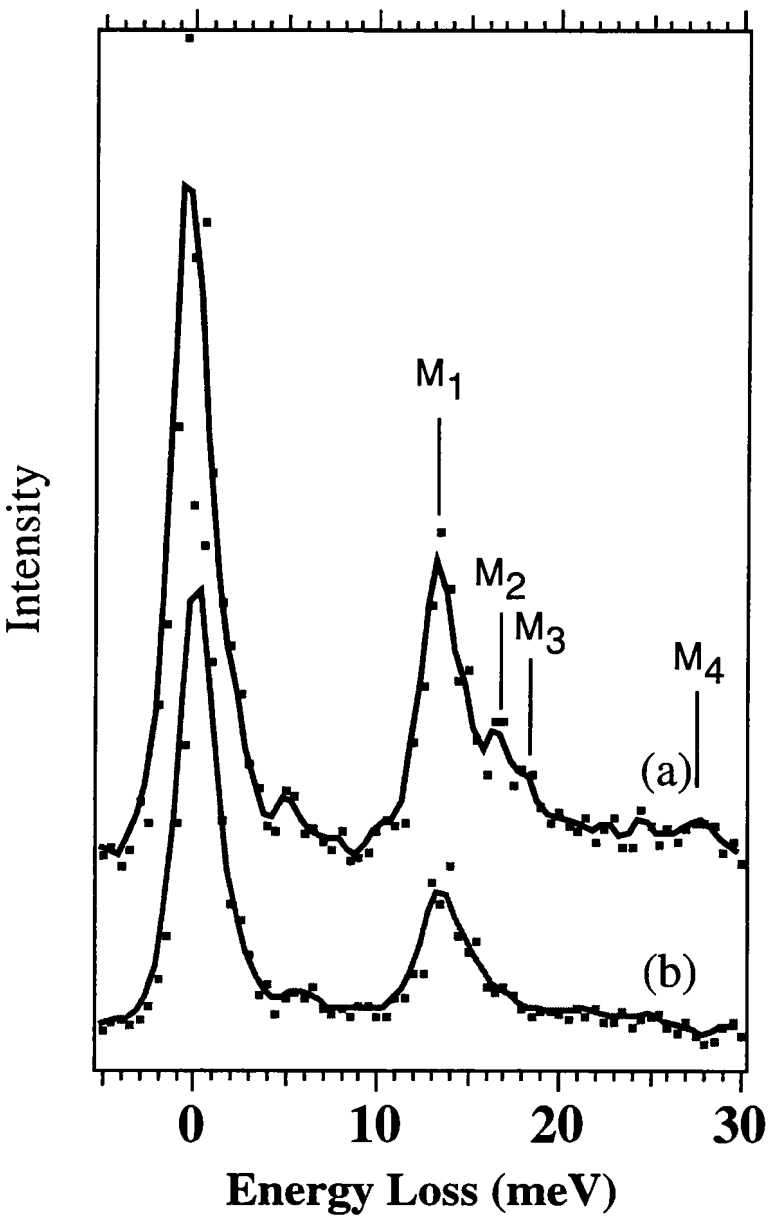


Figure 4.6: EELS spectra at $\overline{M}$ from two different directions: a) along the $\overline{\Gamma}$-$\overline{K}$-$\overline{M}$ direction, and b) along the $\overline{\Gamma}$-$\overline{M}$ direction.

constants of Mg are central forces (axially symmetric forces), which are listed in Table 4.1. Figure 4.7 shows the measured and bulk-truncated calculated phonon dispersions of the Mg(0001) surface. The shaded regions represent the projection of bulk phonon modes onto the (0001) face. The filled (unfilled) circles indicate the intense (weak) intensity losses. The filled squares indicate the contribution from the surface modes which have more than 50 per cent of the total displacements localized in the first two layers. The measured and calculated RW at $\overline{K}$ point are 14.50 meV and 12.96 meV, respectively, and at $\overline{M}$ are 13.50 meV and 12.83 meV, respectively. The Rayleigh mode at $\overline{K}$ has the polarization of the atomic displacements mainly vertical or normal to the surface; while the Rayleigh mode at $\overline{M}$ has the polarization of the atomic displacements sagittal vertical normal to the surface (sagittal plane is the plane that contains the propagation direction and the normal of the surface).

Table 4.1: Force constants (FC's) for bulk magnesium determined from Neutron scattering data [16].

Neighbor Number	(Φ'/r) [N/m] (bending FC's)	(Φ'') [N/m] (stretching FC's)
1NN	-0.31	10.48
2NN	-0.29	10.10
3NN	-0.25	-0.22
4NN	-0.49	0.31
5NN	0.01	0.75
6NN	0.09	0.53
7NN	0.16	-0.05

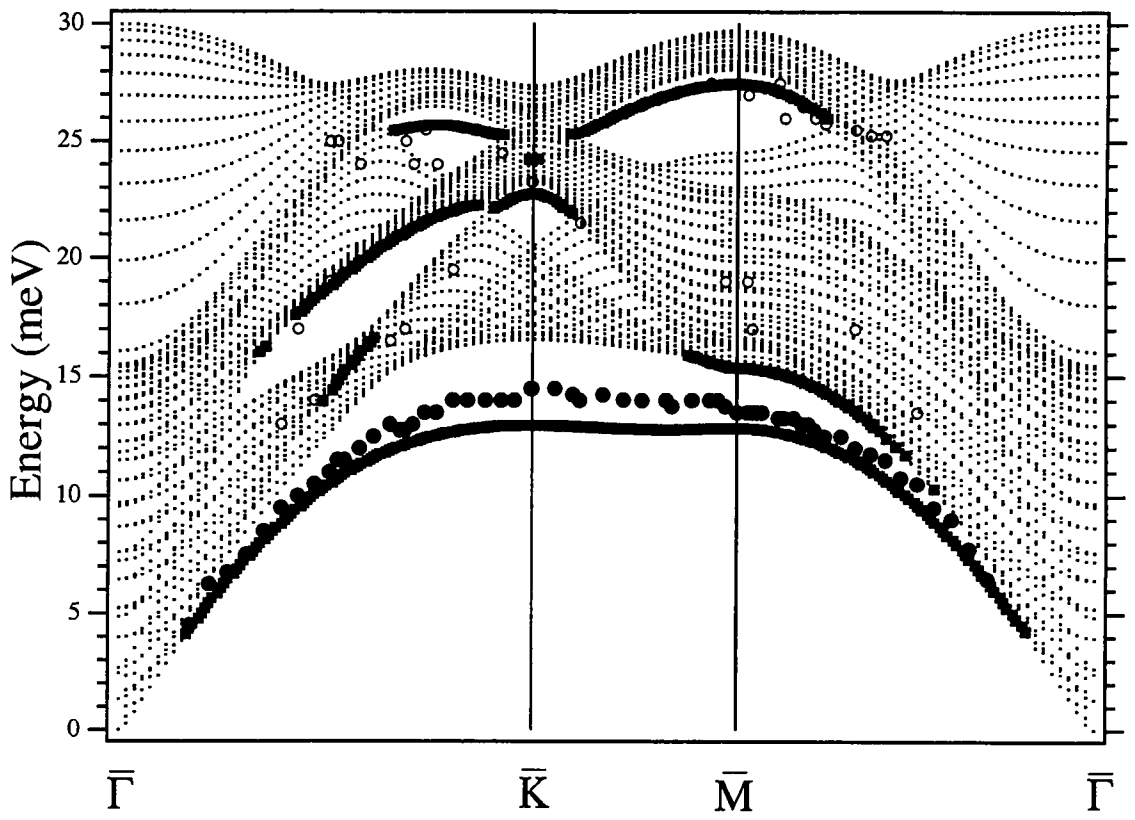


Figure 4.7: Measured surface phonon dispersion for Mg(0001) together with a calculation for a bulk-terminated 150 layer slab. The filled (unfilled) circles indicate the intense (weak) intensity losses. The filled squares are the surface modes from bulk truncated (BT) calculations. The shaded area is the projected bulk band onto the (0001) face.

4.2.2 A Comparison of Mg(0001) with Be(0001) and Al(111)

The vibrational mode is determined by the bonding between atoms or the interatomic forces both from the ion-ion interactions and the screening response from the electrons. Therefore, the surface phonon dispersion contains the information of the interatomic potential of the surface region. At a large wavevector or at the zone boundary, the atomic displacement of a Rayleigh mode is localized in the surface layer. Consequently, at a large wavevector, the energy of this mode or the dispersion of the RW is determined by the shape of the interatomic potential or the interatomic forces near the surface region. For a hcp(0001) or fcc(111) surface, the dispersion of the RW from $\overline{\mathrm{K}}$ to $\overline{\mathrm{M}}$ seems to be very sensitive to the nature of the interatomic forces near the surface region. Therefore, we compare the measured RW with the RW from bulk truncated calculations by using bulk force constants from the zone boundaries $\overline{\mathrm{K}}$ to $\overline{\mathrm{M}}$.

If the RW from BT calculations and experimental data were the same exactly, the surface force constants would be identical to the bulk force constants. Nevertheless, the RW from BT calculations are *softer* than the measured RW for both Mg(0001) and Al(111). Moreover, for Be(0001), the RW from BT calculations are *softer* than the measured RW at $\overline{\mathrm{K}}$ but *stiffer* than that at $\overline{\mathrm{M}}$. Now, if we define quantities:

$$\beta(\overline{\mathrm{K}}) = \frac{RW(\overline{\mathrm{K}})_{Exp} - RW(\overline{\mathrm{K}})_{BT}}{RW(\overline{\mathrm{K}})_{Exp}} \times 100\% \qquad (4.1)$$

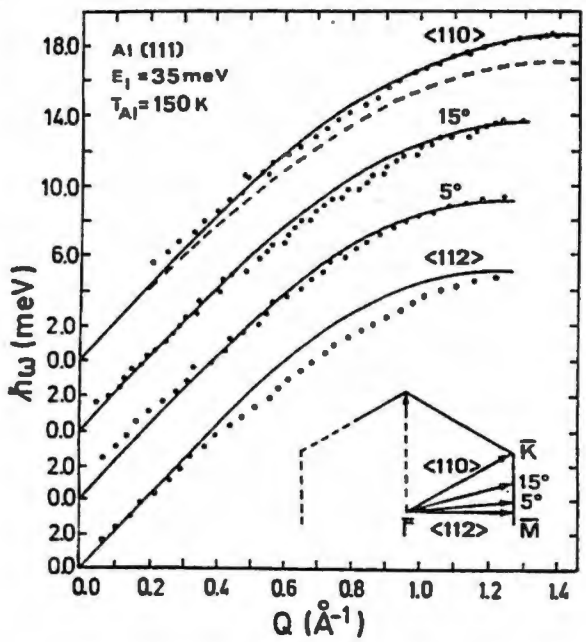
and

$$\chi = \left(1 - \frac{RW(\overline{\mathrm{K}})_{BT} + RW(\overline{\mathrm{M}})_{BT}}{RW(\overline{\mathrm{K}})_{Exp} + RW(\overline{\mathrm{M}})_{Exp}}\right) \times 100\% \qquad (4.2)$$

where $RW(\overline{\mathrm{K}})_{Exp}$ is the measured RW at $\overline{\mathrm{K}}$ and $RW(\overline{\mathrm{K}})_{BT}$ is the RW from BT calculations by using the bulk force constants, then the quantities β and χ represent the qualitative information of the surface force constants in comparison to the bulk force constants at the

zone boundary and along the zone boundaries $\overline{K}$ to $\overline{M}$. For example, if $\beta(\overline{K})\approx 0.0$, then the surface force constants are the same as the bulk force constants at $\overline{K}$. For the Mg(0001) surface, we find that $\beta(\overline{K})=+10.6\%$, $\beta(\overline{M})=+5.0\%$, and $\chi=+7.9\%$, meaning that the bonding of atoms or force constants at $\overline{K}$ and $\overline{M}$ are *stiffer* than in the bulk. The atomic bonding at $\overline{M}$ is closer to the bulk values in comparison with the atomic bonding at $\overline{K}$. Since the magnitude of χ is not the same with $\beta(\overline{K})$ or $\beta(\overline{M})$, qualitatively, we can say that the bonding of atoms or force constants at the surface region of Mg(0001) are slightly anisotropic with respect to the bulk. This behavior could be due to the electron screening as a consequence of the creation of the surface. While for the Al(111) surface, by using the experimental data by Tonnies [17] and the BT calculations by Eguiluz [18], we find that $\beta(\overline{K})=+16.2\%$, $\beta(\overline{M})=+13.8\%$, and $\chi=+15.0\%$, see Figure 4.8. The situation is similar to the case of the Mg(0001) surface, where the bonding of atoms at $\overline{K}$ and $\overline{M}$ are *stiffer* than the bulk. However, the magnitudes of $\beta(\overline{K})$, $\beta(\overline{M})$, and χ for Al(111) are much larger than those for Mg(0001), meaning the bonding of atoms at the Al(111) surface is much more stiffer than the bulk in comparison to the case of the Mg(0001) surface. For the Be(0001) surface, by using the experimental data and BT calculations by Hannon [6], we find that $\beta(\overline{K})=+9.8\%$, $\beta(\overline{M})=-13.9\%$, and $\chi=-1.5\%$. These tell us that the bonding of atoms at the Be(0001) surface is *stiffer* than the bulk at $\overline{K}$, but *softer* at $\overline{M}$; therefore the bonding of atoms at the Be(0001) is much more anisotropic than the bulk. The sign of $\beta(\overline{K})$ at the Be(0001) surface is positive, which is the same as in the cases of Mg(0001) and Al(111), but it is not true at $\overline{M}$. We summarize the values of $\beta(\overline{K})$, $\beta(\overline{M})$, and χ for Mg(0001), Al(111), and Be(0001) in Table 4.2.

(a)



(b)

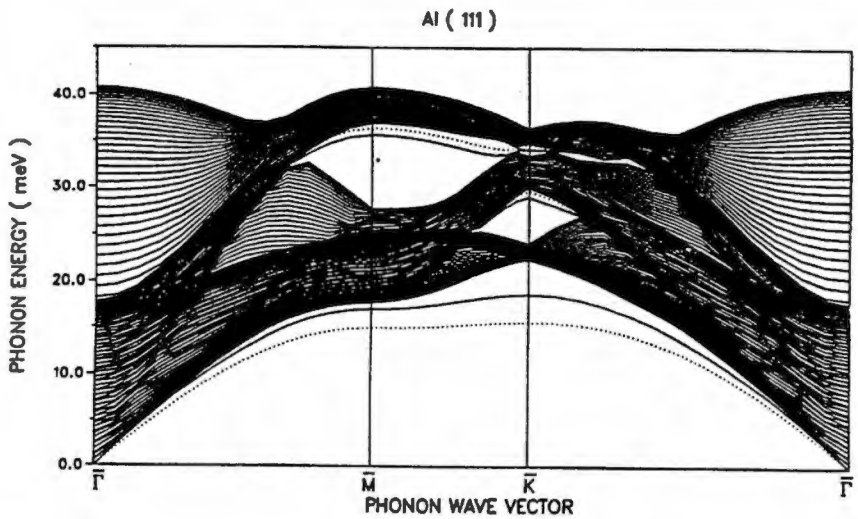


Figure 4.8: Surface phonons for the Al(111) surface: (a) dispersion of the Rayleigh waves, filled circles are experimental data and solid lines are calculations (a slab model where the force constants were adjusted) [17], (b) first principles calculations (solid lines) and surface modes as obtained from the force constants in the bulk (dotted lines) [18].

Table 4.2: Measured Rayleigh wave (*RW*) with respect to the *RW* from BT calculations (using bulk force constants) at the zone boundaries for close packed simple metal surfaces. β and χ are defined in equations (4.1) and (4.2) in the text.

	$\beta(\overline{K})$[%]	$\beta(\overline{M})$ [%]	χ [%]
Mg(0001) [this work]	+10.6	+5.0	+7.9
Be(0001) [6]	+9.8	-13.9	-1.5
Al(111) [17,18]	+16.2	+13.8	+15.0

In general, the bulk force constants can reproduce qualitatively the measured RW dispersions in the cases of the Mg(0001) and Al(111) surfaces. However, it is not true in the case of the Be(0001) surface. Before we discuss in detail the discrepancies between the measured RW and the RW from BT calculations, let's discuss the trend of the measured RW for close packed simple metal surfaces. If we define a quantity:

$$\Delta = \frac{RW(\overline{K}) - RW(\overline{M})}{(RW(\overline{K}) + RW(\overline{M}))/2} \times 100\% \qquad (4.3)$$

where $RW(\overline{K})$ and $RW(\overline{M})$ are the Rayleigh waves at $\overline{K}$ and $\overline{M}$, respectively, then the quantity Δ represents the information of the strength of the slope of the RW along the zone boundaries $\overline{K}$ to $\overline{M}$, i.e., if $\Delta = 0$, this means the RW along the zone boundaries $\overline{K}$ to $\overline{M}$ is dispersionless. The measured RW for the Mg(0001) surface at $\overline{K}$ and $\overline{M}$ is 14.50 meV and 13.50 meV, respectively, i.e., the surface phonon Rayleigh mode at $\overline{M}$ is *softer* than at $\overline{K}$. This behavior is similar to the case of Al(111) [17] and Be(0001) [4,6]. For Al(111), the measured Rayleigh modes at $\overline{K}$ and $\overline{M}$ are about 18.5 meV and 17.0 meV, respectively; while the measured Rayleigh modes of the Be(0001) surface are 43.50 meV at $\overline{K}$ and 39.50 meV at $\overline{M}$. By using equation (4.3), we find that $\Delta_{Mg(0001)}$(Exp)=+7.1%, $\Delta_{Be(0001)}$(Exp)=+9.6%, and $\Delta_{Al(111)}$(Exp)=+6.1%. The signs of the Δ's for Mg(0001), Be(0001), and Al(111) are the same, meaning the measured Rayleigh modes of the Mg(0001), Be(0001), and Al(111) surfaces have the same trend along the zone boundaries $\overline{K}$-$\overline{M}$. In fact, the sign of the Δ's for other close surfaces, such as Cu(111), Ag(111), and Au(111), are also positive [see ref. 19]. This might be a general rule that the surface phonon Rayleigh mode of a close-packed surface at $\overline{K}$ is higher than at $\overline{M}$. The magnitude of the Δ determines the strength of the dispersion of the surface phonon RW along the $\overline{K}$-$\overline{M}$ direction. This quantity should relate to the atomic bonding and the surface electronic

properties. The magnitude of the Δ's for the Mg(0001) surface is comparable to those of the Al(111) and Be(0001) surfaces, as expected from their electronic properties.

As shown in Figure 4.7, the surface phonon RW of Mg(0001) from BT calculations at $\overline{K}$ and $\overline{M}$ are 12.96 meV and 12.83 meV, respectively, or the values of the Δ from BT calculations for Mg(0001); $\Delta_{Mg(0001)}$(BT)=+1.0%, which is the same sign with the Δ from the experimental data. This means that, qualitatively, the interatomic force constants near the surface region of Mg(0001) are similar to the interatomic force constants in the bulk Mg. This behavior is similar to the case of Al(111) but contradicted to the Be(0001) surface, as shown in Figures 4.8 and 4.1, respectively. For the Al(111) surface, the surface phonon RW obtained from BT calculations at $\overline{K}$ and $\overline{M}$ are 15.4 meV and 15.0 meV [18], respectively; or $\Delta_{Al(111)}$(BT)=+3.3%. However, for the Be(0001) surface, as shown in Figure 4.1, the RW obtained from BT calculations at $\overline{K}$ and $\overline{M}$ are 39.25 meV and 45.0 meV [6], respectively; or $\Delta_{Be(0001)}$(BT)=-13.7%. Clearly, the sign of the Δ from BT calculations is different than from the experimental data, meaning the interatomic force constants near the surface region of Be(0001) is significantly different than in the bulk Be. The values of the RW and Δ for all cases are summarized in Table 4.3.

We have shown that the trend of the measured RW along the zone boundaries is the same for the three cases (Mg, Be, and Al), as was discussed above. However, when we compare the measure RW with the RW from BT calculations, we find that the trend of the measured RW is the same as obtained from BT calculations for Mg(0001) and Al(111), but it is not true in the case of the Be(0001) surface. In order to understand what happens here, we need to compare the bulk force constants for these three elements (Mg, Be, and Al). Figure 4.9 shows the measured and calculations (solid lines) bulk phonon dispersion for Mg [16] and Be [20] from Γ (zone center point) to K points in the bulk Brillouin zone. T_2 and T_3 branches denote the modes polarized perpendicular to the (0001) planes; while the other branches (T_1 and T_4) denote the modes polarized parallel to the (0001) planes.

Table 4.3: Rayleigh wave (*RW*) at the zone boundaries from experiment and BT calculations for close packed simple metal surfaces. Δ is the quantity defined in equation (4.3) in the text.

	$RW(\overline{K})$ [meV]	$RW(\overline{M})$ [meV]	Δ [%]
Experiment:			
Mg(0001) [this work]	14.5	13.5	+7.1
Be(0001) [6]	43.50	39.50	+9.6
Al(111) [17]	18.5	17.4	+6.1
BT Calculations:			
Mg(0001) [this work]	12.96	12.83	+1.0
Be(0001) [6]	39.25	45.0	-13.7
Al(111) [18]	15.5	15.0	+3.3

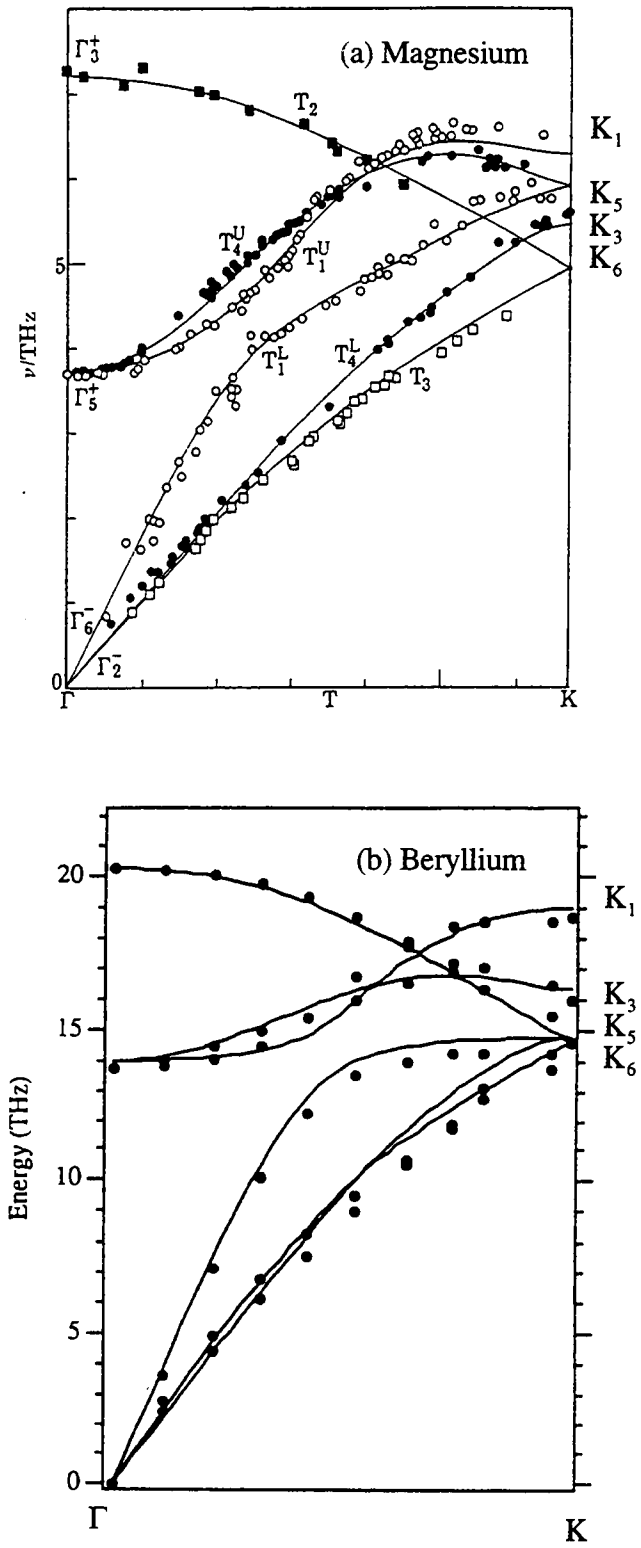


Figure 4.9: Measured bulk phonon dispersions along the Γ-K direction for magnesium [16] and beryllium [20].

There are three optical modes at Γ point with energies 15.2 meV, 15.2 meV, and 30 meV for Mg; and 57 meV, 57 meV, and 84 meV for Be. The atomic displacements for these modes are shown in Figure 6.1 of the reference 6. The lowest modes have the equal and opposite shear atomic displacements parallel to the (0001) planes; while the highest mode has the atomic displacements perpendicular to the (0001) planes. For Mg, the calculations by summing over eight nearest-neighbor shells of central forces (axially symmetric forces) are able to reproduce the experimental data very well [16]. The bulk phonon dispersion for Mg is similar to Be, except the mode K_5. For Mg, the energy of this mode lies between the modes K_1 and K_3; while for Be, this mode lies below the mode K_3 (see Figure 4.9). The important of this mode in the case of Be was examined by Roy *et al.* [21]. They found that if the interatomic force constants of Be were central forces, this mode (K_3) would lie between the modes K_1 and K_3; however, the interatomic force constants of Be should be non-central forces in order reproduce the experimental data. As shown in Figure 4.9(b), the calculations using non-central forces up to eight nearest-neighbor shells produce the experimental data very well. The measured bulk phonons of the Al together with the best-fit curves are shown in Figure 4.10 [22]. There is no optical mode for Al at Γ point and there are three modes at K and X points (one longitudinal mode and two transverse modes). Overall, the agreement between the experimental data and calculations by using eight-nearest-neighbor axially symmetric force constants (central forces) is excellent.

It is clear that the interatomic forces in the bulk Mg and Al are central forces (axially symmetric), but the interatomic forces in the bulk Be is non-central forces. The differences between the interatomic forces in the bulk Mg, Al and Be come from their electronic properties. The electronic properties of bulk Mg and Al are nearly-free-electron-like [23]; while the electronic properties of bulk Be are nearly semiconducting [5]. On the other hand, the electronic properties of the surfaces of Mg(0001) [13], Be(0001) [5], and Al(111) [24] are nearly-free-electron-like. Therefore, it is understood that the surface lattice dynamics of

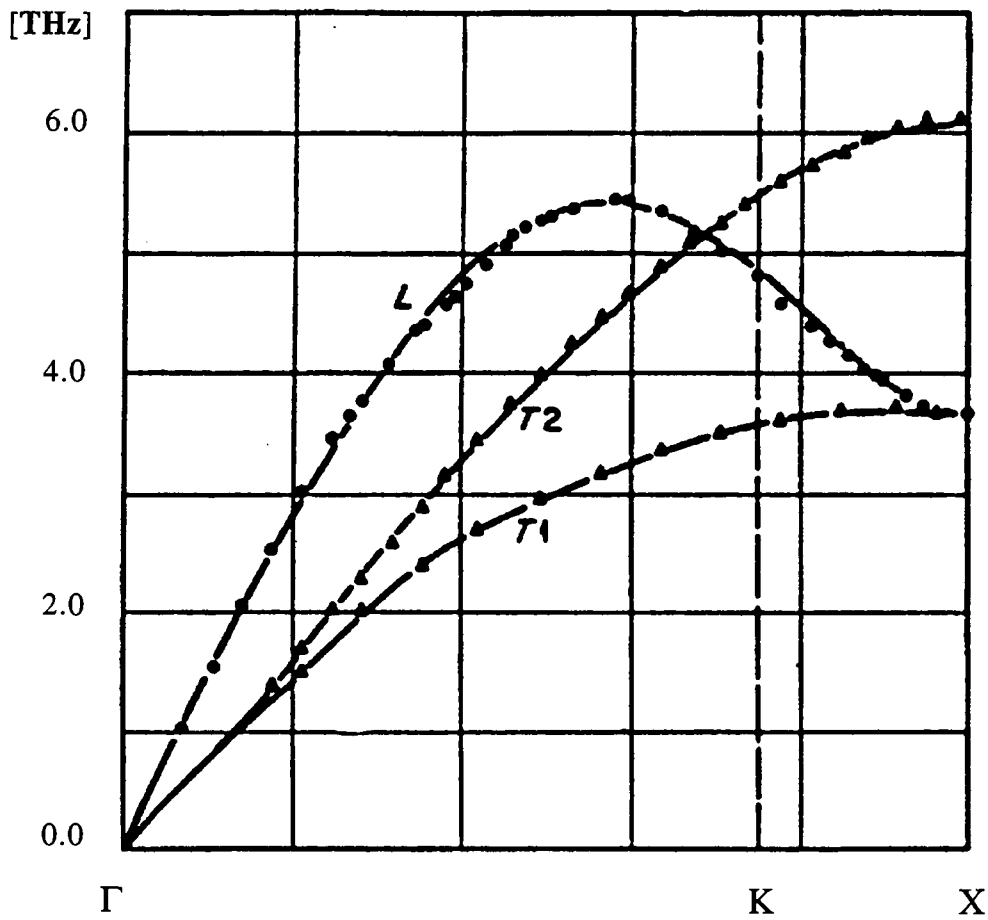


Figure 4.10: Measured bulk phonons (filled circles and triangles) for Al together with the calculations by using central forces (axially symmetric forces) [22].

Mg(0001), Be(0001), and Al(111) are similar. Furthermore, for Mg(0001) and Al(111), the bulk force constants are able to reproduce qualitatively the surface phonon dispersions, but not in the case of Be(0001) since the interatomic forces at the Be(0001) surface are significantly different than in the bulk Be. The values of $\beta(\overline{K})$, $\beta(\overline{M})$, and χ discussed above tell us qualitatively that the surface force constants become anistropic than in the bulk, and for the Be(0001), the surface forces are very anisotropic as reflected in the difference sign between $\beta(\overline{K})$ and $\beta(\overline{M})$. This simple argument is in agreement with the self-consistent calculations, showing enhanced non-central forces at the surface [1] due to the surface anisotropic-electronic environment.

4.2.3 Ab initio Calculations at T=0 K

The measured surface phonons at the Mg(0001) surface are also compared with the *ab initio* calculations by using density-functional perturbation theory (DFPT) by Bungaro and Kress [25]. The surface phonons were obtained by using a periodically repeated slab geometry with Mg(0001) slabs of 9 atomic layers separated by a vacuum region of $\approx$ 13 Å (equivalent to 5 atomic layers) with 21 k-points in the irreducible BZ. Energy minimization was performed in order to obtain the surface structure, finding the inter-layer spacings with respect to the bulk are Δd_{12}=+1.8(±0.3)%, Δd_{23}=+0.3(±0.3)%, and Δd_{34}=-0.5(±0.3)% which are in excellent agreement with our experimental data (see Chapter 3).

The calculated surface dispersion curves along the main symmetry directions of the surface Brillouin zone are shown in Figure 4.11, where they are compared to the experimental data. The solid lines indicate surface localized modes, defined by having more than 30% of the displacement amplitude in the first two layers and decaying exponentially into the bulk. Full circles indicate broad bands of surface resonances. The shaded areas are the range of surface projected bulk modes. The present EELS data are indicated by filled (open) diamonds which are intense (weak) losses.

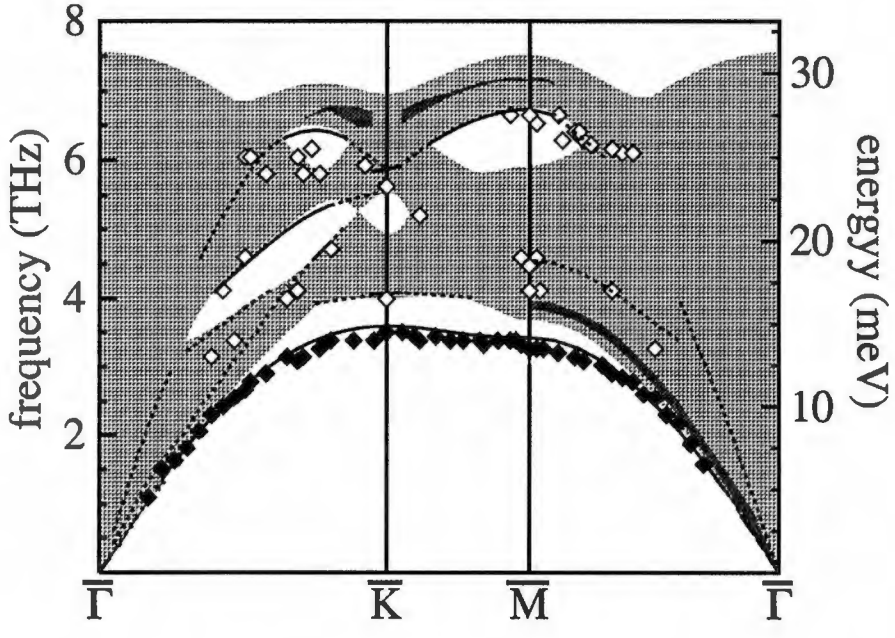


Figure 4.11: Surface phonon dispersion at the Mg(0001) surface. Solid lines are surface localized modes which are 30% in the first two layers; short-dashed lines are surface localized modes and surface resonances which are 15% in the first three layers; full circles are broad bands of surface resonances; EELS data are indicated by filled (open) diamonds which are intense (weak) losses, shaded area is surface-projected bulk modes.

Table 4.4 lists the surface phonon frequencies of Mg(0001) at two high-symmetry points ($\overline{K}$ and $\overline{M}$) of the surface BZ determined from *ab initio* calculations and experiment. Theoretically, three modes were found at $\overline{K}$ (see Table 4.4), where the square amplitudes of the atomic displacements for the modes at $\overline{K}$ are shown in Figure 4.12. The lowest mode (K_1) at energy 14.9 meV is the Rayleigh mode where the polarization of the atomic displacements is mainly vertical or normal to the surface. The atomic displacement of this mode is localized at the surface layer and decay exponentially into the bulk (see Figure 4.12). The amplitude of the atomic displacements perpendicular to the surface (z-component) can be described by [26]:

$$u_z = A_0 e^{-\lambda z} \cos(q_z z + \varphi) \qquad (4.4)$$

where λ is the penetration depth that depends on the energy of the phonon mode with respect to the bulk band edge. For example, if the energy difference between the RW and the bulk band edge is small (the RW is close to the band edge), the RW mode will decay slowly into the bulk. The Rayleigh mode K_1 is far from the bulk band edge, therefore this mode is localized in the top layer and fast decays perpendicular to the surface. There are two surface localized modes (K_2 and K_3) at 16.8 meV and 24.3 meV, respectively. Because these modes at the band edge, they penetrate deeper into the bulk and become the surface resonances as the wavevector emerges from $\overline{K}$. The lower frequency mode (K_2) is mainly polarized perpendicular to the surface. The displacement pattern of this mode has a maximum in the subsurface layer whereas the vibration amplitude of the surface layer only has a very small component in the sagittal plane. The displacement amplitude of the higher frequency mode (K_3) exhibits a peak at the surface layer, and it is polarized parallel to the surface. Along the $\overline{\Gamma}$-$\overline{K}$ direction, there are two surface modes near the upper edge of each of the two gaps in the bulk continuum. The mode at higher frequency, at about 26.5 meV, is mostly localized on the surface layer and is mainly longitudinally polarized. The surface

Table 4.4: Calculated and measured surface phonon frequencies of Mg(0001) at the two high symmetry points of SBZ, $\overline{K}$ and $\overline{M}$ [25]. Character and polarization of the corresponding atomic vibrations are described. Our experimental data are reported in parenthesis.

	ω (meV)	Character	Polarization
$\overline{K}$ point:			
K_1	14.9(14.5)	Rayleigh	Mainly Vertical
K_2	16.8(16.5)	Surface Mode	Mainly Vertical
K_3	24.3(23.5)	Surface Mode	Parallel to the surface
$\overline{M}$ point:			
M_1	14.2(13.5)	Rayleigh	Sagittal Vertical
M_2	15.8-16.4(17.0)	Resonances	Shear
M_3	18.9(18.5)	Resonance	Shear
M_4	27.8(27.5)	Surface Mode	Sagittal Longitudinal
M_5	29.7	Resonance	Sagittal (mainly Longitudinal)

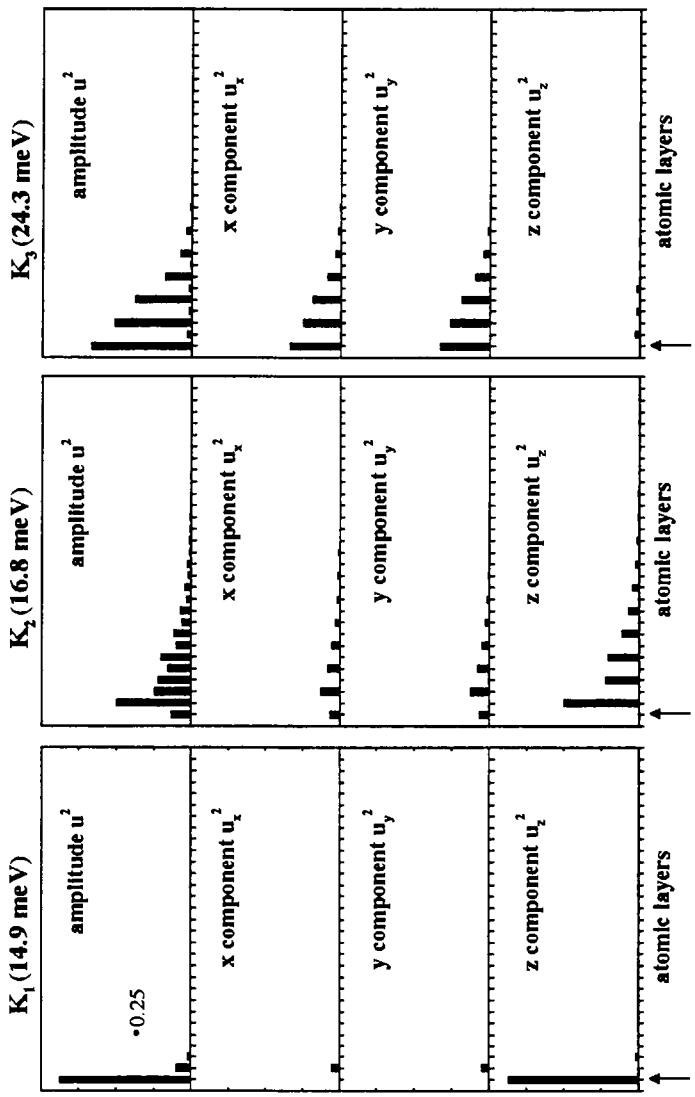


Figure 4.12: Square of the amplitude of the atomic displacements for the surface vibration at $\overline{K}$ point at the Mg(0001) surface. Arrow indicates the surface layer, x and y are in the plane, and z is normal to surface.

mode at lower frequency has a mixed sagittal and shear horizontal (SH) character. As the wavevector increases, the vertical component of the displacement amplitude develops a maximum in the second layer, and the vibration of the surface layer develops a dominant SH character. This mode is therefore detected by EELS only for smaller wave vectors, where the vibration of the surface layer still has a component in the sagittal plane. In the lower part of the spectrum we find the acoustic resonances with mainly SH and longitudinal polarization, respectively. At high frequencies, we also find a broad band of surface resonances which are mainly longitudinally polarized and have no displacement amplitude in the first layer.

There are five modes found theoretically at $\overline{M}$, which are listed in Table 4.4. The square amplitudes of the atomic displacements for the modes at $\overline{M}$ point are shown in Figure 4.13. The lowest mode (M_1) with energy of 14.2 meV is the Rayleigh mode where the polarization of the atomic displacements is sagittal vertical normal to the surface. Since this mode is far from the band edge, the atomic displacements of this mode is localized at the surface layer and fast decay exponentially into the bulk (see Figure 4.13). In the lower part of the spectrum, just above the Rayleigh mode, there are surface resonances at $\overline{M}$ called M_2 with energies of 16.8 - 16.4 meV and the SH mode (M_3) with energy of 18.9 meV. This surface resonance mode (M_2) goes to zero at $\overline{\Gamma}$ while the Shear mode (M_3) dies about half way across the zone. Both these modes are in the bulk band (see Figure 4.11), therefore the atomic displacements of these modes do not decay into the bulk. In the higher frequency region, at the edge of the gap at $\overline{M}$, there is a sagittal surface mode (M_4) with energy 27.8 meV with the atomic displacements mainly polarized along the $\overline{\Gamma}$-$\overline{M}$ direction. The polarization of this mode is therefore predominantly longitudinal for wave vectors parallel to $\overline{\Gamma}$-$\overline{M}$, but becomes of increasing SH character in the $\overline{K}$-$\overline{M}$ direction. The displacement pattern of this mode has a maximum in the first layer but penetrates deeper

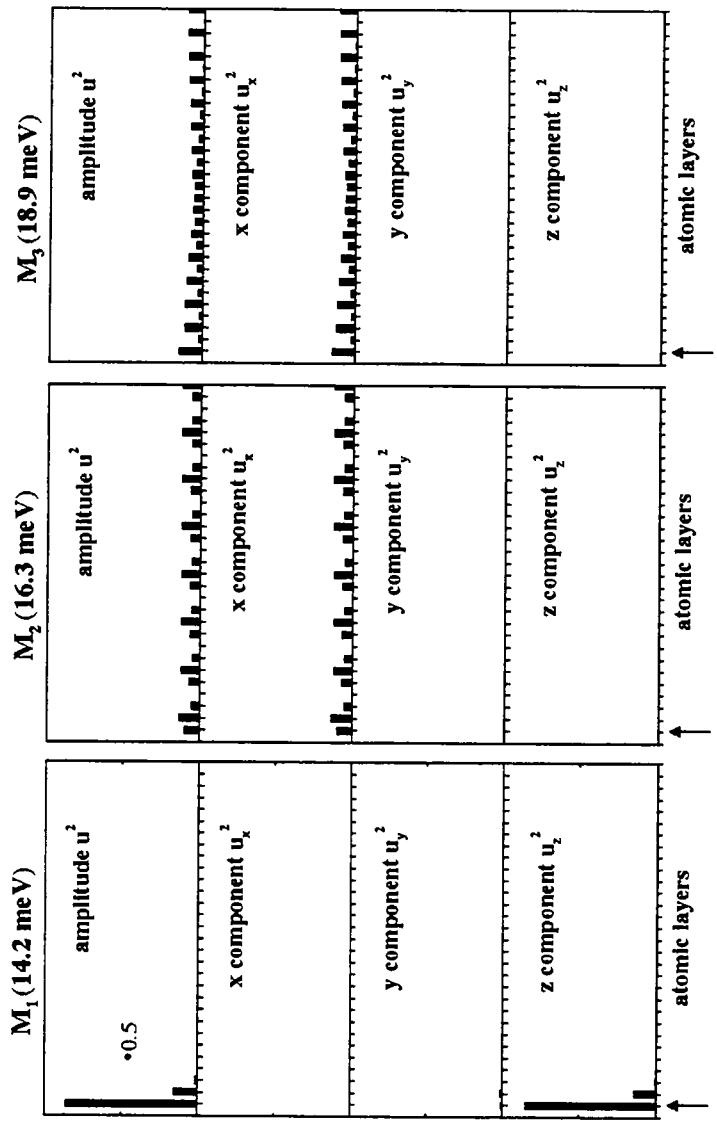


Figure 4.13: Square of the amplitude of the atomic displacements for the surface vibrations at the $\overline{M}$ points at the Mg(0001) surface. Arrow indicates the surface layer, x and y are in the plane, and z is normal to surface.

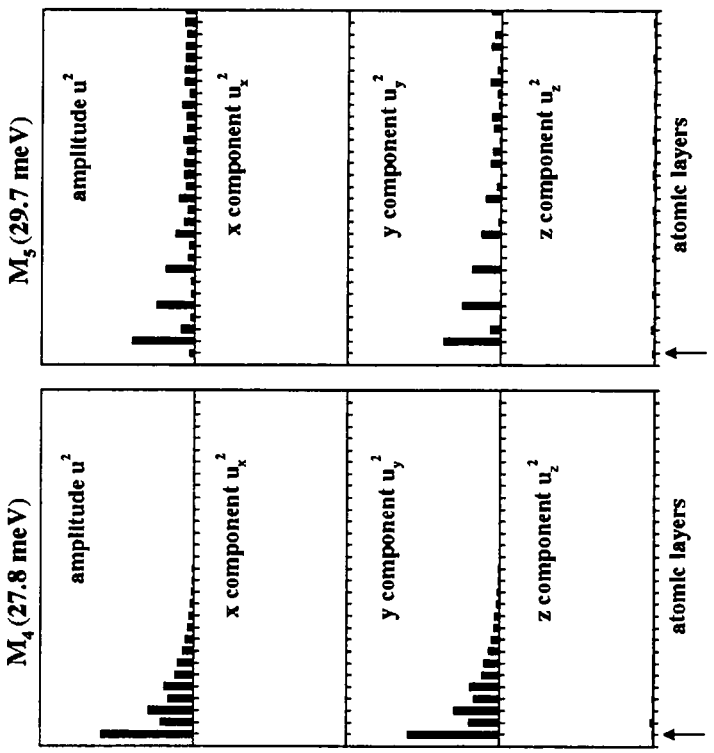


Figure 4.13: (continued)
Square of the amplitude of the atomic displacements for the surface vibrations at the $\overline{M}$ points at the Mg(0001) surface. Arrow indicates the surface layer, x and y are in the plane, and z is normal to surface.

into the bulk or decays slowly because this mode is at the edge of band gap. Above this surface mode at a frequency of approximately 29.7 meV, there is a broad band of the surface resonances (M_5), which is mainly polarized parallel to the $\overline{\Gamma}$-$\overline{M}$ direction. The displacement patterns of these surface resonances exhibit a maximum in the second layer while the atoms in the first layer are practically at rest. This mode is therefore difficult to be detected in surface sensitive experiments. Since these modes lay in the bulk band, therefore the atomic displacements of these modes penetrate deeper into the bulk. In general, our experimental data are in excellent agreement with the *ab initio* calculations, showing that three layers are involved in the surface dynamics.

4.2.4 Surface Anharmonicity of Mg(0001)

Temperature dependent surface phonons of Mg(0001) were measured at the zone boundary $\overline{K}$ (q=1.304 Å^{-1}) along the $\overline{\Gamma}$-$\overline{K}$ direction, as shown in Figure 4.14. From the surface phonon energy shifts and the intrinsic phonon widths, the surface anharmonicity at Mg(0001) can be obtained. At the zone boundary $\overline{K}$, the energy loss of the Rayleigh modes at room-temperature and low-temperature are 14.50 meV and 14.75 meV, respectively. The intrinsic widths of these modes at room-temperature and low-temperature are 1.30 meV and 1.00 meV, respectively. The extrapolation of our temperature-dependent experimental data (the Rayleigh modes) at $\overline{K}$ to T=0 K is in excellent agreement with the *ab initio* calculations [25], as shown in Figure 4.15(a). As the temperature increases, the phonon energy shifts linearly with the equation $E=14.9 - 0.0013.T$ meV (where T is the temperature in degree Kelvin). The slope of the surface phonon energy of the Mg(0001) surface is equal to - 0.0013 meV/K. The plot of the intrinsic width of the surface phonons at $\overline{K}$ as a function of the temperature is shown in Figure 4.15(b). It shows that the intrinsic width shifts linearly with temperature with the equation $W=0.796 + 0.0017.T$ meV. The slope of intrinsic width energy of the Mg(0001) surface is equal to +0.0017 meV/K that is

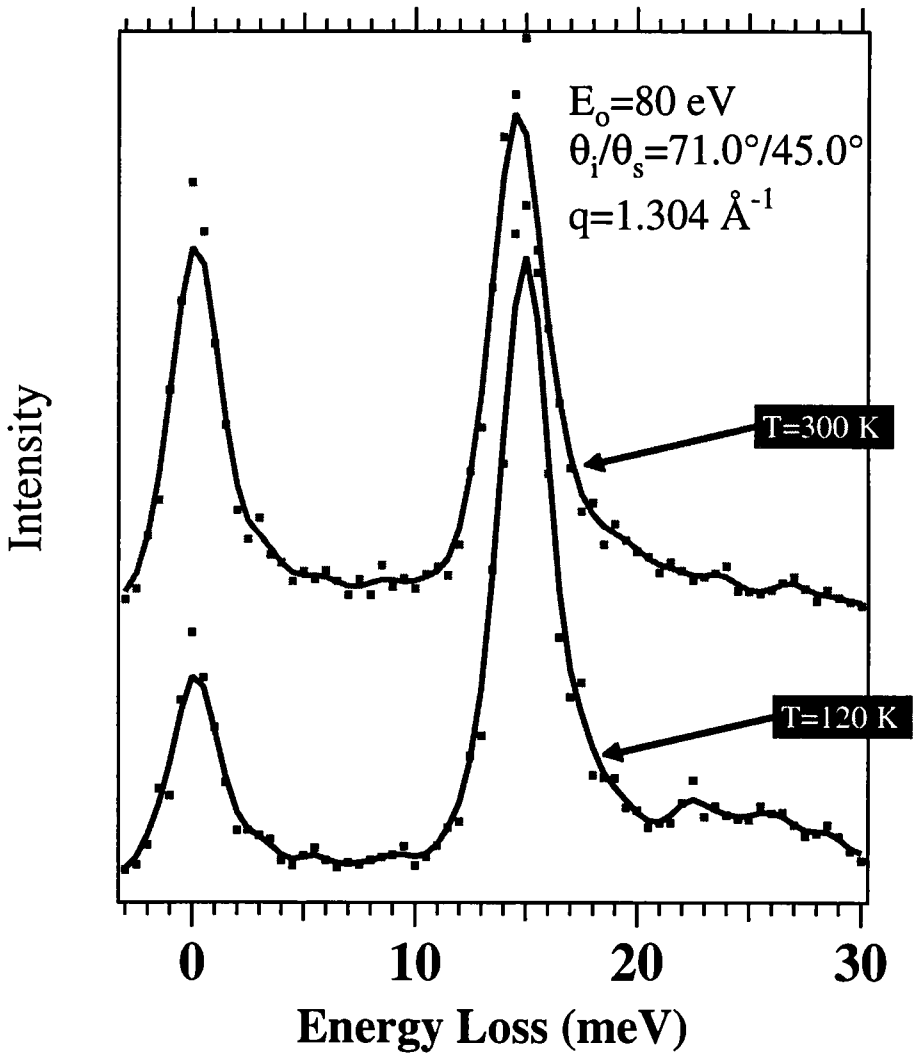


Figure 4.14: Temperature dependent phonons at the Mg(0001) surface along the $\overline{\Gamma}$-$\overline{K}$ direction at q=1.304 Å^{-1} (at $\overline{K}$ point).

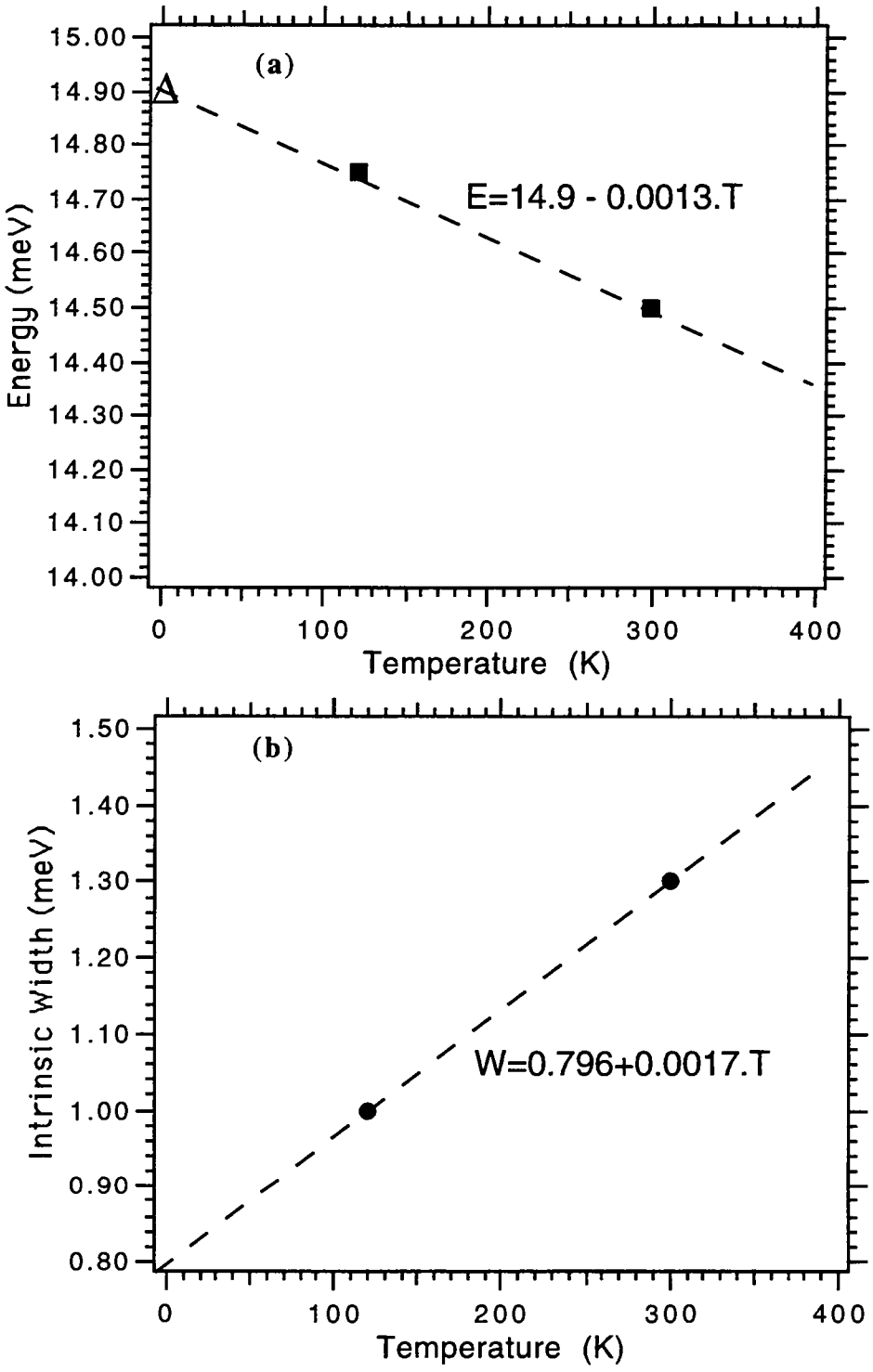


Figure 4.15: (a) Energy and (b) intrinsic width of surface phonons for the Mg(0001) surface as a function of temperatures at the zone boundary $\overline{K}$ along the $\overline{\Gamma}$-$\overline{K}$ direction.

almost the same as the magnitude of the slope of the phonon energy. To our knowledge, the temperature dependent bulk phonon of magnesium is still unknown. Since the thermal expansion of bulk aluminum is almost the same as that of magnesium, we assume that the slope of phonon energy of bulk magnesium is the same as that of bulk aluminum equal to -0.0014 meV/K [27]. In this assumption, the surface anharmonicity of Mg(0001) is almost the same as in the bulk. This behavior is similar to the case of the surfaces of Al(111) [28] and Be(0001) [6], where both surface anharmonicities of Be(0001) and Al(111) are almost the same as in the bulk. The observation of the surface anharmonicity at Mg(0001) is consistent with the temperature dependent structure measurements, as was discussed in Chapter 3; where the thermal expansion in the first interlayer at the Mg(0001) surface is the same as in the bulk.

4.3 Surface Phonons of Mg($10\bar{1}0$)

4.3.1 Experimental Data

The dispersion of the surface phonons along the high symmetry $\bar{\Gamma}$-$\bar{M}$ and $\bar{\Gamma}$-$\bar{A}$ directions of the Mg($10\bar{1}0$) surface were measured by HREELS at room-temperature with the energy resolutions of 4 - 7 meV. Figure 4.16 shows the geometry of the bulk truncated model of hcp($10\bar{1}0$) and its surface Brillouin zone. The impact energy was varied between 50 eV and 80 eV in order to obtain the highest phonon cross sections (intensities) at the zone boundaries. At $\bar{M}$ point (q=0.980 Å^{-1}) along the $\bar{\Gamma}$-$\bar{M}$ direction in the surface Brillouin zone, we found that the impact energy E_o=72 eV with the scattering geometry of incident angle θ_i=63.95° and scattering angle θ_s=45.0° produces the highest phonon cross sections, as shown in Figure 4.17. The intense feature in the spectrum at energy loss 14.0 meV is the Rayleigh mode. At the energy loss zero is the quasi-elastic peak, where it is small in comparison to the phonon peak. This means that the crystal has less defects and

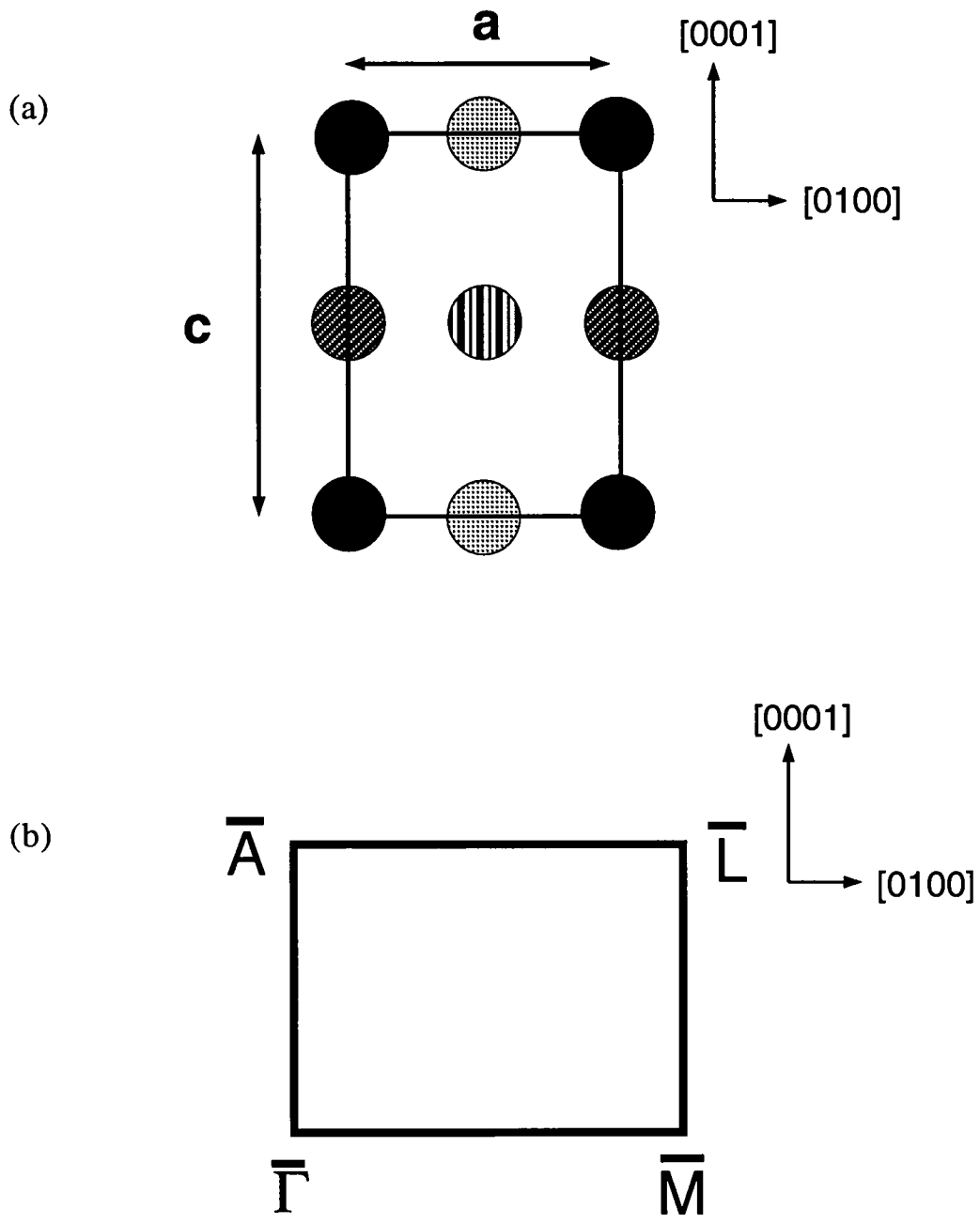


Figure 4.16: (a) Top view of the bulk truncated geometric of the hcp($10\bar{1}0$) surface and (b) its surface Brillouin zone.

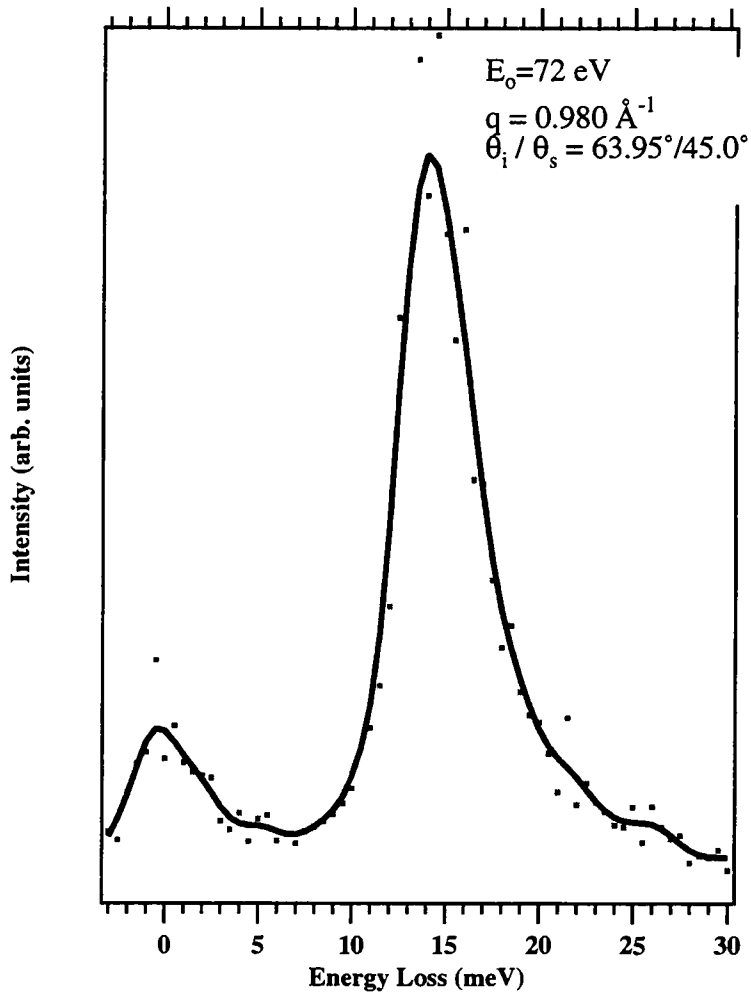


Figure 4.17: EELS spectrum from the Mg(10$\bar{1}$0) surface at $\overline{M}$ along the $\overline{\Gamma}$-$\overline{M}$ direction. Dots are raw data and solid line is smoothed data.

we have the "correct" scattering geometry and impact energy at $\overline{M}$. At the zone boundary $\overline{A}$ point (q=0.60 Å^{-1}) along the $\overline{\Gamma}$-$\overline{A}$ direction of the surface Brillouin zone, we found that the impact energy E_o=65.5 eV, with the scattering geometry of incident angle θ_i=58.3° and scattering angle θ_s=45.0, produces the highest phonon cross sections, as shown in Figure 4.18. The intense feature in the spectrum at energy loss 9.0 meV is the Rayleigh mode. A series of EELS spectra was measured along the $\overline{\Gamma}$-$\overline{M}$ and $\overline{\Gamma}$-$\overline{A}$ directions of the surface Brillouin zone (SBZ). Some of our EELS spectra along the $\overline{\Gamma}$-$\overline{M}$ and $\overline{\Gamma}$-$\overline{A}$ directions are shown in Figures 4.19 and 4.20, respectively. The dots are raw data and the solid lines are the smoothed data. The energy of the Rayleigh mode is assigned by the peak position indicated by a vertical line.

We performed slab calculations by using the Born-von Kármán model for the Mg(10$\bar{1}$0) surface with a bulk truncated (BT) termination as was described in the previous section. A 254 layer slab of Mg with force constants for up to seventh nearest-neighbor interactions, where the force constants (central force) were determined by a fit to bulk phonons of Mg measured by neutron scattering [16] listed in Table 4.1, was used in the calculations. The calculation for a layer slab more than 254 layers produced the same result as a 254 layer slab calculation. The measured and bulk truncated calculated phonon dispersions of the Mg(10$\bar{1}$0) surface are shown in Figure 4.21. The shaded regions represent the projection of bulk phonon modes onto the Mg(10$\bar{1}$0) surface. The filled squares indicate the contribution from the surface modes and unfilled circles are the experimental data. We adopt the convention of calling the vibrational modes at the zone boundaries by their ordering, starting with the lowest to highest energy, i.e., M_1, M_2, M_3, etc. There are seven modes predicted at $\overline{M}$ by BT calculations where their atomic displacement amplitudes (normalized to unity) and the phases (given in degree) are listed in Table 4.5. The lowest mode with energy 13.26 meV (M_1) is the Rayleigh mode with the

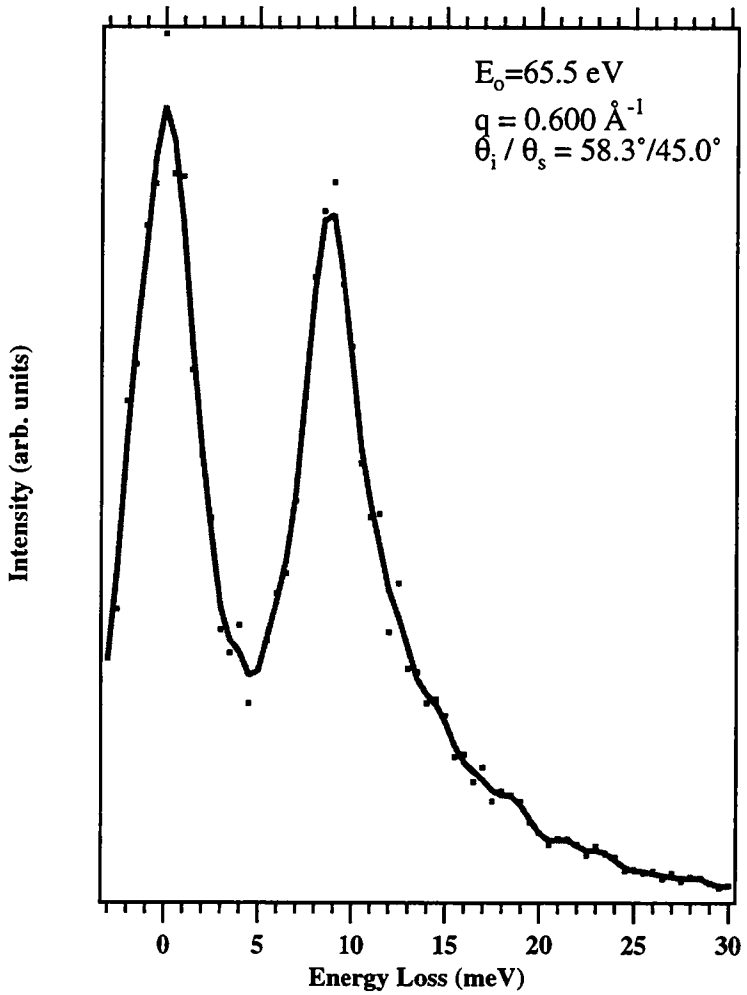


Figure 4.18: EELS spectrum from the Mg(10$\bar{1}$0) surface at $\overline{A}$ along the $\overline{\Gamma}$-$\overline{A}$ direction. Dots are raw data and solid line is smoothed data.

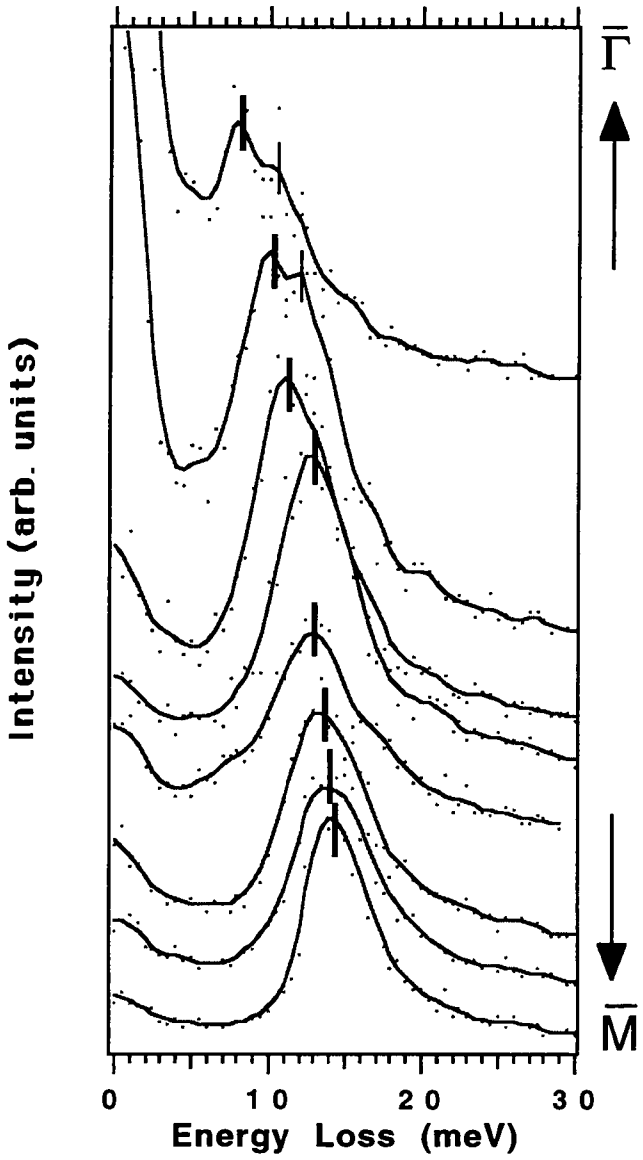


Figure 4.19: A series of EELS spectra at the Mg(10$\bar{1}$0) surface along the $\bar{\Gamma}$-$\bar{M}$ direction. Dots are raw data and solid line is smoothed data. The Rayleigh modes are indicated by peak positions (vertical lines).

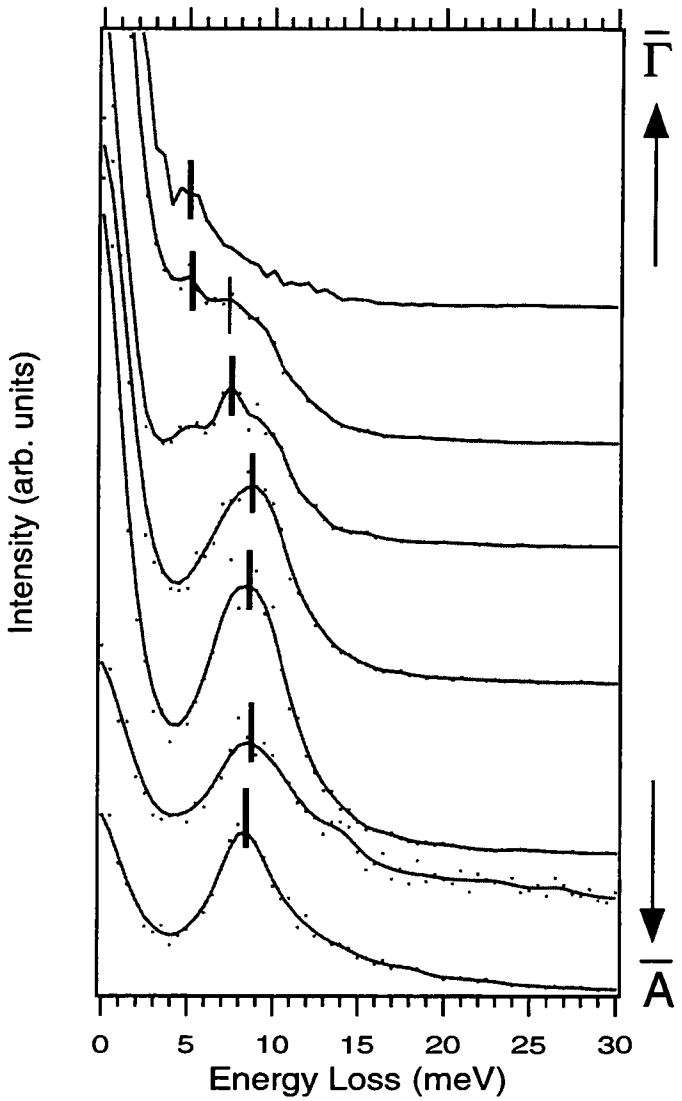


Figure 4.20: A series of EELS spectra at the Mg(10$\bar{1}$0) surface along the $\bar{\Gamma}$-$\bar{A}$ direction. Dots are raw data and solid lines are smoothed data. The Rayleigh modes are indicated by peak positions (vertical lines).

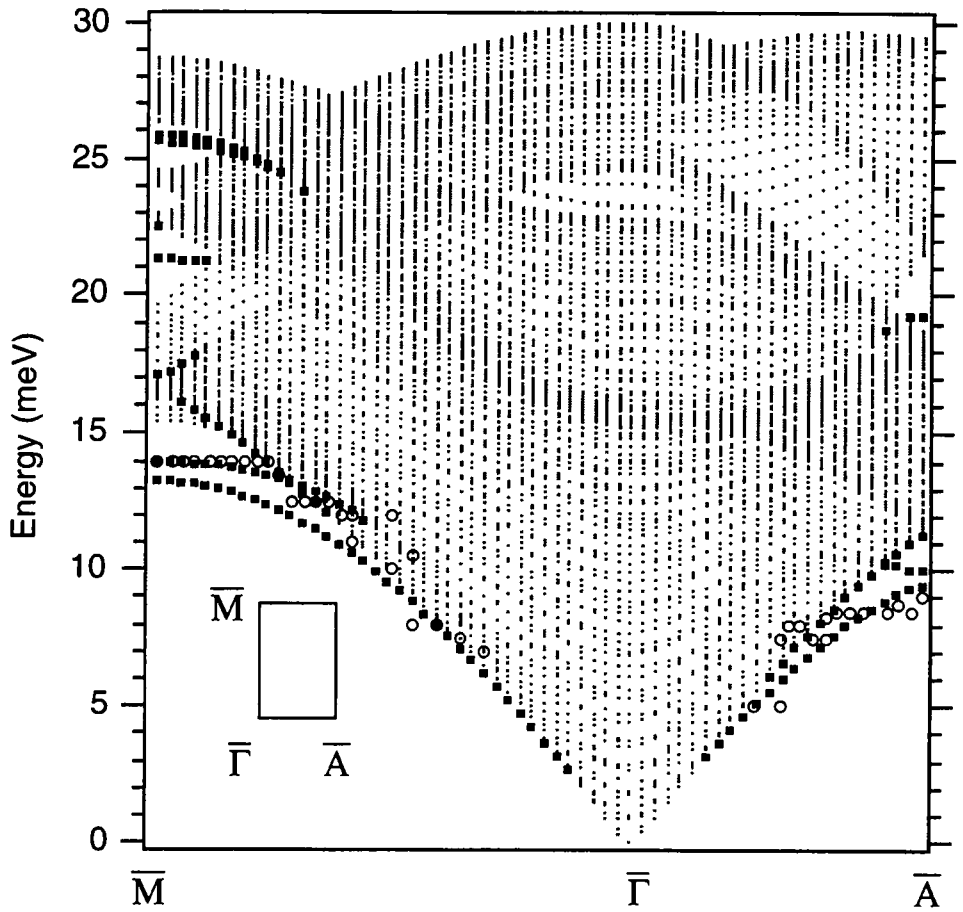


Figure 4.21: Measured surface phonon dispersion for Mg($10\bar{1}0$) together with a calculation for a bulk-terminated 254 layer slab. The filled squares are calculated modes and unfilled circles are experimental data. The shaded area is the projected bulk band. The inset shows the irreducible quarter of the surface Brillouin zone.

Table 4.5: Displacement amplitudes (normalized to unity) and the phase (in degree) for surface modes at the zone boundary $\overline{M}$ of the Mg($10\bar{1}0$) surface.

	M_1	ϕ_1	M_2	ϕ_2	M_3	ϕ_3	M_4	ϕ_4
x1	0.000	+0.0	0.000	+0.0	0.905	+25.0	0.000	+0.0
y1	0.001	+0.0	0.210	+90.0	0.000	+0.0	0.214	-30.0
z1	0.912	+0.0	0.003	+0.0	0.000	+0.0	0.001	+0.0
x2	0.000	+0.0	0.000	+0.0	0.013	+25.0	0.000	+0.0
y2	0.179	+90.0	0.001	+0.0	0.000	+0.0	0.001	+0.0
z2	0.003	+0.0	0.777	+180.0	0.000	+0.0	0.475	-120.0
x3	0.000	+0.0	0.000	+0.0	0.014	+25.0	0.000	+0.0
y3	0.220	+90.0	0.001	+0.0	0.000	+0.0	0.000	+0.0
z3	0.003	+0.0	0.455	+180.0	0.000	+0.0	0.771	+60.0
x4	0.000	+0.0	0.000	+0.0	0.266	+25.0	0.000	+0.0
y4	0.001	+0.0	0.244	-90.0	0.000	+0.0	0.001	+0.0
z4	0.230	+180.0	0.003	+0.0	0.000	+0.0	0.004	+0.0
x5	0.000	+0.0	0.000	+0.0	0.303	+25.0	0.000	+0.0
y5	0.001	+0.0	0.001	+0.0	0.000	+0.0	0.152	+150.0
z5	0.150	+180.0	0.189	-0.0	0.000	+0.0	0.001	+0.0
x6	0.000	+0.0	0.000	+0.0	0.009	+25.0	0.000	+0.0
y6	0.075	-90.0	0.001	+0.0	0.000	+0.0	0.000	+0.0
z6	0.001	+0.0	0.132	-0.0	0.000	+0.0	0.073	+60.0

Table 4.5: (continued)
Displacement amplitudes (normalized to unity) and the phase (in degree) for surface modes at the zone boundary $\overline{M}$ of the Mg($10\bar{1}0$) surface.

	M_5	ϕ_5	M_6	ϕ_6	M_7	ϕ_7
x1	0.000	+0.0	0.000	+0.0	0.000	+0.0
y1	0.004	+0.0	0.001	+0.0	0.900	+70.0
z1	0.079	+180.0	0.057	-10.0	0.000	+0.0
x2	0.000	+0.0	0.000	+0.0	0.000	+0.0
y2	0.321	+90.0	0.819	-100.0	0.001	+0.0
z2	0.003	+0.0	0.000	+0.0	0.094	-20.0
x3	0.000	+0.0	0.000	+0.0	0.000	+0.0
y3	0.106	-90.0	0.223	+80.0	0.002	+0.0
z3	0.008	+0.0	0.000	+0.0	0.197	-20.0
x4	0.000	+0.0	0.000	+0.0	0.000	+0.0
y4	0.007	+0.0	0.001	+0.0	0.015	+70.0
z4	0.506	+180.0	0.254	+170.0	0.000	+0.0
x5	0.000	+0.0	0.000	+0.0	0.000	+0.0
y5	0.003	+0.0	0.000	+0.0	0.337	+70.0
z5	0.494	-0.0	0.170	-10.0	0.000	+0.0
x6	0.000	+0.0	0.000	+0.0	0.000	+0.0
y6	0.004	+0.0	0.305	-100.0	0.000	+0.0
z6	0.019	-0.0	0.000	+0.0	0.072	-20.0

atomic displacement mainly vertical localized in the first layer. For this mode, the atom in the fourth layer also moves vertically with the opposite phase (+180°) as shown in the Table 4.5. Experimentally, we observed this mode with energy loss 14 meV, as shown in Figure 4.17 (intense feature). The second lowest mode with energy 13.93 meV(M_2) is also the Rayleigh mode with the atomic displacement mainly vertical but localized in the second and third layers. This mode was not observed experimentally since it is in the sublayer. The mode with energy 17.13 meV(M_3) is the SH mode with the atomic displacement parallel to the $\overline{\Gamma}$-$\overline{A}$ direction; therefore, this mode can not be observed experimentally in this direction since the displacement is odd with respect to the scattering plane, such vibrational mode can not be excited in this direction. The mode with energy 21.27 meV(M_4) is the surface mode with the atomic displacement mainly vertical but localized in the third layer, making it difficult to be detected experimentally. There is a surface mode with energy 22.53 meV(M_5) with the atomic displacement mainly vertical localized in the fourth layer. The surface mode with energy 25.6 meV(M_6) has the atomic displacement parallel to the $\overline{\Gamma}$-$\overline{M}$ direction localized in the second layer that is also difficult to be detected. The highest mode with energy 25.87 meV(M_7) is the surface mode localized in the surface layer with the atomic displacement parallel to the $\overline{\Gamma}$-$\overline{M}$ direction. Experimentally, we observed this mode with energy about 26 meV, i.e., the small peak as shown in Figure 4.17. At the zone boundary $\overline{A}$ point, BT calculations predict four modes where their atomic displacement amplitudes (normalized to unity) and the phases (given in degree) are listed in the Table 4.6. The lowest mode with energy 9.44 meV (A_1) is the Rayleigh mode with the atomic displacement mainly vertical localized in the first and third layers as shown in Table 4.6. This mode was observed experimentally with energy loss 9.0 meV as shown in Figure 4.18. The second lowest mode with energy 10 meV(A_2) is the Rayleigh mode with the atomic displacement mainly vertical but localized in the second and fourth layers. This mode was not observed experimentally since it is in the sublayer. The mode with energy

Table 4.6: Displacement amplitudes (normalized to unity) and the phase (in degree) for surface modes at the zone boundary $\bar{A}$ of the Mg($10\bar{1}0$) surface.

	A_1	ϕ_1	A_2	ϕ_2	A_3	ϕ_3	A_4	ϕ_4
x1	0.016	-90.0	0.391	-90.0	0.000	+0.0	0.779	-90.0
y1	0.000	+0.0	0.000	+0.0	0.080	-180.0	0.000	+0.0
z1	0.785	-0.0	0.039	+180.0	0.000	+0.0	0.010	+0.0
x2	0.079	+90.0	0.008	+0.0	0.000	+0.0	0.005	+0.0
y2	0.000	+0.0	0.000	+0.0	0.649	-180.0	0.000	+0.0
z2	0.033	-0.0	0.710	+0.0	0.000	+0.0	0.371	-180.0
x3	0.004	+0.0	0.074	+90.0	0.000	+0.0	0.500	-90.0
y3	0.000	+0.0	0.000	+0.0	0.076	-180.0	0.000	+0.0
z3	0.499	-0.0	0.021	-180.0	0.000	+0.0	0.006	+0.0
x4	0.082	+90.0	0.004	+0.0	0.000	+0.0	0.011	-90.0
y4	0.000	+0.0	0.000	+0.0	0.485	-180.0	0.000	+0.0
z4	0.021	-0.0	0.455	+0.0	0.000	+0.0	0.012	+0.0
x5	0.004	+0.0	0.071	+90.0	0.000	+0.0	0.026	+90.0
y5	0.000	+0.0	0.000	+0.0	0.067	-180.0	0.000	+0.0
z5	0.282	+0.0	0.010	-180.0	0.000	+0.0	0.006	+0.0
x6	0.048	+90.0	0.002	+0.0	0.000	+0.0	0.010	-90.0
y6	0.000	+0.0	0.000	+0.0	0.367	-180.0	0.000	+0.0
z6	0.013	-0.0	0.277	+0.0	0.000	+0.0	0.033	-180.0

11.32 meV (A_3) has a SH character localized in the second and fourth layers with atomic displacement perpendicular to the $\bar{\Gamma}$-$\bar{A}$ direction; therefore, this mode can not be observed experimentally because it is in the sublayer and the atomic displacement is odd with respect to the scattering plane (such vibrations can not be excited). The surface mode with energy 19.29 meV(A_4) has the atomic displacement parallel to $\bar{\Gamma}$-$\bar{A}$ direction localized in the surface layer. However, this mode was not observed experimentally because of the impact energy and scattering geometry of EELS experiment.

4.3.2 A Comparison of Mg(10$\bar{1}$0) with Be(10$\bar{1}$0) and Al(110)

Similar to the previous section, by using the BT calculations, we compare the surface lattice dynamics of Mg(10$\bar{1}$0) with Be(10$\bar{1}$0) and Al(110) in an attempt to understand the nature of the surface force constants at open surface metals and correlate them with the electronic and structural properties.

As shown in Figure 4.21, the measured RW at $\bar{M}$ and $\bar{A}$ of Mg(10$\bar{1}$0) are 14.0 meV and 9.0 meV, respectively. So, the measured RW at $\bar{M}$ is higher than that of at $\bar{A}$. This behavior is similar to Be(10$\bar{1}$0) [15] and Al(110) [29]. For the Be(10$\bar{1}$0) surface, the measured RW at $\bar{M}$ is 40.0 meV and at $\bar{A}$ is 31.5 meV [15]; while for the Al(110) surface, the measured RW at $\bar{X}$ is 14.6 meV and at $\bar{Y}$ is 8.9 meV [29]. This means that the atomic bonding at $\bar{A}$ (or at $\bar{Y}$ for fcc(110)) is softer than that at $\bar{M}$ (or at $\bar{X}$). By using equation (4.3), we find that $\Delta_{Mg(10\bar{1}0)}$(Exp)=+21.7%, $\Delta_{Be(10\bar{1}0)}$(Exp)=+11.9%, and $\Delta_{Al(110)}$(Exp)=+24.3%. The measured RW mode at $\bar{A}$ is softer than that of at $\bar{M}$ for the Mg(10$\bar{1}$0) and Be(10$\bar{1}$0) surfaces and the measured RW mode at $\bar{Y}$ is softer than that of at $\bar{X}$ for the Al(110) surface. These mean that the atomic bonding at $\bar{A}$ (or at $\bar{Y}$) is *softer* than that at $\bar{M}$ (or at $\bar{X}$). While from the BT calculations, we find that

$\Delta_{Mg(10\bar{1}0)}$(BT)=+16.8%, $\Delta_{Be(10\bar{1}0)}$(BT)=+6.2% [15], and $\Delta_{Al(110)}$(BT)=+27.5% [30]. The values of the RW and Δ from experimental data and BT calculations for all three cases are listed in Table 4.7. Clearly, the measured and calculated Rayleigh modes of the Mg(10$\bar{1}$0), Be(10$\bar{1}$0), and Al(110) surfaces have the same trend at the zone boundaries. The magnitude of the Δ of the Mg(10$\bar{1}$0) surface is comparable to that of the Al(110) as expected from the electronic properties. However, the magnitude of the Δ of the Be(10$\bar{1}$0) surface is rather smaller than that of Mg(10$\bar{1}$0).

For the Mg(10$\bar{1}$0) surface; there are two the Rayleigh modes with the energies of 13.26 meV (M_1) and 13.93 meV(M_2) predicted by BT calculations at $\overline{M}$. The lowest Rayleigh mode (M_1) has the atomic displacements mainly vertical localized in the first layer; while the second lowest mode with energy 13.93 meV(M_2) has the atomic displacement mainly vertical but localized in the second layer. Experimentally, we just observed one mode with energy loss 14.0 meV, as shown in Figure 4.17. We believe this mode is the Rayleigh mode corresponding to M_1 mode because the Rayleigh mode M_2 is difficult to be detected experimentally since it is localized in the sublayer. By using equation (4.1), we find that $\beta(\overline{M})$=+5.3%. Thus, for the Mg(10$\bar{1}$0), the RW from BT calculations at $\overline{M}$ is *softer* than the measured RW. This behavior is similar to the case of the Mg(0001) surface. At $\overline{A}$ point, there are also two Rayleigh modes with energies 9.44 meV (A_1) and 10.0 meV(A_2) predicted by BT calculations; while experimentally we just observed one mode with energy loss 9.0 meV, as shown in the Figure 4.17, and this mode is the Rayleigh mode corresponding to A_1 mode since the Rayleigh mode A_2 is localized in the sublayer that cannot be detected experimentally. At the zone boundary $\overline{A}$, $\beta(\overline{A})$=-4.9%, meaning the RW from BT calculations is *stiffer* than the measured one at Mg(10$\bar{1}$0). By using equation (4.2), we find the slope of the RW from BT calculations with respect to the

Table 4.7: Rayleigh wave (*RW*) at the zone boundaries from experiment and BT calculations for open simple metal surfaces. Δ is the quantity defined in equation (4.3) in the text.

	$RW(\overline{M})$ or $RW(\overline{X})$ [meV]	$RW(\overline{A})$ or $RW(\overline{Y})$ [meV]	Δ [%]
Experiment:			
Mg($10\bar{1}0$) [this work]	14.0	9.0	+21.7
Be($10\bar{1}0$) [15]	40.0	31.5	+11.9
Al(110) [29]	14.6	8.9	+24.3
BT Calculations:			
Mg($10\bar{1}0$) [this work]	13.26	9.44	+16.8
Be($10\bar{1}0$) [15]	43.0	38.0	+6.2
Al(110) [30]	15.3	8.7	+27.5

measured RW χ=+1.3%. Since the sign of $\beta(\overline{M})$ is different than that of $\beta(\overline{A})$ and χ, qualitatively, the atomic bonding near the surface region of Mg(10$\bar{1}$0) is not isotropic and the surface force constants is *significantly* different than in the bulk.

In comparison with the surface phonons of Be(10$\bar{1}$0); as shown in Figure 4.22, BT calculations predicted two the Rayleigh modes with energies 43.0 meV (M_1) and 43.50 meV(M_2) at $\overline{M}$ with the atomic displacements mainly vertical localized in the first layer and second layer, respectively [15]. There was only one surface mode observed experimentally with energy loss about 40.0 meV [15], corresponding to M_1 mode. Thus, for Be(10$\bar{1}$0), the RW from BT calculations at $\overline{M}$ is *stiffer* than the measured RW, $\beta(\overline{M})$=-7.5%, which is different than in the case of the Mg(10$\bar{1}$0) surface. At $\overline{A}$ of Be(10$\bar{1}$0), there are two Rayleigh modes with energies about 37.0 meV (A_1) and 38.0 meV(A_2) predicted by BT calculations [15] with the atomic displacements polarized in the sagittal plane localized in the second and first layer, respectively. These are contradicted with the atomic displacements at $\overline{A}$ for Mg(10$\bar{1}$0); where the modes A_1 and A_2 localized in the first and second layer, respectively. The measured RW for Be(10$\bar{1}$0) is with energy loss about 31.5 meV, corresponding to A_2 mode [15]. Thus, the RW from BT calculations is *stiffer* than the measured one, $\beta(\overline{A})$=-20.6%, that is similar to the case of the Mg(10$\bar{1}$0) surface. The slope of the RW from BT calculations with respect to the measured RW for Be(10$\bar{1}$0) χ is -13.3%, which is opposite sign with that of Mg(10$\bar{1}$0). In contrast to Be(10$\bar{1}$0), there is no any mode observed at the center of zone boundary $\overline{\Gamma}$ of the Mg(10$\bar{1}$0) surface.

Figure 4.23 shows the surface phonons of Al(110) for relaxed and unrelaxed surface by Ho and Bohnen [30] together with the experimental data by Tonnies [29]. At $\overline{X}$ of Al(110), there are three modes predicted from BT calculations (unrelaxed surface with bulk force constants) below the projected bulk band with energies 15.3 meV (X_1) and 16.0

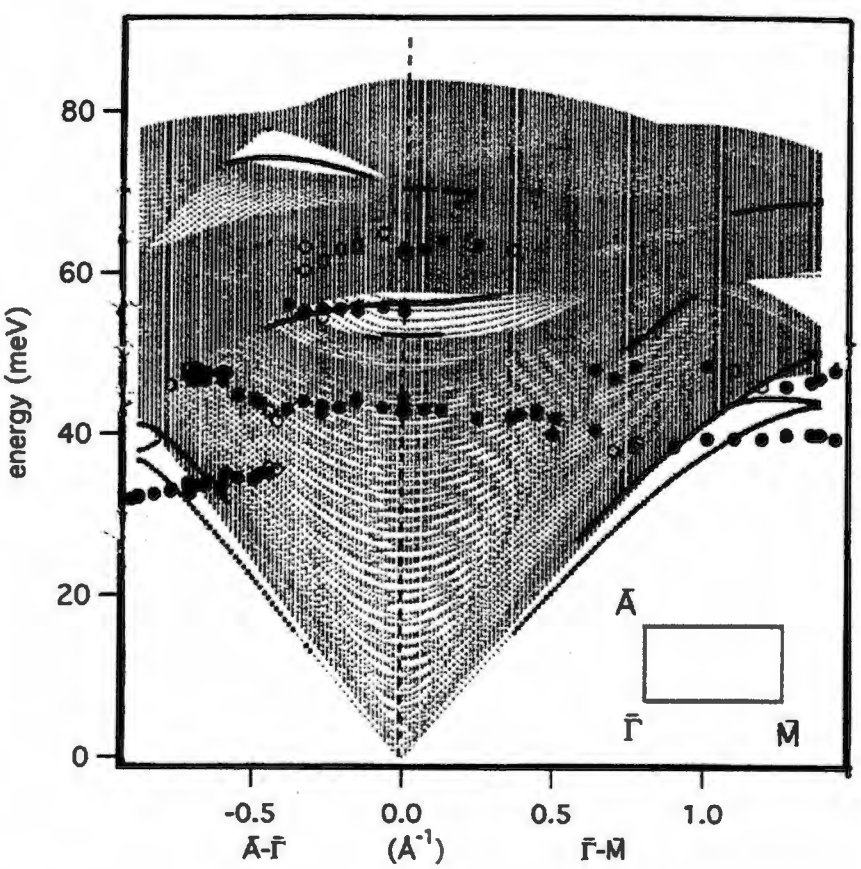


Figure 4.22: Measured surface phonon dispersion for the Be($10\bar{1}0$) surface (filled and unfilled circles) together with a bulk-truncated calculations by using the bulk force constants [15].

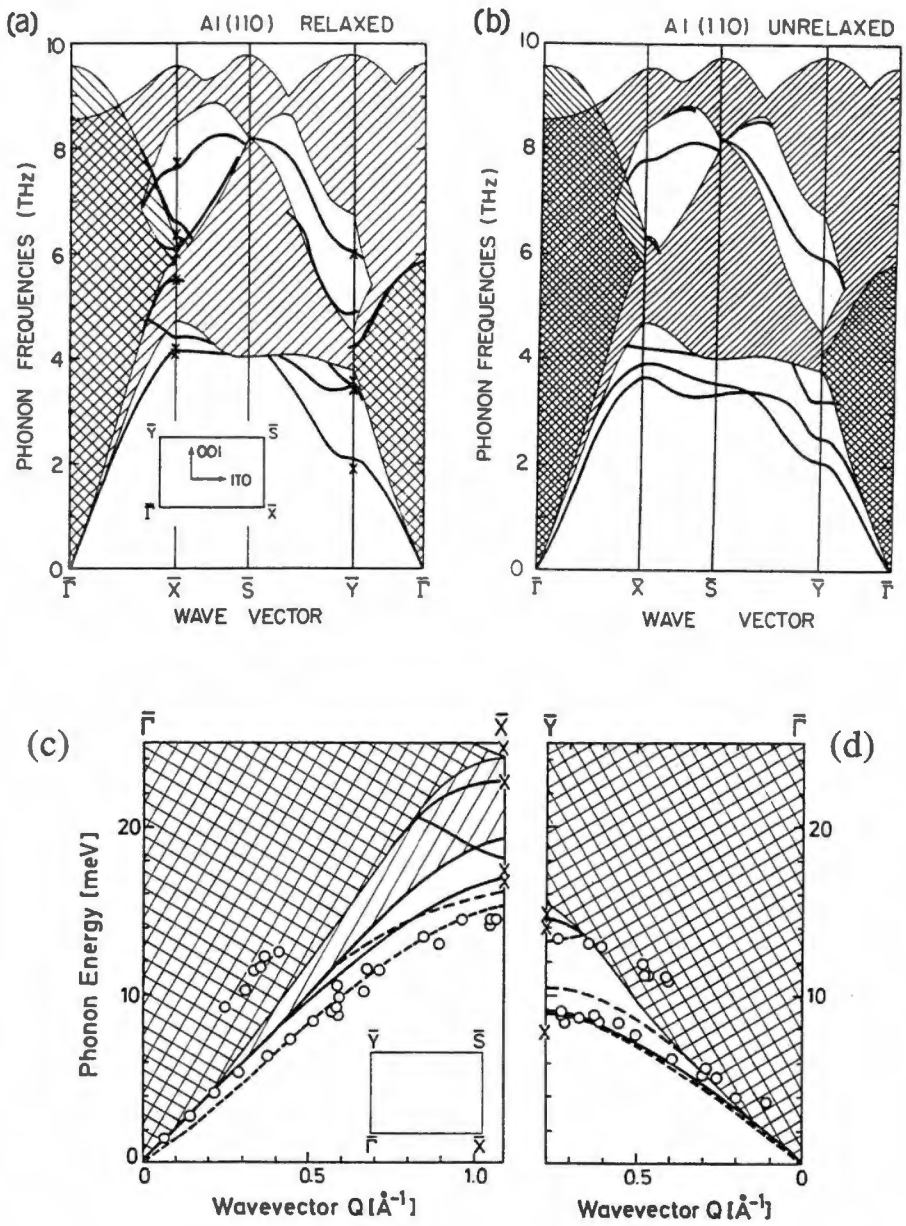


Figure 4.23: Surface phonon dispersion for the Al(110) surface: (a) relaxed surface and (b) unrealxed surface by using the bulk force constants [30]; (c) and (d) the measured phonon dispersion (unfilled circles) [29] together with calculations [30]; the solid line indicate the surface modes for relaxed surface, the crosses indicate frozen phonons, dashed lines indicate the surface phonon dispersion for the unrelaxed surface as obtained from the bulk force constants.

meV (X_2), 17.3 meV (X_3) with the atomic displacements perpendicular (X_1) and parallel (X_2 and X_3) to the surface; while experimentally, there was only one mode observed with energy 14.6 meV [29], corresponding to X_1 mode. Therefore, the surface mode from BT calculations is *stiffer* than the measured surface mode at $\overline{X}$ for the Al(110) surface, $\beta(\overline{X})$=-4.8%, which is contradicted with the mode at $\overline{M}$ for Mg(10$\bar{1}$0) but similar with Be(10$\bar{1}$0). At $\overline{Y}$ of Al(110), there are three modes predicted by BT calculations with energies 8.7 meV (Y_1), 10.3 meV (Y_2), and 13.2 meV (Y_3) for the Al(110) surface with the atomic displacements parallel to the surface (Y_1 and Y_2 modes) and perpendicular to the surface (Y_3 mode), respectively [30]; while there was two modes observed experimentally with energies 8.9 meV and 13.5 meV [29], corresponding to the Y_1 and Y_3 modes, respectively. So, at $\overline{Y}$, the modes predicted by BT calculations are a little bit softer than the experimental observations, with the value $\beta(\overline{Y})$ of +2.3%, which is different sign with that of Mg(10$\bar{1}$0) and Be(10$\bar{1}$0). The slope of the RW from BT calculations with respect to the measured RW for Al(110) χ is -2.1%, which is opposite sign with that of Mg(10$\bar{1}$0) but the same as that of Be(10$\bar{1}$0). The values of β and χ for Mg(10$\bar{1}$0), Be(10$\bar{1}$0), and Al(110) are listed in Table 4.8.

Table 4.8: Measured Rayleigh wave (*RW*) with respect to the *RW* from BT calculations (using bulk force constants) at the zone boundaries for open simple metal surfaces. β and χ are defined in equations (4.1) and (4.2) in the text.

	$\beta(\overline{M})$ or $\beta(\overline{X})$ [%]	$\beta(\overline{A})$ or $\beta(\overline{Y})$ [%]	χ [%]
Mg(10$\bar{1}$0) [this work]	+5.3	-4.9	+1.3
Be(10$\bar{1}$0) [15]	-7.5	-20.6	-13.3
Al(110) [29,30]	-4.8	+2.3	-2.1

It is very surprising that, even though the surface electronic properties of Mg(10$\bar{1}$0) are similar to the bulk (free-electron-like metal), the RW from BT calculations has different trend with the measure RW at the zone boundaries, i.e., the RW from BT calculations at $\overline{M}$ is *softer* than the measured RW ($\beta(\overline{M})$=+5.3%), but at the zone boundary $\overline{A}$, the RW from BT calculations is *stiffer* than the measured one or $\beta(\overline{A})$=-4.9%. This behavior is similar to that of Al(110), see Table 4.8. This means that the nature of surface force constants is *significantly* different than in the bulk for an open surface metal.

In general, the lattice dynamics of the Mg(10$\bar{1}$0) surface is different with those of the Al(110) and Be(10$\bar{1}$0) surfaces. The differences could come from the electronic properties and the stacking sequence. In contrast to Mg(10$\bar{1}$0), the electronic properties of the Be(10$\bar{1}$0) surface is dominated by the surface states. The electronic properties of the Mg(10$\bar{1}$0) surface are similar to those of the Al(110) surface but the stacking sequence of these two surfaces is different; i.e., the stacking sequence of the Mg(10$\bar{1}$0) surface is ABCDABCD; while the stacking sequence of the Al(110) surface is ABAB.

The lattice dynamics of the Mg(10$\bar{1}$0) surface involve many layers (or deep layers), as shown in Tables 4.5 and 4.6. Figure 4.24 shows the vertical atomic displacements at $\overline{M}$ of Mg(10$\bar{1}$0). For the RW mode (M_1), this mode is localized in the first layer (surface layer) where the atoms vibrate outward direction, the atoms in the second and third planes stay at rest but the atoms in the fourth and fifth layers vibrate inward direction. The RW mode (M_2) is localized in the second and third layers. The atoms in the first and fourth layers of this mode stay fix but the atoms in the second and third layers vibrate inward direction while the atoms in the fifth and sixth layers vibrate outward direction. The surface mode (M_4) is localized in the second and third layers where the atoms in the second and

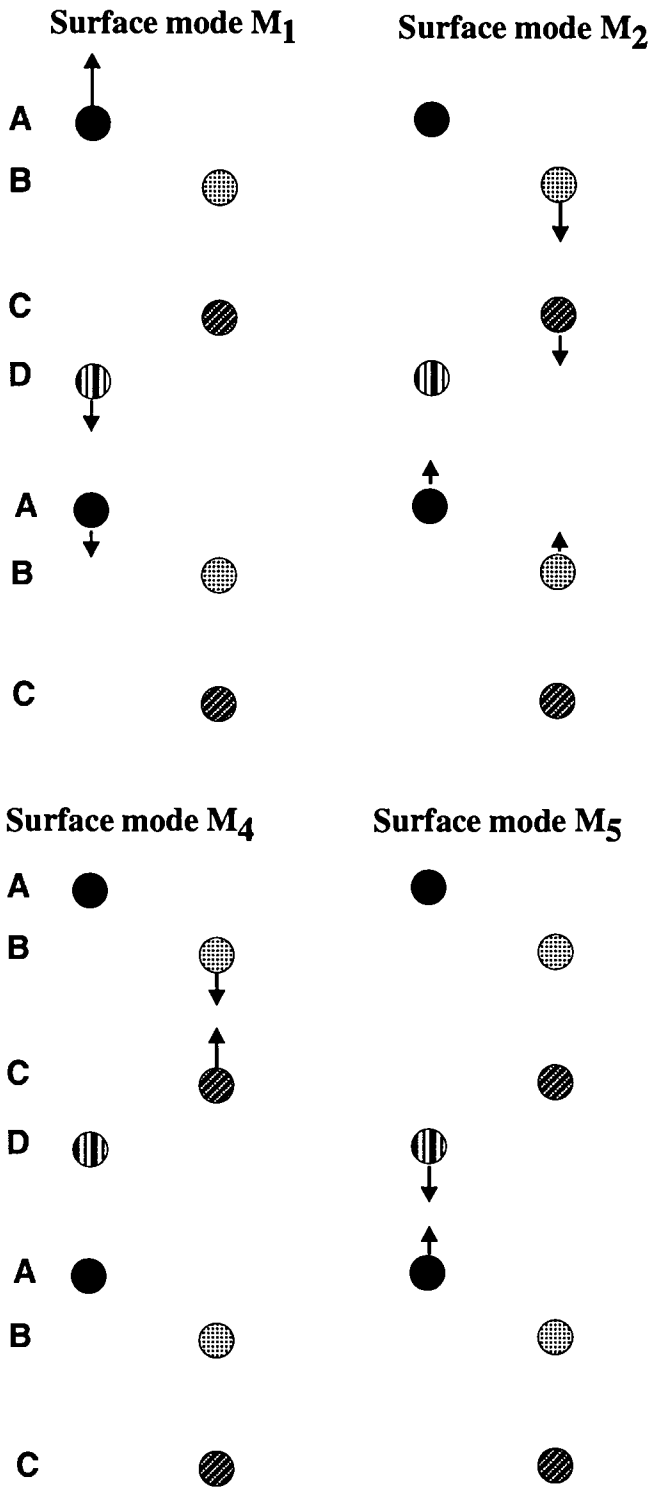


Figure 4.24: Vertical atomic displacements at $\overline{M}$ for the Mg(10$\bar{1}$0) surface.

third layers vibrate against each other while the atoms in the other layers stay fix. The surface mode (M_5) is localized in the fourth and fifth layers where the atoms in the fourth and fifth layers vibrate against each other while the atoms in the other layers stay fix (do not vibrate vertically). The vertical atomic displacement for RW at $\bar{A}$ is shown in Figure 4.25. The RW mode (A_1) is localized in the first and third layers where the atoms in the first, third, fifth, and seventh layers vibrate vertically outward direction while the atoms in the other plane stay fix. However, the RW mode (A_2) is localized in the second and fourth layers where the atoms in the second, fourth, and sixth layers vibrate vertically outward direction while the atoms in the other planes stay fix vertically. Clearly, the surface lattice dynamics of Mg(10$\bar{1}$0) is very complicated and involve six layers (or deep layers). It is very interesting to compare the atomic displacements at Mg(10$\bar{1}$0) surface with the those of Al(110) and Be(10$\bar{1}$0) surfaces. Nevertheless, the authors of the papers of Al(110) and Be(10$\bar{1}$0) surfaces did not explain the atomic displacements at these surfaces in deep layers [15,29,30].

4.3.3 Ab initio Calculations at T=0 K

We compare our experimental data of the surface-phonon dispersion at the Mg(10$\bar{1}$0) surface with the preliminary results from *ab initio* calculations using density-functional perturbation theory (DFPT) by Bungaro [31]. The surface phonon was obtained by using a periodically repeated slab geometry Mg(10$\bar{1}$0) slabs of 20 atomic layers separated by a vacuum region of 5 atomic layers by sampling the surface BZ using 24 *k*-points in the irreducible wedge. Energy minimization was performed in order to obtain the surface structure. *Ab initio* calculations showed the changes relative to the inter-layer spacings of the bulk are Δd_{12}=-20.0%, Δd_{23}=+9.3%, and Δd_{34}=-11.4% which are not quite in good agreement quantitatively with the previous first principles calculations by Cho *et al.*

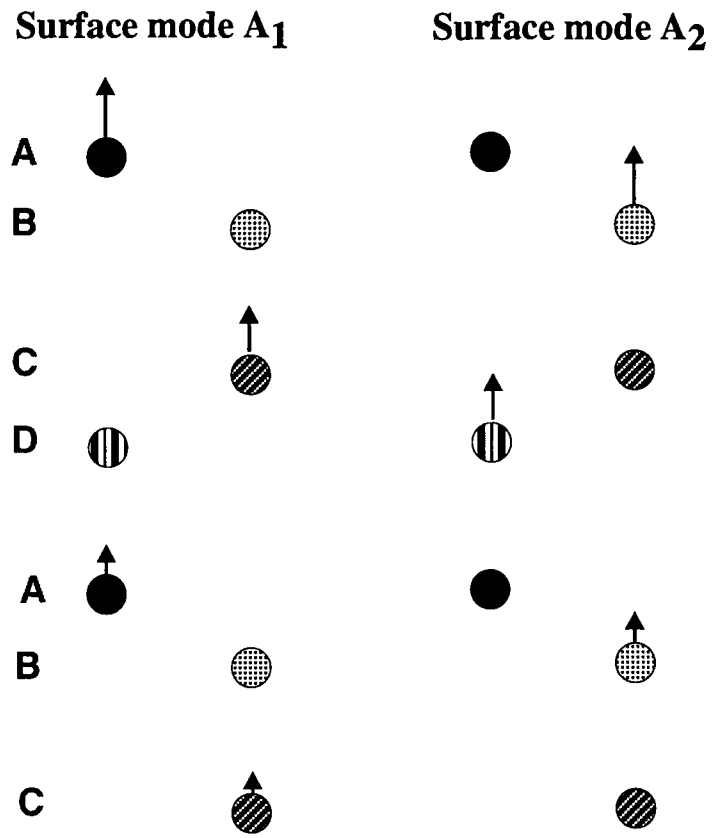


Figure 4.25: Vertical atomic displacements at $\overline{A}$ for the Mg(10$\bar{1}$0) surface.

[32], i.e., Δd_{12}=-14.9%, Δd_{23}=+6.9%, and Δd_{34}=-7.5% and our experimental data, as shown in Chapter 3. The cause of the discrepancies could be due to an insufficient number of *k*-points (24 points) sampling the surface BZ in the recent calculations [31].

Figure 4.26 shows the measured surface phonon dispersion at the Mg(10$\bar{1}$0) surface together with the results obtained from *ab initio* calculations along the $\bar{\Gamma}$-$\bar{M}$ direction. The shaded areas are the projected bulk band onto the surface. The present EELS data are indicated by filled diamonds, which are intense losses. The solid lines below the projected bulk band indicate Rayleigh modes which are localized in the surface region and decay exponentially into the bulk. In general, there is in good agreement between our experimental data and *ab initio* calculations. At zone boundary $\bar{M}$, *ab initio* calculations predict two Rayleigh waves (RW) with both energies 14 meV. Both RW are polarized in the sagittal plane and perpendicular to the normal surface. Figure 4.27 shows the square amplitudes of the atomic displacements for both the Rayleigh modes at the zone boundary $\bar{M}$ point. The first Rayleigh mode RW(1) is localized in the top layer (surface layer) mainly vertical motion polarized in the sagittal plane and perpendicular to the normal surface. Since this mode is far from the bulk band edge, the atomic displacements of this mode fast decay perpendicular to the surface. The second Rayleigh mode RW(2) is polarized in the sagittal plane and exhibits a maximum displacement in the *second* layer perpendicular to the normal surface, while the atoms in the first layer have small displacement. For a wave vector smaller than $\bar{M}$ (approach the center of surface Brillouin zone $\bar{\Gamma}$), the overlapping Rayleigh modes at $\bar{M}$ split, therefore RW(1) and RW(2) can be distinguished clearly, see Figure 4.26.

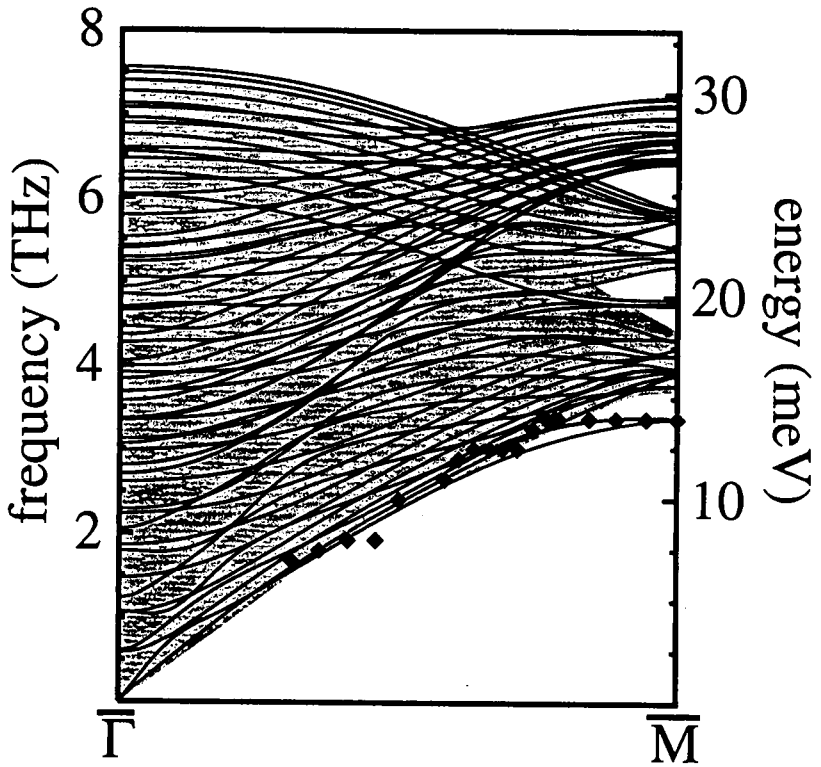


Figure 4.26: Surface phonon dispersion at the Mg(10$\bar{1}$0) surface from *ab initio* calculations [31] together with our experimental data (filled diamonds).

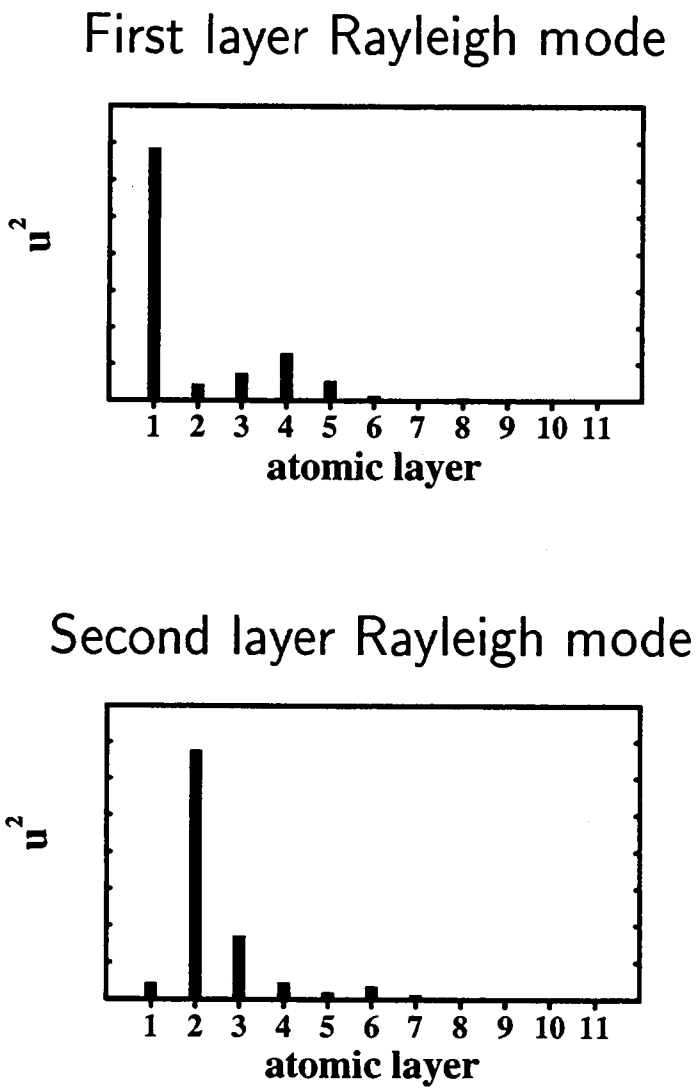


Figure 4.27: Square of the amplitude of the atomic displacements for the Rayleigh waves in the surface layer and second layer at $\overline{\mathrm{M}}$ points for the Mg(10$\bar{1}$0) surface from *ab initio* calculations [31].

4.3.4. Surface Anharmonicity of Mg(10$\bar{1}$0)

We measured the temperature-dependent surface phonons at the zone boundaries $\overline{M}$ (along the $\overline{\Gamma}$-$\overline{M}$ direction) and $\overline{A}$ (along the $\overline{\Gamma}$- direction), i.e., at room-temperature and liquid-nitrogen-temperature. From the energy and intrinsic width shifts of the temperature-dependent surface Rayleigh modes, we can obtain the information of the anharmonicity at the Mg(10$\bar{1}$0) surface. Our temperature-dependent EELS spectra at the zone boundaries $\overline{A}$ and $\overline{M}$ are shown in Figures 4.28 and 4.29, respectively. The intense losses are the Rayleigh modes. At the zone boundary $\overline{M}$, the energy loss of the Rayleigh mode at room-temperature (low-temperature) is 14.10 (14.25) meV with the intrinsic widths of 3.50 (3.00) meV; while at the zone boundary $\overline{A}$, the Rayleigh mode at room-temperature (low-temperature) is at 8.90 (9.10) meV with the intrinsic widths of 2.40 (2.00) meV. Figures 4.30 (a) and (c) show that, as the temperature increases, the surface phonon energy at $\overline{A}$ and $\overline{M}$ shifts linearly with the equation $E=9.20-0.001.T$ meV (with the slope of -0.001 meV/K) and $E=14.34-0.0008.T$ meV (with the slope of -0.0008 meV/K), respectively. The plots of the intrinsic widths of the surface phonons at $\overline{A}$ and $\overline{M}$ as a function of temperature, $W=1.80+0.002.T$ and $W=2.69+0.0027.T$, are shown in Figures 4.30 (b) and (d), respectively. Again, by assuming the bulk anharmonicity of Mg is the same as that of Al. We find that the anharmonicity at the Mg(10$\bar{1}$0) surface is the same as in the bulk. This is very surprising since our temperature dependent measurements of atomic structure showed the oscillatory thermal expansion at this surface.

The possible reasons why we did not observe the enhanced surface anharmonicity at Mg(10$\bar{1}$0) are: first, the anharmonic effects could be from the optical mode, where this mode was not observed since we did not have the "correct" impact energy and scattering geometry of EELS experiment; second, it could be in the sublayer, where it is difficult to be detected, not sensitive to the instrument. Both simple and *ab initio* calculations show that

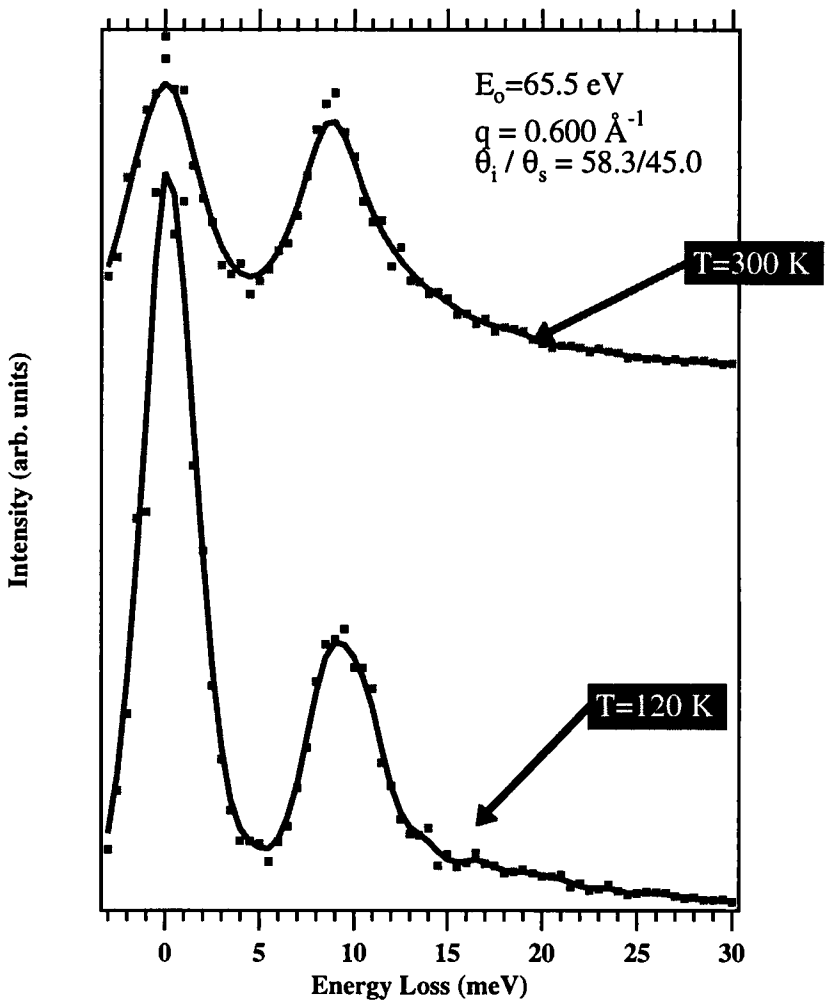


Figure 4.28: Temperature dependent phonons for the Mg(10$\bar{1}$0) surface at $\bar{A}$ along the $\bar{\Gamma}$-$\bar{A}$ direction. Dots are raw data and solid lines are smoothed data.

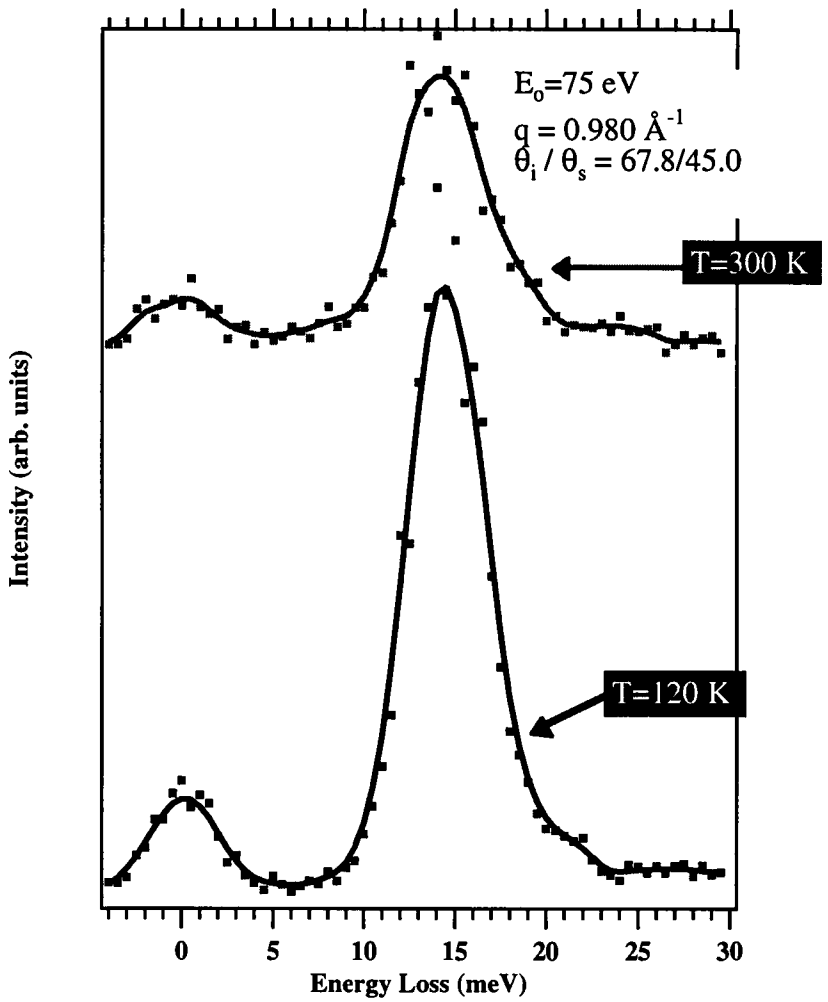


Figure 4.29: Temperature dependent phonons for the Mg(10$\bar{1}$0) surface at $\overline{M}$ along the $\overline{\Gamma}$-$\overline{M}$ direction. Dots are raw data and solid lines are smoothed data.

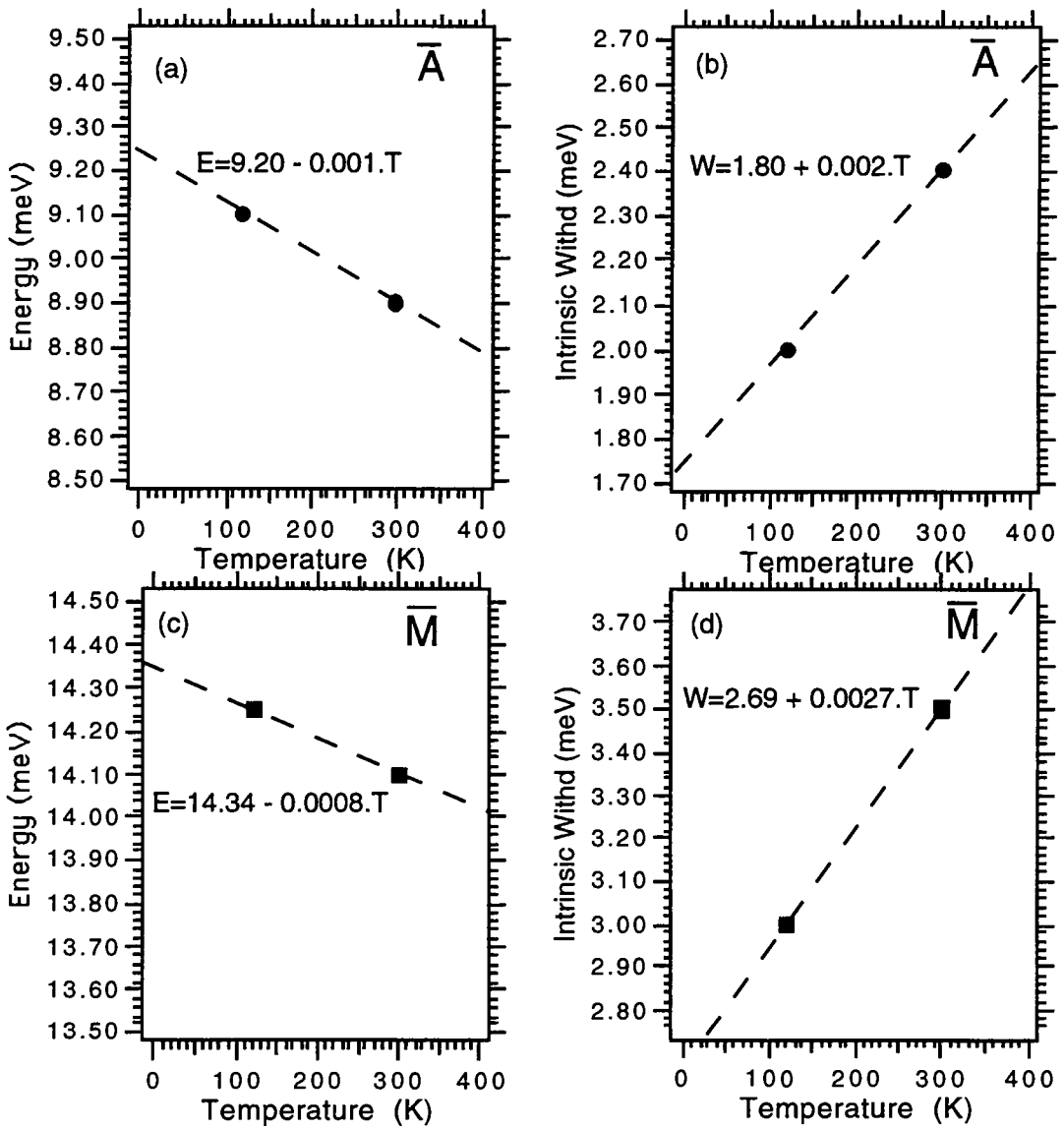


Figure 4.30: Temperature dependent energy and intrinsic width of the surface phonons for the Mg(10$\bar{1}$0) surface at $\bar{A}$ along the $\bar{\Gamma}$-$\bar{A}$ direction [(a) and (b)] and at $\bar{M}$ along the $\bar{\Gamma}$-$\bar{M}$ direction [(c) and (d)].

there are two Rayleigh modes at zone boundary $\overline{M}$. One mode is in the surface layer and the other one is in the second layer. The later mode (localized in the second layer) could be an important mode to explain the negative thermal expansion in the first interlayer at the Mg(10$\bar{1}$0) surface. At a finite temperature, the atomic displacement of this mode in the second layer could become larger causing anharmonic motion in the second layer. The mechanism of the thermal contraction at this surface could be is similar to the case of the Al(110) surface proposed by a finite temperature molecular dynamics simulation [12]. The oscillatory thermal expansion at the Mg(10$\bar{1}$0) surface might be directed by the anharmonicity in the deep layers (see the atomic displacements for the RW mode (A_2) in Figure 4.25), where it is difficult to be detected experimentally. A better understanding of the thermal expansion at the Mg(10$\bar{1}$0) surface could be achieved from a finite temperature surface phonon calculation.

4.4 Conclusions

We have presented measurements of the surface phonon dispersions on Mg(0001) and Mg(10$\bar{1}$0) by using electron energy loss spectroscopy. Our experimental data are in good agreement with the *ab initio* calculations. For Mg(0001), there are three layers involved in the surface dynamics; while for Mg(10$\bar{1}$0), the surface dynamics involve up to six layers (deep layers). The number of layers involved in the surface dynamics is strongly related to the distance of the interlayer spacing.

In general, the surface lattice dynamics of Mg(0001) are similar to those of Be(0001) and Al(111). Qualitatively, the bulk force constant model is able to reproduce the measured RW dispersion along the zone boundary $\overline{K}$-$\overline{M}$ for the Mg(0001) surface that is similar to the case of the Al(111) surface, but contradicted to the Be(0001) surface. This behavior seems to be consistent with their electronic properties and true for close packed

surfaces. Nonetheless, this is not true for open surfaces. The nature of surface force constants is *significantly* different than in the bulk for open surface metals, even though the surface electronic properties are similar to the bulk. From the experimental data and BT calculations, qualitatively, we find that the surface force constants of open surfaces become more anisotropic than in the bulk, due to the screening at the surface (as a consequence of the creation of a surface).

We found that the surface anharmonicity of Mg(0001) is the same as in the bulk, which is consistent with the temperature dependent structure measurements. But, this behavior is *not* true for the Mg($10\bar{1}0$) surface. We did not observe the enhanced surface anharmonicity of Mg($10\bar{1}0$), even though our temperature dependent measurements of atomic structure showed the oscillatory thermal expansion at this surface. This behavior is similar to the case of the Be(0001), where the surface anharmonicity is the same as in the bulk, but the temperature dependent structure measurements showed an anomalously large surface thermal expansion. One of possible reasons why we did not observe the enhanced surface anharmonicity is because it is in the sublayer, which is difficult to be detected experimentally or the anharmonic effects are from the optical mode, where this mode was not observed since we did not have the "correct" impact energy and scattering geometry of EELS experiment.

In conclusions, in order to establish the relationship between the lattice dynamics, electronic structure, and temperature dependent atomic structure, we need to challenge: first, calculate the electron scattering cross section (EELS spectra) in order to have the "right" geometry and impact energy for doing experiment. Second, we need to perform the surface phonon calculations at a finite temperature in order to understand the nature of the surface force constants and the surface anharmonicity. The surface modes localized in the sublayer could be important to explain the surface thermal expansion or thermal contraction.

4.5 References

1. J. A. Gaspar and A. G. Eguiluz, Phys. Rev. B **40**, 11976 (1989).

2. G. Brusdeylins, R.B. Doak, and J.P. Toennies, Phys. Rev. Lett. **46**, 437(1981); Phys. Rev. B **27**, 3662 (1983).

3. S. Lehwald, F. Wolf, H. Ibach, T.S. Rahman, and D.L. Mills, Phys. Rev. Lett. **50**, 518 (1983).

4. J. B. Hannon, E. J. Mele, and E. W. Plummer, Phys. Rev. B **53**, 2090 (1996).

5. E. V. Chulkov, V. M. Silkin, and E. N. Shirykalov, Surf. Sci. **188**, 287 (1987).

6. J. B. Hannon, Ph.D. thesis, University of Pennsylvania-USA, 1994.

7. K. Pohl, J.-H. Cho, K. terakura, M. Scheffler, and E. W. Plummer, Phys. Rev. Lett. 80, 2853 (1998).

8. M. Lazzeri and S. de Gironcoli, Surf. Sci. **402**, 715 (1998).

9. S. Narasimhan and M. Scheffler. Z. Phys. Chem. 202, 253 (1997): J.-H. Ch and M. Scheffler, Phys. Rev. Lett. 78, 1299 (1997).

10. M. Lazzeri and S. de Gironcoli, Phys. Rev. Lett. **81**, 2096 (1998).

11. H. Göbel and P. von Blanckenhagen, Phys. Rev. B **47**, 2378 (1993).

12. N. Marzari, D. Vanderbilt, A. De Vita, and M. C. Payne, Phys. Rev. Lett. **82**, 3296 (1999).

13. R.A. Bartynski, R.H. Gaylord, T. Gustafsson, and E. W. Plummer, Phys. Rev. B **33**, 3644 (1986).

14. R.E. Allen, G.P. Alldredge, and F.W. de Wette, Phys. Rev. B **4**, 1648 (1971).

15. Ph. Hofmann and E. W. Plummer, Surf. Sci. **377-379**, 330 (1997).

16. R. Pynn and G. L. Squires, Proc. Roy. Soc. (London) A **326**, 347 (1972).

17. A. Lock, J.P. Toennies, and Ch. Wöll; V. Bortolani, A. Franchini, and G. Santoro, Phys. Rev. B **37**, 7087 (1988).

18. A.G. Eguiluz, in *Surface Phonons*, Edited by W. Kress and F.W. de Wette, pp. 258, Springer-Verlag, Berlin, 1991.

19. C.S. Jayanthi, H. Bilz, W. Kress, and G. Benedek, Phys. Rev. Lett. **59**, 795 (1987).

20. R. Stedman, Z. Amilius, R. Pauli, and O. Sundin, J. Phys. F **6**, 157 (1976).

21. A.P. Roy, B.A. Dasannacharya, C.L. Thaper, and P.K. Iyengar, Phys. Rev. Lett. **30**, 906 (1973).

22. G. Gilat and R.M. Nicklow, Phys. Rev. **143**, 487 (1966).

23. V. L. Moruzzi, J. F. Janak, and A. R. Williams: *Calculated Electronic Properties of Metals*, (Pergamon Press Inc., 1978).

24. M. Heinrichsmeier, A. Fleszar, and A.G. Eguiluz, Surf. Sci. **285**, 129 (1993).

25. Ismail, Ph. Hofmann, E. W. Plummer, Claudia Bungaro, W. Kress, To be published.

26. M. Mostoller, R.M. Nicklow, D.M. Zehner, S.-C. Lui, J.M. Mundenar, and E.W. Plummer, Phys. Rev. B **40**, 2856 (1989).

27. R. Stedman and G. Nilsson, Phys. Rev. **145**, 492 (1966).

28. M. Gester, D. Kleinhesselink, P. Ruggerone, and J.P. Toennies, Phys. Rev. B **49**, 5777 (1994).

29. J.P. Toennies and Ch. Wöll, Phys. Rev. B **36**, 4475 (1987).

30. K. M. Ho and K. P. Bohnen, Phys. Rev. Lett. **56**, 934 (1986).

31. Claudia Bungaro, private communication.

32. J.-H. Cho, Ismail, Z. Zhang and E. W. Plummer, Phys. Rev. B **59**, 1677 (1999).

Chapter 5

Overview: The Interplay between the Structure and Dynamics of Simple Metal Surfaces

The main goal of the research presented in this thesis was to understand the interplay between the geometric structure and dynamical properties of surfaces, which relates to the surface electronic structure in the broken symmetry and reduced dimensionality at a surface. We have chosen magnesium as a prototypical system in this study because magnesium is a free-electron-like metal; therefore, it is simpler in the analysis and an ideal test for first-principles calculations. The bulk thermal expansion of magnesium is $\alpha_B = 25\text{x}10^{-6}\ \text{K}^{-1}$, which is almost the same as the bulk thermal expansion of aluminum (where aluminum is a free-electron-like metal). The research in this thesis was focused on two low Miller index surfaces of magnesium: (i) Mg(0001) that is a close packed metal surface with the interlayer spacing d_0 of 2.5944 Å (long interlayer spacing). (ii) Mg(10$\bar{1}$0) that is an open metal surface with the interlayer spacings d_{12} and d_{23} of 0.923 Å and 1.846 Å, allowing us to observe the effects of the surface relaxations and lattice dynamics in deep layers.

5.1 Geometric Structure of Surfaces

No reconstruction on the Mg(0001) surface was found at temperatures T=130 K to T=400 K, which is consistent with the prediction by T=0 K calculations [1]. The observed (1x1) LEED pattern exhibited a six-fold symmetry, indicating a natural averaging over the two possible bulk terminations (A or B) of the 'ideal' Mg(0001) surface or a fcc(111) termination with a complete Mg adlayer. This behavior is similar to the case of the Be(0001) surface [2]. The possibility of a fcc(111) termination at the Be(0001) surface has been examined by Pohl [2] via LEED *I-V* analysis, and he found that the agreement

between the calculated and experimental spectra was poor, meaning that the model (a fcc(111) termination at the Be(0001) surface) has to be rejected. In addition, Pohl found that the Be(0001) surface was terminated by the average of A and B terminations with ABAB stacking sequence [2]. We did not examine the possibility of a fcc(111) termination at the Mg(0001) surface. However, since our *Rp* factors of all temperatures (T=130 K, T=300 K, and T=400 K) are quite good, we are very confident that this surface has a natural averaging over the A and B terminations with ABAB stacking sequence, which is similar to the case of the Be(0001) surface.

At T=130 K, we found that the surface relaxations of Mg(0001) are as follows: $\Delta d_{12}/d_o$ = +2.0(±0.5)%, $\Delta d_{23}/d_o$ = +0.2(±0.6)%, and $\Delta d_{34}/d_o$ =+0.0(±0.9)%. These values are comparable with the surface relaxations for the Al(111) surface, where $\Delta d_{12}/d_o$ =+1.7(±0.3)%, $\Delta d_{23}/d_o$ =+0.5(±0.7)%, and $\Delta d_{34}/d_o$ =+0.00% [3]. It seems to be a general rule that the first interlayer spacing of a close packed surface of high-density simple metal is expanded by about 1 - 2% with respect to the bulk. However, the expansion of the first interlayer spacing for the Be(0001) surface at T=110 K is rather large, i.e., $\Delta d_{12}/d_o$ =+3.1(±0.7)% [2]. In general, the relaxations of a close packed metal surface involves only two surface layers.

Even though calculation predicted a possibility of reconstruction on the Mg(10$\bar{1}$0) surface [1], our observed (1x1) LEED pattern indicated no reconstruction on this surface at temperatures T=120 K to T=400 K, which concurs with the other hcp(10$\bar{1}$0) surfaces (Re [4], Ti [5], Co [6,7], and Be [8]). The preferred termination of this surface is short termination that is the same as in the case of the other hcp(10$\bar{1}$0) surfaces [4-8]. At T=120 K, for the Mg(10$\bar{1}$0) surface, we found that the relaxation pattern is of an oscillatory character with the alternating contraction and expansion following the trend - + - + - + , where $\Delta d_{12}/d_o$ = -16.0(±2.0)%, $\Delta d_{23}/d_o$ = +9.0(±1.0)%, and $\Delta d_{34}/d_o$ =-10.5(±3.0)%,

$\Delta d_{45}/d_o$ =+4.0(±1.6)%, $\Delta d_{56}/d_o$ =-6.0(±3.0)%, and $\Delta d_{67}/d_o$ =+1.0(±2.0)%. While the relaxation of the Be(10$\bar{1}$0) surface at T=120 K, $\Delta d_{12}/d_o$ = -25%, $\Delta d_{23}/d_o$ = +5.0%, and $\Delta d_{34}/d_o$ =-11%, and $\Delta d_{45}/d_o$ =+2% [42]; and for the Al(110) surface, $\Delta d_{12}/d_o$ = -8.6%, $\Delta d_{23}/d_o$ = +5.0%, and $\Delta d_{34}/d_o$ =-1.6%, and $\Delta d_{45}/d_o$ =+1.0% [9]. Therefore, an oscillatory character with the alternating contraction and expansion will be a general rule for open metal surfaces (i.e., hcp(10$\bar{1}$0) and fcc(110)). The relaxations of open metal surfaces involve deep layers. We found that *it is very important to vary sufficient layers in the calculations in order to be able to observe the oscillatory relaxations at a metal surface.*

We summarize the surface relaxations for simple metal surfaces in Figures 5.1(a)-(c). Filled and unfilled circles are experimental data and calculations, respectively. In general, the calculations are in very good agreement with the experimental data. The change in the first interlayer spacing with respect to the bulk truncation is a linear function of the inverse area per unit cell (normalized to the volume per bulk atom), as shown in Figure 5.1(a). The first interlayer spacing is expanded for a close packed surface metal, while for an open surface, the first interlayer spacing is contracted. The change in the interlayer spacing between the second and third layers (Δd_{23}) with respect to the bulk is linear as a function of the inverse area per unit cell (Figure 5.1(b)). However, it is the opposite sign from the trend of the change in first interlayer spacing. For a close surface metal, the interlayer spacing of d_{23} is almost the same as in the bulk. But for an open surface metal, the interlayer spacing the second and the third layers (d_{23}) is expanded. Figure 5.1(c) shows the change in the interlayer spacing between the first and third layers as a function of the inverse area per unit cell. Its trend is similar to the trend of Δd_{12}, i.e., the interlayer spacing between the first and third layers is expanded for open surface simple metals, while the interlayer spacing between the first and third layers is contracted for a close packed surface. Figures 5.1(a) - (c) show the interesting feature of the relaxation at the metal surface, where *the relaxations at a metal surface might be controlled to a desired*

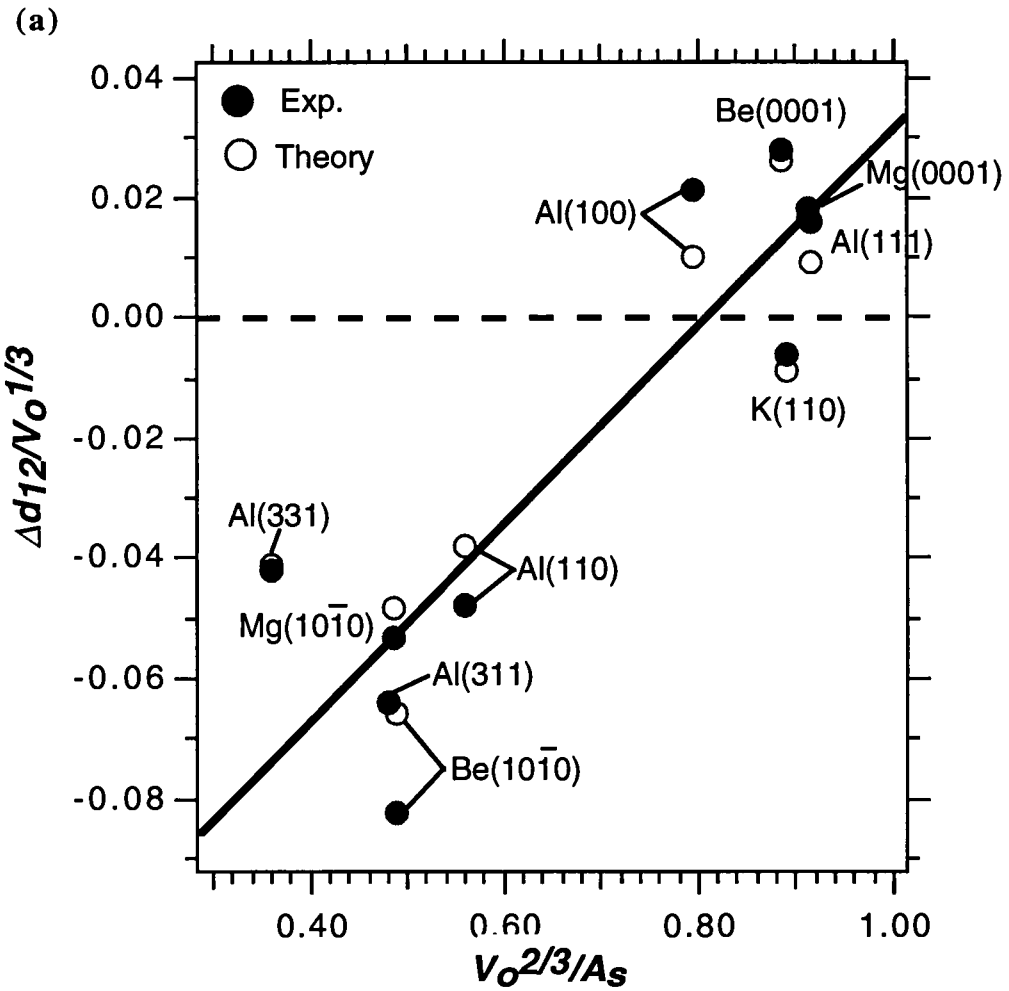


Figure 5.1: Measured and calculated relaxations of simple metal surfaces. Solid line is a linear fit of the data. The references for the points are given in Chapter 3 (see Figure 3.13).

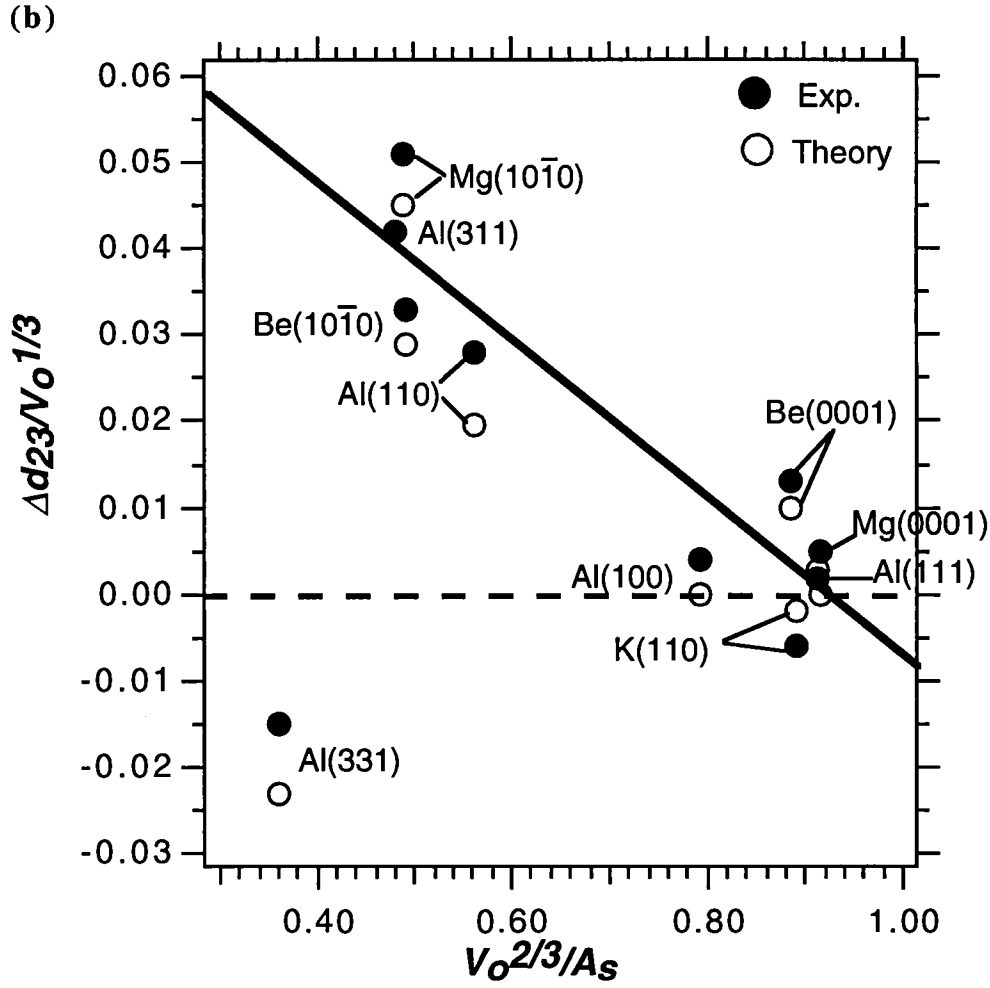


Figure 5.1: (continued)
Measured and calculated relaxations of simple metal surfaces. Solid line is a linear fit of the data, where the data of Al(331) are excluded. The references for the points are given in Chapter 3 (see Figure 3.13).

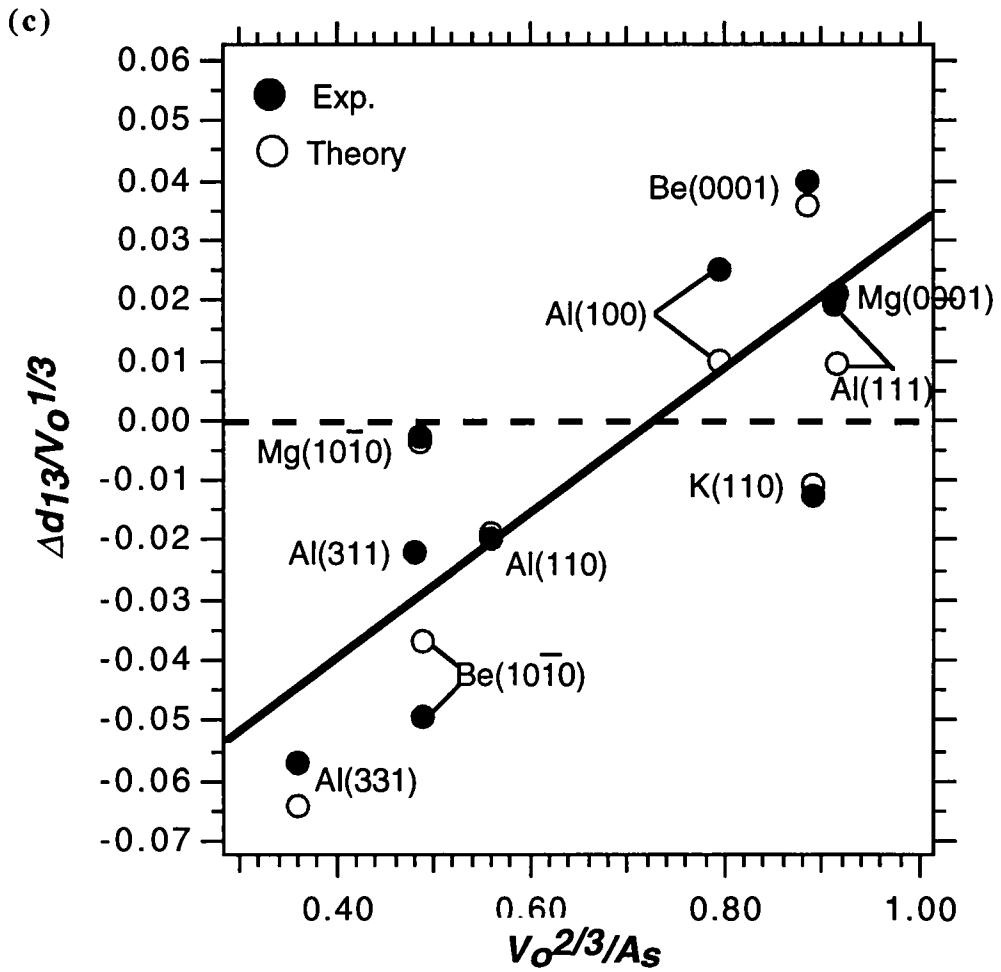


Figure 5.1: (continued)
Measured and calculated relaxations of simple metal surfaces. Solid line is a linear fit of the data. The references for the points are given in Chapter 3 (see Figure 3.13).

value by engineering a certain material. For example, by engineering a certain face of a simple metal such that the value of $V_0^{2/3}/A_s$ is equal to 0.8, where V_0 is the volume of bulk unit cell per atom and A_s is the area of surface unit cell, then we will have the first interlayer spacing of that material as in the bulk, i.e., Δd_{12}=0. Similarly, if we would like to have the spacing of the first and third layers the same as in the bulk, then we need to engineer a certain face of a simple metal such that the values of $V_0^{2/3}/A_s$ are about 0.72, and so on.

5.2 Surface Dynamics

The measured surface phonon Rayleigh wave (RW) of the Mg(0001) surface at $\overline{\text{K}}$ point is higher than that of at $\overline{\text{M}}$ point, which is similar to the case of Al(111) [16] and Be(0001) [17]. This might be a general rule that the surface phonon Rayleigh wave of a close packed metal surface at $\overline{\text{K}}$ is always higher than at $\overline{\text{M}}$. From the surface electronic properties, where Mg(0001)], Be(0001), and Al(111) are nearly-free-electron-like metals, it is understood that the surface lattice dynamics of Mg(0001), Be(0001), and Al(111) are similar. Furthermore, for Mg(0001) and Al(111), the bulk force constants are able to reproduce qualitatively the surface phonon dispersions since the electronic properties of these surfaces are similar to their bulk, but not in the case of Be(0001) since the interatomic forces at the Be(0001) surface are significantly different than in the bulk Be. By using bulk terminated calculations, qualitatively, we found that the surface force constants become more anistropic than in the bulk, and for the Be(0001), the surface forces are very anisotropic, as reflected in the difference sign between $\beta(\overline{\text{K}})$ and $\beta(\overline{\text{M}})$ (see Chapter 4). This simple argument is in agreement with the self-consistent calculations, showing enhanced non-central forces at the surface [22] due to the surface anisotropic-electronic environment.

For the Mg(10$\bar{1}$0) surface, we found that the RW at $\overline{M}$ is stiffer than at $\overline{A}$ points, meaning the bonding at $\overline{A}$ is softer than at $\overline{M}$, which could be related to the stacking sequence of an hcp(10$\bar{1}$0) surface. This behavior is true in the cases of Be(10$\bar{1}$0) [20] and Al (110) [21]. In contrast to the Mg(0001) surface, there are many layers (up to six - seven layers) involved in the lattice dynamics of the Mg(10$\bar{1}$0) surface, as shown in Figures 5.2 and 5.3. The number of layers involved in the surface dynamics is strongly related to the interlayer spacing, i.e., the shorter interlayer spacing the more layers involved in the surface dynamics, which is consistent with the behavior of the surface relaxations. The nature of surface force constants of open surface metals, such as Mg(10$\bar{1}$0) and Al(110), is *significantly* different than in the bulk, even though their surface electronic properties are similar to their bulk.

5.3 Thermal Effects at Metal Surfaces

Our temperature dependent interlayer relaxation measurements for the Mg(0001) surface showed that the surface thermal expansion for the first interlayer spacing is almost similar to the bulk, as shown in Figure 5.4. From the surface electronic structure properties point of view, the surface thermal expansion for the Al(111) and Be(0001) surface should be similar to that of the Mg(0001) surface. However, it is not true for the Be(0001) surface, where the surface thermal expansion surface is about 6 times larger than in bulk [3]. The reason why large outward expansion and thermal expansion of the first interlayer spacing of Be(0001) surface is still *not* clear. It could be because the surface is much more metallic than the bulk, due to the surface states.

The Mg(10$\bar{1}$0) surface exhibits a *remarkable oscillatory thermal relaxation.* As the temperature increases, the short interplanar spacings $d_{1,2}$, $d_{3,4}$, and $d_{5,6}$ contract, while the long interplanar spacings $d_{2,3}$, $d_{4,5}$, and $d_{6,7}$ expand. The surface thermal expansion for the

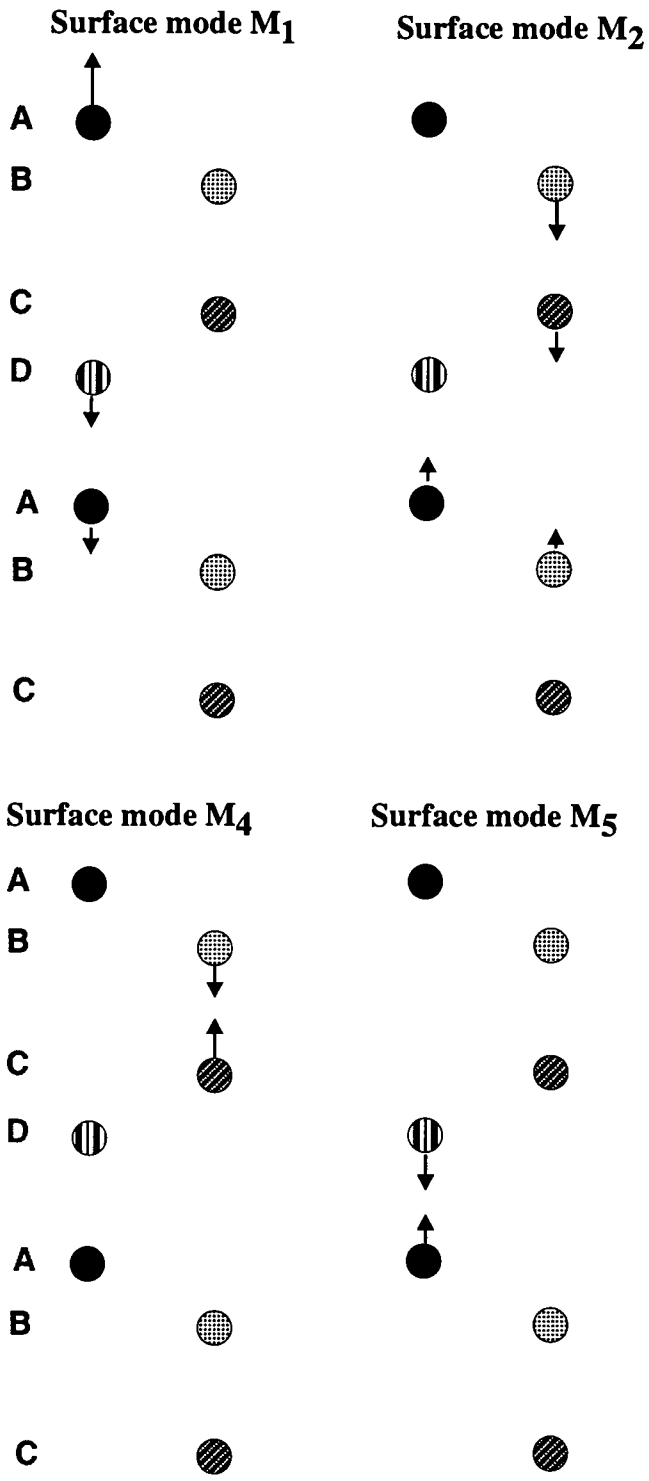


Figure 5.2: Vertical atomic displacements at $\overline{M}$ of the Mg(10$\bar{1}$0) surface, see Chapter 4 for modes assignments.

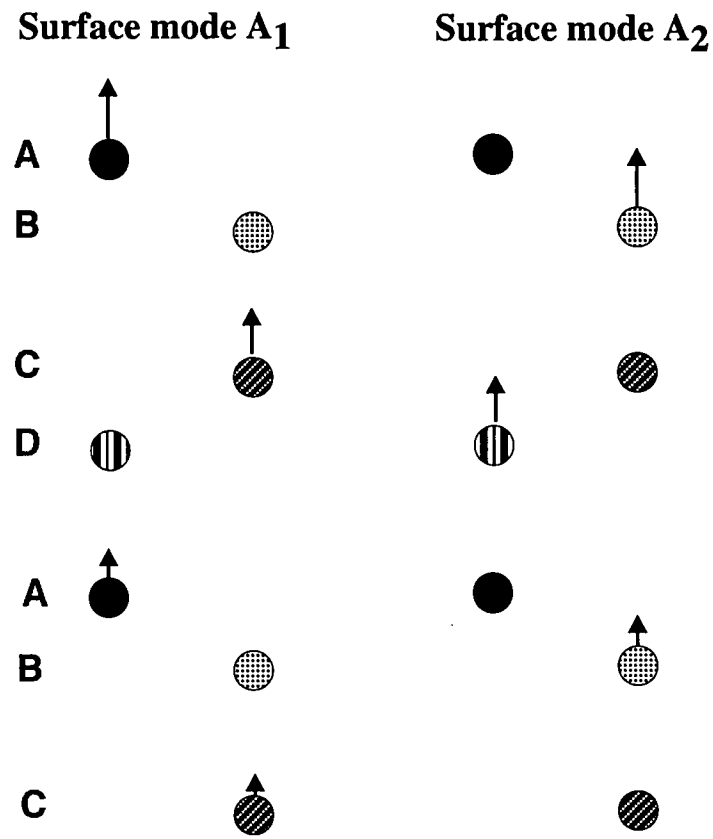


Figure 5.3: Vertical atomic displacements at $\overline{A}$ of the Mg($10\bar{1}0$) surface, see Chapter 4 for modes assignment.

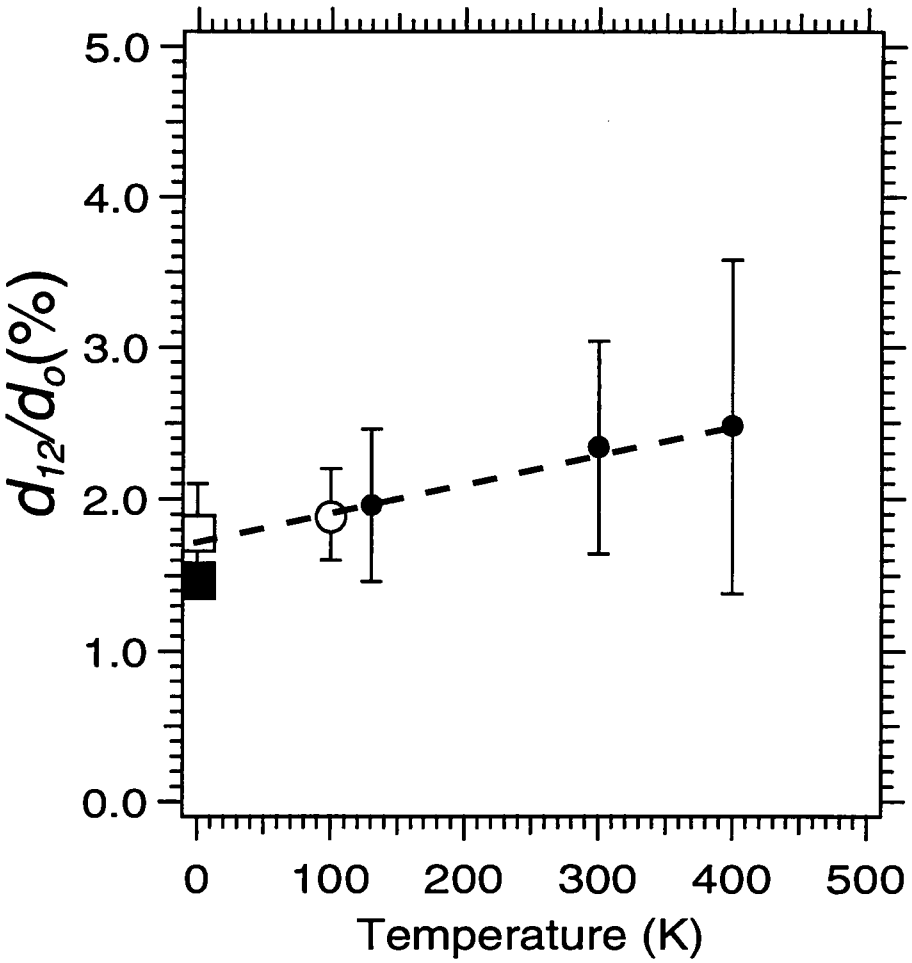


Figure 5.4: Measured (circles) interplanar relaxations as a function of temperature for Mg(0001) together with the previous experimental study (unfilled circle) [ref. 13], and theoretical studies at T=0 K; filled square [ref. 14] and unfilled square [ref. 1, 15]. $\Delta d_{ij}(T) = \{d_{ij}(T) - d_0(T)\}/d_0(T)$, where $d_0(T)$ is the bulk interplanar spacing as a function of temperature.

first short interlayer spacing is -7 x α_B, where $\alpha_B \approx 25 \times 10^{-6}$ K^{-1} (bulk thermal expansion), while the first long interlayer spacing exhibits a large thermal expansion, i.e., +5 x α_B, etc., as shown in Figure 5.5. A negative thermal expansion in the first interlayer spacing has been observed experimentally at the Al(110) surface [10]. This observation was supported by finite temperature density functional molecular dynamics simulations, revealing a thermal contraction in the first layer (the interlayer spacing becomes shorter as temperature increases) as *a consequence strongly anharmonic mean square displacement of atoms in the second layer perpendicular to surface* [11]. Therefore, a negative thermal expansion or thermal contraction might be a general behavior of open simple metal surfaces. A closer look at the thermal expansion of other open simple metal surfaces will be very interesting, such as the Be($10\bar{1}0$) surface.

The anharmonicity at the Mg(0001) surface is similar to the bulk. This behavior is similar to the case of the Al(111) [19] and Be(0001) [18] surfaces. Our anharmonicity observation is consistent with our surface thermal expansion evaluated from the temperature dependent structure measurements. The temperature dependent surface phonon data (Rayleigh modes) showed no enhanced anharmonicity at the Mg($10\bar{1}0$) surface, even though we observed an oscillatory thermal expansion at this surface. This behavior is similar to the case of the Be(0001) surface, where the surface anharmonicity is the same as in the bulk, but the temperature dependent structure measurements showed an anomalously large surface thermal expansion. It could be that the enhanced surface anharmonicity is in the sublayer, which is difficult to be detected experimentally or the anharmonic effects are from the optical mode, where this mode was not observed since we did not have the "correct" impact energy and scattering geometry of EELS experiment.

As shown in Figures 5.4 and 5.5, there are several modes where the atomic displacements are localized in the sublayer or deep layers. These modes could be important to explain the negative thermal expansion in the first interlayer and oscillatory thermal

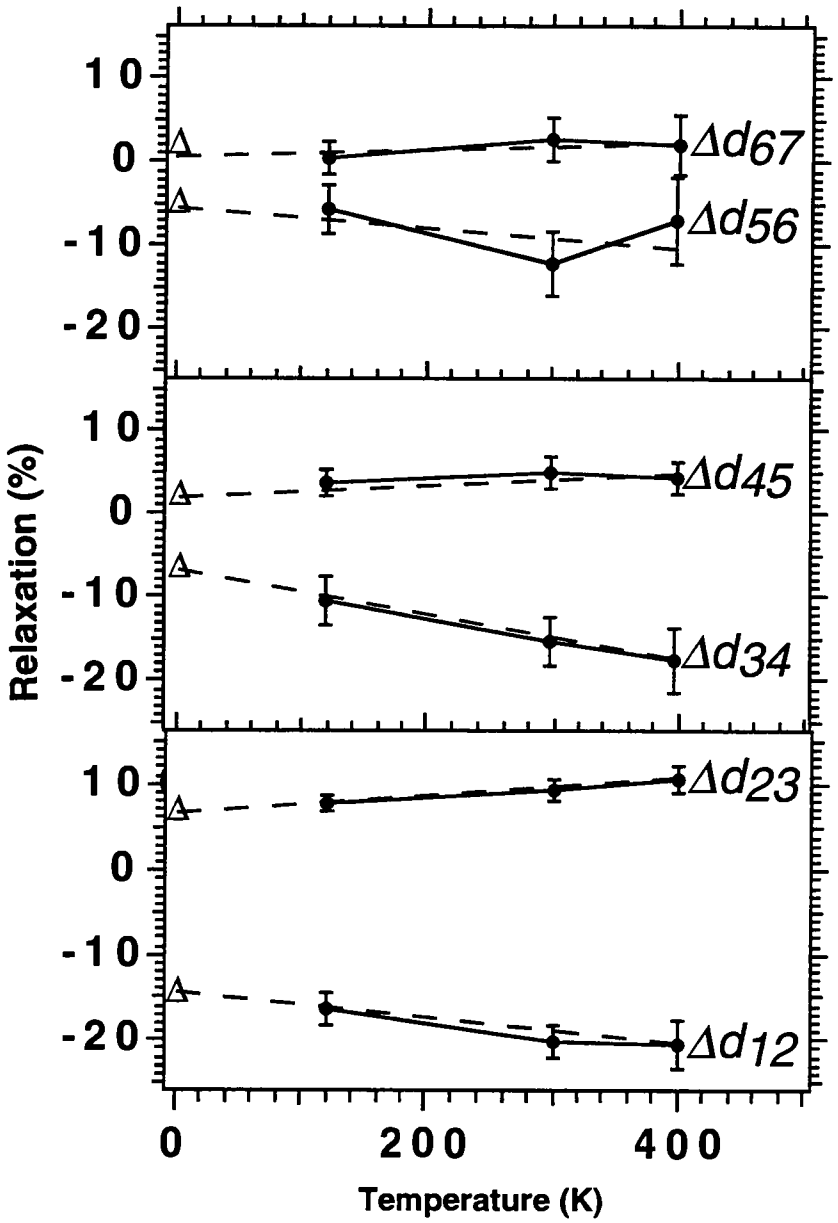


Figure 5.5: Relaxations of the Mg(10$\bar{1}$0) surface as a function of temperature. Unfilled triangles are from calculations by Cho *et al.* [12].

expansion at the Mg($10\bar{1}0$) surface. At a finite temperature, the atomic displacements of the mode localized in the second layer could become larger, causing large anharmonic motion in the second layer than in the first layer. Therefore, the mechanism of the thermal contraction at this surface could be similar to the case of the Al(110) surface proposed by a finite temperature molecular dynamics simulation [11].

5.4 Conclusions

We conclude the following for a close packed simple metal surface: (i) the first interlayer spacing of a high-density simple metal is expanded with respect to the bulk by a small amount, i.e., 1 - 2%, while the second and the third interlayer spacings are almost the same as in the bulk; (ii) the atomic bondings at the surface are similar as in the bulk (isotropic), and there are few top surface layers involved in the surface dynamics. However, for an open simple metal surface; (i) the first interlayer spacing is contracted and the second interlayer layer is expanded etc., where the relaxation pattern is of an oscillatory character with the alternating contraction and expansion following the trend - + - + - + ; (ii) negative thermal expansion (thermal contraction) in the first interlayer, positive thermal expansion in the second interlayer (for an hcp($10\bar{1}0$) surface, the surface thermal expansion has a pattern of an oscillatory character with the alternating thermal contraction and expansion following the trend - + - +); (iii) there is no observable enhanced anharmonicity at the surface since it could be in the sublayer not at the surface layer, and therefore it can not be detected experimentally; (iv) the bonding of atoms in the vicinity of the surface is anisotropic, and there are six layers involved in the surface dynamics.

A better understanding of the relationship between the lattice dynamics, the electronic structure, and the temperature dependent atomic structure can be achieved by some challenges: first, calculate the electron scattering cross section (EELS spectra) in order to have the "right" geometry and impact energy for EELS experiment; second,

perform the surface phonon calculations at a finite temperature in order to understand the nature of surface force constants and the surface anharmonicity, i.e., if it is at the surface layer or in the sublayer. The study of the thermal expansion at the open surface of simple metals will be a very interesting subject in the future.

5.5 References

1. Pavlin Staikov and Talat S. Rahman, To be published.
2. K. Pohl, J. -H. Cho, K. Terakura, M. Scheffler, and E. W. Plummer, Phys. Rev. Letter. **80**, 2853 (1998)., K. Pohl, Ph.D. Thesis, University of Pennsylvania, 1997.
3. J.R. Noonan and H.L. Davis, J. Vac. Sci. Tech. A **8**, 2671(1991).
4. H.L. Davis and D. M. Zehner, J. Vac. Sci. Technol. **17** (1980), 190.
5. J. Mischenko III and P. R. Watson, Surf. Sci. **220** (1989), L667.
6. H. Over, G. Kleinle, G. Ertl, W. Moritz, K. -H. Ernst, H. Wohlgemuth, K. Christmann, and E. Schwarz, Surf. Sci. **254** (1991), L469.
7. M. Lindroos, C. J. Barnes, P. Hu, and D. A. King, Chem. Phys. Lett. **173** (1990), 92.
8. Ph. Hofmann, K. Pohl, R. Stumpf, and E.W. Plummer, Phys. Rev. B **53** (1996), 13715.
9. J.N. Andersen, H.B. Nielsen, L. Petersen, and D.L. Adams, J. Phys. C **15**, L1113(1982).
10. H. Göbel and P. von Blanckenhagen, Phys. Rev. B **47**, 2378 (1993).
11. N. Marzari, D. Vanderbilt, A. De Vita, and M. C. Payne, Phys. Rev. Lett. **82**, 3296 (1999).
12. J.-H. Cho, Ismail, Z. Zhang and E. W. Plummer, Phys. Rev. B **59**, 1677 (1999).
13. P.T. Sprunger, K. Pohl, H.L. Davis, and E.W. Plummer, Surf. Sci. **297** (1993), L48.
14. Alan F. Wright, P. J. Feibelman, Susan R. Atlas, Surf. Sci. **302**, 215 (1994).
15. Ismail, Ph. Hofmann, E. W. Plummer, Claudia Bungaro, and W. Kress, To be published.
16. A. Lock, J.P. Toennies, and Ch. Wöll; V. Bortolani, A. Franchini, and G. Santoro, Phys. Rev. B **37**, 7087 (1988).

17. J. B. Hannon, E. J. Mele, and E. W. Plummer, Phys. Rev. B **53**, 2090 (1996).

18. J. B. Hannon, Ph.D. Thesis, University of Pennsylvania (1994).

19. M. Gester, D. Kleinhesselink, P. Ruggerone, and J.P. Toennies, Phys. Rev. B **49**, 5777 (1994).

20. Ph. Hofmann and E. W. Plummer, Surf. Sci. **377-379**, 330(1997).

21. A. Lock, J.P. Toennies, and Ch. Wöll; V. Bortolani, A. Franchini, and G. Santoro, Phys. Rev. B **37**, 7087 (1988).

22. J.A. Gaspar and A.G. Eguiluz, Phys. Rev. B **40**, 11976 (1989).

BIBLIOGRAPHY

Bibliography

Adams, D. L., H. B. Nielsen, M. A. Van Hove, and A. Ignatiev, Surf. Sci. **104**, 47 (1981).

Adams, D. L., V. Jensen, X. F. Sun, and J. H. Vollesen, Phys. Rev. B **38**, 7913 (1988).

Adams, D.L., and C.S. SØrensen, Surf. Sci. **166**, 495 (1986).

Adams, D.L., L. Petersen, C.S. SØrensen, J. Phys. C **18**, 1753 (1985).

Allen, R. E., and F. W. de Wette, Phys. rev. **179**, 873 (1969).

Allen, R. E., F. W. deWette, and A. Rahman, Phys. Rev. **179**, 887 (1969).

Allen, R.E., G.P. Alldredge, and F.W. de Wette, Phys. Rev. B **4**, 1648 (1971).

American Institute of Physics Handbook – 3 ed. McGraw-Hill, New York, 1972.

Andersen, J.N., H.B. Nielsen, L. Petersen, and D.L. Adams, J. Phys. C **17**, 173 (1984).

Ashcroft, N. W., and N. D. Mermin, *Solid State Physics*, Holt, Rinehart, and Winston, 1976.

Baddorf, A. P., and E. W. Plummer, Phys. Rev. Lett. **66**, 2770 (1991).

Baddorf, A.P., and E.W. Plummer, J. Electron Spec. And Related Phenomena, **54/55**, 541 (1990).

Baddorf, A.P., Ph.D. Thesis, University of Pennsylvania (1987).

Barbieri, A., and M.A. Van Hove, private communication.

Barbieri, A., and M.A. Van Hove: *Symmetrized Automated Tensor LEED* package, Version 4.1, available from M.A. Van Hove.

Bardeen, J., Phys. Rev. **49**, 653 (1936).

Barnes, C.J., M.Q. Ding, M. Lindroos, R.D. Diehl, and D.A. King, Surf. Sci. **162**, 59 (1985).

Barnett, R. N., U. Landman, and C. L. Cleveland, Phys. Rev. B **28**, 1685 (1983).

Barnett, R.N., and Uzi Landman, Phys. Rev. B **44**, 3226 (1991).

Bartynski, R.A., E. Jepsen, T. Gustafsson, and E. W. Plummer, Phys. Rev. B **32**, 1921 (1985).

Bartynski, R.A., R.H. Gaylord, T. Gustafsson, and E. W. Plummer, Phys. Rev. B **33**, 3644 (1986).

Beeby, J.L., J. Phys. C **1**, 82 (1968).

Begley, A.M., S.K. Kim, F. Jona, and P.M. Marcus, Phys. Rev. B **48**, 12326 (1993).

Bennett, A.J., and C.B. Duke, in *Structure and Chemistry of Solid Surfaces*, edited by G. A. Somorjai (Wiley, New York, 1969).

Berndt, W., D. Weick, C. Stampfl, A.M. Bradshaw, and M. Scheffler, Surf. Sci. **330**, 182 (1995).

Born, M., and K. Huang: *Dynamical Theory of Crystal Lattice* (Oxford Univ. Press, London, 1954).

Brusdeylins, G., R.B. Doak, and J.P. Toennies, Phys. Rev. Lett. **46**, 437 (1981).

Bungaro, C., S. de Gironcoli, and S. Baroni Phys. Rev. Lett. **77**, 2491 (1996).

Cao, Y., and E. Conrad, Phys. Rev. Lett. **65**, 2808 (1990).

Chan, C.-M., and M. A. Van Hove, Surf. Sci. **171**, 226 (1986).

Chen, E.T., R.N. Barnett, and Uzi Landman, Phys. Rev. B **41**, 439 (1990).

Cho, J. -H., and M. Scheffler, Phys. Rev. Lett. **78**, 1299 (1997).

Cho, J.-H., Ismail, Z. Zhang and E. W. Plummer, Phys. Rev. B **59**, 1677 (1999).

Chulkov, E. V., V. M. Silkin, and E. N. Shirykalov, Surf. Sci. **188**, 287 (1987).

Chulkov, E.V., and V.M. Silkin, Solid State Comm. **58**, 273 (1986).

Chung, J.W., in *Electronic Surface and Interface States on Metallic Systems*, Proceeding of the 134th We-Heraeus Seminar, ed. E. Bertel and M. Donath, pg. 127, World Sci., Singapore, 1995.

Claudia Bungaro, private communication.

Daum, W., C. Stuhlmann, and H. Ibach, Phys. Rev. Lett **60**, 2741 (1988).

Davis, H. L., and J.R. Noonan, Surf. Sci. **126**, 245 (1983).

Davis, H.L., and D. M. Zehner, J. Vac. Sci. Technol. **17**, 190 (1980).

Davisson, C., and L.H. Germer, Phys. Rev. **30**, 705 (1927).

DeWette, F.W., R.M.J. Cotterill, and M.Doyama, Phys. Lett. **23**, 309 (1966).

Egelhoff, W. F., Phys. Rev. Lett. **50**, 587 (1983).

Eguiluz, A. G., A. A. Maradudin, and R. F. Wallis, Phys. Rev. Lett. **60**, 309 (1988).

Eguiluz, A. G., and A. A. Quong, *Dynamical Properties of Solids*, Ed. G. K. Horton and A. A. Maradudin, Vol. 7 (North-Holland, Amsterdam, 1995).

Eguiluz, A. G., Phys. Rev. B **31**, 3303 (1985).

Eguiluz, A. G., Phys. Rev. B **35**, 5473 (1987).

Eguiluz, A.G., in *Surface Phonons*, Edited by W. Kress and F.W. de Wette, pp. 258, Springer-Verlag, Berlin, 1991.

Electronic Surface and Interface States on Metallic Systems, Proceeding of the 134th We-Heraeus Seminar, ed. E. Bertel and M. Donath, World Sci., Singapore, 1995.

Feynman, R. P., Phys. Rev. **56**, 340 (1939).

Finnis, M. W., and V. Heine, J. Phys. F **4**, L37 (1974).

Frenken, J.W., F. Huussen, and J.F. van der Veen, Phys. Rev. Lett. **58**, 401 (1987).

Frenken, J.W., J.F. van er Veen, R.N. Barnett, U. Landman, and C.L. Cleveland, Surf. Sci. **172**, 319 (1986).

Friedel, J., Nuovo Cimento Suppl. **7**, 287 (1958).

Gaspar, J. A., and A. G. Eguiluz, Phys. Rev. B **40**, 11976 (1989).

Gester, M., D. Kleinhesselink, P. Ruggerone, and J.P. Toennies, Phys. Rev. B **49**, 5777 (1994).

Gilat, G. and R.M. Nicklow, Phys. Rev. **143**, 487 (1966).

Göbel, H., and P. von Blanckenhagen, Phys. Rev. B **47**, 2378 (1993).

Grepstad, J.K., P.O. Gartland, and B.J. Slagvold, Surf. Sci. **57**, 348 (1976).

Hannon, J. B., E. J. Mele, and E. W. Plummer, Phys. Rev. B **53**, 2090 (1996).

Hannon, J. B., K. Pohl, P. J. Rous, and E. W. Plummer, Surf. Sci. **364**, L617 (1996).

Hannon, J. B., Ph.D. Thesis, University of Pennsylvania (1994).

Hansson, G.V., and S.A. Flodström, Phys. Rev. B **18**, 1562 (1978).

Heinrichsmeier, M., A. Fleszar, and A.G. Eguiluz, Surf. Sci. **285**, 129 (1993).

Heinz, K., Surf. Sci. **229/300**, 433 (1994).

Helgesen, G., D. Gibbs, A.P. Baddorf, D.M. Zehner, and S.G.J. Mochrie, Phys. Rev. **48**, 15320 (1993).

Herring, C., *The Physics of Powder Metallurgy,* Ed. W. E. Kingston (McGraw Hill, New York, 1951).

Ho, K. M., and K. P. Bohnen, Phys. Rev. B **32**, 3446 (1985).

Ho, K. M., and K. P. Bohnen, Phys. Rev. Lett. **56**, 934 (1986).

Hoffman, D.M., B. Singh, and J.H. Thomas, *Handbook of Vacuum Science and Technology* (Academic Press, San Diego, 1998).

Hofmann, Ph., and E. W. Plummer, Surf. Sci. **377-379**, 330 (1997).

Hofmann, Ph., B.G. Briner, M. Doering, H.-P. Rust, E.W. Plummer, and A.M. Bradshaw, Phys. Rev. Lett. **79**, 265 (1997).

Hofmann, Ph., K. Pohl, R. Stumpf, and E.W. Plummer, Phys. Rev. B **53**, 13715 (1996).

Hohenberg, P., and W. Kohn, Phys. Rev. **136**, B864 (1964).

Ibach, H. : *Electron Energy Loss Spectrometers - The Technology of High Performance* (Springer, Heidelberg, 1991).

Ibach, H., and D.L. Mills: *Electron Energy Loss Spectroscopy* (Academic Press, New York, 1982).

International Tables for X-Ray Crystallography Vol. III, The Kynoch Press, Birmingham, England, 1962. *Thermal Expansion: Metallic Elements and Alloys*, edited by

Thermophysical Properties Research Center at Perdue University, Thermophysical Properties of Matter Vol. 12, (IFI/Plenum New York, 1970).

Ismail , J.-H. Cho, Z. Zhang and E. W. Plummer, To be published

Ismail, A. T. Hanbicki , S. Chandravakar, D. M. Zehner, and E. Ward Plummer, To be published.

Ismail, Ph. Hofmann, E. W. Plummer, Claudia Bungaro, and W. Kress, To be published.

Itchkawitz, B. S., A. P. Baddorf, H. L. Davis, and E. W. Plummer, Phys. Rev. Lett. **68**, 2488 (1992).

Jayanthi, C. S., E. Tosatti, and L. Pietronero, Phys. Rev. B **31**, 3456 (1985).

Jayanthi, C.S., H. Bilz, W. Kress, and G. Benedek, Phys. Rev. Lett. **59**, 795 (1987).

Jiang, P., P. M. Marcus, and F. Jona, Solid State Comm. **59**, 275 (1986).

Kalkstein, D., and P. Soven, Surf. Sci. **26**, 85 (1971).

Kara, A., P. Staikov, A. N. Al-Rawi, and T. S. Rahman, Phys. Rev. B **55**, R13440 (1997).

Karlsson, U. O., G. Hansson, P. Persson, and S. A. Flodström, Phys. Rev. B **26**, 1852 (1982).

Kevan, S.D., in *Electronic Surface and Interface States on Metallic Systems*, edited by E. Bertel and M. Donath, page 1-11 (World Scientific, Singapore, 1995).

Kittel, C. : *Introduction to Solid State Physics* – 7th ed. Wiley, New York, 1996.

Kohn, W., and L. J. Sham, Phys. Rev. **140**, A1133 (1965).

Kuk, Y., and L.C. Feldman, Phys. Rev. B **30**, 5811(1984).

Landau, L.D., and E.M. Lifshitz, *Theory of Elasticity*, Course of Theoretical Physics, vol. 7, Permagnon Press, Oxford, 1986.

Landman, U., R. N. Hill, and M. Mostoller, Phys. Rev. B **21**, 448 (1980).

Lang, N. D., and W. Kohn, Phys. Rev. B **1**, 4555 (1970).

Lazzeri, M., and S. de Gironcoli, Surf. Sci. **402**, 715 (1998).

Lazzeri, M., and Stefano de Gironcoli, Phys. Rev. Lett. **81**, 2096 (1998).

Lehwald, S., F. Wolf, H. Ibach, B. M. Hall, and D. L. Mills, Surf. Sci. **192**, 131 (1987).

Lehwald, S., F. Wolf, H. Ibach, T.S. Rahman, and D.L. Mills, Phys. Rev. Lett. **50**, 518 (1983).

Lindroos, M., C. J. Barnes, P. Hu, and D. A. King, Chem. Phys. Lett. **173**, 92 (1990).

Lizzit, S., K. Pohl, A. Baraldi, G. Comeli, V. Fritzsche, E.W. Plummer, R. Stumpf, and Ph. Hofmann, Phy. Rev. Lett. **81**, 3271 (1998).

Lock, A., J.P. Toennies, and Ch. Wöll; V. Bortolani, A. Franchini, and G. Santoro, Phys. Rev. B **37**, 7087 (1988).

Loucks, T. : *Augmented Plane Wave Method* (Benjamin, New York, 1967).

Ma, S. K. S., F. W. de Wette, and G. P. Alldredge, Surf. Sci. **78**, 598 (1978).

Maradudin, A. A. : *The Dynamical Properties of Solids,* Vol. 1 edited by G.K. Horton, A.A. Maradudin (Nort-Holland, Amsterdam, American Elsevier, New York 1974).

Marzari, N., D. Vanderbilt, A. De Vita, and M. C. Payne, Phys. Rev. Lett. **82**, 3296 (1999).

Mattheiss, L.F., Phys. Rev **133**, A1399 (1964).

Mischenko III, J., and P. R. Watson, Surf. Sci. **220**. L667 (1989)

Mohamed, M. H., and L. L. Kesmodel, Phys. Rev. B **37**, 6519 (1988).

Moritz, W., and D. Wolf, Surf. Sci. **163**, L655 (1985).

Moruzzi, V. L., J. F. Janak, and A. R. Williams, *Calculated Electronic Properties of Metal,* Plenum, New York, 1978.

Mostoller, M., R.M. Nicklow, D.M. Zehner, S.-C. Lui, J.M. Mundenar, and E.W. Plummer, Phys. Rev. B **40**, 2856 (1989).

Müller, K., and K. Heinz, in The Structure of Surface, edited by S.Y. Tong and M. A. Van Hove, Springer Series in Surface Science Vol. 2, pp. 105-112 (Springer, Berlin, 1985).

Narasimhan, S., and M. Scheffler, Z. Phys. Chem. **202**, 253 (1997).

Needs, R. J., M. J. Godfrey, and M. Mansfield, Surf. Sci. **242**, 215 (1991).

Needs, R. J., Phys. Rev. Lett. **58**, 53 (1987).

Nelson, J. S., and P. J. Feibelman, Phys. Rev. Lett. **68**, 2188 (1992).

Nielsen, H. B., and D. L. Adams, J. Phys. C **15**, 615 (1982).

Ning, T., Q. Yu, and Y.Ye, Surf. Sci. Lett. **206**, L857 (1988).

Noonan, J. R., and H. L. Davis, Phys. Rev. B **29**, 4349 (1984).

Noonan, J.R., and H. L. Davis, J. Vac. Sci. Tech. A **8**, 2671(1990).

Noonan, J.R., and H.L. Davis, Science **234**, 310 (1986).

Noonan, J.R., H.L. Davis, and W. Erley, Surf. Sci. **152/153**, 142 (1985).

O'Hanlon, J.F. : *A User's Guide to Vacuum Technology* (Wiley, New York, 1989).

Over, H., G. Kleinle, G. Ertl, W. Moritz, K. -H. Ernst, H. Wohlgemuth, K. Christmann, and E. Schwarz, Surf. Sci. **254**, L469 (1991).

Park, R.L., and H.E. Farnsworth, Surf. Sci. **2**, 527 (1964).

Payne, M.C., N. Roberts, R. J. Needs, M. Needels, and J.D. Joannopoulos, Surf. Sci. **211/212,** 1 (1989).

Pendry, J. B., *Low Energy Electron Diffraction* , Academic Press., London, 1974.

Pendry, J.B., J. Phys. C **4**, 2514 (1971).

Persson, B.N.J., Solid State Comm. **24**, 573 (1977).

Persson, B.N.J., Surf. Sci. **92**, 265 (1980).

Pines, D., and P. Nozières, *The Theory of Quantum Liquids*, Vol. 1 (Benjamin, New York, 1966).

Pohl, K., J. -H. Cho, K. Terakura, M. Scheffler, and E. W. Plummer, Phys. Rev. Letter. **80**, 2853 (1998).

Pohl, K., Ph.D. Thesis, University of Pennsylvania (1997).

Pynn, R., and G. L. Squires, Proc. Roy. Soc. (London) A **326**, 347 (1972).

Quinn, J., Y.S. Li, D. Tian, H. Li, F. Jona, and P.M. Marcus, Phys. Rev. B **42**, 11348 (1990).

Raphuthi, A.M., X.Q. Wang, F. Ercolessi, and J.B. Adam, Phys. Rev. B **52**, R5554 (1995).

Rosenstock, H.B., Phys. Rev. B **9**, 1963 (1974).

Rous, P.J., and J.B. Pendry, Surf. Sci. **219**, 355 (1989).

Rous, P.J., and J.B. Pendry, Surf. Sci. **219**, 373 (1989).

Rous, P.J., J.B. Pendry, D.K. Saldin, K. Heinz, K. Müller, and N. Bickel, Phys. Rev. Lett. **57**, 2951 (1986).

Rous, P.J., Progr. Surf. Sci. **39**, 3 (1992).

Roy, A.P., B.A. Dasannacharya, C.L. Thaper, and P.K. Iyengar, Phys. Rev. Lett. **30**, 906 (1973).

Sakurai, J.J. : *Modern Quantum Mechanics* (Addison-Wesley, New York, 1985).

Schwarz, K., Phys. Rev. B **5**, 2466 (1972).

Seitsonen, A. P., B. Hammer, and M. Scheffler (unpublished).

Slater, J.C. : *Insulators Semiconductors and Metals* (McGraw Hill, New York, 1967).

Smoluchowski, R., Phys. Rev. **60**, 661 (1941).

Sprunger, P. T., K. Pohl, H. L. Davis, and E. W. Plummer, Surf. Sci. **297**, L48 (1993).

Sprunger, P. T., Ph.D. Thesis, Univeristy of Pennsylvania, 1993.

Sprunger, P.T., K. Pohl, H.L. Davis, and E.W. Plummer, Surf. Sci. **297**, L48 (1993).

Sprunger, P.T., L. Petersen, E.W. Plummer, E. Laegsgaard, and F. Besenbacher, Science **275**, 1764 (1997).

Staikov, P., and Talat S. Rahman, To be published.

Statiris, P., H.C. Lu, and T. Gustafsson, Phys. Rev. Lett. **72**, 3574 (1994).

Stedman, R., and G. Nilsson, Phys. Rev. **145**, 492 (1966).

Stedman, R., Z. Amilius, R. Pauli, and O. Sundin, J. Phys. F **6**, 157 (1976).

Stumpf, R., J.B. Hannon, P.J. Feibelman, and E.W. Plummer, in *Electronic Surface and Interface States on Metalic Systems,* edited by E. Bertel and M. Donath, pp. 151 (World Scientific, Singapore, 1995).

Toennies, J.P., and Ch. Wöll, Phys. Rev. B **36**, 4475 (1987).

Van Hove, M.A., and R.J. Koestner, in *Determination of Surface Structure by LEED,* edited by P.M. Marcus and F. Jona, The IBM Research Symposia Series (Plenum, New York, 1984).

Van Hove, M.A., and S.Y. Tong: *Surface Crystallography by LEED* (Springer, Berlin, 1979).

Van Hove, M.A., W. Moritz, H. Over, P.J. Rous, A. Wander, A. Barbieri, N. Materer, U. Starke, and G.A. Samorjai, Surf. Sci. Rep. **19**, 191 (1993).

Van Hove, M.A., W.H. Weinberg, and C.-M. Chan: *Low-Energy Electron Diffraction* (Springer, Berlin, 1986).

Wright, Alan F., and D. C. Chrzan, Phys. Rev. Lett. **70**, 1964 (1993).

Wright, Alan F., P. J. Feibelman, Susan R. Atlas, Surf. Sci. **302**, 215 (1994).

Wuttig, M., R. Franchy, and H. Ibach, Solid State Comm. **57**, 455 (1986).

Xie, J., and M. Scheffler, Phys. Rev. B **78**, 4768 (1998).

Zangwill, A. : *Physics at Surfaces* (Cambridge University Press, Cambridge, 1988).

Zhang, X.-G., M.A Van Hove, G.A. Somorjai, P.J. Rous, D. Tobin, A. Gonis, J.M. MacLaren, K. Heinz, M. Michl, H. Linder, and K. Müller, Phys. Rev. Lett. **67**, 1298 (1991).

APPENDICES

Appendix A

Atomic Phase Shifts

Table A.1: Phase shifts for magnesium (in radian units) for l=0, 1, 2,..., 14 as a function of the kinetic energy of electron.

.3675	Hartree	10 eV												
-.0696	.2755	.1015	.0059	.0003	.0000	.0000	.0000	.0000	.0000	.0000	.0000	.0000	.0000	.0000
.5514		15 eV												
-.2611	.3026	.2350	.0197	.0016	.0001	.0000	.0000	.0000	.0000	.0000	.0000	.0000	.0000	.0000
.7352		20 eV												
-.4223	.2796	.3906	.0437	.0046	.0004	.0000	.0000	.0000	.0000	.0000	.0000	.0000	.0000	.0000
.9191		25 eV												
-.5594	.2359	.5343	.0770	.0103	.0011	.0001	.0000	.0000	.0000	.0000	.0000	.0000	.0000	.0000
1.1029		30 eV												
-.6771	.1859	.6503	.1172	.0190	.0024	.0002	.0000	.0000	.0000	.0000	.0000	.0000	.0000	.0000
1.2868		35 eV												
-.7795	.1359	.7389	.1608	.0308	.0046	.0005	.0000	.0000	.0000	.0000	.0000	.0000	.0000	.0000
1.4706		40 eV												
-.8695	.0889	.8074	.2046	.0457	.0080	.0011	.0001	.0000	.0000	.0000	.0000	.0000	.0000	.0000
1.6545		45 eV												
-.9497	.0457	.8623	.2459	.0630	.0126	.0019	.0002	.0000	.0000	.0000	.0000	.0000	.0000	.0000
1.8383		50 eV												
-1.0220	.0063	.9084	.2835	.0820	.0185	.0032	.0004	.0000	.0000	.0000	.0000	.0000	.0000	.0000
2.7576		75 eV												
-1.3092	-.1505	1.0679	.4151	.1772	.0646	.0182	.0039	.0007	.0001	.0000	.0000	.0000	.0000	.0000
3.6768		100 eV												
-1.5263	-.2732	1.1509	.5013	.2448	.1178	.0474	.0148	.0036	.0007	.0001	.0000	.0000	.0000	.0000
4.5961		125 eV												
-1.6992	-.3732	1.1983	.5667	.2947	.1592	.0807	.0337	.0110	.0028	.0006	.0001	.0000	.0000	.0000
5.5153		150 eV												
-1.8416	-.4553	1.2300	.6141	.3372	.1914	.1087	.0560	.0235	.0076	.0019	.0004	.0001	.0000	.0000
6.4346		175 eV												
-1.9637	-.5258	1.2510	.6508	.3717	.2200	.1311	.0761	.0389	.0159	.0050	.0012	.0003	.0000	.0000

Table A.1:(continued)
Phase shifts for magnesium (in radian units) for l=0, 1, 2,..., 14 as a function of the kinetic energy of electron.

==========

7.3538 200 eV
-2.0699 -.5868 1.2664 .6801 .4003 .2451 .1514 .0926 .0538 .0267 .0104 .0031 .0007 .0001 .0000
8.2731 225 eV
-2.1622 -.6388 1.2784 .7025 .4257 .2661 .1703 .1075 .0666 .0381 .0179 .0066 .0019 .0004 .0001
9.1923 250 eV
-2.2444 -.6849 1.2854 .7215 .4473 .2852 .1865 .1220 .0777 .0483 .0265 .0116 .0039 .0010 .0002
10.1116 275 eV
-2.3208 -.7287 1.2881 .7401 .4639 .3040 .2003 .1355 .0887 .0570 .0349 .0180 .0072 .0022 .0005
11.0308 300 eV
-2.3930 -.7707 1.2904 .7572 .4776 .3209 .2138 .1466 .0999 .0651 .0421 .0248 .0117 .0042 .0011
11.9501 325 eV
-2.4593 -.8081 1.2955 .7695 .4921 .3338 .2283 .1560 .1102 .0738 .0484 .0310 .0170 .0071 .0023
12.8693 350 eV
-2.5171 -.8383 1.3012 .7768 .5083 .3433 .2426 .1656 .1184 .0829 .0546 .0364 .0224 .0110 .0040
13.7886 375 eV
-2.5668 -.8630 1.3030 .7830 .5234 .3528 .2539 .1770 .1249 .0913 .0616 .0410 .0273 .0154 .0066
14.7078 400 eV
-2.6122 -.8870 1.2989 .7928 .5335 .3652 .2612 .1894 .1315 .0979 .0693 .0458 .0313 .0199 .0099
15.6271 425 eV
-2.6583 -.9143 1.2921 .8068 .5383 .3801 .2666 .2004 .1399 .1026 .0767 .0514 .0348 .0239 .0137
16.5463 450 eV
-2.7070 -.9449 1.2882 .8204 .5416 .3938 .2738 .2076 .1505 .1068 .0826 .0580 .0384 .0271 .0175
17.4656 475 eV
-2.7565 -.9746 1.2908 .8283 .5485 .4023 .2851 .2113 .1614 .1123 .0865 .0648 .0428 .0297 .0208
18.3848 500 eV
-2.8023 -.9980 1.2983 .8289 .5614 .4049 .2994 .2141 .1700 .1204 .0890 .0706 .0483 .0323 .0235
19.3041 525 eV
-2.8400-1.0128 1.3045 .8258 .5776 .4051 .3127 .2195 .1746 .1306 .0920 .0745 .0546 .0356 .0256
20.2233 550 eV
-2.8685-1.0214 1.3036 .8252 .5910 .4082 .3208 .2298 .1758 .1406 .0971 .0765 .0605 .0400 .0274

Table A.1:(continued)
Phase shifts for magnesium (in radian units) for l=0, 1, 2,..., 14 as a function of the kinetic energy of electron.

21.1426	575 eV												
-2.8913	-1.0301	1.2945	.8323	.5968	.4179	.3224	.2438	.1765	.1478	.1050	.0777	.0650	.0454	.0296
22.0618	600 eV												
-2.9147	-1.0451	1.2813	.8469	.5948	.4337	.3202	.2576	.1801	.1508	.1150	.0798	.0674	.0513	.0328
22.9811	625 eV												
-2.9440	-1.0682	1.2710	.8635	.5897	.4506	.3193	.2666	.1889	.1503	.1246	.0845	.0682	.0566	.0372
23.9003	650 eV												
-2.9808	-1.0961	1.2695	.8746	.5879	.4622	.3243	.2687	.2024	.1490	.1313	.0922	.0684	.0602	.0426
24.8196	675 eV												
-3.0219	-1.1227	1.2780	.8755	.5948	.4649	.3372	.2654	.2170	.1504	.1337	.1021	.0697	.0617	.0482
25.7388	700 eV												
-3.0617	-1.1413	1.2920	.8673	.6109	.4597	.3552	.2609	.2281	.1570	.1322	.1118	.0737	.0615	.0530
26.6581	725 eV												
-3.0941	-1.1485	1.3029	.8558	.6315	.4518	.3723	.2604	.2324	.1692	.1293	.1188	.0809	.0609	.0561
27.5773	750 eV												
-3.1149	-1.1458	1.3038	.8485	.6483	.4479	.3822	.2676	.2299	.1843	.1281	.1215	.0906	.0613	.0572

Table A.2: Phase shifts for Sn (in radian units) for l=0, 1, 2,..., 14 as a function of the kinetic energy of electron.

==========

.3675 Hartree 10 eV
.7819 1.3434 .1001 .0227 .0006 .0000 .0000 .0000 .0000 .0000 .0000 .0000 .0000 .0000 .0000
.5514 15 eV
.4180 1.1355 .2361 .0955 .0035 .0001 .0000 .0000 .0000 .0000 .0000 .0000 .0000 .0000 .0000
.7352 20 eV
.1400 .9396 .3763 .2860 .0111 .0006 .0000 .0000 .0000 .0000 .0000 .0000 .0000 .0000 .0000
.9191 25 eV
-.0851 .7637 .4735 .7093 .0266 .0019 .0001 .0000 .0000 .0000 .0000 .0000 .0000 .0000 .0000
1.1029 30 eV
-.2732 .6069 .5176 1.3128 .0536 .0044 .0003 .0000 .0000 .0000 .0000 .0000 .0000 .0000 .0000
1.2868 35 eV
-.4333 .4670 .5205 1.7420 .0952 .0091 .0007 .0000 .0000 .0000 .0000 .0000 .0000 .0000 .0000
1.4706 40 eV
-.5715 .3422 .4967 1.9777 .1540 .0165 .0015 .0001 .0000 .0000 .0000 .0000 .0000 .0000 .0000
1.6545 45 eV
-.6919 .2309 .4571 2.1302 .2307 .0277 .0029 .0002 .0000 .0000 .0000 .0000 .0000 .0000 .0000
1.8383 50 eV
-.7979 .1315 .4089 2.2550 .3230 .0434 .0051 .0005 .0000 .0000 .0000 .0000 .0000 .0000 .0000
2.7576 75 eV
-1.1928 -.2309 .1570 2.7936 .7863 .2054 .0378 .0056 .0007 .0001 .0000 .0000 .0000 .0000 .0000
3.6768 100 eV
-1.4900 -.4708 -.0195 3.0108 .9849 .4470 .1277 .0266 .0044 .0006 .0001 .0000 .0000 .0000 .0000
4.5961 125 eV
-1.7573 -.6792 -.1296 3.0701 1.1001 .6117 .2674 .0769 .0168 .0029 .0004 .0000 .0000 .0000 .0000
5.5153 150 eV
-1.9985 -.8792 -.2257 3.1283 1.2446 .6863 .3986 .1588 .0446 .0098 .0017 .0003 .0000 .0000 .0000
6.4346 175 eV
-2.2067-1.0631 -.3314 3.1897 1.3861 .7354 .4803 .2535 .0917 .0248 .0054 .0009 .0001 .0000 .0000
7.3538 200 eV
-2.3807-1.2222 -.4398 3.2235 1.4823 .7974 .5217 .3337 .1542 .0512 .0132 .0028 .0005 .0001 .0000
8.2731 225 eV
-2.5263-1.3549 -.5382 3.2283 1.5443 .8728 .5488 .3858 .2200 .0894 .0274 .0067 .0014 .0002 .0000

Table A.2:(continued)
Phase shifts for Sn (in radian units) for l=0, 1, 2,..., 14 as a function of the kinetic energy of electron.

==========

9.1923 250 eV
-2.6537-1.4667 -.6195 3.2221 1.5995 .9425 .5806 .4147 .2759 .1361 .0494 .0141 .0033 .0006 .0001
10.1116 275 eV
-2.7721-1.5666 -.6852 3.2201 1.6605 .9936 .6228 .4324 .3150 .1842 .0790 .0260 .0069 .0015 .0003
11.0308 300 eV
-2.8868-1.6620 -.7419 3.2266 1.7230 1.0283 .6699 .4500 .3386 .2267 .1141 .0433 .0131 .0033 .0007
11.9501 325 eV
-2.9989-1.7564 -.7968 3.2367 1.7760 1.0565 .7125 .4736 .3527 .2590 .1508 .0659 .0226 .0063 .0015
12.8693 350 eV
-3.1070-1.8498 -.8538 3.2428 1.8139 1.0868 .7450 .5034 .3636 .2807 .1848 .0925 .0358 .0112 .0029
13.7886 375 eV
-3.2087-1.9400 -.9132 3.2406 1.8393 1.1225 .7675 .5357 .3764 .2939 .2128 .1209 .0527 .0183 .0053
14.7078 400 eV
-3.3020-2.0244 -.9727 3.2309 1.8588 1.1614 .7843 .5655 .3937 .3026 .2336 .1486 .0728 .0282 .0089
15.6271 425 eV
-3.3861-2.1012-1.0290 3.2174 1.8787 1.1983 .8004 .5893 .4152 .3101 .2475 .1732 .0949 .0408 .0142
16.5463 450 eV
-3.4614-2.1695-1.0794 3.2050 1.9021 1.2287 .8196 .6064 .4388 .3193 .2564 .1932 .1175 .0559 .0214
17.4656 475 eV
-3.5298-2.2302-1.1227 3.1968 1.9288 1.2509 .8430 .6182 .4615 .3316 .2625 .2082 .1388 .0729 .0306
18.3848 500 eV
-3.5941-2.2854-1.1594 3.1941 1.9553 1.2665 .8695 .6276 .4809 .3471 .2678 .2186 .1576 .0909 .0418
19.3041 525 eV
-3.6568-2.3380-1.1916 3.1954 1.9776 1.2789 .8960 .6376 .4955 .3648 .2741 .2254 .1731 .1089 .0546
20.2233 550 eV
-3.7202-2.3907-1.2224 3.1974 1.9929 1.2919 .9193 .6502 .5057 .3829 .2825 .2301 .1850 .1259 .0687
21.1426 575 eV
-3.7851-2.4451-1.2547 3.1967 2.0011 1.3082 .9372 .6666 .5124 .3995 .2933 .2338 .1937 .1411 .0835
22.0618 600 eV
-3.8513-2.5016-1.2901 3.1907 2.0041 1.3288 .9493 .6859 .5177 .4133 .3063 .2379 .1996 .1539 .0981

Table A.2:(continued)
Phase shifts for Sn (in radian units) for l=0, 1, 2,..., 14 as a function of the kinetic energy of electron.

22.9811	625 eV												
-3.9174	-2.5596	-1.3289	3.1792	2.0055	1.3523	.9571	.7065	.5235	.4235	.3206	.2432	.2035	.1642	.1121
23.9003	650 eV												
-3.9815	-2.6171	-1.3698	3.1637	2.0085	1.3758	.9631	.7258	.5316	.4301	.3351	.2503	.2064	.1719	.1248
24.8196	675 eV												
-4.0416	-2.6721	-1.4107	3.1470	2.0160	1.3958	.9701	.7414	.5430	.4340	.3482	.2594	.2090	.1775	.1359
25.7388	700 eV												
-4.0962	-2.7226	-1.4490	3.1322	2.0285	1.4098	.9805	.7522	.5576	.4365	.3591	.2702	.2121	.1814	.1451
26.6581	725 eV												
-4.1443	-2.7670	-1.4824	3.1221	2.0448	1.4175	.9955	.7582	.5743	.4392	.3670	.2820	.2162	.1839	.1526
27.5773	750 eV												
-4.1862	-2.8050	-1.5097	3.1179	2.0617	1.4199	1.0145	.7608	.5912	.4436	.3718	.2941	.2218	.1857	.1582

Table A.3: Phase shifts for Ge (in radian units) for l=0, 1, 2,..., 14 as a function of the kinetic energy of electron.

==========

.3675 Hartree 10 eV
.8867 1.1725 .0650 .0055 .0002 .0000 .0000 .0000 .0000 .0000 .0000 .0000
.0000 .0000 .0000
.5514 15 eV
.5778 1.1246 .1634 .0205 .0010 .0000 .0000 .0000 .0000 .0000 .0000 .0000
.0000 .0000 .0000
.7352 20 eV
.3435 1.0198 .2903 .0505 .0031 .0002 .0000 .0000 .0000 .0000 .0000 .0000
.0000 .0000 .0000
.9191 25 eV
.1544 .9077 .4153 .0995 .0074 .0005 .0000 .0000 .0000 .0000 .0000 .0000
.0000 .0000 .0000
1.1029 30 eV
-.0035 .8003 .5141 .1695 .0149 .0012 .0001 .0000 .0000 .0000 .0000 .0000
.0000 .0000 .0000
1.2868 35 eV
-.1382 .7009 .5793 .2589 .0263 .0024 .0002 .0000 .0000 .0000 .0000 .0000
.0000 .0000 .0000
1.4706 40 eV
-.2548 .6103 .6152 .3622 .0424 .0044 .0004 .0000 .0000 .0000 .0000 .0000
.0000 .0000 .0000
1.6545 45 eV
-.3569 .5282 .6295 .4705 .0637 .0075 .0007 .0001 .0000 .0000 .0000 .0000
.0000 .0000 .0000
1.8383 50 eV
-.4473 .4542 .6293 .5742 .0902 .0118 .0012 .0001 .0000 .0000 .0000 .0000
.0000 .0000 .0000
2.7576 75 eV
-.7877 .1787 .5538 .9013 .2811 .0602 .0098 .0013 .0001 .0000 .0000 .0000
.0000 .0000 .0000
3.6768 100 eV
-1.0397 -.0071 .4915 1.0466 .4624 .1550 .0362 .0064 .0009 .0001 .0000 .0000
.0000 .0000 .0000
4.5961 125 eV
-1.2586 -.1658 .4605 1.1815 .5625 .2652 .0861 .0203 .0037 .0005 .0001 .0000
.0000 .0000 .0000
5.5153 150 eV
-1.4535 -.3151 .4281 1.3094 .6187 .3504 .1526 .0466 .0107 .0019 .0003 .0000
.0000 .0000 .0000
6.4346 175 eV
-1.6225 -.4519 .3830 1.3999 .6713 .4013 .2187 .0853 .0242 .0053 .0009 .0001
.0000 .0000 .0000
7.3538 200 eV
-1.7661 -.5707 .3336 1.4594 .7308 .4326 .2699 .1309 .0456 .0120 .0025 .0004
.0001 .0000 .0000
8.2731 225 eV
-1.8887 -.6714 .2902 1.5081 .7883 .4602 .3032 .1751 .0740 .0232 .0057 .0011
.0002 .0000 .0000

Table A.3:(continued)
Phase shifts for Ge (in radian units) for l=0, 1, 2,..., 14 as a function of the kinetic energy of electron.

==========

9.1923 250 eV
-1.9971 -.7580 .2561 1.5567 .8341 .4921 .3244 .2110 .1064 .0394 .0112 .0025 .0005 .0001 .0000
10.1116 275 eV
-2.0970 -.8364 .2286 1.6037 .8674 .5275 .3414 .2364 .1384 .0601 .0197 .0051 .0011 .0002 .0000
11.0308 300 eV
-2.1917 -.9106 .2028 1.6435 .8941 .5612 .3598 .2532 .1661 .0838 .0315 .0092 .0022 .0004 .0001
11.9501 325 eV
-2.2818 -.9822 .1756 1.6737 .9197 .5889 .3816 .2654 .1873 .1080 .0466 .0154 .0041 .0009 .0002
12.8693 350 eV
-2.3667-1.0507 .1470 1.6966 .9470 .6102 .4052 .2769 .2022 .1303 .0642 .0239 .0071 .0017 .0003
13.7886 375 eV
-2.4452-1.1147 .1189 1.7160 .9748 .6272 .4278 .2901 .2125 .1489 .0828 .0348 .0114 .0030 .0007
14.7078 400 eV
-2.5174-1.1734 .0932 1.7349 1.0006 .6431 .4469 .3058 .2208 .1630 .1011 .0477 .0174 .0051 .0012
15.6271 425 eV
-2.5838-1.2269 .0707 1.7538 1.0224 .6599 .4620 .3227 .2291 .1731 .1175 .0621 .0250 .0080 .0021
16.5463 450 eV
-2.6460-1.2764 .0509 1.7714 1.0405 .6779 .4742 .3392 .2389 .1803 .1310 .0768 .0344 .0120 .0034
17.4656 475 eV
-2.7054-1.3234 .0323 1.7862 1.0564 .6961 .4852 .3536 .2506 .1864 .1414 .0911 .0451 .0173 .0054
18.3848 500 eV
-2.7632-1.3691 .0136 1.7974 1.0718 .7129 .4966 .3652 .2633 .1926 .1491 .1039 .0568 .0239 .0080
19.3041 525 eV
-2.8197-1.4142 -.0061 1.8058 1.0881 .7271 .5092 .3745 .2760 .1999 .1546 .1146 .0688 .0317 .0115
20.2233 550 eV
-2.8746-1.4585 -.0264 1.8129 1.1050 .7389 .5227 .3826 .2876 .2087 .1593 .1230 .0803 .0406 .0160
21.1426 575 eV
-2.9271-1.5011 -.0463 1.8203 1.1216 .7492 .5361 .3907 .2972 .2185 .1639 .1292 .0908 .0502 .0215
22.0618 600 eV
-2.9764-1.5411 -.0645 1.8290 1.1364 .7595 .5481 .3998 .3048 .2288 .1693 .1338 .0998 .0600 .0279

Table A.3:(continued)
Phase shifts for Ge (in radian units) for l=0, 1, 2,..., 14 as a function of the kinetic energy of electron.

==========

22.9811 625 eV
-3.0219-1.5778 -.0801 1.8386 1.1485 .7709 .5581 .4100 .3111 .2385 .1759 .1375 .1071 .0697 .0352
23.9003 650 eV
-3.0637-1.6109 -.0929 1.8482 1.1579 .7837 .5661 .4210 .3169 .2469 .1836 .1410 .1126 .0787 .0431
24.8196 675 eV
-3.1025-1.6410 -.1037 1.8561 1.1656 .7975 .5727 .4318 .3232 .2537 .1920 .1450 .1167 .0866 .0513
25.7388 700 eV
-3.1393-1.6693 -.1138 1.8613 1.1729 .8111 .5793 .4415 .3306 .2590 .2004 .1498 .1198 .0932 .0595
26.6581 725 eV
-3.1756-1.6971 -.1248 1.8633 1.1815 .8230 .5868 .4493 .3392 .2634 .2081 .1557 .1226 .0984 .0674
27.5773 750 eV
-3.2125-1.7258 -.1376 1.8627 1.1922 .8324 .5960 .4551 .3487 .2676 .2146 .1625 .1254 .1023 .0746

==========

Appendix B
Conversions

$$k_B = 8.617 \times 10^{-5} \frac{eV}{K} \tag{B.1}$$

$$\frac{\hbar^2}{2\, m_e} = 3.810 \text{ eV Å}^2 \tag{B.2}$$

$$\lambda\,[\text{Å}] = \sqrt{150 / E\,[\text{eV}]} \tag{B.3}$$

$$1 \text{ Torr} = 133.3 \text{ Pa} = 0.780 \text{ bar} \tag{B.4}$$

$$1 \text{ bohr} \equiv a_0 \equiv \frac{\hbar^2}{m_e\, e^2} = 0.529177 \text{ Å} \tag{B.5}$$

$$1 \text{ Ry}_{[\text{dberg}]} \equiv \frac{m_e\, e^4}{2\, \hbar^2} = 13.6058 \text{ eV} \tag{B.6}$$

$$1 \text{ H}_{[\text{artree}]} \equiv 2 \text{ Ry} = 27.2116 \text{ eV} \tag{B.7}$$

Appendix C

Formulae for the Free Electron Gas

$$\frac{4\pi}{3} r_s^3 = \frac{1}{n_0 a_0^3} \tag{C.1}$$

$$n_0 = 2 \int \frac{\mathrm{d}^3 k}{(2\pi)^3} n_k = \frac{1}{\pi^2} \int_0^{k_F} k^2 \, \mathrm{d}k = \frac{k_F^3}{3\pi^2} \tag{C.2}$$

$$k_F a_0 = \left(\frac{9\pi}{4}\right)^{1/3} \frac{1}{r_s} = \frac{1.9192}{r_s} \tag{C.3}$$

$$k_F = \frac{3.6267}{r_s} \text{ Å}^{-1}$$

$$E_F = \frac{\hbar^2 k_F^2}{2 m_e} = \frac{3.6832}{r_s^2} \text{ Ry} = \frac{50.113}{r_s^2} \text{ eV} \tag{C.4}$$

$$g(E) = \frac{3}{2} \frac{n_0}{E_F} \sqrt{\frac{E}{E_F}} \tag{C.5}$$

$$g(E_F) = \frac{m k_F}{\hbar^2 \pi^2} = \frac{3}{2} \frac{n_0}{E_F} = \frac{0.048223}{r_s} \frac{\text{states}}{\text{eV Å}^3} \tag{C.6}$$

$$N(E_F) = \frac{0.048223}{r_s / V_0} \frac{\text{states}}{\text{eV - atom}} \tag{C.7}$$

VITA

Ismail was born in Sigli, small city in the province of Aceh, Indonesia on January 14, 1963. He graduated from high school in his home town in 1982. He received a Sarjana's degree in Engineering Physics with major in Instrumentation at the Sepuluh Nopember Institute of Technology, Surabaya, Indonesia in 1987. Right after getting a Sarjana's degree, he jointed to the Physics Department and Chemical Engineering Department as a teaching staff at the University of Syiah Kuala, Banda Aceh, Indonesia. He afterward attended the University of Tennessee, Knoxville, where he received a Master of Science degree in Physics in 1993, and a Doctor of Philosophy degree in Physics with major in Solid State Physics (Surface Physics) in 1999. He was a Graduate Research Assistant with Prof. E. Ward Plummer (Physics Department) from 1996 to 1999. Areas of his research interest include: investigations of the thermal effects on the atomic structure and dynamics at surfaces. He has significant ultrahigh vacuum (UHV) experiences, including Low Energy Electron Diffraction (LEED), High Resolution Energy Loss Spectroscopy (HREELS), Auger Electron Spectroscopy (AES), and Mass Spectroscopy. He also has significant computer programming experiences: calculate atomic phase shifts for many elements, such as H, Be, Mg, Al, Ni, Sn, Ge, and Cu, and perform multiple electron scattering calculations (LEED *I-V* analysis) in determining the surface structures and surface domains of metals, alloys, and semiconductors.